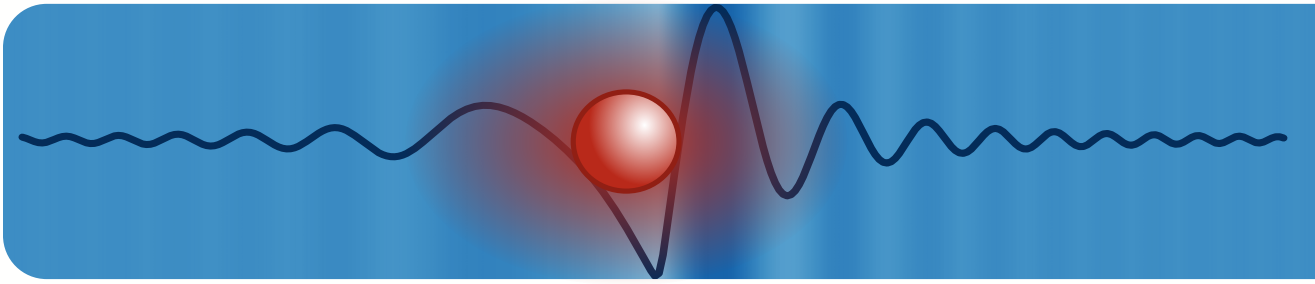

Equilibrium, non-equilibrium, and steady-state properties of quantum impurities in 1D Bose gases

or

heavy quantum dirt in cold thin air

– Dissertation –

Martin Heinrich Will

Dezember 2023

RPTU Rheinland-Pfälzische Technische Universität Kaiserslautern Landau

Physik

Equilibrium, non-equilibrium, and steady-state properties of quantum impurities in 1D Bose gases

– Dissertation –

Martin Heinrich Will

Vom Fachbereich Physik der Rheinland-Pfälzischen Technischen Universität
Kaiserslautern-Landau zur Verleihung des akademischen Grades
„Doktor der Naturwissenschaften“ genehmigte Dissertation

Betreuer: **Prof. Dr. Michael Fleischhauer**
Zweitgutachter: **Prof. Dr. Artur Widera**

Datum der wissenschaftlichen Aussprache:
08. Dezember 2023

DE-386

The Road goes ever on and on
Down from the door where it began.
Now far ahead the Road has gone,
And I must follow, if I can,
Pursuing it with eager feet,
Until it joins some larger way
Where many paths and errands meet.
And whither then? I cannot say.

Bilbo Baggins
John Ronald Reuel Tolkien

Abstract

The Bose polaron, a quasi-particle formed by an impurity interacting with a gas of condensed bosonic atoms, is a fundamental problem of many-body physics. The Fröhlich model accurately describes the polaron's properties for scenarios with weak impurity-boson coupling. In this model, the interaction is characterized by the generation, emission, and binding of Bogoliubov phonons, which are small excitations of a homogeneous condensate. However, the Fröhlich model is no longer adequate for strong coupling between impurity and boson, as the impurity deforms the Bose gas substantially. In this thesis, a different model is developed to describe the one-dimensional Bose polaron. It takes into account the feedback effect of the impurity on the condensate at the mean-field level and is suitable for treating the strong impurity-boson coupling limit. Both equilibrium and non-equilibrium properties of the Bose polaron are investigated, focusing on one-dimensional systems.

First, the ground state properties of a single polaron are characterized. As the impurity becomes dressed by the deformation cloud, it undergoes a shift in energy and an increase in the effective mass. Both quantities are derived analytically and compared to exact diffusion Monte Carlo simulation results, showing excellent agreement.

The theory is then extended to a pair of impurities to study the polaron interaction induced by the many-body environment, leading to the formation of a bipolaron. The induced potential is derived in Born-Oppenheimer approximation of heavy impurities and extended to include the leading order Born-Huang correction. Both the potential, and the binding energy of the bipolaron exhibit excellent agreement with the results obtained from exact Monte Carlo simulations.

Subsequently, non-equilibrium properties are investigated by generalizing to a fluctuating impurity coupling. It is demonstrated how noise tuning of this interaction can be employed to control coherent currents in the condensate flowing towards the impurity and accompanied by an incoherent counterflow of excited atoms. Depending on the strength of the noise and the velocity of a single impurity, three distinct dynamical regimes emerge: I. A linear response regime, II. a Zeno regime with suppressed currents, and III. a regime of continuous soliton emission. This analysis is further extended to a pair of noisy impurities, where the influence of induced currents by the individual impurities on each other is investigated.

Finally, the thesis examines the polaron formation dynamics after either a sudden quench or quasi-adiabatic turn-on of the impurity-boson coupling strength. A diverse range of dynamical regimes is found, including reversible and non-reversible deceleration of the impurity. Surprisingly, even backscattering of the impurity can occur, which is correlated to the emission of solitons. To analyze the influence of quantum fluctuation, the time evolution is simulated in a harmonically trapped system, using a Truncated-Wigner formalism.

Overall, this thesis presents a new and efficient method for describing heavy impurities in weakly interacting Bose-condensates, accurately predicting polaron properties even for large impurity-boson coupling.

Zusammenfassung

Das Bose-Polaron, ein Quasiteilchen, welches aus einer Verunreinigung innerhalb eines Gases bosonischer Teilchen entsteht, ist ein fundamentales Problem der Vielteilchenphysik. Bei schwacher Kopplung zwischen Verunreinigung und Bosonen beschreibt das Fröhlich-Modell präzise die Eigenschaften des Polarons. Innerhalb dieses Modells wird die Wechselwirkung als der Prozess der Erzeugung, Emission und Bindung von Bogoliubov-Phononen beschrieben, welche schwache Anregungen eines ungestörten Kondensats darstellen. Bei starker Kopplung erweist sich das Fröhlich-Modell jedoch als unzureichend, da die Verunreinigung das Bose-Gas dann stark deformiert. In dieser Dissatation wird deshalb ein alternatives Modell zur Beschreibung des 1D Bose-Polarons genutzt, das die Rückkopplung der Verunreinigung auf das Kondensat in Molekularfeldnäherung berücksichtigt. Sowohl Gleichgewichts- als auch Nicht-Gleichgewichtseigenschaften von Bose-Polaronen werden analysiert, wobei der Schwerpunkt auf eindimensionalen Systemen liegt.

Zunächst werden die Grundzustandseigenschaften eines einzelnen Polarons charakterisiert. Da die Verunreinigung von einer Deformationswolke umgeben wird, ergibt sich eine Energieverschiebung, sowie die Zunahme der effektiven Masse des Teilchens. Beide Größen werden analytisch abgeleitet und mit exakten Monte-Carlo-Simulationen verglichen, wobei sich eine hervorragende Übereinstimmung zeigt.

Um anschließend die Wechselwirkungen zwischen den Polaronen zu untersuchen, erfolgt eine Verallgemeinerung von einer auf zwei Verunreinigungen. Die Vielteilchenumgebung induziert eine Kopplung, welche zur Bildung eines Bipolarons führt. Das induzierte Potenzial wird in Born-Oppenheimer-Näherung für schwere Verunreinigungen hergeleitet, einschließlich der Born-Huang-Korrektur. Sowohl das Potential als auch die Bindungsenergie des Bipolarons zeigen exzellente Übereinstimmung mit Resultaten aus exakten Monte-Carlo-Simulationen.

Im Anschluss werden nicht-Gleichgewichtseigenschaften durch Verallgemeinerung auf eine fluktuierende Kopplung zwischen Kondensat und Verunreinigung untersucht. Es wird aufgezeigt, wie durch Anpassung der Rauschparameter kohärente Ströme im Kondensat kontrolliert werden können. In Abhängigkeit der Intensität des Rauschens und der Geschwindigkeit der einzelnen Verunreinigung zeigen sich drei dynamische Regime: I. Ein lineares Regim, II. ein Zeno Regime mit unterdrückten Strömen und III. ein Regime mit kontinuierlicher Solitonenemission. Die Analyse wird auf ein Paar rauschender Verunreinigungen verallgemeinert, wobei der Einfluss der induzierten Ströme der einzelnen Verunreinigungen aufeinander untersucht wird.

Zuletzt wird die Dynamik der Polaron-Bildung bei kohärenter Kopplung zwischen Kondensat und Verunreinigung untersucht, sowohl nach plötzlichen als auch nach adiabatischen Einschalten der Kopplungsstärke. Es werden verschiedene dynamische Regime identifiziert, darunter sowohl eine reversible als auch nicht-reversible Verlangsamung der Verunreinigung. Sogar die Rückstreuung der Verunreinigung kann auftreten, was mit Emission von Solitonen einhergeht. Um den Einfluss von Quantenfluktuation zu analysieren, wird die Zeitentwicklung in einem harmonisch gefangenen System mit Hilfe des *Truncated*-Wigner-Formalismus simuliert.

Zusammenfassend präsentiert diese Arbeit eine Methode zur Beschreibung schwerer Verunreinigungen in schwach wechselwirkenden Bose-Gasen, die selbst bei starker Kopplung gültig ist.

Contents

List of publications contained in this thesis

[P1] J. Jager, R. Barnett, M. Will, and M. Fleischhauer, *Strong-coupling Bose polarons in one dimension: Condensate deformation and modified Bogoliubov phonons*, Phys. Rev. Res. **2**, 033142 (2020).

[P2] M. Will, G. E. Astrakharchik, and M. Fleischhauer, *Polaron Interactions and Bipolarons in One-dimensional Bose Gases in the Strong Coupling Regime*, Phys. Rev. Lett. **127**, 103401 (2021).

[P3] M. Will, J. Marino, H. Ott, and M. Fleischhauer, *Controlling superfluid flows using dissipative impurities*, SciPost Phys. **14**, 064 (2023).

[P4] M. Will and M. Fleischhauer, *Dynamics of polaron formation in 1D Bose gases in the strong-coupling regime*, New Journal of Physics **25**, 083043 (2023).

[P5] B. Nagler, M. Will, S. Hiebel, S. Barbosa, J. Koch, M. Fleischhauer, and A. Widera, *Ultracold Bose Gases in Dynamic Disorder with Tunable Correlation Time*, Phys. Rev. Lett. **128**, 233601 (2022).

List of abbreviations

BdG	Bogoliubov-de-Gennes
BEC	Bose–Einstein condensate
BO	Born-Oppenheimer
DMC	Diffusion Monte Carlo
DMRG	Density matrix renormalization group
GPE	Gross–Pitaevskii equation
LLP	Lee-Low-Pines
MF	Mean-field
PBC	Periodic boundary condition
PDE	Partial differential equation
SPDE	Stochastic partial differential equation
TEBD	Time-evolving block decimation

1 Introduction

The polaron is a paradigmatic quasiparticle in condensed matter physics, emerging as a composite of a mobile impurity interacting with a surrounding many-body system of bosons or fermions. It was first introduced by Landau and Pekar [1, 2] to describe the motion of a single electron in a crystal lattice. The electron displaces the atoms in the lattice from their equilibrium position and polarizes the surrounding medium, which can be described as a dressing by phonons. The polaron concept has been generalized to a wide range of applications across condensed-matter physics, ranging from charge transport in organic semiconductors to high-T_c superconductors [3–5]. It is vital for understanding transport, response, and induced interaction in a variety of different systems.
More recently, ultra-cold quantum gases have become a versatile experimental platform for studying polaron physics with high precision and in novel regimes. Length and energy scales are very different from solids and can be controlled and manipulated more easily. The Fermi-polaron, an impurity immersed in a gas of fermions, has been studied in a number of different experiments [6–14]. However, fewer experiments have been conducted on the Bose polaron [15–21]. Due to the high compressibility of a Bose gas, the presence of an impurity can lead to a substantial number of excitations, and interactions within the Bose gas become essential. One-dimensional systems, experimentally studied in Refs. [15, 16, 20], are of particular interest because they exhibit pronounced quantum effects, given that the particles must tunnel through each other when they exchange positions. Furthermore, it is advantageous that analytically exact solutions and efficient numerical methods are available in one spatial dimension [22]. In addition, the suppressed g_3 correlation function reduces three-body losses compared to the three-dimensional case [23].
The interaction strength between the impurity and the surrounding medium can be effectively adjusted over a wide range, spanning from weak to strong coupling. This tuning can be

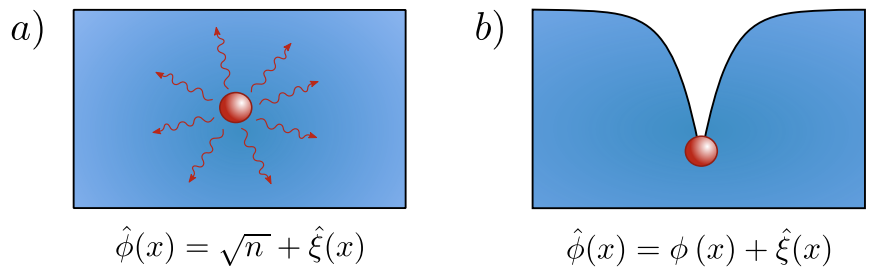

Figure 1.1: a) Illustration of the extended Fröhlich model. A large number of phonons are created around the impurity, such that phonon-phonon interactions are relevant. b) The approach of a deformed condensate avoids this problem, resulting in small quantum fluctuations. Reprinted figure with permission from [P2]. Copyright (2021) by the American Physical Society.

achieved using methods such as Feshbach [24] or confinement-induced resonances [25].
Many theoretical works addressing the Bose polaron describe the interaction between the impurity and bosons as a coupling, binding, and emission of Bogoliubov phonons of a uniform superfluid. This results in a Hamiltonian similar to the Fröhlich model used in solid-state systems [26], which has been used to predict ground state [27–34] and dynamical [35–44] properties of single impurities, as well as induced interactions between multiple polarons [45–48]. However, for strong impurity-bath coupling, the Bose gas becomes highly deformed, leading in this picture to a large phonon density, such that phonon-phonon interactions become crucial.
The aim of this thesis is to analyze a different theory of the Bose polaron, which incorporates the back action of the impurity already on a mean-field (MF) level. The new approach effectively minimizes quantum fluctuations for all impurity-boson coupling constants. By modeling the system in the Lee-Low-Pines (LLP) frame [49], effectively co-moving with the impurity, the treatment developed here keeps the entanglement between impurity and bosons. Since the theory employs a MF approximation, it is limited to parameter regimes where quantum fluctuations are small. The two necessary conditions are, first, a weakly interacting Bose gas indicated by a small Tonks parameter $\gamma = gm/n$ [50, 51], which scales as the ratio of the kinetic to interaction energy of a 1D Bose gas. Here, g represents the Bose-Bose coupling constant, and m (n) corresponds to the boson mass (density). Second, the LLP transformation introduces a different kind of interaction, which is small for a heavy impurity mass M. Therefore, the necessary conditions for the applicability of the approach are

$$\gamma \overset{!}{\ll} 1 \tag{1.1}$$

$$m \overset{!}{\ll} M, \tag{1.2}$$

which is discussed in detail in Section 1.4. Notably, unlike the Fröhlich model, this new theory provides reasonable results for arbitrary impurity-boson coupling constants g_{IB}, even in the strong coupling limit. Prior to and during the development of this thesis, other publications have employed similar methodologies to predict equilibrium properties of polarons [52–57] and bipolarons [55, 58, 59]. Additionally, some works have also explored related non-equilibrium properties [57, 60]. A comparison of these studies to the publications contained in this thesis is provided in Section 1.3.5.

This thesis aims to further investigate the equilibrium, non-equilibrium, and steady-state properties of one-dimensional Bose polarons in the strong coupling limit using this novel technique. It seeks to address important questions such as

- What are the steady state properties of Bose polarons?
- How does its energy and effective mass scale at large impurity-boson coupling strengths?

During the formation of the Bose polaron, the impurity significantly deforms the condensate, especially for large impurity-bath coupling. This results in an energy shift and alterations in the transport characteristics. The latter can be attributed to the increase in the effective mass of the polaron. Different theories have been developed to compute this effective mass for one-dimensional Bose polarons [33, 52, 61], each based on different assumptions. Furthermore, experimental measurements of the effective mass have been conducted, as shown in Ref. [16]. Using the novel technique, we calculate this mass, which exhibits excellent agreement with exact diffusion Monte Carlo (DMC) simulation [P1].

- What is the nature of induced interactions between polarons?
- How do they contribute to the formation of bipolarons?

Interactions mediated by a many-body environment play a crucial role in the field of many-body physics. One noteworthy example is Cooper paring [62], which emerges from the phonon-mediated interaction between electrons, offering an explanation for conventional superconductivity. For Bose polarons in the strong coupling regime, the formation of quasi-particles and the induced interactions are closely intertwined. These mediated interactions have the capability to bind pairs of impurities, resulting in the creation of bipolarons. Bipolarons are subjected to play an essential role in high-T_c superconductivity [5], and play an important role in the conductivity of polymers [63–67].

- How can a noisy impurity be used to control superfluid currents in a Bose gas?

A remarkable feature of cold bosonic atoms is the phenomena of superfluid flow. It has been experimentally observed in various contexts [68, 69], including one-dimensional ring geometries demonstrating persistent flows [70–72]. Despite these advancements, attaining precise control over superfluid flow remains challenging in cold atom experiments. While conventional methods for inducing currents often rely on establishing chemical potential differences, employing moving barriers, or introducing synthetic magnetic fields, the present study introduces a novel approach. It demonstrates that superfluid currents can be controlled precisely using local fluctuating potentials.

- What dynamical processes occur when an impurity is injected into a Bose gas?
- How and in which time scale is a polaron formed?

A question that naturally arises after studying the steady-state properties of polarons is whether and how the system evolves into this state after the impurity is injected into the system. Numerous theoretical investigations based on the Fröhlich model have delved into these dynamical properties [35, 37–42]. In the Fröhlich model the polaron is formed and an initially moving impurity decelerated by the emission of phonons. However, in the limit where the impurity substantially deforms the condensate, only little is known [57, 60]. Apart from emitting Bogoliubov phonon-like density waves, the impurity also has the capability to generate grey solitons, which substantially impact the system's dynamic behavior. The intricate effects of these solitons are very difficult to accurately account for using a Fröhlich approach but are naturally incorporated in the novel approach used in this work.

The MF model of the deformed condensate analyzed in this thesis serves as a robust theoretical framework for addressing these questions. It provides analytical solutions for steady-state properties and enables efficient computational simulations for studying non-equilibrium states. The model exhibits remarkable agreement with exact ab initio simulations, and corrections to the MF approximation are often negligible or can be incorporated by semiclassical phase-space methods. In summary, this thesis introduces a model that proves to be highly effective in describing Bose polarons within the strong coupling regimes.

1.1 Outline

In this thesis, we will discuss the development and application of a new approach, modeling the Bose polaron in one spatial dimension. The advantage of the model developed here lies in its ability to correctly include the deformation of the condensate induced by the impurity on a MF level. This feature makes it particularly advantageous for sizeable impurity-boson coupling, making it superior in that limit to models like the Fröhlich model [26, 27]. Additionally, the new model correctly accounts for the correlation between the impurity and the bosons, which is neglected in other approaches like the model of coupled MF equations for a separate impurity and condensate wave functions [73–76]. These other two methods are presented in Section 1.2. The disadvantages of these two methods compared to the one used in this thesis are discussed there.
The MF equation, primarily used to describe the Bose polaron in this thesis, is derived from the microscopic Hamiltonian in Section 1.3. In particular, details of this derivation that were only briefly mentioned in the publications [P1–P4] are discussed more thoroughly. There are two significant steps involved. First, the system is transformed into a frame co-moving with the impurity. In this way, the impurity is described quantum mechanically without losing correlations between impurity and bath. The second step involves a MF approximation, which includes the condensate deformation.
Following this, Section 1.4 examines the prerequisites necessary for the applicability of the MF approximation. It discusses the constraints of certain parameters and compares them to current experiments. Subsequently, the order of significant length and time scales is brought to the attention. To accomplish this, data from an experiment documented in Ref. [16] is employed, wherein Bose polarons were realized in a one-dimensional system.
The final section of the introduction establishes solutions of a homogeneous Gross–Pitaevskii equation (GPE), which characterizes a weakly interacting Bose gas in itself without an impurity. This exploration is a foundational step towards deriving the stationary states of polarons and bipolarons while also contributing to the interpretation of numerical simulations in non-equilibrium scenarios. The section presents localized solutions, known as solitons, and spatially periodic states.

Afterwards, the primary results, the publications upon which this cumulative thesis is based, are presented. The different regimes in which the system is studied are sketched in Figure 1.2. First, the ground state polaron properties are examined in Chapter 2 [P1]. For this, an analytic expression of the stationary MF ground state is derived by solving a generalized GPE. The impurity deforms the condensate on a length scale given by the healing length of the condensate. This can be described as a dressing of the impurity by the deformation cloud and the formation of a polaron. During this formation, the quasiparticle experiences a shift in energy and an increase in the effective mass compared to the bare impurity. Both of these quantities are derived analytically from the MF state and show good agreement to quasi-exact DMC simulations, the latter being derived in Ref. [33]. Jonas Jager numerically simulated quantum corrections to the MF solution to estimate the influence of quantum fluctuations. These corrections involve considering modified Bogoliubov phonons as excitations of the deformed condensate, and they further improve the agreement with DMCs.
In Chapter 3[P2], the MF theory is generalized to a pair of impurities to investigate polaron-polaron interaction meditated by the condensate. Since the induced potential is attractive, it binds the two polarons, forming a bipolaron. At first, the MF equation is derived and

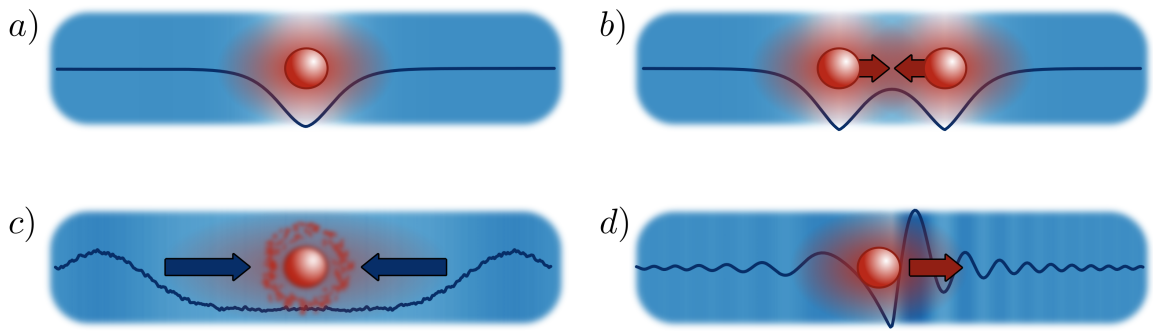

Figure 1.2: Illustration of the different polaron properties studied in this thesis. a) Ground state properties (polaron energy and mass) of a single mobile impurity [P1]. b) Polaron-polaron interaction potential mediated by the Bose gas [P2]. c) Superfluid currents induced by a noisy impurity [P3]. d) Dynamics of polaron formation[P4].

analytically solved in Born-Oppenheimer (BO) approximation, which is appropriate for heavy impurity masses. This leads to a semi-analytic expression of the polaron interaction potential, which is in excellent agreement with DMC simulations. Gregory Astrakharchik executed the latter [P2]. To estimate the effect of a finite impurity mass, the Born-Huang correction [77, 78] to the BO approximation is derived. The section concludes by calculating the bipolaron binding energy for both bosonic and fermionic impurities, which is in excellent agreement with DMC for impurity-boson mass ratios as low as three.
Up to this point, the system has been investigated with a constant impurity-boson coupling. However, Chapter 4 [P3] examines the effect of an in-time stochastic/noisy coupling constant. It shows that noise can be utilized to control coherent superfluid currents. In the first part, we analyze a static noisy impurity and demonstrate its similar impact on the condensate to that of a local loss of particles [79–82]. This occurs because the noisy potential scatters particles into highly excited states, effectively removing them from the condensate. As a result, a coherent current is induced to counteract the local effective particle loss. The current increases monotonically with growing noise up to a critical value, at which the system becomes dominated by the quantum Zeno effect [83], leading to a reduction in transport. Subsequently, we generalize to a noise source in an externally driven current or, equivalently, one dragged through the condensate at a fixed velocity. Here, a new regime of continuous soliton emission emerges. Following the approach of Chapter 3 [P2], the publication concludes by generalizing to a pair of noisy impurities. We analyze how the currents induced by each contact influence each other and show how noise tuning can be employed to control or stabilize the superfluid current.
The publication in Chapter 5[P4] is once again focused on a single mobile impurity interacting coherently with the Bose gas, however, with a focus on the formation dynamics of the polaron. First, we further analyze the stationary states from Chapter 2 [P1] for an arbitrarily large polaron momentum, revealing a periodic dependency of the polaron energy and velocity on the total momentum. Furthermore, the time evolution after either an adiabatic turn-on or rapid quench of the impurity-boson coupling constant is investigated. Our findings reveal a diverse range of dynamical regimes. For velocities exceeding a critical threshold, the impurity experiences a non-reversible slowdown due to a friction force associated with the emission

of Cherenkov radiation. Additionally, for subcritical initial impurity velocities, we observe a reversible slowdown resulting from an increase in the effective mass during polaron formation. Remarkably, for initially fast and heavy impurities, we uncover a backscattering phenomenon caused by the emission of solitons. Lastly, the effect of quantum fluctuation is analyzed, where we consider a trapped condensate to avoid 1D divergencies. Using a Truncated Wigner simulation, we show under what conditions quantum fluctuations are small.
The final publication discussed in Chapter 6[P5] is a supplementary project of this thesis. It presents an experiment conducted primarily by Benjamin Nagler in the research group of Artur Widera. This study explores the impact of a spatiotemporal disorder potential with tunable correlation time on a three-dimensional Bose gas, expanding on the investigations presented in Chapter 4[P3]. The latter focuses on the effects of a local noise potential on a one-dimensional gas. The disorder potential heats the trapped Bose gas, leading to an evaporative particle loss induced by the noise. The potential generates both a heating of the residual thermal particles and creates excitations in the superfluid. My contribution to this work was mainly the theoretical estimation of the direct excitation rate from superfluid to thermal atoms.

The Artificial Intelligence-based software DeepL and Grammarly were used in the writing process of this thesis.

1.2 Different theoretical approaches to Bose polarons

There are several methods that have been employed to model the Bose polaron. This section presents an overview of some alternative approaches to the one used in this thesis. Two, in particular, are described in more detail. First, the Fröhlich model and an extension of it in Section 1.2.1, which is one of the most commonly used models [27–48]. Second, the model of coupled MF equations [73–76], as it is similar to the approach used in this thesis and is outlined in Section 1.2.2.
In addition to these approaches, several others have been used to predict polaron properties. Two of them are briefly mentioned here. The first is a DMC simulation, which provides quasi-exact ground state properties of Bose polarons and bipolarons [P2, 33, 34, 84]. However, this method comes with a significant computational cost and only applies to finite-sized systems of moderate particle-numbers. Despite its limitations, it serves as a valuable complement to approximate calculations. In this thesis, it is used in Chapters 2 and 3 [P1, P2] to validate the MF approach developed here. A description of this method is available, e.g., in the supplemental material of [P2] written by G. Astrakharchik.
In one-dimensional systems where the impurity and bosons have the same mass, and the coupling between bosons matches that between the impurity and bosons, exact solutions for the ground state can be obtained even analytically. This system is equivalent to an isospin-$\frac{1}{2}$ Bose gas, known as the Yang-Gaudin model, and corresponds to treading a single gas particle distinguishable from the other. The model has exact solutions for the ground state and excitation spectrum derived through a Bethe ansatz [22, 85–87]. The authors of Ref. [61] determine the properties of the polaron in this way.

All methodologies used to model the Bose polaron begin with the Hamiltonian of a single mobile impurity within a Bose gas. In the case of a homogeneous one-dimensional system, it is given by

$$\hat{H} = \frac{\hat{p}^2}{2M} + \int_{-L/2}^{L/2} \mathrm{d}x\, \hat{\phi}^\dagger(x)\Big[-\frac{\partial_x^2}{2m} + \tfrac{1}{2} g\, \hat{\phi}^\dagger(x)\hat{\phi}(x) + g_{\mathrm{IB}}\, \delta(x-\hat{r})\Big]\hat{\phi}(x), \tag{1.3}$$

where units with $\hbar = 1$ are chosen. This is maintained throughout most parts of the thesis. The boson (impurity) mass is given by m (M), and L is the system size. This thesis employs a system with periodic boundary conditions (PBCs) and models the thermodynamic limit as L approaches infinity. The first quantized operators $\hat{p}$ and $\hat{r}$ represent the impurity momentum and position operators respectively, while $\hat{\phi}^{(\dagger)}(x)$ is the second quantized annihilation (creation) operator of a boson at position x. The operators fulfill the commutation relations

$$\Big[\hat{r}, \hat{p}\Big] = i \tag{1.4}$$

$$\Big[\hat{\phi}(x), \hat{\phi}^\dagger(y)\Big] = \delta(x-y) \tag{1.5}$$

$$\Big[\hat{\phi}^{(\dagger)}(x), \hat{\phi}^{(\dagger)}(y)\Big] = 0. \tag{1.6}$$

At the ultra-cold temperatures of Bose–Einstein condensates (BECs), the kinetic energy of the atoms is low compared to the interaction potentials, such that the interparticle article potentials can be described in s-wave approximation [88, 89]. Therefore, a Fermi-Huang pseudo contact potential [25, 90, 91] is used in Equation (1.3), where the boson-boson (impurity-boson) coupling constant is given by g (g_{IB}).

Note, however, that according to the Mermin-Wagner-Hohenberg theorem[92, 93] there is no true BEC in one spatial dimension. Quasi-condensation, characterized by long wavelength phase fluctuations, is nonetheless possible [88]. More on this subject is discussed in Section 1.3.2.
Since Equation (1.3) represents an interacting many-body quantum system, predicting its behavior involves either computationally intensive simulations or approximative methods.

1.2.1 The (extended) Fröhlich Model

The first approach presented is the Fröhlich model of the Bose polaron, which is closely related to the model developed by Fröhlich in 1954 to describe an electron in a crystal lattice [26]. It was first derived in the context of cold Bose gases in Ref. [27]. The Fröhlich model is commonly used to describe both equilibrium [27–34, 45–48] and non-equilibrium [35–44] properties of Bose polarons in different dimensions. The basic idea is to model the homogeneous Bose gas in Bogoliubov approximation [88, 94] and subsequently introduce the interaction with the impurity as a coupling to phononic excitations of the BEC. However, a major drawback of this approach is its limited applicability to strong impurity-boson coupling. Some works have attempted to address this limit using an extended Fröhlich model [33, 39]. Nevertheless, Chapter 2 [P1] shows that this often leads to incorrect results. This issue occurs since the impurity becomes dressed by many phonons at a large impurity-boson coupling constant. Consequently, phonon-phonon interactions become significant even for weak boson-boson coupling.
The model is briefly introduced in the following, emphasizing the problematic approximations made in the case of large impurity-boson coupling.

The first step in deriving the Fröhlich model is to disregard the impurity from the total Hamiltonian operator (1.3) and simplify the Hamiltonian of the Bose gas

$$\hat{H}_{\mathrm{B}} = \int_{-L/2}^{L/2} \mathrm{d}x\, \hat{\phi}^\dagger(x)\Big[-\frac{\partial_x^2}{2m} + \tfrac{1}{2} g \hat{\phi}^\dagger(x)\hat{\phi}(x)\Big]\hat{\phi}(x). \tag{1.7}$$

To proceed, the field operators are expanded around the MF solution of a homogeneous condensate at density n, including fluctuations $\hat{\xi}(x)$

$$\hat{\phi}(x) = \sqrt{n} + \hat{\xi}(x). \tag{1.8}$$

Although this step is not an approximation, it already foreshadows the main problem of the Fröhlich model. In the case of a large impurity-boson coupling, the impurity significantly deforms the MF condensate density, as shown in Chapters 2, 3 and 5 [P1, P2, P4]. The expansion in Equation (1.8) is therefore not centered around the MF ground state of the whole system, such that the fluctuations $\hat{\xi}(x)$ are no longer small for large g_{IB}. Nonetheless, the standard derivation of the Fröhlich model involves neglecting terms larger than second order in $\hat{\xi}(x)$ in the Hamiltonian given by Equation (1.7) and then diagonalizing it using a Bogoliubov transformation [88, 94]

$$\hat{\xi}(x) = \frac{1}{\sqrt{L}} \sum_{k\neq 0} \left[u_k\, e^{ikx}\, \hat{b}_k \,-\, v_{-k}^*\, e^{-ikx}\, \hat{b}_{-k}^\dagger \right]. \tag{1.9}$$

The factors u_k and v_k are defined so that the transformed Hamilton operator is diagonal and given explicitly in Refs. [88, 94]. The transformation results in the Hamiltonian

$$\hat{H}_{\mathrm{B}} = E_0 + \sum_{k\neq 0} \omega_k \hat{b}_k^\dagger \hat{b}_k + \mathcal{O}(\hat{b}_k^4), \tag{1.10}$$

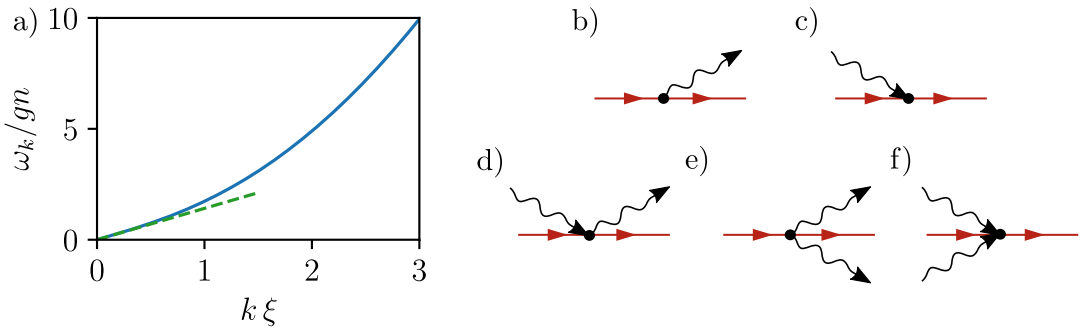

Figure 1.3: a) Bogoliubov dispersion relation (blue), being linear for small $k \ll 1/\xi$ and quadratic for large momenta $k \gg 1/\xi$. b)-f) Diagrammatic representation of phonon couplings given by the terms proportional to g_{IB} in Fröhlich Hamiltonian (1.11). The impurity is represented by red arrows and phonons by black ones. Included are single phonon b) emission and c) absorption, as well as d) phonon scattering and two phonon e) emission and f) absorption.

where $\hat{b}_k^{(\dagger)}$ describe the annihilation (creation) of a bosonic Bogoliubov-phonon with momentum k. The Bogoliubov dispersion-relation is given by $\omega_k = c|k|\sqrt{1+\frac{1}{2}k^2\xi^2}$, displayed in Figure 1.3a). It is linear for large wavelengths (small k) compared to the healing length $\xi = 1/\sqrt{2gnm}$, where the speed of sound $c = \sqrt{gn/m}$ is the velocity of these phonons. For short wavelengths, ω_k crosses over to a single-particle-like quadratic dispersion. E_0 is a constant energy offset that can be disregarded.
As a next step the impurity is introduced back into the system by expressing the total Hamiltonian given by Equation (1.3) in terms of Bogoliubov phonons, resulting in the extended Fröhlich Hamiltonian

$$\begin{aligned}\hat{H} =& \frac{\hat{p}^2}{2M} + \sum_{k\neq 0}\omega_k \hat{b}_k^\dagger \hat{b}_k + g_{\mathrm{IB}}\sqrt{\frac{n}{L}}\sum_{k\neq 0} W_k\, e^{ik\hat{r}}\left(\hat{b}_{-k}^\dagger + \hat{b}_k\right) \\ &+ \frac{g_{\mathrm{IB}}}{2L}\sum_{k,k'\neq 0} e^{i(k-k')\hat{r}}\Big[\left(W_k W_{k'} + W_k^{-1}W_{k'}^{-1}\right)\hat{b}_{k'}^\dagger \hat{b}_k \\ &\quad + \tfrac{1}{2}\left(W_k W_{k'} - W_k^{-1}W_{k'}^{-1}\right)\left(\hat{b}_{k'}^\dagger \hat{b}_{-k}^\dagger + \hat{b}_k \hat{b}_{-k'}\right)\Big] + \mathcal{O}(\hat{b}_k^4),\end{aligned} \tag{1.11}$$

where the structure factors are given by $W_k = \sqrt{\epsilon_k/\omega_k}$, with the free boson dispersion relation $\epsilon_k = k^2/2m$. The Hamiltonian describes the interaction between the impurity and the bosons as a coupling to phononic excitation of the BEC, which consists of one-phonon terms (linear in $\hat{b}_k^{(\dagger)}$) and two-phonon terms (quadratic in $\hat{b}_k^{(\dagger)}$). These terms are depicted diagrammatically in Figure 1.3b)-f). In many cases, the two-phonon terms can be neglected; in that case, the Hamiltonian is equivalent to the one described by Fröhlich [26].
The aim of this thesis is not to analyze this Hamiltonian, as it has already been done in many other publications [27–48]. However, the subsequent discussion gives an estimate of how the phonon number scales with the coupling constant g_{IB}. The ground state is straightforward to derive in the special case of a very heavy impurity, i.e. $M \to \infty$, and neglecting the two phonon terms. In that case, the Hamiltonian is independent of the impurity momentum $\hat{p}$, so the position operator can be replaced by a c-number $\hat{r} = r$. Without loss of generality, the

impurity is localized in the center of the system, so $r = 0$. The Fröhlich model Hamiltonian is then simplified to

$$\hat{H} = \sum_{k\neq 0} \left[\omega_k \hat{b}_k^\dagger \hat{b}_k + g_{\mathrm{IB}} \sqrt{\frac{n}{L}} W_k \left(\hat{b}_k^\dagger + \hat{b}_k \right) \right]. \tag{1.12}$$

With these approximations, the ground state is given by a multi-mode coherent state $|\beta_k\rangle$ with the amplitudes

$$\beta_k = -g_{\mathrm{IB}} \sqrt{\frac{n}{L}} W_k / \omega_k. \tag{1.13}$$

This leads to a rough scaling estimate of the phonon number in the Fröhlich model

$$\langle \hat{b}_k^\dagger \hat{b}_k \rangle \propto g_{\mathrm{IB}}^2. \tag{1.14}$$

As a result, a large coupling g_{IB} leads to a significant increase in the phonon density, making phonon-phonon interactions relevant. Although the estimate is modified when solving the full model given by Equation (1.11), the trend of a large phonon occupation number remains. As shown in Chapter 2 [P1] and Ref. [33], this imposes the condition $g_{\mathrm{IB}} \ll gn\xi$ for the applicability of the Fröhlich model. A possible approach to address this limitation is to include higher order in terms $\hat{b}_k^{(\dagger)}$ in Equation (1.11), resulting in phonon-phonon interactions. However, this Hamiltonian is as complicated, if not even worse, than the initial Hamiltonian for the bare particles, given by Equation (1.3).

1.2.2 Theory of coupled mean-field equations

The subsequent section presents a first approach to include the condensate deformation on a MF level. The method involves solving coupled equations for distinct impurity and condensate wave functions. It has been used in [73–76] to characterize the system for strong impurity-boson coupling, surpassing the limitations of the Fröhlich model. Nevertheless, a limitation of this approach is its omission of all correlations between the impurity and the bosons.
To derive the coupled MF equation it is instructive to rewrite the total Hamiltonian (1.3) in second quantization for the boson and impurity

$$\begin{aligned} \hat{H} = \int_{-L/2}^{L/2} \mathrm{d}x \Big\{ & \hat{\phi}^\dagger(x) \Big[-\frac{\partial_x^2}{2m} + \tfrac{1}{2} g \hat{\phi}^\dagger(x) \hat{\phi}(x) \Big] \hat{\phi}(x) \\ & + \hat{\psi}^\dagger(x) \Big[-\frac{\partial_x^2}{2M} + g_{\mathrm{IB}} \hat{\phi}^\dagger(x) \hat{\phi}(x) \Big] \hat{\psi}(x) \Big\}, \end{aligned} \tag{1.15}$$

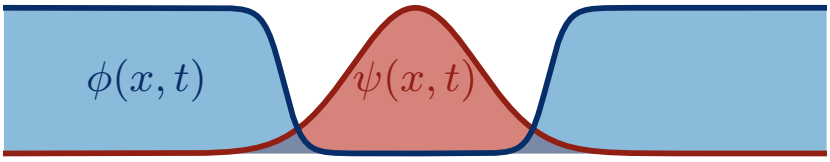

Figure 1.4: Schematic depiction of the coupled MF approach. It is assumed that the system is in a product state of a wave function each for the impurity $\psi(x,t)$ and bosons $\phi(x,t)$. Impurity-boson correlations are neglected.

where $\hat{\psi}^{(\dagger)}(x)$ are the impurity field operators. One way to derive the MF equations is, first to calculate the Heisenberg equations of motion $\partial_t \bullet = i[\hat{H}, \bullet]$ for $\hat{\phi}(x)$ and $\hat{\psi}(x)$. Subsequently, a product state ansatz $|\phi(x,t)\rangle \otimes |\psi(x,t)\rangle$ is applied, where both impurity and Bose gas are in a coherent state with complex amplitudes $\psi(x,t)$ and $\phi(x,t)$. As a result, the complex wave functions need to fulfill the coupled GPEs

$$\begin{aligned} i\partial_t\, \phi(x,t) &= \Big[-\frac{\partial_x^2}{2m} + g_{\mathrm{IB}}|\psi(x,t)|^2 + g|\phi(x,t)|^2 \Big]\, \phi(x,t) \\ i\partial_t\, \psi(x,t) &= \Big[-\frac{\partial_x^2}{2M} + g_{\mathrm{IB}}|\phi(x,t)|^2 \Big]\, \psi(x,t). \end{aligned} \tag{1.16}$$

By the application of the product state ansatz, impurity-boson correlations are neglected, which is an inadequate approximation. For a large impurity-boson coupling, the coupled MF model predicts a phase separation of the gas and the impurity, which is shown in Ref. [75] and depicted in Figure 1.4. Since both $\psi(x)$ and $\phi(x)$ are wave packets, it is evident that the system is not in an eigenstate of the total momentum operator. However, the Hamiltonian (1.3) is translationally invariant, implying that the true ground state of the system must also be an eigenstate of the total momentum operator.
In this thesis, a different MF approach is primarily employed, which has the capability to incorporate correlations between the impurity and bosons. The stationary states derived in this way are eigenstates of the total momentum operator.

1.3 Polaron mean-field theory in the co-moving frame

This section introduces the theory used mostly in this thesis to describe the properties of Bose polarons. Compared to the approaches discussed in Section 1.2, it has some advantages. First, it is a MF theory that includes the deformation of the condensate. This corresponds to a similar expansion of the field operators as used in the Fröhlich model discussed in Section 1.2.1 and is given by

$$\hat{\phi}(x) = \phi(x) + \hat{\xi}(x). \tag{1.17}$$

Compared to the expansion in the Fröhlich model, given by Equation (1.8), the MF wavefunction $\phi(x)$ includes the coupling to the impurity. As a result, the fluctuations $\hat{\xi}(x)$ are small for arbitrary g_{IB} and can often even be neglected.
Compared to the approach of coupled MF equations of Section 1.2.2, the approach derived here includes correlations between impurity and bosons. This is archived by working in a frame of reference, co-moving with the impurity using the LLP or polaron transformation [49]. This corresponds to a MF approximation for the impurity-boson correlation function rather than treating each species individually.
This novel technique is used in this thesis to predict the ground state [P1] and dynamical [P4] properties of a single impurity and generalized to either include a dissipative impurity-boson interaction [P3] or describe two impurities [P2] to predict mediated impurity-impurity interaction. A short derivation is shown in these publications, still, since it is a central part of this thesis, a more comprehensive derivation of the technique is presented in the subsequent section.
First, the LLP transformation is introduced in Section 1.3.1. Second, the MF equations are derived in Section 1.3.2. Subsequently, some additional remarks about the approach are mentioned. The role of impurity-bath correlations are discussed in Section 1.3.3 and an expression for the particle current is derived in Section 1.3.4. The section concludes by mentioning other publications that apply the method described in the following and compares these works with the ones contained in this thesis in Section 1.3.5.

1.3.1 Lee-Low-Pines transformation

The first step of analyzing the polaron Hamiltonian given by Equation (1.3) is to eliminate the impurity degrees of freedom. For this purpose, the conservation of the total momentum $\hat{p} + \hat{P}_{\mathrm{B}}$ is utilized, where

$$\hat{P}_{\mathrm{B}} = -i \int_{-L/2}^{L/2} \mathrm{d}x \, \hat{\phi}^{\dagger}(x) \partial_x \hat{\phi}(x) \tag{1.18}$$

is the total momentum operator of the Bose gas. It is conserved in homogeneous systems with PBCs, which are predominantly studied in this thesis. The conservation law can be exploited using the unitary LLP transformation

$$\hat{U}_{\mathrm{LLP}} = \exp(-i\hat{r}\hat{P}_{\mathrm{B}}), \tag{1.19}$$

which represents a translation of the Bose gas into a frame co-moving with the impurity. More precisely, the previous impurity operators $\hat{p}$ and $\hat{r}$ represent in the LLP frame the center of

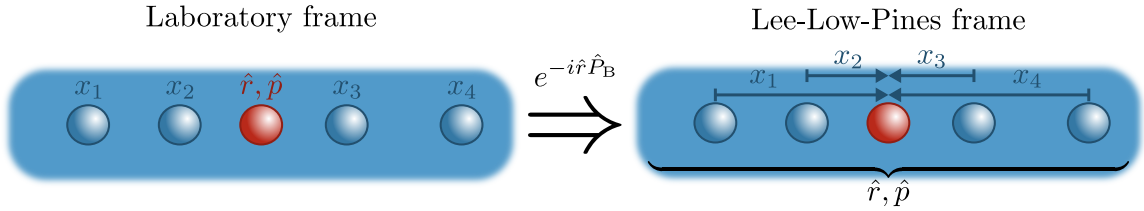

Figure 1.5: Illustration of the LLP transformation. In the laboratory frame, the position of impurity (red) and bosons (blue) is used as a coordinate. In contrast, in the LLP frame, the boson coordinates are defined relative to the impurity's position, and the center-of-mass operators of the entire system replace the impurity operators.

mass operators of the entire system. In contrast, the field operator $\hat{\phi}^{(\dagger)}(x)$ annihilates (creates) a boson relative to the position of the impurity. This is shown by the transformation rules

$$\text{center of mass:} \qquad \hat{p} \;=\; \hat{U}^\dagger_{\mathrm{LLP}} \left(\hat{p} + \hat{P}_{\mathrm{B}}\right) \hat{U}_{\mathrm{LLP}} \tag{1.20}$$

$$\text{relative coordinate:} \quad \hat{\phi}^{(\dagger)}(x-\hat{r}) = \hat{U}^\dagger_{\mathrm{LLP}}\, \hat{\phi}^{(\dagger)}(x)\, \hat{U}_{\mathrm{LLP}}, \tag{1.21}$$

and is illustrated in Figure 1.5. By applying the LLP transformation to the Hamilton operator in Equation (1.3), one arrives at

$$\begin{aligned} \hat{H}_{\mathrm{LLP}} &= \hat{U}^\dagger_{\mathrm{LLP}}\, \hat{H}\, \hat{U}_{\mathrm{LLP}} \\ &= \frac{1}{2M}(\hat{p} - \hat{P}_{\mathrm{B}})^2 \\ &\quad + \int_{-L/2}^{L/2} \mathrm{d}x\, \hat{\phi}^\dagger(x-\hat{r}) \Big[-\frac{\partial_x^2}{2m} + \tfrac{1}{2} g \hat{\phi}^\dagger(x-\hat{r})\hat{\phi}(x-\hat{r}) + g_{\mathrm{IB}}\delta(x-\hat{r}) \Big] \hat{\phi}(x-\hat{r}). \end{aligned} \tag{1.22}$$

Given the presence of PBCs, the Hamiltonian can be made independent of $\hat{r}$, by shifting x within the integral by $\hat{r}$. Thus the total momentum $\hat{p}$ commutes with the Hamiltonian, is conserved, and can be replaced by a c-number p, what results in

$$\hat{H}_{\mathrm{LLP}} = \frac{1}{2M} :(p - \hat{P}_{\mathrm{B}})^2: + \int_{-L/2}^{L/2} \mathrm{d}x\, \hat{\phi}^\dagger(x) \Big[-\frac{\partial_x^2}{2\tilde{m}} + \tfrac{1}{2} g \hat{\phi}^\dagger(x)\hat{\phi}(x) + g_{\mathrm{IB}}\delta(x) \Big] \hat{\phi}(x). \tag{1.23}$$

Here, the symbol :: denotes normal ordering, i.e., interchanging all creation operators to the left and annihilation operators to the right, and $\tilde{m} = (1/M + 1/m)^{-1}$ is the reduced mass. The main advantage of this technique is that it allows for the exact removal of impurity operators from the system without making any additional approximations. As a result, it ensures the inclusion of impurity-boson correlations. An inherent drawback lies in the additional non-local interaction term $\hat{P}_{\mathrm{B}}^2/2M$ present in the LLP Hamiltonian, which is quartic in the field operators $\hat{\phi}^{(\dagger)}(x)$. This term represents an interaction between the bosons mediated by the mobile impurity. Nevertheless, its effects can be reasonably approximated, particularly when dealing with heavy impurity masses $M \gg m$.

1.3.2 Mean-field approximation

Next, since the Hamiltonian in Equation (1.23) still describes an interacting many-body system, further approximations are needed to predict the properties of the system. This is done

in most parts of this thesis using a MF approximation. In order to derive the MF equation, first, the Heisenberg equation of motion $\partial_t\hat{\phi}(x) = i[\hat{H}_{\mathrm{LLP}}, \hat{\phi}(x)]$, for the field operator is calculated. Secondly, it is assumed that the bosons are all condensed , such that the system is in a multi-mode coherent state $|\phi(x,t)\rangle$ with a complex wave-function $\phi(x,t)$. This is equivalent to replacing the operators $\hat{\phi}(x,t)$ by a complex field $\phi(x,t)$ in the Heisenberg equation. As a result, the complex field has to fulfill a nonlinear partial differential equation (PDE)

$$i\partial_t\, \phi(x,t) = \Big[-\frac{\partial_x^2}{2\tilde{m}} + i\, v(t)\, \partial_x + g|\phi(x,t)|^2 + g_{\mathrm{IB}}\delta(x)\Big]\phi(x,t), \tag{1.24}$$

where the $v(t)$ is the velocity of the impurity

$$\begin{aligned} v(t) &= \frac{1}{M}\left[p - P_{\mathrm{B}}(t)\right] \\ &= \frac{1}{M}\left[p + i\int_{-L/2}^{L/2} \mathrm{d}x\; \phi(x,t)^*\, \partial_x\, \phi(x,t)\right]. \end{aligned} \tag{1.25}$$

Equation (1.24) is a GPE, as for example derived in Refs. [88, 89], except of the additional derivative proportional to $v(t)$. The additional term appears because Equation (1.24) describes the Bose gas in the LLP frame, co-moving with the impurity at velocity $v(t)$. Since the impurity velocity given by Equation (1.25) depends on the total Bose gas momentum $P_{\mathrm{B}}(t)$, the new term describes a rather unusual nonlinear and nonlocal coupling.
Stationary solutions of this equation have been studied analytically for a fixed velocity v in Refs. [P1, 52, 95]. In general, the time-evolution for an arbitrary initial condition must be simulated numerically, as done in Ref. [P4, 57, 60]. The results of these studies are compared in more detail in Section 1.3.5. Appendix B presents an efficient numerical method for solving Equation (1.24), which incorporates the nonlocal interaction term.

However, special care must be taken when treating a one-dimensional Bose gas using a coherent state approximation. As stated by the Mermin-Wagner-Hohenberg theorem [92, 93] there is no true BEC in homogeneous systems in less than three spatial dimensions. Nevertheless, quasi-condensates, characterized by long wavelength phase fluctuations, exist in one-dimensional systems [88]. These fluctuations prevent a true long-range order, so a coherent field $\phi(x,t)$ cannot describe a macroscopic quasi-condensate. As shown in Ref. [88] this is quantified by an exponentially decaying density matrix, with a length scale L_ϕ given by

$$L_\phi = \frac{n}{mk_BT}, \tag{1.26}$$

where k_B is the Boltzmann constant. However, this thesis investigates the impact of impurities on such a 1D Bose gas, which only influences the system locally on the scale of the healing length $\xi = 1/\sqrt{2gnm}$. At sufficiently low temperatures, the system is coherent within the influence of the impurity and, therefore, can be described by a coherent field $\phi(x,t)$ within this range. However, if the effects of quantum corrections to the MF approximation are to be investigated, as done in Chapters 2 and 5, the phase fluctuations lead to infrared divergences. The way in which these can be handled is mentioned in the corresponding sections.

1.3.3 Impurity-boson correlation

In the following, the significance of impurity-boson correlations is emphasized. It is shown that these correlations are inherently integrated into this approach, making it superior to other

methods which neglect them, such as coupled GPEs, which employ separate wave-functions for each impurity and boson [73–76], see Section 1.2.2. As previously mentioned, the total momentum $\hat{p}$ commutes with the Hamiltonian $\hat{H}_{\mathrm{LLP}}$, see Equation (1.23). The energy eigenstates are, therefore, always a product state of the center of mass state $|p\rangle$ and a state for the bosons in the co-moving frame, which is assumed to be a coherent state $|\phi(x)\rangle$. While it might seem that correlations are not relevant due to the system being separated in the LLP frame, it is important to note that impurity-boson correlations in the laboratory frame are, in fact, non-trivial. This can be demonstrated by transforming the product state back into the laboratory frame resulting in

$$\hat{U}_{\mathrm{LLP}} |p\rangle \otimes |\phi(x)\rangle = \frac{1}{L} \int_{-L/2}^{L/2} \mathrm{d}r \; e^{-ipr} |r\rangle \otimes |\phi(x+r)\rangle \,. \tag{1.27}$$

Here $|r\rangle$ is an eigenstate of the position operator $\hat{r}$, and given by the Fourier transformation $|p\rangle = \frac{1}{L} \int_{-L/2}^{L/2} \mathrm{d}r \; e^{-ipr} |r\rangle$. Equation (1.27) is not a product state of the impurity and bosons if $\phi(x)$ is not a constant function. This indicates that impurity-boson correlations are included in the approach.
An argument where the incorporation of correlations becomes even more evident is that the Bose gas density $n(x) = |\phi(x)|^2$ in the LLP frame corresponds to the relative impurity-boson density-density correlation function in the laboratory reference frame. This follows directly from the transformation rule in Equation (1.21)

$$n(x) = \left\langle \hat{\phi}^\dagger(x - \hat{r}) \, \hat{\phi}(x - \hat{r}) \right\rangle \tag{1.28}$$

$$= \int \mathrm{d}r \left\langle \hat{\phi}^\dagger(x - r) \, \hat{\phi}(x - r) \, \hat{\psi}^\dagger(r) \, \hat{\psi}(r) \right\rangle . \tag{1.29}$$

Here $\hat{\psi}^{(\dagger)}(r)$ are second quantized impurity field operators, which are related to $\hat{r}$ in the subspace of a single impurity by $\hat{\psi}^\dagger(r) \, \hat{\psi}(r) = \delta(r - \hat{r})$. Since $n(x)$ is not constant (see. [P1–P4]), it proves that non-trivial impurity-boson correlations are included in this approach.

1.3.4 Particle current

An important property, particularly for [P3], is the particle current within the Bose gas. To calculate it, a continuity equation for the bosons is derived from Equation (1.24)

$$\partial_t \, n(x,t) = \, - \, \partial_x \, j(x,t), \tag{1.30}$$

where the particle density is $n(x,t) \coloneqq |\phi(x,t)|^2$ and the current

$$j(x,t) \coloneqq \frac{1}{\tilde{m}} \, \mathrm{Im} \left[\phi(x,t)^* \, \partial_x \, \phi(x,t) \right] - v(t) \, n(x,t). \tag{1.31}$$

It is noteworthy that the term $-v(t) \, n(x,t)$ does not appear in the standard definition of a particle current. It arises because the continuity equation follows from the particle-number conservation in the laboratory, not the LLP frame. So $j(x,t)$ is the current in the laboratory frame, while $\phi(x,t)$ describes the Bose gas in the co-moving LLP frame, resulting in the additional term.

1.3.5 Other publications using this model

Apart from the publications included in this thesis [P1–P4], other studies have employed the approach described in this section to model Bose polarons. In the following, I will discuss the similarities and differences between these works.
Ref. [95] discusses a nonlinear flow past a delta potential in one spatial dimension. The equation that was investigated for this purpose is equivalent to Equation (1.24) for an infinitely heavy impurity $M \to \infty$, or fixed velocity $v(t) = v$. The stationary solutions in this limiting case are derived in this publication.
The ground state MF solution of a single polaron was studied for a vanishing total momentum $p = 0$ in Ref. [52], where they arrived at the same expression for the MF polaron energy as presented in this thesis in Chapter 2 [P1]. However, Ref. [52] did not discuss the impact of quantum fluctuations. The MF ground state solution was extended to encompass a finite, although not arbitrarily large, total momentum in Refs. [53, 57], where they derived a part of the energy-momentum relation for small to intermediate p compared to the gas density n. Nevertheless, neither of these publications determined the complete relation for arbitrary p, which is thoroughly discussed in Chapter 5 [P4]. We show that the energy and velocity of the polaron exhibit periodic behaviors with respect to the total momentum.
Around the same time as our publication on induced polaron interactions, detailed in Chapter 3[P2], two other manuscripts were also published, both of which identified the same MF potentials within the BO approximation [55, 59]. However, there were distinct differences in their focus and findings. The study in Ref. [55] is limited to the scenario where at least one of the two impurities is infinitely repulsive. In contrast, Ref. [59] and our work explore the case of two impurities with arbitrary but equal coupling constants. Moreover, in addition to the MF potential, Ref. [59] accounts for the effects of quantum fluctuations, leading to a different asymptotic scaling of the potential for large impurity distances. The first-order Born-Huang correction, which incorporates the impact of a finite impurity mass on the interaction potential, is only determined in our study. Furthermore, the bipolaron energy is calculated in our work but not in the other two publications [55, 59].
In addition to the studies on ground state properties, there are investigations of the polaron formation dynamics, akin to the analysis presented in Chapter 5 [P4]. Specifically, Refs. [57, 60] explore the time evolution following a quench of the coupling constant. However, their analysis is not as detailed as those contained in this thesis. In Ref. [60], besides examining the MF dynamics, the authors also consider the impact of quantum corrections and derive the absorption spectrum. On the other hand, Ref. [57] quantifies the strength of the friction force resulting from the emission of density waves. Nevertheless, the effects of the three distinct mechanisms responsible for impurity deceleration (emission of density waves, an increase in effective mass, and soliton emission) are comprehensively discussed only in our work in Chapter 5 [P4]. Furthermore, our study addresses the time evolution during a quasi-adiabatic turn-on of the coupling constant. It investigates the effects of quantum fluctuations in a harmonically trapped system, which sets it apart from the works mentioned above.
Besides the studies of the one-dimensional Bose polarons, the approach was also generalized to higher dimensions in Refs. [54, 56, 58]. More on the application of the theory in higher dimensions is discussed in Section 7.2.1.

1.4 Limitation of the theory and experimental consideration

Given that the central model employed in this thesis, detailed in Section 1.3, relies on a MF approximation, it is important to acknowledge its limitations. This section outlines the prerequisites for the applicability of this theory and contrasts it with current experimental findings. Some experiments have explored three-dimensional Bose polarons [17–19, 21]. Nevertheless, this section will primarily focus on Ref. [16] as it was conducted using a weakly interacting one-dimensional Bose gas, which is mainly studied in this thesis. The discussion focuses on the parameters utilized in this experiment. Their result, the measurement of the polaron mass, is addressed in Appendix A. Other experiments have also analysed 1D Bose polarons, but in the limiting case of strong Bose-Bose interaction [15, 20], which cannot be characterized with the methods used in this thesis. To avoid confusion when comparing the theory with experimental data, SI units are used in this section, including for the reduced Planck constant $\hbar \approx 1.055 \times 10^{-34}\,\mathrm{Js}$.

A necessary condition for the applicability of the MF approximation is that interaction terms in the LLP Hamiltonian given by Equation (1.23) are small compared to the kinetic energy of the particles. This concerns besides the usual contact interaction $\frac{g}{2}\int \mathrm{d}x\, \hat{\phi}^\dagger(x)^2\hat{\phi}(x)^2$ in between bosons, also the term $\hat{P}_\mathrm{B}^2/2M$ as it is quartic in the field operators.

The impact of the usual contact interaction has already been explored in many works. To quantify the interacting strength in a 1D Bose gas Refs. [50, 51] introduce the Tonks parameter $\gamma = gm/\hbar^2 n$ where g is the boson-boson coupling constant, m the boson mass and n the particle density. It represents how the interaction energy of the particles scales compared to the kinetic energy. If γ is small, interaction effects are weak, allowing the Bose gas to be treated within the MF approximation, i.e., we have to require

$$\gamma \overset{!}{\ll} 1. \tag{1.32}$$

The experiment of Ref [16] gives a realistic order of magnitude for the Tonks parameter γ. This experiment used a quasicondensate of ^{87}Rb atoms, corresponding to a mass of $m = 87\mathrm{u}$. According to their data, the 1D Bose-Bose coupling constant is $g = 2.36 \times 10^{-37}\mathrm{Jm}$ and the peak gas density $n = 7\mu\mathrm{m}^{-1}$. After back-inserting the necessary factors of $\hbar$, this corresponds to a Tonks parameter of $\gamma = 0.44$. This value is smaller than 1, however, not significantly. In principle, it should be possible to reduce this parameter further in experiments.
One way to achieve this is the employment of confinement-induced resonances as derived in Ref. [25]. One-dimensional Bose gases are usually realized by employing a tight transversal confinement potential at frequency ω on a three-dimensional gas of atoms. The effective 1D limit is reached as soon as the length scale related to this potential $l = \sqrt{2\hbar/m\omega}$ is the smallest length scale of the system. It is important to note that the 1D scattering length $a_\mathrm{1D} = -2\hbar/mg$ depends on this length scale l and, consequently, the trapping frequency ω. Ref. [25] shows that it is related to the 3D scattering length a by

$$a_\mathrm{1D} = -\frac{l^2}{2a}\left(1 + \zeta(\tfrac{1}{2})\,\frac{a}{l}\right), \tag{1.33}$$

where $\zeta(\frac{1}{2}) \simeq -1.46$ is the Riemann zeta function. Thus, different Tonks parameters can be realized by tuning the trapping frequency. The tuning of γ can also be realized utilizing a magnetic Feshbach resonance [24]. In the experiment of Ref. [16], a Feshbach resonance is

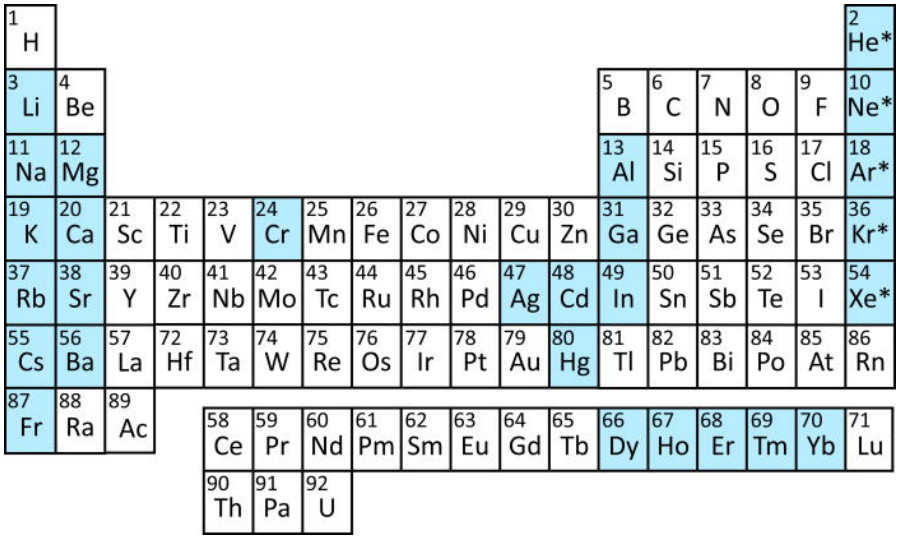

Figure 1.6: Periodic table of the elements, showing the atomic species in which laser cooling has been demonstrated up to March 2016. Note that noble gases are typically cooled in a metastable state. The figure was published in Ref. [96] under the terms of the Creative Commons Attribution 3.0 Unported license (CC BY 3.0).

used to tune the impurity-boson coupling constant to an arbitrary value. However, using this technique to independently tune g and g_{IB} is impossible.

Next, the unusual nonlocal interaction term $\hat{P}_{\mathrm{B}}^2/2M$ is to be investigated. It describes an interaction between the bosons mediated by the impurity and originates from the description in the LLP frame, see Section 1.3. The term is small compared to the kinetic energy of the Bose gas if the impurity mass is large compared to the boson mass

$$M \overset{!}{\gg} m. \tag{1.34}$$

This is the second necessary condition for the applicability of the MF approximation.
The mass ratio is, however, not arbitrarily selectable in cold gas experiments since laser-coolable atoms must realize both impurity and bath. Atomic species in which laser cooling has been demonstrated are shown in Figure 1.6 [96]. Some experiments [18] realize the distinction between impurity and bath by using different metastable hyperfine states of the same atomic species, restricting the investigation to equal mass ratio $M = m$. Others use different atoms, e.g., Ref. [16] use ^{87}Rb for the gas and ^{41}K for the impurities, resulting in a mass ratio of $M = 0.47m$, which unfortunately represents a light impurity. If the experiment would change the role of impurity and bath, it would result in a for the MF approach much more favorable ratio of $M = 2.1m$. According to current technical possibilities [96], the upper limit for the mass ratio would be given by a ^{204}Hg impurity atom [97] immersed in a BEC of ^{4}He atoms [98, 99] (if radioactive elements are excluded). This corresponds to an upper bound of $M = 51m$.

It is important to emphasize that the two conditions $\gamma = gm/\hbar^2 n \ll 1$ and $M \gg m$ are independent of the impurity-boson coupling constant g_{IB}. Remarkably, the approach of this thesis yields accurate results for a wide range of g_{IB} values. Chapters 2, 3 and 5 [P1, P2, P4]

demonstrate that significant condensate deformation occurs for

$$g_{\mathrm{IB}} \gtrsim gn\xi. \tag{1.35}$$

The commonly used Fröhlich model discussed in Section 1.2.1 fails to provide reasonable results in this limit, whereas the MF model in the LLP frame does.

Finally, this section provides an estimate of the relevant scales in SI units for the context of this work, using the experimental parameters from Ref. [16] once again.
The healing length $\xi = \hbar/\sqrt{2gnm} \approx 150$nm is a significant length scale. It appears, for instance, as the characteristic length of the deformation induced by the impurity. Additionally, the range of the induced polaron-polaron interaction, as determined in Section 3 [P2], is also on the order of ξ.
The relevant time scale is the inverse of the chemical potential, $\hbar/gn$, which is approximately 64µs. Non-equilibrium phenomena studied in Sections 4 and 5 [P3, P4] occur on this time scale.
An important velocity can be derived from the two scales, the speed of sound $c = \sqrt{gn/m} = \sqrt{2}gn\xi/\hbar$, which is in the order of 3.4mm/s. This velocity represents the speed at which signals propagate through the condensate and is also an order of magnitude estimation for the critical velocity below which polaron formation becomes possible, which is discussed in Section 5 [P4].

1.5 Analytic solution of the homogeneous Gross–Pitaevskii equation

This section excludes the impurity and focuses exclusively on the properties of the Bose gas itself. The gas is assumed to be weakly interacting, and it is described in the MF approximation using a GPE. Presented are some known solutions of this equation, which will later play a crucial role in deriving the stationary states of the Bose polaron in Chapter 2 [P1] and the bipolaron in Chapter 3 [P2]. Additionally, these states are vital for understanding the simulation of the non-equilibrium polaron properties in Chapters 4 and 5 [P3, P4]. In the following, only the essential building blocks necessary for the subsequent analyses in this thesis are presented. For a more comprehensive analysis of the subject of cold Bose gases, the books [88, 89] provide more extensive coverage.

The following section presents solutions of the homogeneous GPE in its simplest form

$$i\partial_t\, \phi(x,t) = \Big[-\frac{\partial_x^2}{2m} + g|\phi(x,t)|^2 \Big]\phi(x,t). \tag{1.36}$$

It includes only dispersion via the kinetic energy and a nonlinearity generated by the Bose-Bose contact interaction. The latter is always repulsive in this thesis, so $g > 0$. Although the GPE is nonlinear, it has several known analytical solutions. A straightforward but vital solution is a constant density n of atoms

$$\phi(x,t) = \sqrt{n}\, e^{-i\mu t}, \tag{1.37}$$

where $\mu = gn$ is the chemical potential. It is the ground state of the system and minimizes the total energy

$$E = \int_{-L/2}^{L/2} \mathrm{d}x\; \phi(x,t)^* \Big[-\frac{\partial_x^2}{2m} + \tfrac{1}{2} g|\phi(x,t)|^2 \Big]\phi(x,t), \tag{1.38}$$

which results in the MF expression for the energy of a homogeneous Bose gas

$$E = \tfrac{1}{2} g n^2 L. \tag{1.39}$$

The subsequent sections present two types of excited states of the GPE. First, local dispersionless wave excitations known as solitons are discussed in Section 1.5.1. Second, stationary states that are periodic in space are explored in Section 1.5.2.

1.5.1 Soliton

A fundamental solution of the GPE is a solitary wave, or simply soliton [88, 100]. It is a localized disturbance that can propagate through the system without a change of form. Nonlinear effects in the medium thereby cancel the dispersion of the wave. Solitons have a long history beyond the field of ultra-cold atoms, starting with the observation of shallow water waves in 1834 by John Scott Russell [101]. They exist for several different nonlinear equations, for example, the Korteweg-de-Vries equation [102], which describes the propagation of these shallow water waves, or the GPE, which is used in this thesis to model Bose condensates.
Despite being realized in various systems, solitons share some common properties, which Russel has already described [101]:

- They are stable waves that can travel long distances without dispersing.
- The size of the soliton wave is related to its speed.
- Solitary waves do not scatter when they interact with each other. They can pass through each other without any disturbance.

The simplest kind of a solitary wave for repulsive Bose-Bose interaction is a dark soliton, given by the wave function

$$\phi(x,t) = \sqrt{n}\, e^{-i\mu t} \tanh\left(\frac{x}{\sqrt{2}\xi}\right), \tag{1.40}$$

where n is the asymptotic density, $\mu = gn$ the chemical potential and $\xi = 1/\sqrt{2gnm}$ the coherence or healing length of the Bose gas. The latter is a typical length scale of a condensate, referring to the distance over which the wave function tends to its bulk value when subjected to a local disturbance. A dark soliton is a stationary state, corresponding to a soliton at zero velocity. It represents a local density disturbance where the density drops to zero at the center, which is why it is named a "dark" soliton. The density depletion is accompanied by a discontinuous phase jump of π, see Figure 1.7.
However, besides the stationary solitary waves, those moving at a fixed velocity do exist. To show this a Galilean transformation is applied to the GPE (1.36), into a frame moving at fixed velocity v by

$$\phi(x,t) = \tilde{\phi}(x - vt, t), \tag{1.41}$$

resulting in the transformed equation

$$i\partial_t\, \tilde{\phi}(x,t) = \Big[-\frac{\partial_x^2}{2m} + iv\,\partial_x + g|\tilde{\phi}(x,t)|^2 \Big]\tilde{\phi}(x,t). \tag{1.42}$$

As a side note, this differential equation is very similar to Equation (1.24), which describes the Bose gas in the LLP frame co-moving with the impurity. This is rather not surprising since

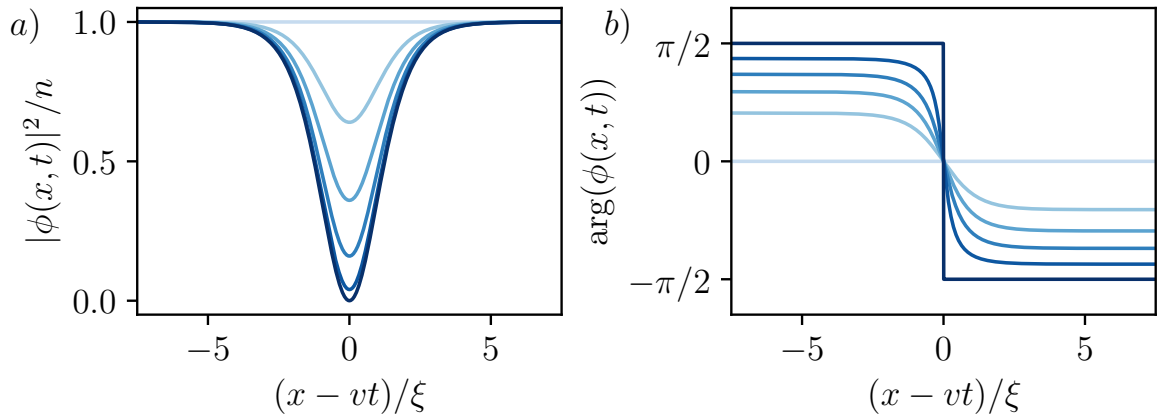

Figure 1.7: a) Density and b) phase of a grey soliton for different velocities. The shades of blue, from darkest to lightest, correspond to $v/c = 0.0, 0.2, 0.4, 0.6, 0.8, 1.0$. As the velocity increases, the soliton becomes less depleted, and the phase jump becomes smaller.

the Galilean transformation (1.41) resembles a classical version of the LLP transformation $\hat{U}_{\mathrm{LLP}} = \exp(-i\hat{r}\hat{P}_{\mathrm{B}})$, where the impurity operator $\hat{r}$ is replaced by the c-number $v\,t$.
A solution to Equation (1.42), the wave function describing the moving soliton, is given by

$$\phi(x,t) = \sqrt{n}\left[i\,\frac{v}{c} + \sqrt{1-\frac{v^2}{c^2}}\,\tanh\left(\frac{x-vt}{\sqrt{2}\,\xi}\right)\right] e^{-i\mu t}, \tag{1.43}$$

where $c = \sqrt{\frac{gn}{m}} = \sqrt{2}gn\xi$ is the speed of sound in the condensate. Notably, moving solitons can only exist if their velocity v is below the speed of sound. In Figure 1.7, the density and phase of this solution are depicted for different velocities v. In contrast to a stationary dark soliton, the minimum density of a moving one is nonzero, but it scales with $n_{\mathrm{min}} = nv^2/c^2$, which is why they are often referred to as grey solitons. Furthermore, the phase of a grey soliton also exhibits a "jump"; However, this "jump" is continuous and always less than π. For a vanishing velocity $v = 0$, the wave function of a moving soliton goes over into the dark soliton state given by Equation (1.40). However, as v increases up to c, the soliton vanishes, and the state crosses over to a condensate of constant density, see Equation (1.37).
The energy of a moving soliton can be determined from Equation (1.38). After subtraction of the MF energy $\frac{1}{2}gn^2L$ of a homogeneous condensate, the grey soliton energy is given by

$$E = \frac{4}{3}nc\left(1-\frac{v^2}{c^2}\right)^{3/2} \simeq \frac{4}{3}nc - \frac{2n}{c}\,v^2 + \mathcal{O}\left(v^4\right) \tag{1.44}$$

Notably the soliton energy decreases with increasing velocity, which corresponds to a negative effective soliton mass of $-4n/c$. This behavior can be understood by considering that solitons represent hole excitations in the condensate.

1.5.2 Periodic solution

In addition to the localized solutions, solitary waves, the GPE also admits solutions that are periodic in space. These periodic solutions are essential in deriving the stationary bipolaron wave function in Chapter 3 [P2], as the Bose gas in between the two impurities is given by such a state. In this context, the focus remains solely on stationary solutions, analogous to dark solitons at zero velocity. While periodic solutions can also be generalized to running waves, as shown in Ref. [103], such generalization is irrelevant in this thesis.
The wave function for the periodic solutions is expressed as

$$\phi(x,t) = \sqrt{\frac{2n\,\nu}{1+\nu}}\,e^{-i\mu t}\,\mathrm{sn}\left(\frac{x}{\xi\sqrt{1+\nu}},\nu\right), \tag{1.45}$$

where sn represents a Jacobi-elliptic function [104], which is a generalization of trigonometric and hyperbolic function. The healing length $\xi = 1/\sqrt{2gnm}$ and chemical potential $\mu = gn$ is defined as in Section 1.5.1. The second parameter ν of the elliptic function is real-valued and between 0 and 1. It is related to the period length X of the state by

$$X = 4\xi\sqrt{1+\nu}\,\mathrm{K}(\nu), \tag{1.46}$$

where $\mathrm{K}(\nu)$ it the complete elliptic integral of the first kind [104]. The relation between X and ν is shown in Figure 1.8b), from which it becomes apparent that the solution exists only for waves

with a period $X > 2\pi\xi$. The density, corresponding to the wave function in Equation (1.45), is displayed for different period lengths X in Figure 1.8. As X approaches infinity, the state becomes exactly equal to a single dark soliton located at $x = 0$, given by Equation (1.40). For large but finite values of $X \gg \xi$, the condensate forms a lattice of solitons with a distance of $X/2$ between them. The density remains flat in the space between these solitons with a bulk value of n. However, as X approaches the minimum value of $2\pi\xi$, the Bose gas cannot reach a bulk value, resulting in sinusoidal density oscillations. Since the healing length ξ is the characteristic length scale on which the Bose gas is deformable, no stable periodic solution exists below the critical value.
An energetic argument can also explain the vanishing solution for a small lattice spacing. The ratio of interaction energy $\langle\hat{V}\rangle$ to kinetic $\langle\hat{T}\rangle$ is given by

$$\frac{\langle\hat{V}\rangle}{\langle\hat{T}\rangle} = \frac{\frac{1}{2}g\int \mathrm{d}x\,|\phi(x,t)|^4}{\frac{1}{2m}\int \mathrm{d}x\,|\partial_x\,\phi(x,t)|^2} = \frac{(2+\nu)K(\nu) - 2(1+\nu)E(\nu)}{(-1+\nu)K(\nu) + (1+\nu)E(\nu)}, \tag{1.47}$$

where $\mathrm{E}(\nu)$ it the complete elliptic integral of the second kind [104]. This ratio is plotted as a function of the lattice spacing X in Figure 1.8b). For large $X \gg \xi$, the majority of the condensate has a constant density, resulting in a small kinetic energy $\langle\hat{T}\rangle \ll \langle\hat{V}\rangle$. However, as X is lowered towards the critical value, the curvature of the wave function increases, leading to an increase in the kinetic energy, until $\langle\hat{T}\rangle$ becomes much larger than $\langle\hat{V}\rangle$. The interaction energy drops to zero at the critical value, which is only possible for a vanishing gas density. Therefore, the critical value of $X = 2\pi\xi$ marks the boundary below which stable periodic solutions do not exist due to the resulting vanishing gas density.
This critical value is essential in Chapter 3[P2] for modeling a strong repulsive bipolaron ($g_{\mathrm{IB}} \gg g$). We will see that the impurities must be positioned at a node of such a periodic function, as they repel the gas strongly. If their distance is smaller than the critical value $X/2 = \pi\xi$, the condensate density must vanish between them.

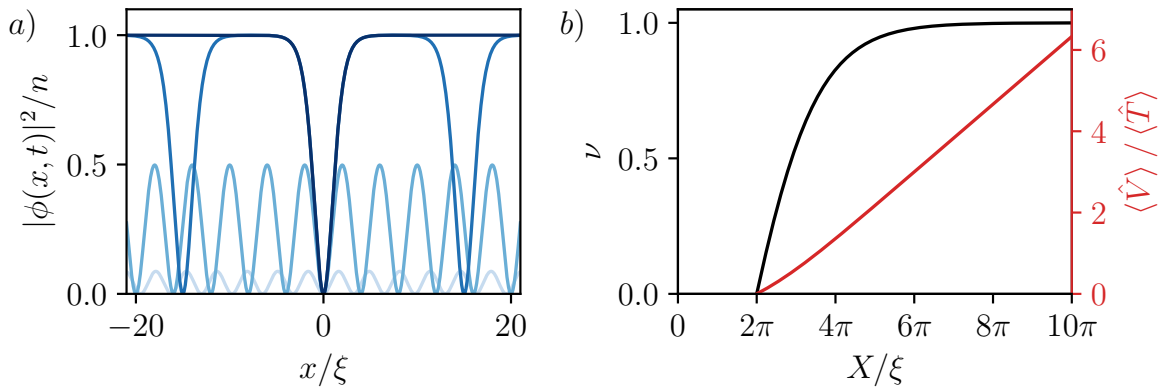

Figure 1.8: a) Density of the periodic solution of a GPE. The shades of blue, from darkest to lightest, correspond to different period lengths $X/\xi = \infty$, 30, 10, 7. The condensate is a lattice of evenly spaced dark solitons for a large spacing $X \gg \xi$. However, the density becomes sinusoidal for small $X \gtrsim 2\pi\xi$. b) The parameter ν is represented in black as a function of the period of the wave function. The red curve depicts the ratio of interaction $\langle\hat{V}\rangle$ to kinetic energy $\langle\hat{T}\rangle$. A stable solution only exists for $X > 2\pi\xi$.

2 Strong-coupling Bose polarons in one dimension: Condensate deformation and modified Bogoliubov phonons

Jonas Jager, Ryan Barnett, Martin Will, and Michael Fleischhauer,
Phys. Rev. Research **2**, 033142 (2020).

This study investigates the ground state properties of a single 1D Bose-polaron, particularly emphasizing the regime of a strong impurity-boson coupling strength g_{IB}. Our primary objectives are determining the polaron energy E_{B} and effective mass m^*. To accomplish this, we employ a MF theory, which includes the deformation of the condensate induced by the impurity. In order to account for the effect of quantum fluctuations, we add phononic excitation on top of the deformed MF solution by solving the Bogoliubov-de-Gennes (BdG) equation.
First, we determine the MF ground state of the polaron for both repulsive and attractive impurity-boson interactions. The state is derived in the thermodynamic limit and for a small polaron momentum p. We employ the MF approximation of the ground state wave-function to calculate the polaron energy and mass. The expressions given in the publication can be simplified to

$$E_{\mathrm{P}} = \tfrac{4}{3} n\tilde{c} \left[1 + \tfrac{3}{2}\,\chi + \chi^3 - \left(1+\chi^2\right)^{3/2}\right], \tag{2.1}$$

$$m^* = M + 4\sqrt{2}\, n\tilde{\xi}\, \tilde{m} \left[\sqrt{1+\chi^2} - 1\right]. \tag{2.2}$$

Here, the dimensionless parameter $\chi = g_{\mathrm{IB}}/(2\sqrt{2} g n \tilde{\xi})$ indicates if the condensate undergoes substantial deformation when $|\chi| \gtrsim 1$. Other parameters are the impurity and boson masses, M and m, and the reduced mass $\tilde{m} = (1/M + 1/m)^{-1}$. The rescaled healing length is $\tilde{\xi} = 1/\sqrt{2\tilde{m} g n}$, and the speed of sound $\tilde{c} = \sqrt{gn/\tilde{m}}$. Note that the result obtained from the dispersive definition of the mass $E = E_{\mathrm{P}} + p^2/2m^* + \mathcal{O}(p^4)$, is consistent with the kinematic definition $M/m^* = \lim_{p\to 0}(1 - P_{\mathrm{B}}/p)$. Here, P_{B} is the momentum of the Bose gas.
The mass and energy expressions are compared to results from other theoretical approaches in Figure 2.1. Notably, both quantities exhibit good agreement with results obtained from quasi-exact DMC simulation. However, theories based on the extended Fröhlich model deviate for $g_{\mathrm{IB}} \gtrsim g n \tilde{\xi} \approx 2g$, for the parameters of Ref. [16]. This occurs because the Fröhlich model does not properly account for the condensate deformation (see Section 1.2.1). In the case of a strongly repulsive polaron, the impurity repels the condensate away from its position, leading to an identical density profile and energy as those of a dark soliton. However, for a large coupling $g_{\mathrm{IB}} \gg g$, there is a substantial discrepancy between the polaron mass results obtained from MF and DMC. While DMC predicts a finite value, the MF theory suggests a divergent result. Further investigation revealed that this discrepancy arises due to finite size effects in the DMC simulations, as the total mass of the system bounds the polaron mass (see supplemental material B of Chapter 3 [P2]).

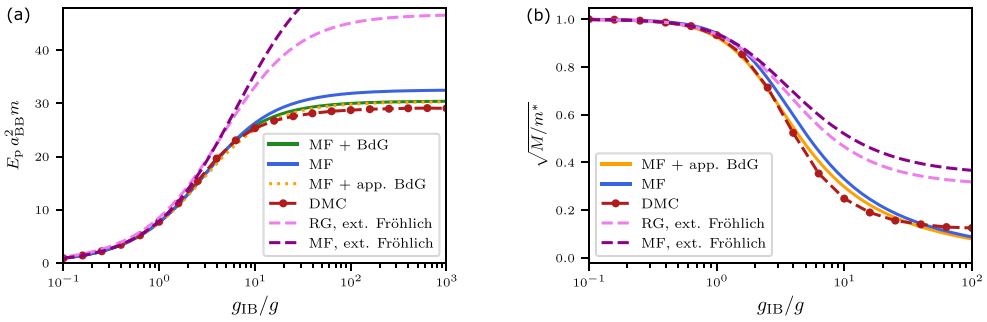

Figure 2.1: a) Polaron energy E_P and b) mass m^* as a function of the impurity-boson coupling constant g_{IB} for the parameters of the experiment of Ref. [16]. The Tonks parameter is $\gamma = gm/n = 0.44$ and the mass ratio $M = 0.47m$. The 1D boson-boson scattering length is $a_{BB} = -2m/g$. The MF theory developed here, in- and excluding the BdG correction, is compared to a quasi-exact DMC simulation and results based on the extended Fröhlich model, both derived in Ref. [33].

Next, we highlight the significance of employing PBCs in calculating the effective polaron mass m^*. When PBCs are applied, a phase gradient in the order of the inverse system size $1/L$ is present far away from the impurity. While this gradient tends to zero in the thermodynamic limit, it results in a non-zero contribution to the total Bose gas momentum P_B. It is crucial to account for this term to ensure the equality of the kinematic and dispersive polaron mass. Moreover, additional reasons are mentioned in the publication for employing PBCs, but an important one is missing. As discussed in Section 1.3.1, the LLP transformation only decouples the center-of-mass motion if the system obeys PBCs. Otherwise, the total momentum is not conserved, and the momentum operator cannot be replaced by a c-number, which is a fundamental assumption throughout the publication.
Finally, the influence of quantum fluctuations is investigated by expanding the bosonic field operators $\hat{\phi}(x)$ around the MF solution $\phi(x)$, by

$$\hat{\phi}(x) = \phi(x) + \hat{\xi}(x). \tag{2.3}$$

Since the MF approximation already yields good results, quantum fluctuations are small, such that we only keep terms up to quadratic order in $\hat{\xi}(x)$. Afterward, the Hamiltonian is diagonalized numerically by a BdG transformation. Figure 2.1 shows that the agreement with results from DMC is further improved by including the BdG correction.

Author contributions

In this study, Jonas Jager and I developed and applied the MF theory described in Section 1.3. We solved it analytically for the steady-state solution and deduced an analytic expression for the polaron energy and mass. Furthermore, Jonas Jager and Ryan Barnett performed numerical simulations to account for corrections to the MF approximation using a BdG theory. The original idea for this approach came from Michael Fleischhauer, who also supervised the entire project. All authors were involved in discussions on results and contributed to the writing and reviewing process of the manuscript.

Copyright

Strong-coupling Bose polarons in one dimension: Condensate deformation and modified Bogoliubov phonons

J. Jager,[1] R. Barnett,[1] M. Will,[2] and M. Fleischhauer[2]
[1]*Department of Mathematics, Imperial College London, London SW7 2AZ, United Kingdom*
[2]*Department of Physics and Research Center OPTIMAS, University of Kaiserslautern, 67663 Kaiserslautern, Germany*

(Received 3 February 2020; accepted 2 July 2020; published 24 July 2020; corrected 22 April 2021)

We discuss the interaction of a quantum impurity with a one-dimensional degenerate Bose gas forming a Bose polaron. In three spatial dimension, the quasiparticle is typically well described by the extended Fröhlich model, in full analogy with the solid-state counterpart. This description, which assumes an undepleted condensate, fails, however, in 1D, where the backaction of the impurity on the condensate leads to a self-bound mean-field polaron for arbitrarily weak impurity-boson interactions. We present a model that takes into account this backaction and describes the impurity-condensate interaction as coupling to phononlike excitations of a deformed condensate. A comparison of polaron energies and masses to diffusion quantum Monte Carlo simulations shows very good agreement already on the level of analytical mean-field solutions and is further improved when taking into account quantum fluctuations.

DOI: 10.1103/PhysRevResearch.2.033142

I. INTRODUCTION

The polaron, introduced by Landau and Pekar [1,2] to describe the interaction of an electron with lattice vibrations in a solid, is a paradigmatic model of quasiparticle formation in condensed-matter physics. A hallmark feature of the quasiparticle is mass enhancement: the electron becomes dressed by a cloud of phonons which in turn affects its dynamical properties. The polaron concept has wide applications across condensed-matter physics ranging from charge transport in organic semiconductors to high-T_c superconductivity [3,4].

More recently, neutral atoms immersed in quantum gases have attracted much attention since they are experimentally accessible platforms for studying polaron physics with high precision and in novel regimes. For example, the impurity-bath interaction can be tuned from weak to strong coupling employing Feshbach resonances [5]. In such systems, the impurity atom is immersed in a superfluid and a polaron is formed by its interaction with the collective excitations of the superfluid. The Fermi-polaron, i.e., an impurity in a degenerate Fermi gas, has been studied in a number of experiments [6–14]. In contrast, only a few experiments on Bose polarons exist [15–18]. Due to the compressibility of a Bose gas, a large number of excitations can be generated, and interactions within the Bose gas are important.

Theoretical works addressing the Bose polaron most often describe the interaction with the impurity as a coupling to Bogoliubov phonons of a *uniform* superfluid [19–24]. The resulting (extended) Fröhlich Hamiltonian is formally identical to the one used in solid-state systems [25], amended with two-phonon scattering terms. Efficient approaches for its solution beyond the perturbative regime have been developed in the past, including variational [24,26,27], field-theoretical [19,28–30], renormalization group (RG) [23,31], and open-system approaches [32], as well as quantum Monte-Carlo simulations [23,33,34]. However, as well known from the example of electrons in superfluid helium, a strongly interacting impurity can also distort the superfluid itself [35]. This deformation creates a potential for the impurity which can lead to a self-bound state. In 3D, the normalized impurity-Bose interaction has to exceed a critical value for this, given by the inverse gas parameter [36–38]. Since for typical condensates the gas parameter is very small, the extended Fröhlich model remains adequate.

The situation is different in 1D, which was experimentally realized in Ref. [15]. Here an arbitrarily weak deformation of the condensate leads to a self-localized impurity [37]. This restricts the accuracy of the Fröhlich model to the perturbative regime. In fact, a comparison between exact diffusion Monte Carlo (DMC) simulations of the full model with RG solutions of the extended Fröhlich model in Ref. [23] shows that this model is only accurate for weak interactions and breaks down completely for attractive interactions at intermediate interactions.

In this paper, we follow a different approach, and expand the Bose quantum field about the exact mean-field solution in the presence of the mobile impurity in the Lee-Low-Pines (LLP) frame [39]. Such a treatment incorporates the backaction of the impurity already at the mean-field level as in Refs. [36–38], but keeps the entanglement between impurity and BEC by working in the LLP frame. Quantum effects are then taken into account by the coupling to phononlike excitations of the deformed superfluid. Motivated by

experiments [15] and the availability of semianalytic mean-field solutions, we here consider a 1D quasi condensate with weak to moderate boson-boson interactions. While the experiments are performed in a harmonic trap, we assume periodic boundary conditions when introducing phonons. Strictly speaking, there is no BEC in a homogeneous 1D system and also the quasiparticle concept is believed to break down [40,41] due to a diverging number of low-energy excitations emitted by the impurity. Thus, special care must be taken when calculating quantum effects. We derive the effective Hamiltonian for the deformed phonons and solve them in the Bogoliubov approximation. Our treatment carries over naturally to higher dimensional systems with the only difference that the mean-field solutions have to be obtained numerically. Other treatments of the 1D polaron based on a factorization of the N-particle wave function in the LLP frame exist that take the deformation of the condensate into account [42–45]. The scope of extending them to incorporate quantum fluctuations is limited, however. We note that the standard arguments to define the polaron mass, applicable for Fröhlich-type models, give nonsensical results here and require a careful reconsideration. We derive analytical expressions for the mean-field polaron wave function, from which we reproduce previous approximations for the polaronic mass and energy. We then calculate quantum corrections by solving the Bogoliubov deGenne equations in a self-consistent approach. Our results are benchmarked against recent DMC results [23]. We find very good agreement in all regimes for repulsive interactions underpinning the hypothesis that expanding about the nonuniform condensate is an excellent starting point. We also present results for attractive interactions. Here we find again very good agreement with DMC for the energy of the polaron but less good agreement for the mass. We attribute this discrepancy to the existence of many-particle bound states in the attractive regime [23,33].

II. MODEL AND PROPER DEFINITION OF POLARON MASS

Our starting point is a single impurity atom coupled to N identical bosons in one dimension, described by the Hamiltonian

$$\hat{\mathcal{H}} = \int dx\, \hat{\phi}^\dagger(x)\Big(-\frac{1}{2m}\partial_x^2 + \frac{g_{\rm BB}}{2}\hat{\phi}^\dagger(x)\hat{\phi}(x) - \mu + g_{\rm IB}\delta(x-\hat{X})\Big)\hat{\phi}(x) + \frac{\hat{P}^2}{2M}. \tag{1}$$

Here m (M) denotes the mass of the bosons (impurity atom), $\hat{\phi}(x)$ is the Bose field operator, $g_{\rm BB}$ ($g_{\rm IB}$) are the boson-boson (boson-impurity) interaction strength, $\hat{X}$ ($\hat{P}$) denotes the position (momentum) operator of the impurity, and μ is the chemical potential of the Bose gas. Throughout the paper, we set $\hbar = 1$ and employ periodic boundary conditions of length L. The relative interaction strength is denoted by $\eta = g_{\rm IB}/g_{\rm BB}$ and we introduce the healing length $\xi = 1/\sqrt{2m\mu}$ and the speed of sound $c = \sqrt{\mu/m}$. Expanding the bosonic field operator in Eq. (1) around a homogenous condensate as $\hat{\phi}(x) = \sqrt{n_0} + \hat{\xi}(x)$ with $n_0 = N/L$ leads to the extended Fröhlich Hamiltonian [24,25]. In this paper, we choose a different starting point and consider the effects of the impurity already at the level of the condensate.

Before delving into the solutions of the mean-field equations, it is important to point out some fundamental differences between the ground state of the effective Fröhlich and the full Hamiltonian Eq. (1) for finite momentum. For the Fröhlich model, it is easy to show that for fixed total momentum, the ground state is indeed the polaronic solution [23,39,46]. The situation is very different for Eq. (1). Indeed, the ground state for finite momentum for this case is the uniformly boosted system. To see this, we introduce the potential $\hat{\Omega} = \hat{\mathcal{H}} - v\hat{P}_{\rm tot}$, with total momentum $\hat{P}_{\rm tot} = \hat{P}_{\rm B} + \hat{P}$ where $\hat{P}_{\rm B} = -i\int \hat{\phi}^\dagger(x)\partial_x\hat{\phi}(x)\,{\rm d}x$. It is straightforward to see that finding the constrained ground state of Eq. (1) (with fixed total momentum) is equivalent to finding the unconstrained ground state of $\hat{\Omega}$ for a given v which acts as a Lagrange multiplier. Introducing the unitary transformation $\hat{U}_{\rm cm} = \exp(-iM_{\rm tot}\hat{X}_{\rm cm}v)$, with $M_{\rm tot} = Nm + M$ and $\hat{X}_{\rm cm} = \frac{1}{M_{\rm tot}}(m\int {\rm d}x\, x\hat{\phi}^\dagger(x)\hat{\phi}(x) + M\hat{X})$ to boost into the center-of-mass frame, one finds $\hat{\Omega} = \hat{U}_{\rm cm}^\dagger\hat{\mathcal{H}}\hat{U}_{\rm cm} - \frac{1}{2}M_{\rm tot}v^2$. With this expression, one can clearly relate eigenstates of $\hat{\mathcal{H}}$ with those of $\hat{\Omega}$. In particular, the ground state for finite momentum (corresponding to finite v) is the *boosted* ground state and the effective mass of the polaron always equals the total mass. Such a uniformly boosted system is precluded in the Fröhlich model.

We proceed as in the case of the Fröhlich model and eliminate the impurity position operator from Eq. (1) by a LLP- [39] type transformation $\hat{U}_{\rm LLP} = \exp(-i\hat{X}\hat{P}_{\rm B})$. Here, in contrast, the *total* momentum of the bosons $\hat{P}_{\rm B}$ enters. $\hat{U}_{\rm LLP}$ transforms to a comoving frame, where the impurity is at the origin and its momentum is transformed to the conserved total momentum of the system which can be treated as a c-number P. By eliminating the impurity from the problem by an exact transformation, entanglement between the impurity and the condensate is already included on the mean-field level and we do not have to assume a factorized wave function as, for example, done in Refs. [37,38]. At the same time, an impurity-mediated interaction between the bosons $\sim\int {\rm d}x\,(P-\hat{P}_{\rm B})^2/2M$ emerges in the transformed Hamiltonian. To treat this, it will prove helpful to introduce a Hubbard-Stratonovich field $\hat{u}$, which gives

$$\hat{\mathcal{H}}^{\rm S}_{\rm LLP} = \int dx\, \hat{\phi}^\dagger(x)\Big(-\frac{1}{2m_{\rm r}}\partial_x^2 + \frac{g_{\rm BB}}{2}\hat{\phi}^\dagger(x)\hat{\phi}(x) - \mu + g_{\rm IB}\delta(x)\Big) \times\hat{\phi}(x) + \hat{u}(P-\hat{P}_{\rm B}) - \frac{1}{2}M\hat{u}^2, \tag{2}$$

where $\hat{u}$ satisfies $M\hat{u} = P - \hat{P}_{\rm B}$, and can thus be viewed as the impurity velocity. $m_{\rm r} = (M+m)/Mm$ is the reduced mass, and we defined rescaled healing length $\bar{\xi} = \sqrt{m/m_{\rm r}}\xi$ and speed of sound $\bar{c} = \sqrt{m/m_{\rm r}}c$.

III. MEAN-FIELD SOLUTIONS

A. Mean-field equations in the presence of the impurity

We now expand $\hat{\phi}(x) = \phi(x) + \hat{\xi}(x)$ and $\hat{u} = u + \delta\hat{u}$, where $\phi(x)$ and u are chosen to solve the mean-field equations of Eq. (2); for details, see Appendix A,

$$\left(-\frac{1}{2m_{\rm r}}\partial_x^2 + g_{\rm BB}|\phi(x)|^2 - \mu + iu\partial_x\right)\phi(x) = 0, \tag{3}$$

$$\partial_x\phi(x)|_{0^-}^{0^+} = 2m_{\rm r}g_{\rm IB}\phi(0), \tag{4}$$

subject to the boundary conditions $\phi(\frac{L}{2}) = \phi(-\frac{L}{2})$ and $|\phi(\pm L/2)|^2 = n_0 + \mathcal{O}(1/L)$. Note that to remedy the problem of the uniformly boosted system being the ground state, we require that the polaron is a *local* quantity. Thus the condensate must be stationary far away from the impurity up to $1/L$ corrections. Solutions of the mean-field equations exist in the literature where the phase is not periodic [42,47] and have been applied to the 1D polaron before [43–45]. The nonperiodic phase corresponds to unphysical sources at the boundary and leads to wrong predictions such as a negative kinematic polaron mass. We instead find the mean-field solution of the form $\phi(x) = \sqrt{n(x)}e^{i\theta(x)}$ (see Appendix A for more details),

$$n(x) = \frac{\mu}{g_{\rm BB}}(1 - \beta\,\mathrm{sech}^2(\sqrt{\beta/2}(|x| + x_0)/\bar{\xi})), \tag{5}$$

with $\beta = 1 - \frac{u^2}{\bar{c}^2} + \mathcal{O}(1/L^2)$ and $\mu = g_{\rm BB}n_0^{\rm MF} - (\partial_x\theta_1)u + \mathcal{O}(1/L^2)$. If we consider the mean-field solution alone, we fix $n_0^{\rm MF} = n_0(1 + 2\sqrt{2\beta}\bar{\xi}/L(1 - \tanh(\sqrt{\beta/2}x_0/\bar{\xi}))) + \mathcal{O}(1/L^2)$, where $n_0 = N/L$ is the average density of bosons. Upon considering quantum fluctuations later on, the mean-field density needs to be adjusted. For the phase, we find $\theta(x) = \theta_0(x) + (2f(0) - 2f(L/2))x/L$ with

$$f(x) = \arctan\left(\frac{\sqrt{4u^2\beta/\bar{c}^2}}{e^{\sqrt{2\beta}(x+x_0)/\bar{\xi}} - 2\beta + 1}\right)$$

for $x > 0$ and $\theta_0(x) = 2f(0) - f(-x)$ for $x < 0$. Finally, we determine x_0 through the jump condition for the derivative. In the limit $u = 0$, we find for $g_{\rm IB} > 0$: $x_0 = \frac{\bar{\xi}}{\sqrt{2}}\log(y)$, with $y = \sqrt{1 + 8\frac{n_0^2\bar{\xi}^2}{\eta^2}} + 2\frac{\sqrt{2}n_0\bar{\xi}}{\eta}$ and for $g_{\rm IB} < 0$, we have $x_0 \to x_0^{\rm a} = x_0 + i\pi/2\bar{\xi}(2/\beta)^{1/2}$. It is instructive to insert $x_0^{\rm a}$ into Eq. (5) and obtain the density profile for the attractive side explicitly:

$$n^a(x) = \frac{\mu}{g_{\rm BB}}\left(1 + \beta\,\mathrm{csch}^2(\sqrt{\beta/2}(|x| + x_0)/\bar{\xi})\right). \tag{6}$$

It becomes apparent that the density far away of the impurity now is lowered instead of increased, and is given by $n_0^{\rm MFa} = n_0(1 - 2\sqrt{2\beta}\bar{\xi}/L(\coth(\sqrt{\beta/2}x_0/\bar{\xi}) - 1)) + \mathcal{O}(1/L^2)$. This seemingly small correction can have a profound impact for $|\eta| \gg 1$. In this limiting case, $(\coth(\sqrt{\beta/2}x_0/\bar{\xi})$ divergences and a macroscopic large amount of the bosons aggregates around the impurity. For a finite system, this signals a collapse of the condensate onto the impurity. Due to those effects, we restrict our analysis of the attractive side to moderate values of $|g_{\rm IB}|$.

In Fig. 1, mean-field predictions for condensate density and phase are shown for different interaction strengths and a slowly moving impurity. From the analytical solution, we

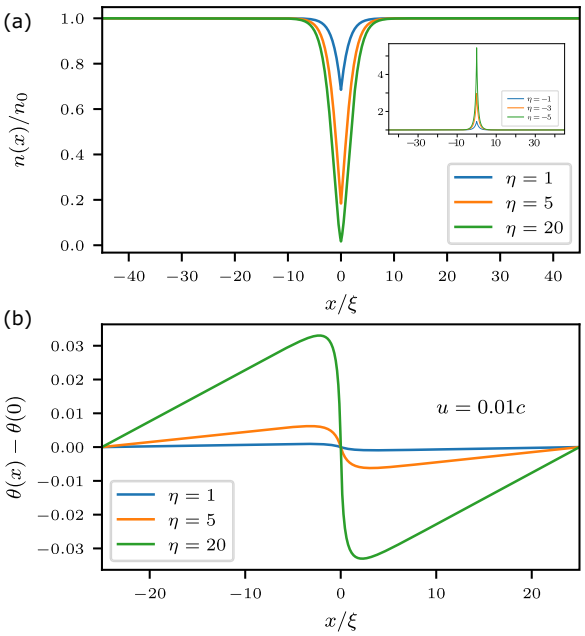

FIG. 1. Mean-field solution for different interactions and various couplings. All other parameters are as in Ref. [15], i.e., $M/m = 0.47$, the peak density $n_0 = 7/\mu$m, and $g_{\rm BB} = 2.36 \times 10^{-37}$ Jm. For the phase, we fixed $u = 0.01c$, which fixes the total momentum on the mean-field level.

can derive a parameter characterizing the relative condensate deformation,

$$\eta/n_0\bar{\xi} = \eta\sqrt{2\bar{\gamma}}, \tag{7}$$

with $\bar{\gamma} = \gamma m_r/m$, where $\gamma = 1/(2n_0^2\xi^2)$ is the so-called Tonks parameter of the 1D Bose gas [48,49], which should be less than unity for the Bogoliubov approximation to hold. The deformation becomes sizable if $\eta/n_0\bar{\xi} \sim 1$.

With the analytical expressions for the condensate density and phase, we can calculate the polaron energy $E_p = E(g_{\rm IB}) - E(g_{\rm IB} = 0)$ and the effective mass m^* of the polaron using $M/m^* = \lim_{p\to 0}(1 - \frac{P_{\rm B}}{p})$, with $P_{\rm B}$ being the mean-field momentum of the condensate, see Ref. [31]. This gives

$$E_{\rm p}^{\rm r,a} = g_{\rm IB}n_0\left(\frac{|y| \mp 1}{|y| \pm 1}\right)^2 + \frac{8}{3}n_0\bar{c}\left(\frac{3|y| \pm 1}{(|y| \pm 1)^3}\right) \tag{8}$$

for the energies of the repulsive ($E_p^{(r)}$, upper sign) and attractive ($E_p^{(a)}$, lower sign) polaron, and for the mass:

$$\frac{M}{m^*} = \frac{M(y^2 - 1)}{8n_0\bar{\xi}m_{\rm r}\sqrt{2} + M(y^2 - 1)}. \tag{9}$$

These expressions agree with previous findings in Refs. [43,45]. It is interesting to note that for $\eta \to \infty$, Eq. (8) approaches the energy of a dark soliton and the effective mass m^* goes to infinity which is in contrast to results from the extended Fröhlich Hamiltonian [23]. At this point, we note that on the attractive side the solution will collapse to a multiparticle bound state for $\eta \gg 1$, which can be easily seen by noting $E_{\rm p}^{\rm a} \to -\infty$ for $\eta \to -\infty$.

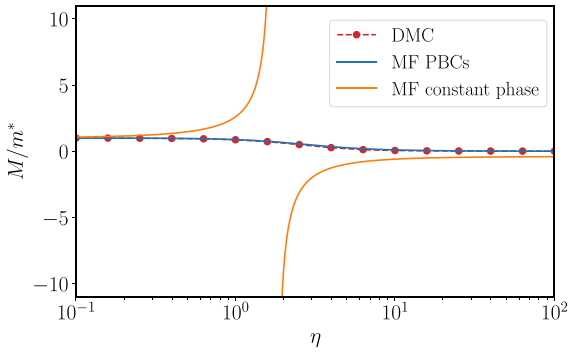

FIG. 2. Polaron mass calculated in mean-field approximation with periodic boundary conditions (PBCs) or constant phase far away from the impurity compared to DMC calculated in Ref. [23]. While the solution using periodic boundary conditions agrees very well with the DMC results, the constant phase solution (or nonperiodic boundary conditions) yields a nonsensical result.

B. Boundary conditions

We are now going to address the aforementioned importance of the periodic boundary conditions for correctly calculating the effective mass. When imposing periodic boundary conditions, one finds, unsurprisingly, a constant density far away from the impurity, but in contrast the phase is linearly changing at the order of $1/L$ and therefore not constant. One might be tempted to use a solution where both density and phase are truly constant far away from the impurity (up to exponentially small corrections). A solution with this different boundary condition would still be given by Eqs. (A2) and (A4), but with $\theta_1(x) = 0$. The effective mass can then be deduced from the wave function in the same fashion as was done for periodic boundary conditions and is plotted in Fig. 2. Calculating the effective mass in this manner, one finds that the effective mass decreases for increasing η and it can even become negative. This unphysical result is in clear disagreement with DMC results. Besides that, it also contains a phase jump at infinity which introduces a source term there, which is nonsensical. Addressing this issue from a more technical point of view, it becomes apparent that, strictly speaking, functional derivatives cannot be taken for the constant-phase solutions. On a mean-field level, this can be alleviated by modifying the functional derivatives by exactly this source term, as has been done in the context of solitons [50,51]. Another possible way to deal with the phase issue is to integrate the phaseout, as has been done in Ref. [45]. Upon considering quantum fluctuations on top of the mean-field solution, none of the above-mentioned methods allow a straightforward generalization. We found expanding about a periodic mean-field solution to be indispensable for the Bogoliubov theory.

We note that this issue persists when extracting the mass from the total momentum dependence of the mean-field energy of the system. That is, when enforcing the nonperiodic phase and expanding the total mean-field energy to quadratic order in the total momentum as $E \approx E_0 + \frac{p^2}{2m^*}$, one obtains an incorrect result for the polaron mass m^*. On the other hand, when extracting the polaron mass from expanding in u as $E \approx E_0 + \frac{1}{2}m^*u^2$, one fortuitously obtains the correct result with both periodic and nonperiodic [44] mean-field solutions.

These difficulties can be traced to the fact that without the phase correction, the mean-field equations of motion do not form a Hamiltonian system. For the full quantum system, one can deduce that the fundamental relation

$$\frac{dE}{dp} = u \tag{10}$$

holds exactly by the Feynman-Hellman theorem. Incidentally, this relation can be used to obtain $M/m^* = \lim_{p\to 0}(1 - \frac{P_B}{p})$, which is used routinely to compute the polaron mass. With periodic boundary conditions, one retains the exact relation Eq. (10) within mean-field theory. On the other hand, when the nonperiodic solution is used, a short calculation gives the relation

$$\frac{dE_{\rm np}}{dp} = u - u\bar{n}\frac{d}{dp}\Delta\theta, \tag{11}$$

where $E_{\rm np}$ is the total mean-field energy of the nonperiodic state, $\bar{n}$ is the average density, and $\Delta\theta$ is the phase change across the condensate.

IV. QUANTUM FLUCTUATIONS

After expanding the fields in $\hat{\mathcal{H}}^{\rm S}_{\rm LLP}$ in the quantum fluctuations, we find up to second order in $\hat{\xi}^\dagger(x)$ and $\delta\hat{u}$

$$\hat{\mathcal{H}}^{\rm S}_{\rm LLP} = \int dx \left[\hat{\xi}^\dagger(x)\left(-\frac{1}{2m_{\rm r}}\partial_x^2 + 2g_{\rm BB}|\phi(x)|^2 - \mu + g_{\rm IB}\delta(x) + iu\partial_x\right)\hat{\xi}(x) + \frac{g_{\rm BB}}{2}\left(\phi(x)^2\hat{\xi}^\dagger(x)^2 + \text{H.a.}\right)\right]$$
$$-i\delta\hat{u}\int \mathrm{d}x\left(\hat{\xi}^\dagger(x)\partial_x\phi(x) + \phi^*(x)\partial_x\hat{\xi}(x)\right) - \frac{1}{2}M\delta\hat{u}^2, \tag{12}$$

with $M\delta\hat{u} = -i\int[\phi^*(x)\partial_x\hat{\xi}(x) + \hat{\xi}^\dagger(x)\partial_x\phi(x)]\,\mathrm{d}x + \mathcal{O}(\hat{\xi}(x)^2)$, which can be diagonalized by a Bogoliubov rotation to a generalized basis of *phonons on a deformed background*. We note that for distances far away from the impurity, i.e., $|x| \to \infty$, these phonons look like the ones of a homogeneous BEC. This allows us to extract the quantum depletion (see Ref. [52] for a detailed discussion on how to regularise the arising UV divergences of the zero point energy). We find for the quantum-corrected density far away from the impurity $n_0 = n_0^{\rm MF} + \frac{1}{\pi}\sqrt{m_{\rm r}g_{\rm BB}n_0^{\rm MF}}$ and thus we have to adjust the mean-field density accordingly. To diagonalize Eq. (12), we note that all terms involving $\delta\hat{u}$ become nonlocal and thus difficult to handle in general, except for the special case $p = 0$. This enables us to diagonalize Eq. (12) and to calculate the polaron energy for $p = 0$. For a moving impurity, we introduce an approximation setting $\delta\hat{u} = 0$ and keep u as

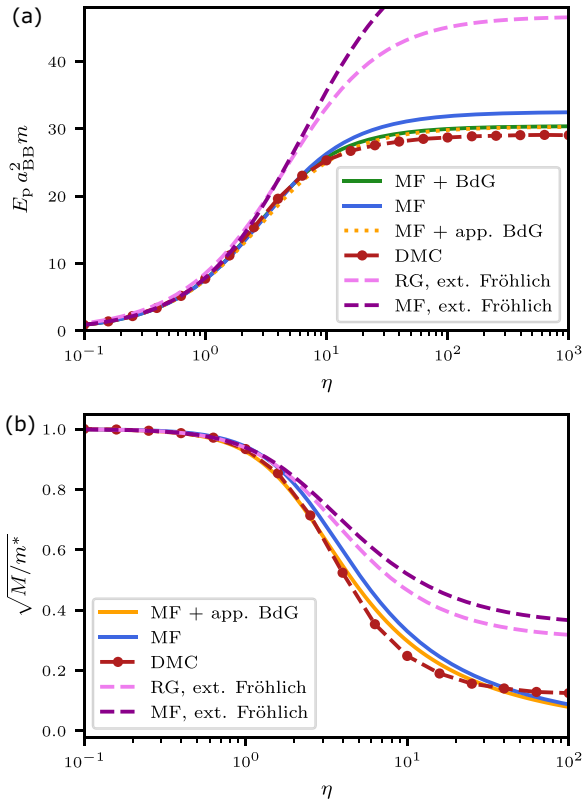

FIG. 3. Polaron energy (a) and effective mass (b) for the repulsive polaron. The curves are obtained using different theoretical methods; all parameters are as in Ref. [15], where $\gamma \approx 0.438$. The DMC, RG, and MF (both based on the extended Fröhlich model) curves were calculated in Ref. [23]. We find exceptional agreement with the DMC results for the energy as well as the effective mass when expanding around the right mean-field solutions and including quantum fluctuations. Only for the very strong coupling regime we do not predict a saturation of the effective mass. The condensate deformation becomes relevant for $\eta/n_0\bar{\xi} > 1$ Eq. (7), corresponding here to $\eta > 1.9$, where predictions from the extended Fröhlich model start to deviate from the full model.

a variational parameter in the mean-field equations. After diagonalizing the remaining quadratic Hamiltonian Eq. (12), u is determined self-consistently,

$$Mu = P - \langle \hat{P}_B \rangle,$$
$$\langle \hat{P}_B \rangle = -i \int \phi^*(x)\partial_x\phi(x)\,dx - i\langle \int \hat{\xi}^\dagger(x)\partial_x\hat{\xi}(x)\,dx \rangle, \tag{13}$$

where the expectation value is taken with respect to the phonon vacuum. For a more detailed description, we refer to Appendix B. Then it is straightforward to calculate the effective mass including the quantum corrections $M/m^* = Mu/p$. As can be seen in Fig. 3(a), where the energies of the full and approximate solution of the BdG equations are shown, the approximate treatment of the Hubbard-Stratonovich field is very good.

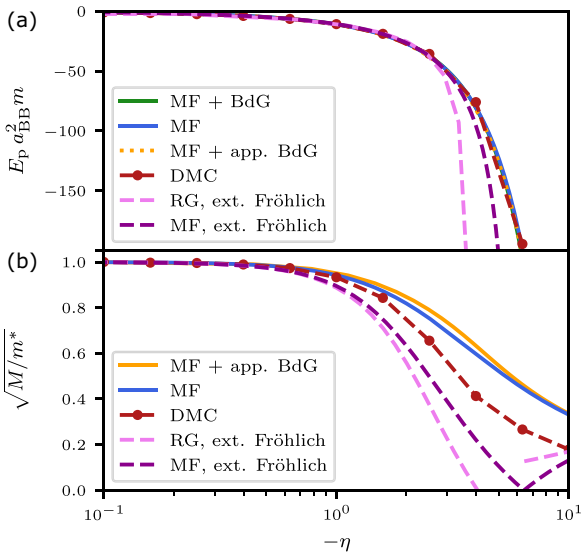

FIG. 4. Polaron energy (a) and mass (b) calculated using different methods for attractive impurity couplings. All parameters are as in Ref. [15] and the RG, MF (based on the extended Fröhlich model), and DMC curves were calculated in Ref. [23]. For the polaron energy, a surprisingly good agreement is achieved with the DMC results, while the agreement is less good for the mass. We explain this by the collapse of the solution to a multiparticle bound state, where we do not expect the mean-field solution to be a good approximation. Furthermore, we do not observe the transition from the attractive to the repulsive polaron observed in the Fröhlich model, signaled by the breakdown of the RG treatment. For more detail on this transition, we refer to Refs. [23,24].

V. DISCUSSION AND SUMMARY

Figure 3 shows that already the mean-field solution improves the agreement with DMC simulations significantly for $g_{IB} > 0$ as compared to the Fröhlich model. Including quantum fluctuations leads to almost perfect agreement for the energy. We find, however, that the effective mass diverges for $g_{IB} \to \infty$, even after including quantum fluctuations, which seem to be in contrast to the DMC results [23]. This divergence is a characteristic of the 1D geometry and is, for example, also observed in the Tonks limit [34]. One would naively expect this to happen since, for $\eta \gg 1$, the condensate is split into two halves by the impurity, preventing any transport of the condensate across it. The only possible contribution could come from tunneling which is highly suppressed for $\eta \gg 1$. The same reasoning explains why the quantum correction to the effective mass is most significant for intermediate couplings since here the classical current is reduced by the strong condensate deformation, but tunneling is still relevant. The question whether the effective mass actually saturates remains open and other approaches such as DMRG could shed more light on this. As shown in Fig. 4(a) the prediction for the polaron energy is also in very good agreement with DMC data for $g_{IB} < 0$. While qualitatively less accurate for the mass, our approach is free of divergences as compared to the extended Fröhlich model [Fig. 4(b)]. Note that these arguments rely on treating the system as one-dimensional. For experimental

systems in the one-dimensional regime, we expect that transverse modes may become important for the limiting behavior of M/m^*. This analysis has to be done on a case to case basis and we want to stress that all our calculations are benchmarked against strict 1D numerical quantum Monte Carlo results. For a detailed discussion on the influence of the transverse mode and when it's admissible to treat the system investigated in Ref. [15] as strictly one-dimensional, we refer to the detailed discussion in Ref. [23]. Another quantity of experimental relevance [15] is the axial width of the polaron $(\langle\hat{X}^2\rangle - \langle\hat{X}\rangle^2)^{1/2}$. In the present paper, which is carried out in the LLP frame and requires translational invariance, such a quantity is infinite. Including a trap potential for the impurity is beyond the scope of the present paper, but could be addressed by using a variational ansatz that is a superposition of ground states (of the infinite system) with different total momenta. On the other hand, studies that do not invoke the LLP transformation can lead to symmetry-broken mean-field states with finite values of the axial width [36,38] even without a trap, but these neglect impurity-BEC entanglement.

In summary, we have shown that a nonperturbative description of the Bose polaron in 1D requires taking into account the backaction to the condensate while keeping the impurity-BEC entanglement. Since the density of phonons defined on such a deformed background remains small, their intrinsic interactions can be neglected to good approximation. Our approach provides a quantitatively accurate and, to a large extent, analytical description of Bose polarons even for strong impurity-boson interactions as long as the boson-boson interactions remain weak. Those findings suggest that a similar method could be used to gain more insight into the polaron formation following a sudden quench. We expect that it will also allow a good description in 3D at and beyond the critical strength of the impurity-boson interaction for self-trapping.

ACKNOWLEDGMENTS

We would like to thank G. Astrakharchik and J. Brand for useful discussions and insights. We also thank G. Astrakharchik and E. Demler for providing the DMC and RG data of Ref. [23]. M.W. and M.F. acknowledge financial support by the DFG through the SFB/TR 185, Project No. 277625399. J.J. is grateful for support from EPSRC under Grant No. EP/R513052/1. R.B. is grateful for support from a Cecilia Tanner Research Impulse Grant and the Aspen Center for Physics, which is supported by NSF No. PHY1607611 and the Simons Foundation.

APPENDIX A

In this Appendix, we provide some details on the solution of the mean-field equations used in the main text. The mean-field equations that need to be solved are

$$\begin{aligned}\left(-\frac{1}{2m_{\rm red}}\partial_x^2 + g_{\rm BB}|\phi(x)|^2 - \mu + iu\partial_x\right)\phi(x) = 0,\\ \partial_x\phi(x)|_{0-}^{0+} = 2m_{\rm red}g_{\rm IB}\phi(0),\\ \phi(L/2) = \phi(-L/2),\\ Mu = p - P_{\rm B}.\end{aligned} \tag{A1}$$

If we do not require periodic boundary conditions, analytical solutions of the form $|\phi(x)|e^{i\theta_0(x)}$ can be found in the literature [42,47]. To make use of those solutions, we make the following ansatz:

$$\phi(x) = \tilde{\phi}(x)e^{i\theta_1(x)}, \tag{A2}$$

where we introduced $\theta_1(x)$, which will be of $\mathcal{O}(x/L)$ and is fixed later on to ensure periodicity of the phase for the mean-field solutions, giving the overall phase $\theta(x) = \theta_0(x) + \theta_1(x)$. Upon inserting our ansatz into Eq. (A1), we arrive at

$$\begin{aligned}\left(-\frac{1}{2m_{\rm red}}\partial_x^2 + g_{\rm BB}|\tilde{\phi}(x)|^2 - \tilde{\mu} + i\tilde{u}\partial_x\right)\tilde{\phi}(x) = 0,\\ \partial_x\tilde{\phi}(x)|_{0-}^{0+} = 2m_{\rm red}g_{\rm IB}\tilde{\phi}(0),\\ e^{i\theta_1(L)}\tilde{\phi}(L/2) = \tilde{\phi}(-L/2),\end{aligned} \tag{A3}$$

with the redefinitions $\tilde{\mu} = \mu + (\partial_x\theta_1)u/M + \mathcal{O}(1/L^2)$ and $\tilde{u} = u - (\partial_x\theta_1)/(m_{\rm r})$. The solution for this problem is now given by [42,47]

$$\begin{aligned}|\tilde{\phi}(x)| &= \sqrt{\mu/g_{\rm BB}}(1 - \beta\,\mathrm{sech}^2(\sqrt{\beta/2}(|x| + x_0)/\bar{\xi}))^{1/2},\\ \theta_0(x) &= \begin{cases} f(x) & x > 0\\ 2f(0) - f(-x) & x < 0,\end{cases}\\ f(x) &= \arctan\left(\frac{\sqrt{4u^2\beta/\bar{c}^2}}{e^{\sqrt{2\beta}(x+x_0)/\bar{\xi}} - 2\beta + 1}\right),\end{aligned} \tag{A4}$$

with $\beta = 1 - \frac{u^2}{\bar{c}^2} + \mathcal{O}(1/L^2)$ and $\mu = g_{\rm BB}n_0^{\rm MF} - (\partial_x\theta_1(x))\,u/M + \mathcal{O}(1/L^2)$. The jump condition determines x_0 through a polynomial of order three, but only one solution is stable. It is possible to extract quantities like the critical momentum herein; for a detailed discussion of this, we refer to Ref. [42]. For finite momentum, the condition for x_0 has to be solved numerically but in the limit $p \to 0$ we can find the analytical solutions stated in the paper. If we consider the mean-field solution alone and require the number of condensed particles N to stay constant on the mean-field level, we fix $n_0^{\rm MF} = n_0[1 + 2\sqrt{2\beta}\bar{\xi}/L(1 - \tanh(\sqrt{\beta/2}x_0/\bar{\xi}))] + \mathcal{O}(1/L^2)$. Lastly, we fix $\theta_1(x)$ to ensure the periodicity of the phase by

$$\theta_1(x) = 2[f(0) - f(L/2)]\frac{x}{L}. \tag{A5}$$

At this point, we note that the $1/L$ corrections are indeed important when calculating physical quantities. This can be seen by considering the Boson momentum $P_{\rm B} = \int n(x)\partial_x\theta(x)\,{\rm d}x = \int n(x)\partial_x\theta_0(x)\,{\rm d}x + n_0[2(f(0) - f(L/2)]$. From there we can derive the expressions for m^* and E_p given in the main text, which are both defined in the limit $p \to 0$, which allows us to state them fully analytically.

APPENDIX B

In the following, we give a short overview of the methods used to obtain the quantum corrections to the mean-field solutions. The major steps have been outlined in the main text, and thus we focus on the numerical details. An extensive overview of the techniques used here can be found in Ref. [53]. We note that this is equivalent to solving the resulting Bogolibouv-de Gennes equations. We start by discretizing $\hat{\mathcal{H}}_{\rm LLP}^{\rm S}$ from the

main text after either making the approximation of treating u as a variational parameter or for $p = 0$ integrating out the $\hat{u}$-field. For all numerical results presented here, the discretization was done in real space and is therefore straightforward apart from the delta distribution, which was approximated by a Kronecker delta in the following way: $\delta(x) \to \delta_{i,0}/a$, where a is the discretization. This comes at the expense of not accounting correctly for the UV behavior. The deviation from the continuum UV behavior is due to discretizing the derivative operators. Nevertheless, for the observables we are interested in here, the UV behavior is not essential, and we found fast convergence; thus, the diagonalization in real space is justified. For notational convenience, we omit the hats on all discretized operators. After discretization, the Hamiltonian can be written as

$$H^{\mathrm{S}}_{\mathrm{LLP}} = \sum_{ij}\left[A_{ij}\phi_i^\dagger\phi_j + \frac{1}{2}(B_{ij}\phi_i^\dagger\phi_j^\dagger + B_{ij}^*\phi_i\phi_j)\right] = \frac{1}{2}\mathbf{\Phi}^\dagger M\mathbf{\Phi} - \frac{1}{2}\mathrm{Tr}(A), \tag{B1}$$

where $\mathbf{\Phi}^\dagger = [\phi_1^\dagger, \phi_2^\dagger, ...\phi_n^\dagger, \phi_1, \phi_2, ...\phi_n]$ is the discrete version of $\hat{\xi}(x)$ and M is the semipositive definite matrix

$$M = \begin{bmatrix} A & B \\ B^* & A^* \end{bmatrix}. \tag{B2}$$

At this point, we already note that the trace term is of fundamental importance in 1D since it renders results like the zero-point energy finite without performing additional regularization. Following the steps outlined in Ref. [53], we now diagonalize

$$\nu M = \begin{bmatrix} A & B \\ -B^* & -A^* \end{bmatrix}, \tag{B3}$$

and thus find T such that $T^\dagger M T = \mathrm{diag}(\omega_1, \omega_2, ..., \omega_n, \omega_1, \omega_2, ..., \omega_n)$, while guaranteeing $T^\dagger \nu T = \nu$, which allows us to introduce new bosonic operators $\mathbf{\Psi}^\dagger = [b_1^\dagger, b_2^\dagger, ...b_n^\dagger, b_1, b_2, ...b_n]$ through

$$\mathbf{\Phi} = T\mathbf{\Psi}, \tag{B4}$$

for which the Hamiltonian takes diagonal form. The new operators b_i can be interpreted as quasiparticlelike bosonic excitations with eigenenergy ω_i. For a stable polaron, the energy of those excitations is minimized, i.e., the system is in its vacuum state $|0\rangle$ with respect to the b_i. From here it is then easy to verify that the quantum corrections to the expectation value of an observable of the form $O_Q = \sum_{ij} O_{ij}\phi_i^\dagger\phi_j$ is

$$\langle O_Q\rangle = \langle 0|\mathbf{\Psi}^\dagger T^\dagger \begin{bmatrix} O & 0 \\ 0 & 0 \end{bmatrix} T\mathbf{\Psi}|0\rangle = \langle 0|\mathbf{\Psi}^\dagger \begin{bmatrix} C & D \\ E & F \end{bmatrix}\mathbf{\Psi}|0\rangle = \mathrm{Tr}(F). \tag{B5}$$

To conclude this section, we will comment on the IR (infrared) divergences that are characteristic in 1D systems and how they are dealt with here. First, we note that quantities like the two-point function

$$\langle\phi_i^\dagger\phi_i\rangle = \langle 0|(\mathbf{\Psi}^\dagger T^\dagger)_i(T\mathbf{\Psi})_i|0\rangle \sim L \tag{B6}$$

are indeed IR divergent in our treatment. For the global quantities and $p = 0$, this can be dealt with as outlined in the main text by considering the zero-point energy,

$$E = \frac{1}{2}\left(\sum_i \omega_i - \mathrm{Tr}(A)\right), \tag{B7}$$

which is UV and IR finite and then taking adequate derivatives (i.e., with respect to the chemical potential for the depletion). When considering $\hat{\mathcal{H}}^{\mathrm{S}}_{\mathrm{LLP}}$ for $p \neq 0$ without any approximations, the phonon momentum seems to be IR divergent and also, for the polaron energy, we found a system-size dependence. Lastly, we remark that in the approximate treatment, i.e., when viewing u as a variational parameter, the phonon momentum remains IR and UV finite. Therefore, we conclude that all results presented in the main text are cutoff independent, and no divergences occur.

[1] L. Landau, Phys. Z. Sowjetunion **3**, 644 (1933).
[2] L. D. L. S. I. Pekar, Zh. Eksp. Teor. Fiz. **16**, 335 (1946).
[3] N. Mott, Phys. C Supercond. **205**, 191 (1993).
[4] A. S. Alexandrov and J. T. Devreese, *Advances in Polaron Physics* (Springer-Verlag, Berlin, 2010), Vol. 159.
[5] H. Bässler and A. Köhler, Top. Curr. Chem. **312**, 1 (2012).
[6] A. Schirotzek, C. H. Wu, A. Sommer, and M. W. Zwierlein, Phys. Rev. Lett. **102**, 230402 (2009).
[7] Y. Zhang, W. Ong, I. Arakelyan, and J. E. Thomas, Phys. Rev. Lett. **108**, 235302 (2012).
[8] C. Kohstall, M. Zaccanti, M. Jag, A. Trenkwalder, P. Massignan, G. M. Bruun, F. Schreck, and R. Grimm, Nature **485**, 615 (2012).
[9] M. Koschorreck, D. Pertot, E. Vogt, B. Fröhlich, M. Feld, and M. Köhl, Nature **485**, 619 (2012).
[10] F. Scazza, G. Valtolina, P. Massignan, A. Recati, A. Amico, A. Burchianti, C. Fort, M. Inguscio, M. Zaccanti, and G. Roati, Phys. Rev. Lett. **118**, 083602 (2017).
[11] M. Cetina, M. Jag, R. S. Lous, J. T. Walraven, R. Grimm, R. S. Christensen, and G. M. Bruun, Phys. Rev. Lett. **115**, 135302 (2015).
[12] M. Cetina, M. Jag, R. S. Lous, I. Fritsche, J. T. Walraven, R. Grimm, J. Levinsen, M. M. Parish, R. Schmidt, M. Knap, and E. Demler, Science **354**, 96 (2016).
[13] M. Parish and J. Levinsen, Phys. Rev. B **94**, 184303 (2016).
[14] P. Massignan, M. Zaccanti, and G. M. Bruun, Rep. Prog. Phys. **77**, 034401 (2014).
[15] J. Catani, G. Lamporesi, D. Naik, M. Gring, M. Inguscio, F. Minardi, A. Kantian, and T. Giamarchi, Phys. Rev. A **85**, 023623 (2012).
[16] N. B. Jørgensen, L. Wacker, K. T. Skalmstang, M. M. Parish, J. Levinsen, R. S. Christensen, G. M. Bruun, and J. J. Arlt, Phys. Rev. Lett. **117**, 055302 (2016).
[17] M. G. Hu, M. J. Van De Graaff, D. Kedar, J. P. Corson, E. A. Cornell, and D. S. Jin, Phys. Rev. Lett. **117**, 055301 (2016).

[18] Z. Z. Yan, Y. Ni, C. Robens, and M. W. Zwierlein, Science **368**, 190 (2020).
[19] S. P. Rath and R. Schmidt, Phys. Rev. A **88**, 053632 (2013).
[20] G. E. Astrakharchik and L. P. Pitaevskii, Phys. Rev. A **70**, 013608 (2004).
[21] J. Tempere, W. Casteels, M. K. Oberthaler, S. Knoop, E. Timmermans, and J. T. Devreese, Phys. Rev. B **80**, 184504 (2009).
[22] W. Casteels, T. Van Cauteren, J. Tempere, and J. T. Devreese, Laser Phys. **21**, 1480 (2011).
[23] F. Grusdt, G. E. Astrakharchik, and E. Demler, New J. Phys. **19**, 103035 (2017).
[24] Y. E. Shchadilova, R. Schmidt, F. Grusdt, and E. Demler, Phys. Rev. Lett. **117**, 113002 (2016).
[25] H. Fröhlich, Adv. Phys. **3**, 325 (1954).
[26] W. Li and S. Das Sarma, Phys. Rev. A: At. Mol. Opt. Phys. **90**, 013618 (2014).
[27] J. Levinsen, M. M. Parish, and G. M. Bruun, Phys. Rev. Lett. **115**, 125302 (2015).
[28] W. Casteels and M. Wouters, Phys. Rev. A: At. Mol. Opt. Phys. **90**, 043602 (2014).
[29] R. S. Christensen, J. Levinsen, and G. M. Bruun, Phys. Rev. Lett. **115**, 160401 (2015).
[30] T. Ichmoukhamedov and J. Tempere, Phys. Rev. A **100**, 043605 (2019).
[31] F. Grusdt and E. Demler, arXiv:1510.04934.
[32] A. Lampo, C. Charalambous, M. Á. García-March, and M. Lewenstein, Phys. Rev. A **98**, 063630 (2018).
[33] L. A. Pena Ardila and S. Giorgini, Phys. Rev. A **92**, 033612 (2015).
[34] L. Parisi and S. Giorgini, Phys. Rev. A **95**, 023619 (2017).
[35] J. P. Hernandez, Rev. Mod. Phys. **63**, 675 (1991).
[36] F. M. Cucchietti and E. Timmermans, Phys. Rev. Lett. **96**, 210401 (2006).
[37] M. Bruderer, W. Bao, and D. Jaksch, Europhys. Lett. **82**, 30004 (2008).
[38] A. A. Blinova, M. G. Boshier, and E. Timmermans, Phys. Rev. A **88**, 053610 (2013).
[39] T. D. Lee, F. E. Low, and D. Pines, Phys. Rev. **90**, 297 (1953).
[40] A. Kantian, U. Schollwöck, and T. Giamarchi, Phys. Rev. Lett. **113**, 070601 (2014).
[41] T. Lausch, A. Widera, and M. Fleischhauer, Phys. Rev. A **97**, 033620 (2018).
[42] V. Hakim, Phys. Rev. E **55**, 2835 (1997).
[43] A. G. Volosniev and H. W. Hammer, Phys. Rev. A **96**, 031601(R) (2017).
[44] S. I. Mistakidis, A. G. Volosniev, N. T. Zinner, and P. Schmelcher, Phys. Rev. A **100**, 013619 (2019).
[45] G. Panochko and V. Pastukhov, Ann. Phys. (NY) **409** (2019).
[46] G. D. Mahan, *Many-Particle Physics* (Springer, Berlin, 2000).
[47] T. Tsuzuki, J. Low Temp. Phys. **4**, 441 (1971).
[48] M. Girardeau, J. Math. Phys. **1**, 516 (1960).
[49] E. H. Lieb and W. Liniger, Phys. Rev. **130**, 1605 (1963).
[50] I. M. Uzunov and V. S. Gerdjikov, Phys. Rev. A **47**, 1582 (1993).
[51] I. V. Barashenkov and E. Y. Panova, Phys. D **69**, 114 (1993).
[52] L. Salasnich and F. Toigo, Phys. Rep. **640**, 1 (2016).
[53] M.-w. Xiao, arXiv:0908.0787.

Correction: The previously published Figures 1(a) and 1(b) contained plotting errors and have been replaced with the corrected plots.

3 Polaron interactions and bipolarons in one-dimensional Bose gases in the strong coupling regime

Martin Will, Gregory E. Astrakharchik, and Michael Fleischhauer,
Phys. Rev. Lett. **127**, 103401 (2021).

The main objective of this study is the extension of the MF theory to a pair of impurities, which do not interact directly with each other. This generalization provides the opportunity to study polaron interactions mediated by the many-body environment. Given the attractive nature of the resulting interaction potential, it leads to the binding of the two polarons, forming a bipolaron.
The MF equation describing a bipolaron can be derived similarly as for a single polaron, as presented in Section 1.3. However, a notable difference is that the LLP transformation does not eliminate both impurity degrees of freedom from the Hamiltonian. It is applied to the center of mass operators of the impurities but not to the relative impurity coordinate. To address the relative degrees of freedom, a Born-Oppenheimer (BO) approximation is applied, which is valid when the impurity mass is significantly larger than that of the surrounding particles. As shown in the publication [P2], the resulting MF equation is given by

$$\Big[-\frac{\partial_x^2}{2m_r} + g|\phi(x)|^2 - \mu + g_{\mathrm{IB}}\Big(\delta(x-\tfrac{1}{2}r) + \delta(x+\tfrac{1}{2}r)\Big)\Big]\phi(x) = 0. \tag{3.1}$$

Here $m_r = (1/m + 1/2M)^{-1}$ denotes the reduced mass of the boson mass m and the total impurity mass $2M$. The chemical potential is given by μ, while r is the distance between the impurities. The ground state of this MF equation, along with the polaron interaction potential in the BO approximation, is derived in the publication [P2]. The potential is shown in Figure 3.1a) and exhibits excellent agreement with results obtained from quasi-exact DMC simulations (symbols). Notably, for strongly repulsive impurities $g_{\mathrm{IB}} \gg gn\tilde{\xi}$ and a short distance $r \leq \pi\tilde{\xi}$ between them, relative to the rescaled healing length $\tilde{\xi} = 1/\sqrt{2gnm_r}$, the potential is linear. This phenomenon arises because the gas is entirely expelled from the space between the impurities, resulting in a constant force exerted by the gas surrounding the pair that pushes the impurities toward each other.
Since the BO approximation is restricted to infinitely heavy impurities, we derive the leading-order Born-Huang diagonal correction [77, 78]. This correction accounts for finite impurity mass effects and introduces an additional potential

$$W(r) = \frac{1}{M}\int \mathrm{d}x\, |\partial_r \phi(x)|^2. \tag{3.2}$$

The total potential is shown in the inset of Figure 3.1b). A remarkable feature of the Born-Huang correction is the onset of a repulsive peak at a distance of $r \simeq \pi\tilde{\xi}$. Note that this

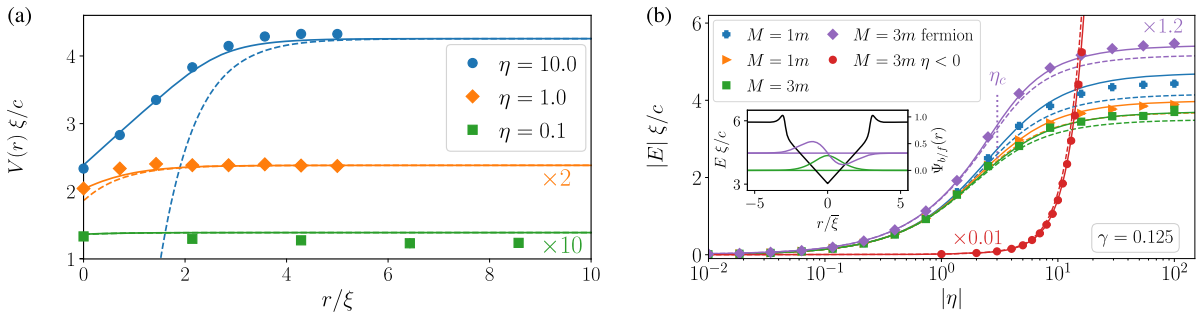

Figure 3.1: a) Effective polaron interaction potential for heavy impurities $M \to \infty$ and different coupling constants $\eta = g_{\mathrm{IB}}/g$. Solid lines represent results obtained from the MF theory, dots are quasi-exact DMC simulations, and dashed lines show a perturbative prediction from [46, 48]. b) Bipolaron energies of the ground- and first excited-state for different mass ratios and the Tonks parameter $\gamma = 1/8$. Dashed lines correspond to the BO potential, and solid include the Born-Huang correction. The different symbols mark the results obtained from a DMC simulation. The inset ($\eta = 30$, $M = 3m$) illustrates the relative impurity wave function of the ground state (bosonic impurities) in green and the first excited state (fermionic impurities) in purple, as well as the potential including the Born-Huang correction in black. The first excited state is a bound state above the critical coupling constant η_c.

maximum is unrelated to Friedel oscillations [105], which exist only in strongly interacting gases ($\gamma \gg 1$) and have an oscillation frequency proportional to $1/n$. Unfortunately, DMC simulations of the interaction potential are difficult for finite impurity masses and involve large statistical noise. Therefore, we were unable to prove the onset of these maxima using DMC. Finally, we derive the bound states of the MF interaction potential. The ground state, as well as the first excited state (which can be mapped to the ground state for fermionic impurities), are illustrated in the inset of 3.1b). The bipolaron energy corresponding to these states is presented in Figure 3.1b). It demonstrates an excellent agreement with results obtained from DMC simulations, even for mass ratios as low as $M = 3m$, particularly when accounting for the Born-Huang correction.

Author contributions

In this study, I derived and solved the MF equation for a pair of impurities and calculated the analytic expression for the induced polaron interaction potential. Moreover, I determined the Born-Huang correction and evaluated the binding energy of the bipolaron within the mentioned approximations. The concept of extending the approach to study mediated interactions involving two impurities was initiated by Michael Fleischhauer, who also supervised the entire project. The exact DMC simulation of the interaction potential and bipolaron energy was executed by Gregory E. Astrakharchik. All authors participated in discussions regarding the results and the manuscript's preparation and review process.

Copyright

Polaron Interactions and Bipolarons in One-Dimensional Bose Gases in the Strong Coupling Regime

M. Will,[1] G. E. Astrakharchik,[2] and M. Fleischhauer[1]
[1]*Department of Physics and Research Center OPTIMAS, University of Kaiserslautern, 67663 Kaiserslautern, Germany*
[2]*Departament de Física, Universitat Politècnica de Catalunya, Campus Nord B4-B5, E-08034, Barcelona, Spain*

(Received 9 February 2021; revised 3 May 2021; accepted 4 August 2021; published 31 August 2021)

Bose polarons, quasiparticles composed of mobile impurities surrounded by cold Bose gas, can experience strong interactions mediated by the many-body environment and form bipolaron bound states. Here we present a detailed study of heavy polarons in a one-dimensional Bose gas by formulating a nonperturbative theory and complementing it with exact numerical simulations. We develop an analytic approach for weak boson-boson interactions and arbitrarily strong impurity-boson couplings. Our approach is based on a mean-field theory that accounts for deformations of the superfluid by the impurities and in this way minimizes quantum fluctuations. The mean-field equations are solved exactly in the Born-Oppenheimer approximation, leading to an analytic expression for the interaction potential of heavy polarons, which is found to be in excellent agreement with quantum Monte Carlo (QMC) results. In the strong coupling limit, the potential substantially deviates from the exponential form valid for weak coupling and has a linear shape at short distances. Taking into account the leading-order Born-Huang corrections, we calculate bipolaron binding energies for impurity-boson mass ratios as low as 3 and find excellent agreement with QMC results.

DOI: 10.1103/PhysRevLett.127.103401

Introduction.—Interactions between quantum particles mediated by a many-body environment play an important role in condensed-matter physics. Examples range from the Ruderman-Kittel-Kasuya-Yodsia interaction of spins in a Fermi liquid [1–3] to Cooper pairing of electrons in a solid induced by lattice vibrations [4]. The mechanism that causes such interactions can also substantially modify the properties of individual impurities by forming quasiparticles. A paradigmatic example is the polaron [5,6] resulting from the electron-phonon coupling, also responsible for Cooper pairing. In the strong coupling limit, impurity interaction and quasiparticle formation are strongly intertwined. Bipolarons are suspected to be essential for high-temperature superconductivity [7–9]. They are important for the electric conductivity of polymers [10–14] or organic magnetoresistance [15]. Their understanding is one of the key questions of many-body physics.

In recent years, neutral atoms immersed in degenerate quantum gases have become versatile experimental platforms for accessing polaron physics in novel regimes and with an unprecedented degree of control [16–31]. Length and energy scales are very different from solids and can be resolved and manipulated much more easily. Most importantly, polarons can be studied out of equilibrium with the prospect of engineering their properties beyond what is possible in equilibrium. One-dimensional (1D) gases are of particular relevance as they show pronounced quantum effects and powerful tools are available for their theoretical description. It is possible to tune the impurity-bath interaction all the way through weak to strong coupling, e.g., by employing Feshbach and confinement-induced resonances [32]. Contrary to higher dimensions, the system remains stable even for infinite coupling since three-body losses are greatly suppressed. Polaron interactions have so far mostly been studied in regimes where the mediated interaction between them is weak. A perturbative treatment yields an exponential (1D) or Yukawa (3D) potential between two impurities with the characteristic length scale set by the healing length ξ [33–36]. A universal low-energy theory of mobile impurities in one dimension has been developed in Ref. [37], restricted to particle separations much larger than ξ where the interaction is weak. A unified treatment for all distances, but for immobile impurities and small impurity-boson couplings has been given in Refs. [38,39]. While quantum Monte Carlo (QMC) methods have been used to obtain polaron properties in a nonperturbative manner [40–45] and there are numerical mean-field studies in trapped systems extending into the nonperturbative regime [46], analytic approaches have been restricted to weak polaron-polaron couplings or noninteracting host gases [47–49]. The first attempt at strong polaron coupling in interacting gases has been made only recently by using a scattering-matrix expansion [50]. The authors predict a deviation from the 3D Yukawa potential in agreement with QMC simulations, but with some notable quantitative differences.

Here we develop an analytic theory of polaron interactions in 1D Bose gases for arbitrary strength of the

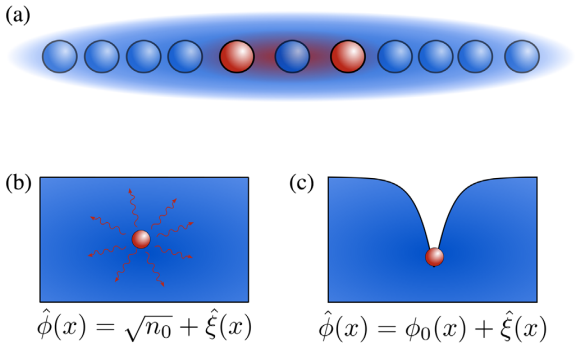

FIG. 1. (a) Sketch of a bipolaron composed of two impurities in a 1D Bose gas. (b) In the commonly used extended Fröhlich model, a large number of phonons are created around the impurity and phonon-phonon interactions need to be taken into account. (c) In a description based on a deformed condensate, this can be avoided.

impurity-boson coupling, see Fig. 1(a) for a sketch. A common description of the Bose-polaron takes into account a coupling of the impurity only to Bogoliubov phonons [36,51], see Fig. 1(b). This extended Fröhlich model is, however, not adequate for strong coupling, $g_{\mathrm{IB}} \gg g$, even if the boson-boson interaction itself is weak, since the impurity generates a high-density cloud of phonons around it and phonon-phonon interactions can no longer be neglected. Here we use a different approach that accounts for deformation of the superfluid by the impurities, see Fig. 1(c) [43,52,53]. As shown in Ref. [53] and elucidated in the Supplemental Material [54], this approach minimizes quantum fluctuations and leads to highly accurate predictions for single-polaron properties already on the mean-field level, precise enough to differentiate finite-size effects. Employing this approach, we develop a mean-field theory of bipolarons assuming a weakly interacting condensate and moderately heavy impurities and verify the semi-analytic predictions with QMC results.

Model.—We consider two impurities of equal mass M in a 1D gas of bosons of mass $m < M$. We assume contact impurity-boson interactions with coupling strength g_{IB} which can be repulsive, $g_{\mathrm{IB}} > 0$, or attractive, $g_{\mathrm{IB}} < 0$. We disregard a direct interaction between the impurities. Introducing center-of-mass (c.m.) and relative impurity coordinates $\hat{R}, \hat{r}$ and momenta $\hat{P}, \hat{p}$, the Hamiltonian reads ($\hbar = 1$)

$$\hat{H} = \frac{\hat{P}^2 + 4\hat{p}^2}{4M} + \int dx\, \hat{\Phi}^\dagger(x)\left\{\frac{-1}{2m}\partial_x^2 + \frac{g}{2}\hat{\Phi}^\dagger(x)\hat{\Phi}(x) - \mu + g_{\mathrm{IB}}\left[\delta\left(x - \hat{R} - \frac{\hat{r}}{2}\right) + \delta\left(x - \hat{R} + \frac{\hat{r}}{2}\right)\right]\right\}\hat{\Phi}(x). \tag{1}$$

Here μ is the chemical potential of the gas, which in mean-field approximation is $\mu = gn_0$, with n_0 being the linear density far away from both impurities. In the thermodynamic limit, n_0 converges to the mean density $n = N/L$. The interaction between the bosons of strength g is assumed to be weak so that a Bogoliubov approximation applies; i.e., the healing length $\xi = 1/\sqrt{2m\mu}$ [56] is large compared to the mean interparticle distance $1/n$. This regime is characterized by a small Lieb-Liniger parameter $\gamma = mg/n$ [57]. The dependence of the c.m. coordinate can be eliminated using a Lee-Low-Pines (LLP) transformation [58] $\hat{U} = \exp(-i\hat{R}\hat{P}_B)$, where $\hat{P}_B = -i\int dx\, \hat{\Phi}^\dagger(x)\partial_x\hat{\Phi}(x)$ is the total momentum of the Bose gas,

$$\hat{H}_{\mathrm{LLP}} = \frac{:(P - \hat{P}_B)^2: + 4\hat{p}^2}{4M} + \int dx\, \hat{\Phi}^\dagger(x)\left\{\frac{-1}{2m_r}\partial_x^2 - \mu + \frac{g}{2}\hat{\Phi}^\dagger\hat{\Phi} + g_{\mathrm{IB}}\left[\delta\left(x - \frac{\hat{r}}{2}\right) + \delta\left(x + \frac{\hat{r}}{2}\right)\right]\right\}\hat{\Phi}(x), \tag{2}$$

where $::$ denotes normal ordering, i.e., interchanging all creation operators to the left and annihilation to the right, and $m_r = 2Mm/(2M + m)$ is the reduced mass. $\hat{P}$, which previously was the c.m. momentum of the two impurities, is in the new frame the total momentum of the system. It is a constant of motion that can be replaced by a c-number P, and we set $P = 0$. Note that the LLP transformation is needed for any $M < \infty$, even if one considers an impurity at rest.

Bipolaron of heavy impurities.—Different from the single-polaron case, the LLP transformation does not remove the impurity coordinates entirely. To this end, we apply a Born-Oppenheimer (BO) approximation, valid for $M \gg m$, where the kinetic energy of the relative motion is neglected and one can replace $\hat{r}$ by a c-number r. This turns $\hat{H}_{\mathrm{LLP}}$ into a pure boson Hamiltonian.

In the following, we determine the ground state of (2) for a weakly interacting gas, which amounts to assume small quantum fluctuations $\hat{\xi}(x)$ on top of the mean-field solution $\phi_0(x)$ of Eq. (2), $\hat{\phi}(x) = \phi_0(x) + \hat{\xi}(x)$. Note that this differs from the common approach, where a small-fluctuation expansion is applied in the absence of the impurities first. In contrast, we take the backaction of the impurity into account already at the mean-field level. As shown in Ref. [53], this (i) leads to modified Bogoliubov phonons, coinciding with the standard ones only in the long-

wavelength limit $k\xi \gg 1$, and (ii) minimizes their generation by the impurity, see Fig. 1. The smallness of quantum fluctuations allows us to ignore them altogether when considering the mediated impurity-impurity interaction at distances of the order of a few rescaled healing lengths, $\bar{\xi} = \sqrt{m/m_r}\xi$. Only at large separations do quantum fluctuations become relevant. They are responsible for weak Casimir-type interactions scaling as $1/r^3$ [37–39] for finite g_{IB} and $1/r^2$ or $1/r$ if either one or both of the static impurities have infinitely strong coupling [59,60]. We will not consider these contributions here, but show *a posteriori* that the corrections are small on absolute scale.

The mean-field solutions of (2) can be obtained analytically in the BO limit, see Supplemental Material [54]. In particular, one finds for the interaction potential between two impurities

$$V(r) = gn_0^2 r\left(\frac{1}{2} - \frac{4+2\nu}{3(\nu+1)^2}\right) + \frac{4}{3}\frac{gn_0^2\bar{\xi}}{\sqrt{1+\nu}}\left\{\sqrt{2\nu+2}\right.$$
$$+ 2E(\mathrm{am}(u,\nu),\nu) - \frac{\sqrt{\tilde{\nu}}^3}{1+\nu}\mathrm{cd}(u,\nu)^{\pm 3}[1+\sqrt{\tilde{\nu}}\,\mathrm{sn}(u,\nu)]$$
$$\left. - \sqrt{\tilde{\nu}}\,\mathrm{cd}(u,\nu)^{\pm 1}\left[\frac{3}{2} + \frac{1+\nu+\tilde{\nu}}{1+\nu}\sqrt{\tilde{\nu}}\,\mathrm{sn}(u,\nu)\right]\right\}, \tag{3}$$

where $u = r/(2\bar{\xi}\sqrt{1+\nu})$ is a normalized distance, and the upper (lower) sign stays for repulsive (attractive) impurity-boson interaction, $E(x,\nu)$ is the incomplete elliptic integral of the second kind, $\mathrm{cd}(x,\nu)$ and $\mathrm{sn}(x,\nu)$ are Jacobi elliptic functions, and $\mathrm{am}(x,\nu)$ is the amplitude of these functions [61]. The dimensionless parameter $\nu = \nu(r,\eta)$ with $|\nu| < 1$ is given implicitly by

$$2\frac{|\eta|}{n_0\bar{\xi}}\frac{\sqrt{\tilde{\nu}(\nu+1)}}{(1-\nu)}\,\mathrm{cn}\,(u,\nu)\,\mathrm{dn}\,(u,\nu) = [1+\sqrt{\tilde{\nu}}\,\mathrm{sn}(u,\nu)]^2,$$

involving the Jacobi elliptic sn, cn, and dn functions and $\eta = g_{\mathrm{IB}}/g$. Here $\tilde{\nu} = \nu$ for $\eta > 0$ and $\tilde{\nu} = 1$ for $\eta < 0$. In general, this equation has several solutions; however, the physically relevant one is that with the largest ν.

Figure 2 shows examples of the effective interaction potential $V(r)$, having a finite range defined by $\bar{\xi}$. The strong coupling regime is reached when $\eta \gtrsim n_0\bar{\xi} = 1/\sqrt{2(m_r/m)\gamma}$ [53]. In this case, the impurity causes a sizable deformation of the Bose gas and $V(r)$ deviates substantially from the perturbative exponential behavior at short distances predicted in Ref. [39]. The logarithmic scale in Fig. 2(b) emphasizes the exponential long-range behavior of our result, $V(r) \sim \exp(-\sqrt{2}r/\bar{\xi})$ (see Supplemental Material [54]), which is sufficient for experimentally relevant energy scales, while the Casimir term $\sim 1/r^3$ [37,38] affects only the already small tails of the potential.

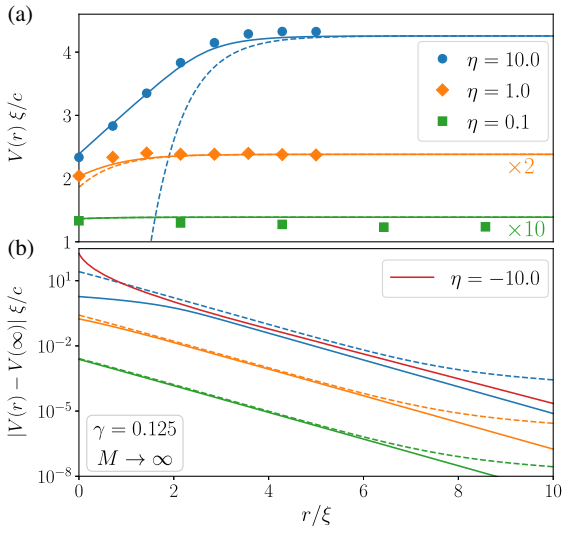

FIG. 2. Effective impurity-impurity interaction as function of distance in units of $\bar{\xi} = \xi$ for different interactions $\eta = g_{\mathrm{IB}}/g$ and $M \to \infty$, where $c = \sqrt{gn_0/m}$ is the speed of sound. Solid lines represent semianalytical approximation Eq. (3), circles are QMC results (error bars smaller than circle size), and dashed lines give perturbative predictions from [38], including Casimir-type contribution. (a) Comparison of effective potential $V(r)$ for repulsive impurity-boson interaction. The perturbative results were shifted to match our predictions at infinite distance. (b) Interaction potential on a semilog scale. Exponential decay for weak impurity-boson couplings, $\eta \lesssim 1$, is seen as straight lines. The Casimir effect (absent in the mean-field description) results in the slower $1/r^3$ decay at $r \gtrsim 6\xi$.

In the limit $\eta \to \infty$, one finds the simple explicit form

$$V(r)|_{\eta\to\infty} = \frac{4}{3}\sqrt{2}gn_0^2\bar{\xi} + \frac{1}{2}gn_0^2 r \quad \text{for } r \le \pi\bar{\xi}, \tag{4}$$

where the potential is linear, corresponding to a constant attractive force acting between the impurities. This is because for strong repulsion the Bose gas is completely expelled in between the impurities, as long as $r \lesssim \pi\bar{\xi}$ and the attractive force results only from the pressure of the Bose gas outside of the pair. This is further illustrated in the Supplemental Material [54].

In the BO limit of massive impurities, the effective interaction potential can be accurately obtained in QMC simulations. In Fig. 2 we compare our analytic predictions for repulsive impurity-boson coupling, $\eta > 0$, with QMC data and find excellent agreement within a few-percent margin. Unless stated otherwise, we used $N = 100$ bosons in the QMC simulations. While lowest-order perturbative theory predicts the same interaction strength in repulsive ($\eta > 0$) and attractive cases ($\eta < 0$), nonperturbative approaches show that $V(r)$ is substantially stronger for

attraction [see Fig. 2(b)]. This can be qualitatively understood, as the maximal density defect produced is limited in the repulsive case by full depletion, while it is unlimited in the attractive case. This makes numerical calculations in the attractive case more challenging.

Bipolaron of finite impurity mass.—The BO approximation applies to infinitely heavy impurities and becomes increasingly inaccurate for light impurities. The leading-order modification is the Born-Huang diagonal correction, $V(r) \to V(r) + W(r)$ [62,63]

$$W(r) = \frac{1}{M} \int dx \, |\partial_r \phi_0(x)|^2, \tag{5}$$

where $\phi_0(x)$ is the mean-field wave function in the presence of two impurities at (fixed) distance r. $W(r)$ accounts for the dependence of the background-gas wave function on the impurity coordinates when calculating the impurity kinetic energy. Including this term, the approach is correct up to terms of order $(m/M)^{3/2}$. Since the derivative of $\phi_0(x)$ with respect to r is analytically complicated, we do not give an explicit expression for $W(r)$. In Fig. 3(a) we plot the total potential for $\eta = 40$ and different characteristic mass ratios. Note that the finite impurity mass enters here in two ways, through the reduced healing length $\bar{\xi}$ and by the Born-Huang term $W(r)$. A prominent feature is the emergence of a local maximum at distance $r_{\max} \simeq \pi\bar{\xi}$ when $W(r)$ is included. As discussed in the Supplemental Material [54] this maximum appears only for strong impurity-boson coupling, i.e., if $\eta \gtrsim n_0\bar{\xi}$. Since for large values of r, $W(r)$ decays faster than $V(r)$, the total potential remains attractive at large distances.

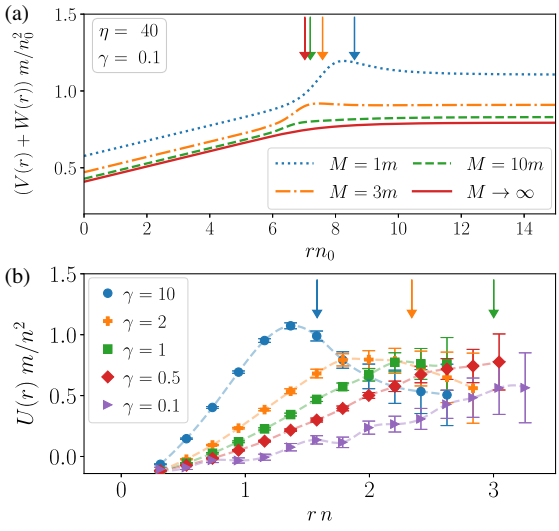

FIG. 3. Interaction potential for mobile impurities. (a) Mean-field potential including Born-Huang correction for different mass ratios. (b) Total interaction potential $U(r)$ from QMC simulations for the mass ratio $M = 3m$, but $\eta \to \infty$ and different Lieb-Liniger parameters. Arrows point to analytical predictions of maxima $r_{\max} = \pi\bar{\xi} = \pi/\sqrt{2m_r\mu}$, where we used the equation of state for μ from Bethe ansatz [64].

While for an infinite impurity mass, the interaction potential can be obtained directly in QMC simulations from the ground-state energy, its estimation is more delicate for finite values of M and involves the impurity-impurity correlation function, $g_{ii}(x)$. Here the degrees of freedom of the gas are integrated out and $\sqrt{g_{ii}(x)}$ is interpreted as a wave function of the effective two-impurity Schrödinger equation. The effective potential is proportional to $[\sqrt{g_{ii}(x)}]''/\sqrt{g_{ii}(x)}$, for details see Supplemental Material [54]. The large statistical noise arising from division by $\sqrt{g_{ii}(x)}$ does not allow one to unambiguously identify a local potential maximum in a weakly interacting gas, $\gamma \ll 1$. The maximum conjectured by the analytic theory is, however, clearly seen in the regime of strong interactions, $\gamma \gtrsim 1$, and although being outside the range of validity, its position is reasonably well predicted, see arrows in Fig. 3(b). Note that, in the limit of a Tonks-Girardeau gas [65], $\gamma \to \infty$, the maxima coincide with the first maximum of Friedel oscillations [66] at $n_0 r = 1$ and in a super-Tonks-Girardeau gas would correspond to quasicrystal lattice spacing. The attractive polaron interactions can lead to bound bipolaron states. In one dimension, at least one two-body bound state exists if the Fourier transform of the interaction potential at zero momentum is negative. We calculated the bipolaron energy of the lowest bound states for repulsive and attractive impurity-boson couplings with and without the Born-Huang corrections and compared the results to QMC simulations. While an attractive contact interaction only allows for a single bound state, here several ones are possible due to the finite extension of the effective potential. Note, however, that the first excited state of two bosonic impurities, mappable to the ground state of two fermions, becomes bound only above a critical interaction strength η_c. In Fig. 4 we plot the energies of the ground and first excited states of the bipolaron as a function of $\eta = g_{\mathrm{IB}}/g$ for a Bose gas with Lieb-Liniger parameter $\gamma = 0.125$ for repulsive and attractive interactions. Since the effective interaction potential is unbounded in the attractive case, much larger bipolaron energies are obtained for $\eta \to -\infty$. Once the Born-Huang corrections are included, an excellent quantitative agreement is found for mass ratios as small $M/m = 3$. As shown in the Supplemental Material [54], the predictions become less precise if the boson-boson interaction is increased, but even for $\gamma = 1$, the discrepancy is below the few-percent level for $\eta \leq 1$ and saturates below 15% for $\eta \to \infty$. The bipolaron energies are in the same order as typical single-polaron energies and in the strongly repulsive regime $g_{\mathrm{IB}} \gg g n_0 \bar{\xi}$ they are comparable to the energy of a dark soliton $E \sim \hbar n_0 c$. For the experimental data of

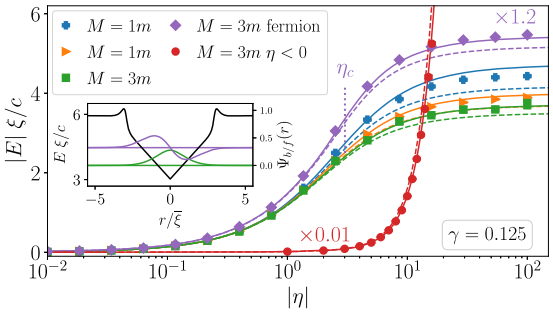

FIG. 4. Comparison of ground- and first excited-state energies of bipolarons with QMC results (dots) for different mass ratios m/M and weak-to-moderate boson-boson coupling $\gamma = 0.125$. Dashed lines correspond to BO potential $V(r)$; solid lines include Born-Huang correction $V(r) + W(r)$. The red curves correspond to attractive impurity-boson interaction (scaled by 0.01) and all others to repulsive. The purple line is the ground-state energy for fermionic impurities (i.e., first excited bipolaron state, scaled by 1.2), where the vertical line marks the interaction strength $\eta_c \simeq 3$, above which the two fermions form a bound state, calculated from the mean-field potential. The inset ($\eta = 30$; $M = 3m$) illustrates the corresponding impurity wave functions in green (purple) for bosonic (fermionic) impurities, as well as $V(r) + W(r)$ (black).

Ref. [26], where $n_0 \approx 7\mu\text{m}^{-1}$ and $c \approx 3.4$ mm/s, the latter corresponds to temperatures of $T = E/k_B \approx 240$ nK.

Conclusions.—We presented a detailed study of bipolarons and polaron-polaron interactions in ground-state 1D Bose gases. We have developed a semianalytical theory applicable for weakly interacting bosons and valid for arbitrarily strong impurity-boson interactions. As opposed to solid-state systems, where impurities couple only to collective excitations, the high compressibility of the Bose gas makes it necessary to take into account the action of the impurity to the quasicondensate. This was done by expanding the quantum field of the bosons around a deformed quasicondensate [53]. In this way the density of phonons created by the impurities remains small also for strong impurity-boson couplings and phonon-phonon interactions can be disregarded. We derived the short-range potential from analytic mean-field solutions in BO approximation and found excellent agreement with QMC simulations. In the limit of strong impurity-boson interactions, $g_{\text{IB}}/g \gg 1/\sqrt{2(m_r/m)\gamma}$, the potential deviates substantially from the perturbative exponential form and attains a linear short-range dependence. When lowest-order corrections to the BO result are included, the potential becomes nonmonotonic and attains a local maximum at a distance of $\pi\tilde{\xi}$. As the interactions in the gas are made stronger, the height of the peak is increased and its position moves toward the first maximum of the Friedel oscillations. Comparison with QMC simulations shows that the analytic model provides a precise prediction for bipolaron energies for bosonic and fermionic impurities. Thus, the mean-field description beyond the Froehlich model constitutes an excellent basis for the analysis of nonequilibrium and many-body properties of Bose polarons. Going away from equilibrium, e.g., by applying periodic drive or similar Floquet techniques, will open new avenues to modify interactions of impurities mediated by a many-body environment with applications to fields such as high-T_c superconductivity and others. For this it is important to have tractable theoretical tools at hand. The application of our approach to the nonequilibrium physics of interacting polarons will be the subject of future work.

We would like to thank Jonas Jager for fruitful discussions. M. W. and M. F. acknowledge financial support by the DFG through SFB/TR 185, Project No. 277625399. M. W. acknowledges support from the Max Planck Graduate Center. G. E. A. acknowledges financial support from the Spanish MINECO (FIS2017-84114-C2-1-P) and from the Secretaria d'Universitats i Recerca del Departament d'Empresa i Coneixement de la Generalitat de Catalunya within the ERDF Operational Program of Catalunya (project QuantumCat, Ref. 001-P-001644). The authors thankfully acknowledge the computer resources at MareNostrum and the technical support provided by Barcelona Supercomputing Center (RES-FI-2020-3-0011).

Note added.—Recently, we became aware of a recent related work on bipolarons in the limiting case of infinite impurity masses, using a different approach [67]. The conclusions are in agreement with ours in this limit.

[1] M. A. Ruderman and C. Kittel, Phys. Rev. **96**, 99 (1954).
[2] T. Kasuya, Prog. Theor. Phys. **16**, 45 (1956).
[3] K. Yosida, Phys. Rev. **106**, 893 (1957).
[4] L. N. Cooper, Phys. Rev. **104**, 1189 (1956).
[5] L. Landau, Phys. Z. Sowjetunion **3**, 644 (1933).
[6] S. I. Pekar, Zh. Eksp. Teor. Fiz. **16**, 335 (1946).
[7] A. S. Alexandrov and A. B. Krebs, Phys. Usp. **35**, 345 (1992).
[8] N. Mott, Physica (Amsterdam) **205C**, 191 (1993).
[9] A. S. Alexandrov and N. F. Mott, Rep. Prog. Phys. **57**, 1197 (1994).
[10] J. L. Bredas and G. B. Street, Acc. Chem. Res. **18**, 309 (1985).
[11] S. Glenis, M. Benz, E. LeGoff, J. L. Schindler, C. R. Kannewurf, and M. G. Kanatzidis, J. Am. Chem. Soc. **115**, 12519 (1993).
[12] M. N. Bussac and L. Zuppiroli, Phys. Rev. B **47**, 5493 (1993).
[13] M. Fernandes, J. Garcia, M. Schultz, and F. Nart, Thin Solid Films **474**, 279 (2005).
[14] I. Zozoulenko, A. Singh, S. K. Singh, V. Gueskine, X. Crispin, and M. Berggren, ACS Appl. Poly. Mater. **1**, 83 (2019).

[15] P. A. Bobbert, T. D. Nguyen, F. W. A. van Oost, B. Koopmans, and M. Wohlgenannt, Phys. Rev. Lett. **99**, 216801 (2007).
[16] A. Schirotzek, C.-H. Wu, A. Sommer, and M. W. Zwierlein, Phys. Rev. Lett. **102**, 230402 (2009).
[17] Y. Zhang, W. Ong, I. Arakelyan, and J. E. Thomas, Phys. Rev. Lett. **108**, 235302 (2012).
[18] C. Kohstall, M. Zaccanti, M. Jag, A. Trenkwalder, P. Massignan, G. M. Bruun, F. Schreck, and R. Grimm, Nature (London) **485**, 615 (2012).
[19] M. Koschorreck, D. Pertot, E. Vogt, B. Fröhlich, M. Feld, and M. Köhl, Nature (London) **485**, 619 (2012).
[20] F. Scazza, G. Valtolina, P. Massignan, A. Recati, A. Amico, A. Burchianti, C. Fort, M. Inguscio, M. Zaccanti, and G. Roati, Phys. Rev. Lett. **118**, 083602 (2017).
[21] M. Cetina, M. Jag, R. S. Lous, J. T. M. Walraven, R. Grimm, R. S. Christensen, and G. M. Bruun, Phys. Rev. Lett. **115**, 135302 (2015).
[22] M. Cetina, M. Jag, R. S. Lous, I. Fritsche, J. T. M. Walraven, R. Grimm, J. Levinsen, M. M. Parish, R. Schmidt, M. Knap, and E. Demler, Science **354**, 96 (2016).
[23] A. Schirotzek, C.-H. Wu, A. Sommer, and M. W. Zwierlein, Phys. Rev. Lett. **102**, 230402 (2009).
[24] C. Kohstall, M. Zaccanti, M. Jag, A. Trenkwalder, P. Massignan, G. M. Bruun, F. Schreck, and R. Grimm, Nature (London) **485**, 615 (2012).
[25] M. Koschorreck, D. Pertot, E. Vogt, B. Fröhlich, M. Feld, and M. Köhl, Nature (London) **485**, 619 (2012).
[26] J. Catani, G. Lamporesi, D. Naik, M. Gring, M. Inguscio, F. Minardi, A. Kantian, and T. Giamarchi, Phys. Rev. A **85**, 023623 (2012).
[27] M. Hohmann, F. Kindermann, B. Gänger, T. Lausch, D. Mayer, F. Schmidt, and A. Widera, Eur. Phys. J. Quantum Technol. **2**, 23 (2015).
[28] M. G. Hu, M. J. Van de Graaff, D. Kedar, J. P. Corson, E. A. Cornell, and D. S. Jin, Phys. Rev. Lett. **117**, 055301 (2016).
[29] N. B. Jørgensen, L. Wacker, K. T. Skalmstang, M. M. Parish, J. Levinsen, R. S. Christensen, G. M. Bruun, and J. J. Arlt, Phys. Rev. Lett. **117**, 055302 (2016).
[30] F. Scazza, G. Valtolina, P. Massignan, A. Recati, A. Amico, A. Burchianti, C. Fort, M. Inguscio, M. Zaccanti, and G. Roati, Phys. Rev. Lett. **118**, 083602 (2017).
[31] Z. Z. Yan, Y. Ni, C. Robens, and M. W. Zwierlein, Science **368**, 190 (2020).
[32] M. Olshanii, Phys. Rev. Lett. **81**, 938 (1998).
[33] C. Pethick, *Bose-Einstein Condensation in Dilute Gases* (Cambridge University Press, Cambridge; New York, 2002).
[34] A. Klein and M. Fleischhauer, Phys. Rev. A **71**, 033605 (2005).
[35] A. Recati, J. N. Fuchs, C. S. Peća, and W. Zwerger, Phys. Rev. A **72**, 023616 (2005).
[36] P. Naidon, J. Phys. Soc. Jpn. **87**, 043002 (2018).
[37] M. Schecter and A. Kamenev, Phys. Rev. Lett. **112**, 155301 (2014).
[38] B. Reichert, A. Petković, and Z. Ristivojevic, Phys. Rev. B **99**, 205414 (2019).
[39] B. Reichert, Z. Ristivojevic, and A. Petković, New J. Phys. **21**, 053024 (2019).
[40] G. E. Astrakharchik and I. Brouzos, Phys. Rev. A **88**, 021602(R) (2013).
[41] F. Grusdt, G. E. Astrakharchik, and E. Demler, New J. Phys. **19**, 103035 (2017).
[42] M. Tylutki, G. E. Astrakharchik, and A. Recati, Phys. Rev. A **96**, 063603 (2017).
[43] S. I. Mistakidis, A. G. Volosniev, N. T. Zinner, and P. Schmelcher, Phys. Rev. A **100**, 013619 (2019).
[44] L. A. Peña Ardila, G. E. Astrakharchik, and S. Giorgini, Phys. Rev. Research **2**, 023405 (2020).
[45] G. E. Astrakharchik, L. A. P. Ardila, R. Schmidt, K. Jachymski, and A. Negretti, Commun. Phys. **4**, 94 (2021).
[46] A. S. Dehkharghani, A. G. Volosniev, and N. T. Zinner, Phys. Rev. Lett. **121**, 080405 (2018).
[47] M. Flicker and E. H. Lieb, Phys. Rev. **161**, 179 (1967).
[48] D. Huber, H.-W. Hammer, and A. G. Volosniev, Phys. Rev. Research **1**, 033177 (2019).
[49] D. S. Dean, P. L. Doussal, S. N. Majumdar, and G. Schehr, SciPost Phys. **10**, 82 (2021).
[50] A. Camacho-Guardian, L. A. Peña Ardila, T. Pohl, and G. M. Bruun, Phys. Rev. Lett. **121**, 013401 (2018).
[51] Y. E. Shchadilova, R. Schmidt, F. Grusdt, and E. Demler, Phys. Rev. Lett. **117**, 113002 (2016).
[52] A. G. Volosniev and H. W. Hammer, Phys. Rev. A **96**, 031601(R) (2017).
[53] J. Jager, R. Barnett, M. Will, and M. Fleischhauer, Phys. Rev. Research **2**, 033142 (2020).
[54] See Supplemental Material at http://link.aps.org/supplemental/10.1103/PhysRevLett.127.103401 for details concerning the quantum Monte Carlo simulations, finite-size effects, and the mean-field solution, which includes Ref. [55].
[55] G. De Rosi, G. E. Astrakharchik, and S. Stringari, Phys. Rev. A **96**, 013613 (2017).
[56] C. J. Pethick and H. Smith, *Bose-Einstein Condensation in Dilute Gases* (Cambridge University Press, Cambridge, 2008).
[57] E. H. Lieb and W. Liniger, Phys. Rev. **130**, 1605 (1963).
[58] T. D. Lee, F. E. Low, and D. Pines, Phys. Rev. **90**, 297 (1953).
[59] B. Reichert, A. Petković, and Z. Ristivojevic, Phys. Rev. B **100**, 235431 (2019).
[60] A. Petković, B. Reichert, and Z. Ristivojevic, Phys. Rev. Research **2**, 043104 (2020).
[61] D. F. Lawden, *Elliptic Functions and Applications*, Applied Mathematical Sciences (Springer-Verlag, New York, 1989).
[62] M. Born and K. Huang, *Dynamical Theory of Crystal Lattices* (Oxford University Press, New York, 1956).
[63] F. M. Fernández, Phys. Rev. A **50**, 2953 (1994).
[64] G. Lang, F. Hekking, and A. Minguzzi, SciPost Phys. **3**, 003 (2017).
[65] M. Girardeau, J. Math. Phys. (N.Y.) **1**, 516 (1960).
[66] J. N. Fuchs, A. Recati, and W. Zwerger, Phys. Rev. A **75**, 043615 (2007).
[67] F. Brauneis, H. Hammer, M. Lemeshko, and A. Volosniev, SciPost Phys. **11**, 008 (2021).

Supplemental Material: Polaron interactions and bipolarons in one-dimensional Bose gases in the strong coupling regime

M. Will,[1] G. E. Astrakharchik,[2] and M. Fleischhauer[1]

[1] *Department of Physics and Research Center OPTIMAS, University of Kaiserslautern, 67663 Kaiserslautern, Germany*

[2] *Departament de Física, Universitat Politècnica de Catalunya, Campus Nord B4-B5, E-08034, Barcelona, Spain*

(Dated: August 4, 2021)

A. Quantum Monte Carlo simulations

In order to obtain non-perturbative results we resort to the diffusion Monte Carlo method. It allows us to find the properties of a many-body system numerically, starting directly from the microscopic Hamiltonian which we take in the following form ($\hbar = 1$)

$$\hat{H} = -\sum_{i=1}^{N} \frac{1}{2m}\frac{\partial^2}{\partial x_i^2} + \sum_{i<j}^{N} g\delta(x_i - x_j) - \sum_{i=1}^{N_{\rm I}} \frac{1}{2M}\frac{\partial^2}{\partial X_i^2} + \sum_{i}^{N}\sum_{j}^{N_{\rm I}} g_{\rm IB}\delta(x_i - X_j), \tag{1}$$

where x_i are positions of N bosons and X_j are positions of $N_{\rm I}$ impurities. The simulation is performed in a box of size L with periodic boundary conditions.

The diffusion Monte Carlo (DMC) method is based on solving the Schrödinger equation in imaginary time. The contributions from excited states are exponentially suppressed for large propagation times and one is able to extract the ground-state energy exactly. The convergence is enhanced by using an importance-sampling technique in which the Schrödinger equation is solved for the product of the wave function and a guiding wave function which we take in the Jastrow pair product form

$$\psi_T(x_1, \cdots, x_N; X_1, \cdots, X_{N_{\rm I}}) = \prod_{i<j}^{N} f_{\rm BB}(x_i - x_j) \prod_{i=1}^{N}\prod_{j=1}^{N_{\rm I}} f_{\rm BI}(x_i - X_j). \tag{2}$$

The Jastrow terms are chosen in such a way that when two bosons (or a boson and an impurity particle) meet, the delta-pseudopotential present in Hamiltonian (1) induces a kink in the wave function of a strength proportional to g (or $g_{\rm IB}$). This is done by using at short distances the two-body scattering solution $f_{\rm BB}(x) = A_{\rm BB}\cos(k_{\rm BB}(x - B_{\rm BB}))$, $|x| < R_{\rm BB}$ which satisfies the Bethe-Peierls boundary condition, $f'_{\rm BB}(0)/f_{\rm BB}(0) = -1/a_{\rm BB}$ where $a_{\rm BB}$ is the s-wave scattering length. At larger distances this solution is matched with the long-range asymptotic obtained from hydrodynamic theory, $f_{\rm BB}(x) = \sin^{1/K_{\rm BB}}(\pi x/L)$ for $R_{\rm BB} < |x| < L/2$. The parameters $A_{\rm BB}$, $B_{\rm BB}$, $K_{\rm BB}$ are chosen from the Bethe-Peierls boundary condition at zero distance, the continuity conditions for the function and its first derivative at the matching distance $R_{\rm BB}$, while the periodic boundary condition $f'_{\rm BB}(L/2) = 0$ is automatically satisfied. We consider a similar structure of the boson-impurity Jastrow terms $f_{\rm BI}(x)$. Here the parameters R_{BB}, R_{BI} and K_{BI} are optimized in variational calculations by minimizing the variational energy. $K_{\rm BB}(x)$ has the meaning of the Luttinger liquid parameter and its value is exactly known from Bethe ansatz.

The calculation of the effective impurity-impurity interaction potential is performed differently in the case of an impurity of an infinite or finite mass:

infinite impurity mass – In this case the interaction potential is calculated from the ground-state energies of the system with two impurities, E_2, at positions X_1 and X_2; and with no impurities E_0 according to

$$V(X_2 - X_1) = E_2 - E_0. \tag{3}$$

The actual dependence on the relative distance between the impurities is obtained by repeating the calculations for different values of $X_2 - X_1$. Each separate energy, E_2 and E_0, corresponds to the ground-state energy of the corresponding system and the DMC method allows exact calculation of such energies.

finite impurity mass – Here we calculate the impurity-impurity correlation function $g_{ii}(X_1 - X_2)$ and interpret it as the square of wave function of the two-impurity solution. By doing so we effectively integrate all degrees of freedom associated with Bose particles. The ground-state wave function $\psi_{ii}(X) = \sqrt{g_{ii}(X)} > 0$ obtained in this way satisfies

the two-impurity Schrödinger equation

$$-\frac{1}{2\mu^*}\psi_{ii}''(X) + V(X)\psi_{ii}(X) = E_{ii}\psi_{ii}(X), \tag{4}$$

where μ^* is the reduced effective polaron mass. Note that we here assumed that the mediated impurity-impurity interaction can be described as an effective interaction $V(X)$ of two well-defined quasi-particles. This is justified for heavy impurities or weak coupling but ignores the possibility of an effective distance-dependent polaron mass. The excellent agreement between analytic calculations of the bipolaron binding energies based on this assumption and QMC data shows that this assumption is justified also for smaller mass ratios and in the strong interaction limit. Here $E_{ii} = E_2 - E_0$ is the bipolaron binding energy, and $V(X)$ is the unknown effective interaction potential, which can be obtained from Eq. (4) according to

$$V(X) = E_{ii} + \frac{1}{2\mu^*}\frac{(\sqrt{g_{ii}(X)})''}{\sqrt{g_{ii}(X)}}. \tag{5}$$

That is, the bipolaron binding energy E_{ii} provides a vertical offset in $V(X)$ while the reduced effective mass μ^* "stretches" the interaction potential vertically. The actual values of E_{ii} and μ^* are not important for observing the predicted non-monotonous behavior, so for simplicity we use the bare impurity mass $\mu^* = M/2$.

B. Single Bose polarons on a 1D ring

The physics of single polarons in infinite one-dimensional Bose gases has been studied in Ref. [1] by assuming small quantum fluctuations on top of a deformed quasi condensate. We here illustrate the quantitative accuracy of this theory by comparison with quantum Monte Carlo simulations and extend the discussion by considering effects from the finite size of the 1D Bose gas.

Analytic solutions of the mean-field equations in the LLP frame were found and quantum fluctuations were taken into account in the lowest order by solving the corresponding Bogoliubov-de Gennes equations in Ref. [1]. While the agreement with QMC data for the polaron energy showed very good agreement, the predictions for the polaron mass m^* had a different asymptotic for $\eta \to \infty$ as the QMC simulations. This discrepancy is a finite-size effect (QMC calculations have been performed with $N = 50$ particles) which is much stronger in the polaron mass as compared to the energy. Indeed, if a finite number of bosons is considered on a ring then the polaron mass is bounded from above by the total mass of the bosons.

Notably, the finite-size corrections can be correctly predicted in the mean-field theory by fixing the total number of particles rather than the condensate density far away from the impurity. In Fig. 1(a) we have shown a comparison of the polaron energy for different system sizes and as a function of the impurity-boson coupling strength η obtained from mean-field solutions and QMC simulations. One recognizes an excellent agreement. Increasing η, more and more bosons are expelled from the immediate surrounding of the impurity which leads to an enhancement of the boson density n_0 in the regions far away from the impurity. This in turn increases their mean-field energy $\propto gn_0^2\xi$.

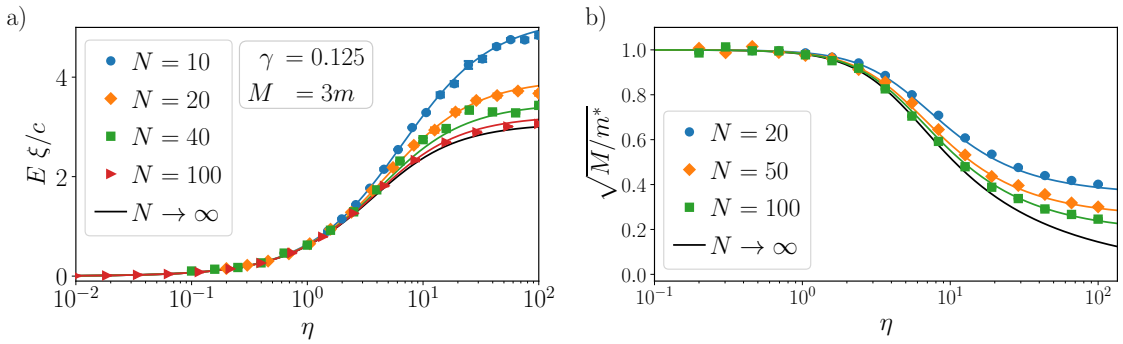

FIG. 1. Polaron (a) energy and (b) mass for a gas on a ring for different number of bosons. Symbols, QMC data; lines, predictions of the analytic theory.

As can be seen from Fig. 1(b) taking into account finite-size corrections also leads to a saturation of the effective polaron mass in the infinite coupling limit in excellent agreement with the predictions of QMC simulations.

We note that contrary to the 3D geometry where the finite-size correction due to periodic boundary conditions is an artifact, in 1D geometry periodic boundary conditions are physical and can be observed in cold gas experiments in a ring-shaped trap. Here qualitative new effects can arise if the relevant length scales, e.g. the reduced healing length $\bar{\xi}$, become comparable to the system size L[2].

C. Details of the mean-field solution

Using a Born-Oppenheimer and a mean-field approximation, one can derive the non-linear Schrödinger equation which determines the ground state of the Bose gas from the many body Hamiltonian (see Eq. (2) in the main text):

$$\left[-\frac{\partial_x^2}{2m_\mathrm{r}} \; + \; g\,|\phi_0(x)|^2 \; - \; \mu + g_\mathrm{IB}\Big(\delta(x-r/2)+\delta(x+r/2)\Big)\right]\phi_0(x) = 0. \tag{6}$$

This non-linear differential equation can be solved semi analytically using the Jacobi elliptic cd function [3].

$$\phi_0(x) = \sqrt{n_0}\begin{cases} \sqrt{\frac{2\tilde{\nu}}{\nu+1}}\,\mathrm{cd}\left(\frac{x}{\bar{\xi}\sqrt{1+\nu}}\,,\,\nu\right)^{\pm 1} & |x| < r/2 \\ \tanh\left(\frac{|x|-x_0}{\sqrt{2}\,\bar{\xi}}\right)^{\pm 1} & |x| > r/2, \end{cases} \tag{7}$$

where the upper (lower) sign corresponds to $\eta = g_\mathrm{IB}/g > 0$ ($\eta < 0$). The chemical potential in mean-field approximation is given by $\mu = gn_0$, where n_0 is the particle density far away from both impurities. In the thermodynamic limit one has $n_0 = n = N/L$. The parameter x_0 is chosen such that the wave function is continuous at $x = \pm r/2$, while $\nu = \nu(r,\eta)$ is determined by the implicit relation in the main text and ensures the correct jump in the first derivative of the wave function, enforced by the double delta potential in Eq. (6).

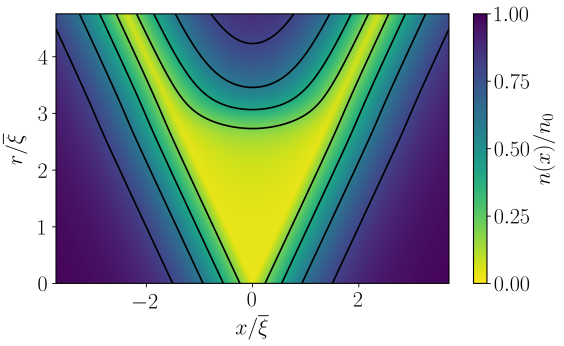

FIG. 2. Bipolaron density $n(x)$ for different distances r between the impurities and fixed interaction strength $\eta = 20n_0\bar{\xi}$.

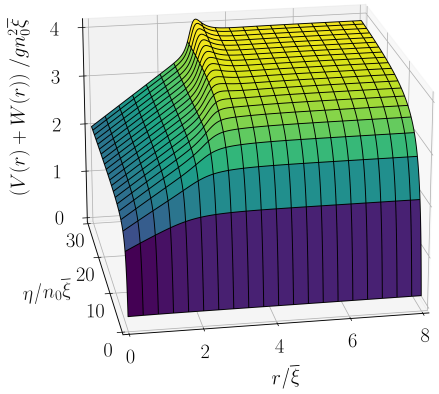

FIG. 3. Effective potential including first-order correction to Born-Oppenheimer for mass ratio $M = 3m$

The density is plotted for two strongly interacting impurities, $\eta = 20n_0\bar{\xi}$, in Fig. 2. For two impurities that are far away from each other, $r \gg \bar{\xi} = 1/\sqrt{2gn_0m_r}$, the density profile is well approximated by the wave functions of two separated impurities [1]. If the distance decreases to about $r \simeq \pi\bar{\xi}$ we find a sudden reduction of the boson density in between the impurities and for a smaller distance all bosons are pushed out of this space. The distance $r/\bar{\xi} \simeq \pi$ at which this depletion takes place is only an approximation for finitely repulsive impurities, but is exact for infinite

repulsion $\eta \to \infty$. The parameter ν is in this limit determined by

$$\begin{aligned} \nu\Big|_{\eta\to\infty} &= 0 \qquad \text{for } r \le \pi\bar{\xi} \\ K(\nu)\sqrt{1+\nu}\Big|_{\eta\to\infty} &= \frac{r}{2\bar{\xi}} \quad \text{for } r > \pi\bar{\xi}, \end{aligned} \tag{8}$$

where $K(\nu)$ is the complete elliptic integral of the first kind. Inserting this into the mean-field wave function, Eq. (7), shows that the condensate density is totally depleted in between the two impurities for $r \le \pi\bar{\xi}$. In the next step the Born-Oppenheimer potential can be calculated as the energy of the mean-field wave function Eq. (7).

$$V(r) = gn_0^2 L - \frac{g}{2}\int_{-L/2}^{L/2} \phi_0(x)^4\, dx - E_0(g_{\mathrm{IB}}=0) \tag{9}$$

where the extensive mean-field ground state energy $E_0(g_{\mathrm{IB}}=0)$ of the Bose gas without impurities is subtracted. In general this evaluates to Eq. (3) in the main text, but the expression can again be simplified for infinitely repulsive impurities, especially the short-range potential in the limit $\eta \to \infty$ reads

$$V(r)\Big|_{\eta\to\infty} = gn_0^2 \begin{cases} \frac{4}{3}\sqrt{2}\bar{\xi} + \frac{1}{2}r & \text{for } r \le \pi\bar{\xi} \\ \frac{4}{3}\bar{\xi}\left[\sqrt{2} + \frac{E(\nu)}{\sqrt{1+\nu}}\right] + r\,\frac{-5+2\nu+3\nu^2}{6(1+\nu)^2} & \text{else,} \end{cases} \tag{10}$$

where $E(\nu)$ is the complete elliptic integral of the second kind. The linear short-range potential is caused by the bosons being expelled from the space in between the impurities. The bosons outside of this space therefore push the impurities towards each other with a constant force, which is equivalent to the linear potential. The potential starts to deviate from the linear slope as soon as the particle density in between the impurities increases. For a large distance $r \gg \bar{\xi}$ between the two impurities we find a exponentially decaying potential which is for repulsive interaction given by

$$V(r)\Big|_{\eta>0\,,\, r\gg\bar{\xi}} = 2E_1 - 128\sqrt{2}\, gn_0^2\bar{\xi}\,\frac{n_0^2\bar{\xi}^2}{\eta^2}\left(\sqrt{1+\eta^2/8n_0^2\bar{\xi}^2} - 1\right)^2 e^{-\sqrt{2}r/\bar{\xi}}, \tag{11}$$

where E_1 is the constant mean-field energy of a single polaron [1].

The first order Born-Oppenheimer correction

$$W(r) = \frac{1}{M}\int dx\, |\partial_r \phi_0(x)|^2\ , \tag{12}$$

accounts for the contribution of the condensate wave function, which depends on the impurity coordinate, when calculating the kinetic energy of the relative motion of the impurities [4, 5]. Since the derivative of the wave function $\phi_0(x)$ (7) with respect to the distance r is analytically difficult, we do not give an explicit expression. A very prominent effect of this correction is the emergence of a local maximum in the two-particle potential Fig. 3. It appears only for strongly interacting impurities $\eta \gg n_0\bar{\xi}$, when the deformation of the quasi-condensate is substantial. For small values of r, where the quasi-condensate in between the impurities is depleted, the correction is only a small constant. For a distance $r \simeq \pi\bar{\xi}$ the density in between becomes nonzero again, and grows rapidly when further increasing the distance r, leading to a large correction. When the impurities are far apart, the contribution of the Bose gas to the kinetic energy of impurities is small again, which results in a local maximum of $W(r)$ at the intermediate distance. Since the relative kinetic energy of the impurities scales inversely with the impurity mass M, the potential correction also decreases with increasing value of M, which is shown in Fig.3a of the main part.

D. Bipolaron binding energy for attractive interactions

For repulsive impurity-boson interactions the two-particle potential approaches an asymptotic value with the linear short-distance behavior given in Eq. (10), when $\eta \to \infty$. The bipolaron binding energy thus saturates as can be seen in Fig. 4 of the main text. This is different in the attractive case, $\eta < 0$, since more and more bosons can be pulled towards the impurities. Thus the bipolaron binding energy grows unlimited for $|\eta| \to \infty$. This can be seen in Fig. 4, where we have plotted the theoretical predictions resulting from the effective potential with and without

BO corrections and compared them to QMC simulations. As one can see, the results are in a perfect quantitative agreement. Note that the discrepancy between $N_B = 20$ and $N_B = 100$ bosons is a finite size effect which becomes sizable for strong interactions, $|\eta| \geq 10$. It has a direct physical relevance in a one dimensional system, since periodic boundary conditions can be realized in experiments using a system on a ring trap. The QMC data for $N_I = 5$ impurities illustrate that a multi-impurity bound state can form in the case of an attractive impurity-boson interaction with a rapidly increasing binding energy.

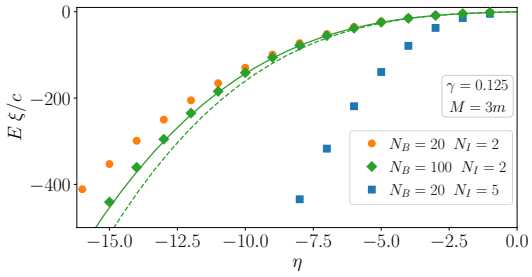

FIG. 4. QMC ground state energy of a system containing N_B bosons and N_I impurities interacting attractively with each other. The solid (dashed) line is the MF prediction of the bipolaron energy including (excluding) the first order BO correction in the thermodynamic limit.

E. Effect of strong boson-boson interactions

The semi-analytic theory presented in the main text is valid for arbitrarily large impurity couplings but is limited to weak boson-boson interactions, corresponding to small Lieb Liniger parameter γ. In Fig. 5 we have plotted the bipolaron binding energies for strong boson-boson interactions ($\gamma = 1$) for different impurity-boson mass ratios as function of the impurity coupling. While there are increasing deviations from exact numerical QMC values, the agreement is still rather good for $\eta \lesssim 1$.

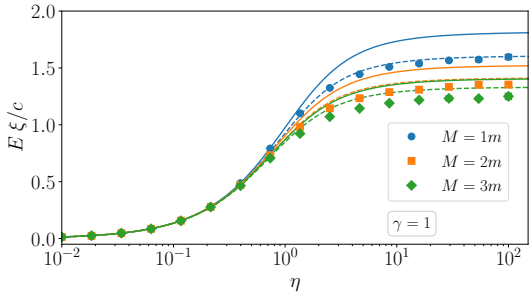

FIG. 5. Comparison of ground state energy of bound bipolaron and QMC for different mass ratios m/M and strong boson-boson coupling $\gamma = 1$. Solid (dashed) lines correspond to theoretical predictions with (without) BO corrections and the dots denote numerical values obtained from QMC simulations.

[1] J. Jager, R. Barnett, M. Will, and M. Fleischhauer, Phys. Rev. Research **2**, 033142 (2020).
[2] G. De Rosi, G. E. Astrakharchik, and S. Stringari, Phys. Rev. A **96**, 013613 (2017).
[3] D. F. Lawden, *Elliptic Functions and Applications* (Applied Mathematical Sciences, 1989).
[4] M. Born and K. Huang, *Dynamical Theory of Crystal Lattices* (Oxford University Press, New York, 1956).
[5] F. M. Fernández, Phys. Rev. A **50**, 2953 (1994).

4 Controlling superfluid flows using dissipative impurities

Martin Will, Jamir Marino, Herwig Ott, and Michael Fleischhauer,
SciPost Phys. **14**, 064 (2023).

In contrast to Chapters 2 and 3 [P1, P2], which focused on a constant and coherent impurity-boson interaction, this part discusses the impact of a temporally fluctuating coupling constant. It demonstrates how a noisy point contact can be used to control currents within the Bose gas. The impurity-boson coupling is modeled using a Markov Gaussian white noise process $\eta(t)$ with mean $\overline{\eta(t)} = 0$ and variance $\overline{\eta(t)\eta(t')} = \delta(t-t')$. This noise term is multiplied by a local potential $V(x) \propto \sqrt{\sigma}$, where σ characterizes the strength of the noise. Consequently, the MF Equation (1.24) is generalized to

$$i\mathrm{d}\phi(x,t) = \Big[-\frac{\partial_x^2}{2m} - iv\partial_x + g|\phi(x,t)|^2 \Big]\phi(x,t)\ \mathrm{d}t + V(x)\,\phi(x,t) \circ \mathrm{d}W. \tag{4.1}$$

It is a Stratonovich stochastic partial differential equation (SPDE), where $\mathrm{d}W = \eta(t)\mathrm{d}t$ is an infinitesimal Wiener process [106]. For a finite impurity mass M, the noise causes a heating of the impurity, resulting in instabilities in the system. Hence, this chapter focuses on the case of an infinitely heavy impurity $M \to \infty$ at a fixed velocity v, or equivalently, a stationary impurity subject to an externally driven current.

The noisy impurity scatters particles from the condensate into highly excited modes, leading to an incoherent current of particles flowing away from the noise contact. The effect on the condensate is, therefore, similar to a localized particle loss, which was studied in Refs. [79–82]. A coherent particle current towards the noise source emerges to counteract this effective particle loss. The strength of the induced coherent current is depicted in Figure 4.1a) as a function of the impurity velocity v and the strength of the noise σ. We identify three dynamical regimes, depending on whether the current increases or decreases as the noise strength varies. In the linear response regime (I), the current increases monotonically with the dissipation strength σ. However, because the local speed of sound bounds the velocity of a coherent current, the system transitions into the Zeno regime (II) at a critical noise strength. In this regime, a grey soliton (a local density depletion) forms at the noise contact, reducing the scattering rate and the strength of the induced current. The critical noise strength is lowered when an externally driven current is present. This effect is modeled analytically in Appendix C of this publication [P3]. At a finite velocity v, another regime (III) exists, where the impurity periodically emits solitons. In the case of a strong dissipation, the particle density at the impurity would drop to zero, obstructing any particle current. However, the externally driven current forces particles to pass the impurity. These effects compete, leading to instabilities and the continuous emission of solitons. As a result, the average scattering rate and particle current increase again.

In the second part, the theory is extended to a pair of point contacts at rest, following the approach of Chapter 3 [P2]. Both contacts induce currents in the condensate that influence

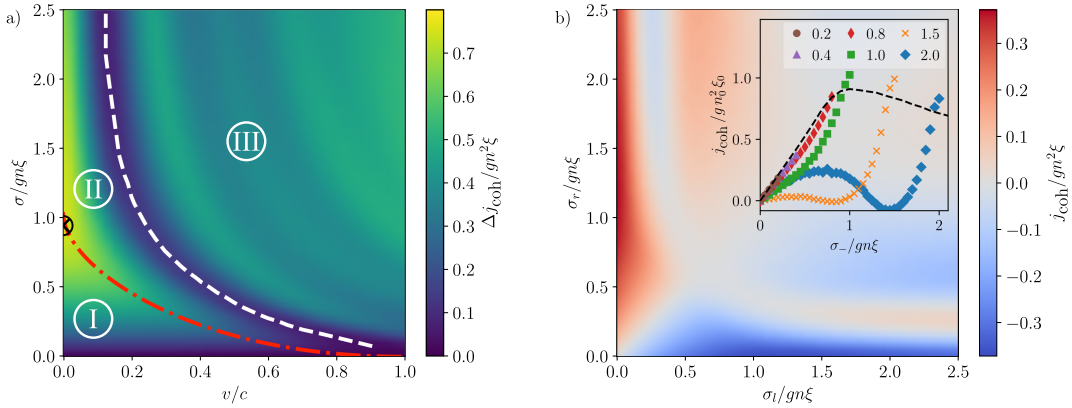

Figure 4.1: a) Phase diagram of a noisy point contact of strength σ in an externally driven current at velocity v. Plotted is the strength of the current induced by the noisy impurity. It is averaged over an interval in space and time, see the publication [P3] for details. The red line marks the analytically estimated transition between linear response I and Zeno regime II. The white line is the numerically determined transition between Zeno II and soliton regime III. b) Coherent current between two point contact of strength σ_r and σ_l. The inset shows the current as a function of the difference σ_- and sum $\sigma_+/gn\xi$ (different colors) of the two noise strengths. It is rescaled to the density n_0 and healing length $\xi_0 = 1/\sqrt{2gn_0m}$ of the gas between the contacts. The black line is the current induced by a single contact.

each other. As a result, the same three dynamical regimes are identified as in the case of a single contact in an externally driven current. The coherent current between the two contacts is displayed in Figure 4.1b), as a function of the individual noise strengths of the two contacts σ_r and σ_l. It is anti-symmetric since exchanging the two noise strengths leads to an inversion of the current. When the sum $\sigma_+ = \sigma_r + \sigma_l$ is small compared to $gn\xi$, where $\xi = 1/\sqrt{gnm}$ is the healing length, both contacts are in the linear response regime. Consequently, the coherent current between the contacts equals the sum of the currents induced by the two independent contacts. This behavior is illustrated in the inset of Figure 4.1b), where the current depends only on the difference $\sigma_- = \sigma_r - \sigma_l$ for a small sum σ_+, and is equal to the current created by a single contact. However, when σ_+ is larger, at least one of the contacts is in the soliton or Zeno regime. This results in a different slope and a non-monotonous dependency of σ_-.

Author contributions

In this study, I extended the theory presented in Section 1.3 to incorporate a white noise impurity-boson coupling constant. To solve the resulting SPDEs, I implemented a numerical simulation based on a time-splitting spectral method [107]. A description of the algorithm can be found in Appendix B. The idea to incorporate dissipative processes originated from Michael Fleischhauer and Jamir Marino, who both supervised the project. The theoretical results were discussed by Michael Fleischhauer, Jamir Marino, and myself. Herwig Ott provided insights regarding the experimental implementation. All authors were engaged in the writing and reviewing process of the manuscript.

Copyright

Controlling superfluid flows using dissipative impurities

Martin Will[1⋆], Jamir Marino[2], Herwig Ott[1] and Michael Fleischhauer[1]

1 Department of Physics and Research Center OPTIMAS, University of Kaiserslautern, 67663 Kaiserslautern, Germany
2 Institute for Physics, Johannes Gutenberg University Mainz, D-55099 Mainz, Germany

⋆ willm@rhrk.uni-kl.de

Abstract

We propose and analyze a protocol to create and control the superfluid flow in a one dimensional, weakly interacting Bose gas by noisy point contacts. Considering first a single contact in a static or moving condensate, we identify three different dynamical regimes: I. a linear response regime, where the noise induces a coherent flow in proportion to the strength of the noise, II. a Zeno regime with suppressed currents, and III. a regime of continuous soliton emission. Generalizing to two point contacts in a condensate at rest we show that noise tuning can be employed to control or stabilize the superfluid transport of particles along the segment which connects them.

Received 05-10-2022
Accepted 09-01-2023
Published 06-04-2023
doi:10.21468/SciPostPhys.14.4.064

Contents

1 Introduction

Quantum interference plays a key role in mesoscopic transport phenomena where impurities or dots are employed as 'shunts' for transferring particles, energy and information without degrading phase coherence in the process [1–3]. In recent years a novel route to investigate this field of *quantum transport* emerged by employing ultracold atoms confined by optical or magnetic potentials [4]. The ability to control and manipulate the effective dimensionality and geometry of the systems, the possibility to tune the inter-particle interaction strength, to add or eliminate disorder and to choose between fermionic or bosonic quantum particles made ultracold atoms an ideal testing ground for quantum transport phenomena [5,6]. In these systems effects are accessible which were out of reach or very challenging to investigate in solid state. E.g. the periodic velocity change of a quantum particle moving in a lattice under the action of a constant driving force, known as Bloch oscillation, is difficult to observe in condensed matter systems due to impurity scattering but has beautifully been demonstrated with ultracold atoms in optical lattices [7,8]. Transport experiments of ultra-cold Fermi atoms through point contacts [9–11] verified the quantization of conductance predicted by the Landauer theory of transport, which has previously been observed only in electronic systems. Both bosonic and fermionic superfluids can be created using ultra-cold atoms and frictionless flow has been observed [12,13]. Persistent currents in ring geometries have been realized in atomic superfluids [14,15] and cold-atom analogues of Josephson junctions have been constructed [16,17] with the potential for an atomtronic analogue of a SQUID. Finally the coupling between particle and heat transport has been observed in fermionic cold atoms providing a cold-atom analogue of the thermoelectric effect [18]. However, despite of all experimental advances in the field, the creation and precise control of superfluid currents remains a challenge in atomtronics. Besides moving potential barriers or time-dependent artificial gauge fields, currents are typically generated by a difference of chemical potentials between the ends of a channel, i.e by fixing "voltage" rather than "current".

In the present work we suggest and analyze a different method to create and manipulate the superfluid flow in a one-dimensional quasi-condensate of Bose atoms, see Fig. 1. Importantly here we control the superfluid current directly rather than fixing chemical potentials. In particular we make use of the interaction of the condensate with quantum impurities that are

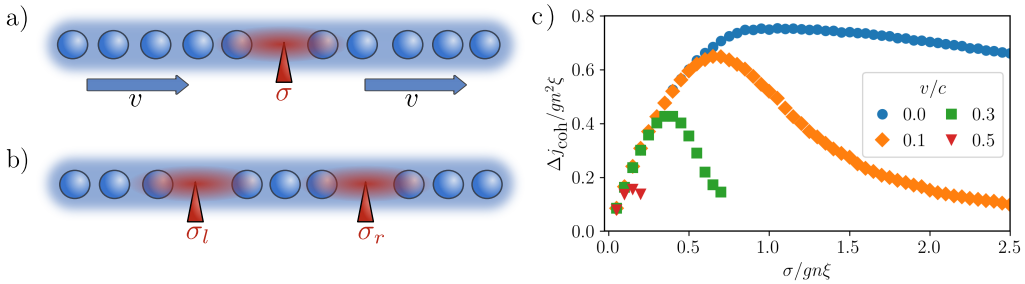

Figure 1: Scheme for controlling superfluid flow in a one dimensional interacting Bose gas using one a) or two b) noisy impurities, with or without an external current at velocity v. c) Induced superfluid current at a noisy point contact of noise strength σ in a moving condensate at velocity v. For weak noise the current grows monotonically with σ, but for stronger noise the system enters a Zeno regime, where the current decreases. For the two largest velocities the system enters a regime of dynamical instabilities beyond a certain value of σ, where the current is no longer stationary and thus not shown.

coupled to the Boson's density with a fluctuating, i.e. noisy strength. Analyzing the system we identify different dynamical regimes, including a linear response regime, a Zeno-regime [19] with negative differential current to noise-strength characteristics, and a regime with dynamical instabilities characterized by continuous soliton emission. Impurities in interacting systems have been instrumental to develop our understanding of the extended pattern of correlations in quantum many particle systems, by employing them as probes [20–22], tunable perturbations, or even seeds for entanglement [23]. In unitary quantum dynamics, examples range from the 'catastrophic' effect of a scattering potential intruding in a Fermi sea [24, 25], to strongly entangled magnetic impurities coupled to fermionic or bosonic reservoirs, or the dressing of static and moving particles in Fermi gases or Bose-Einstein condensates as it occurs in polaron formation [26–34]. The last decade has also witnessed a growth of attention towards the dissipative counterpart of the problem of quantum impurities embedded in interacting extended quantum systems [11, 35–53]. Pioneering results of one decade ago illustrates e.g. the action of a localized dissipative potential on a macroscopic matter wave by shining an electron beam on an atomic BEC [54, 55]. Atomic losses induced by local dissipation were monitored as a function of noise strength, providing a proxy for a many-body version of the Zeno effect. The stabilisation of dark solitons by engineered losses has been studied in [56]. Fluctuations in the condensate can build up strong correlations with localized dissipation, resulting in a suppression of transport at large noise strength which can be regarded as non-equilibrium phase transition [57, 58].

In this work, we illustrate how density rearrangements provoked by local dephasing can be utilized to control coherent superflows in a one-dimensional Bose condensate. Specifically, we consider a static or uniformly moving condensate coupled to a noisy local impurity. The noisy point contact acts as a source of incoherent, i.e. non-condensed atoms, which due to total particle-number conservation creates a superfluid flow towards the impurity. The superfluid flow increases monotonically with growing noise up to some critical value at which the system becomes dominated by the quantum Zeno effect which leads to a reduction of transport corresponding to a negative differential current - noise characteristics. We furthermore demonstrate that the archetypal effect of transport suppression due to Zeno effect is drastically altered in a moving rather than a static condensate. In particular, we observe a lowering of the critical threshold of noise strength for entering the Zeno regime when the background speed of the condensate is increased. This is shown in Fig. 1c where the onset of the Zeno regime drifts towards smaller values of dissipation strength. As outreach, we demonstrate complete tunability of a supercurrent in a static condensate by a pair of noise point contacts.

2 Model

We consider a homogeneous one-dimensional Bose gas with weak repulsive interactions ($g > 0$) and boson mass m. We study the effect of a noisy point contact in a Bose gas moving relative to the impurity with fixed velocity v. The impurity-BEC coupling is modeled by a Gaussian white noise process $\eta(t)$, with mean $\overline{\eta(t)} = 0$ and variance $\overline{\eta(t)\eta(t')} = \delta(t-t')$, multiplied by a local potential $V(x+vt)$, whose profile will be specified subsequently. Since we consider a weakly interacting condensate [59], quantified by a small Lieb-Liniger parameter $\gamma = gm/n \ll 1$, where n is the average boson density in the 1D gas, we apply a phase-space description of the quantum Bose field using the Glauber-P distribution [60]. Due to the action of the noisy point contact, we cannot ignore fluctuations even in the limit of a highly occupied condensate mode at very low temperatures. Within the phase space approach normal-ordered correlations of the Bose field operator $\hat{\psi}(x,t)$ are given by stochastic averages of a c-number field $\psi(x,t)$. The time evolution of $\psi(x,t)$ in the rest frame of the moving Bose

gas is then determined by a Gross-Pitaevskii-type equation with an additional stochastic term (SGPE) [61, 62]

$$i\,\mathrm{d}\psi(x,t) = \Big[-\frac{\partial_x^2}{2m} + g|\psi(x,t)|^2\Big]\psi(x,t)\,\mathrm{d}t + V(x+vt)\,\psi(x,t)\circ\mathrm{d}W\,. \tag{1}$$

Here $dW = \eta(t)\mathrm{d}t$ is a infinitesimal Wiener process [60]. The delta-correlated white noise $\eta(t)$ results in physical systems from colored noise in the limit of small correlation times. As has been shown in [60] the SGPE Eq. (1) becomes in this limit a Stratonovich stochastic differential equation, which is denoted by the symbol "$\circ$". In order to gauge away the explicit time dependence of the potential $V(x+vt)$, we apply a Galilean transformation to the reference frame where the point contact is at rest. This results into a SGPE with static potential and with a spatial gradient term proportional to v:

$$i\,\mathrm{d}\phi(x,t) = \Big[-\frac{\partial_x^2}{2m} - iv\,\partial_x + g|\phi(x,t)|^2\Big]\phi(x,t)\,\mathrm{d}t + V(x)\,\phi(x,t)\circ\mathrm{d}W\,. \tag{2}$$

$\overline{\phi}(x,t)$ describes the average Bose field in the rest-frame of the impurity, which includes both a quantum mechanical average and one over classical fluctuations induced by the noisy point contact. We refer to $\overline{\phi}$ as the coherent amplitude of the Bose field.
It should be emphasised that the noise in Eqs. (1) and (2) is generated externally, e.g. by a fluctuating laser field, which is different to the SGPE derived e.g. in [63], where the noise is induced by the interaction of a thermal cloud with the condensate at finite temperature.

3 Noisy point contact in a static BEC

We start our analysis by reviewing the physics of a single point contact placed at $x = 0$ in a static BEC ($v = 0$). The effect of the noisy impurity on the Bose gas shares at a first sight some similarities with the physics of local losses in Bose wires [54, 55, 64, 65]: they both scatter particles out of the macroscopically populated ground state $\overline{\phi}(x,t)$. However, the dissipative impurity considered here conserves the total number of particles, which is crucial for potential applications in atomtronic devices. In order to compare with the dynamics resulting from local losses, we first analyse the coherent amplitude $\overline{\phi}$. Therefore we consider the noise average of the SGPE Eq. (2)

$$i\frac{\mathrm{d}}{\mathrm{d}t}\overline{\phi} = -\frac{\partial_x^2}{2m}\overline{\phi} + g\,\overline{|\phi|^2\phi} - \frac{i}{2}V(x)^2\,\overline{\phi}\,. \tag{3}$$

While the fluctuating potential vanishes on average it does have an effect on the average field $\overline{\phi}$. This is because it is a *multiplicative* noise and the field $\phi(t)$ at a given time depends on the noise such that $\overline{\phi(x,t)dW} \neq 0$ (Stratonovich calculus [60]). As a result of this, the average field experiences an effective loss, which physically describes nothing else than the scattering of particles out of the condensate into excited modes of the Bose gas, for more details see Appendix A.

Eq. (3) matches the evolution of the noise-averaged amplitude subject to local *particle loss* (cf. [54, 55, 64, 65]) with the identification $V(x)^2 = 2\sigma\delta(x)$. We consider this potential as the limit of a Gaussian potential $V_l(x)^2 = 2\sigma/\sqrt{\pi l^2}\,\exp(-x^2/l^2)$, with the length l acting as a regulator, such that $V(x)$ itself is well defined. If l is chosen smaller than the healing length of the Bose gas $\xi = 1/\sqrt{2gnm} \gg l$ the internal structure of the impurity potential becomes irrelevant.

As shown in [54, 55, 64, 65] the effective local loss in Eq. (3) will induce currents. This can be seen most easily from the continuity equation of the modulus of the average field $|\overline{\phi}|^2$, which contains the coherent current

$$j_{\rm coh} = \frac{1}{m}\,{\rm Im}(\bar{\phi}^*\partial_x\bar{\phi})\,. \tag{4}$$

Note that here the noise is averaged over the individual fields first and then bilinear combinations are formed. $j_{\rm coh}$ is in general not equal to the average total particle current, which is defined by deriving the continuity equation for $\phi^*\phi$ from the original SGPE, Eq. (2), and performing the noise average afterwards. The total current reads

$$j_{\rm tot} = \frac{1}{m}\,\overline{{\rm Im}(\phi^*\partial_x\phi)}\,. \tag{5}$$

We analyze both currents as well as their difference, which we refer to as the incoherent current. It describes the flow of particles in excited modes of the Bose field created by the local noise. To evaluate analytically the dynamics of Eq. (3) we assume that the nonlinear term factorizes under average $\overline{|\phi(x,t)|^2\phi(x,t)} \simeq |\overline{\phi(x,t)}|^2\overline{\phi(x,t)}$; this approximation turns out to be in excellent agreement with numerics provided the coherent state $\overline{\phi(x,t)}$ describing the mean-field dynamics of the Bose gas is macroscopically populated. We show the adequacy of this approximation by solving the full SGPE Eq. (2) and evaluating the coherent $|\overline{\phi(x,t)}|^2$ and total density $\overline{|\phi(x,t)|^2}$ (cf. with Fig. 2).

For weak dissipation the system is in a linear-response phase and the analytic solution of Eq. (3) reads

$$\overline{\phi(x,t)} = \sqrt{n_0}\,\exp(-im\sigma|x| - i\mu t)\,, \tag{6}$$

(cf. also [64]). After switching on the local noise the system will assume this quasi-stationary state within a spatial region which grows in time with the local speed of sound $c_0 = \sqrt{gn_0/m}$. The density of the condensate in this area is reduced to $n_0 < n$ and the constant phase gradient describes a coherent current

$$j_{\rm coh} = -n_0\sigma\,{\rm sgn}(x)\,, \qquad \text{for} \quad \sigma < \sigma_c\,, \tag{7}$$

flowing towards the point contact. As $j_{\rm coh}$ is proportional to the noise strength σ, the regime is called "linear-response regime". Here the chemical potential is $\mu = gn_0 + m\sigma^2/2$.

Above a critical noise strength [64]

$$\sigma_c = \frac{2}{3}c = \frac{2}{3}\sqrt{2}gn\xi\,, \tag{8}$$

the system crosses over into a Zeno phase [19], where the current ceases to further increase with the strength of the dissipation. The critical point is reached when the velocity of the coherent flow $u_0 = j_{\rm coh}/n_0$ attains the local speed of sound. For $\sigma > \sigma_c$ a grey soliton (a local density depletion of the size of the healing length [59]) forms at the position of the point contact, cf. with Fig. 2b. The density reduction associated with the formation of the grey soliton decreases the scattering rate at the point contact, which results in a reduction of the coherent current, which in turn determines self-consistently the depth of the grey soliton. As a consequence the functional dependence of the coherent current from the noise strenth changes from a linear increase σ to an inverse scaling:

$$j_{\rm coh} = -n_0\frac{c_0^2}{\sigma}\,{\rm sgn}(x)\,, \qquad \text{for} \quad \sigma > \sigma_c\,. \tag{9}$$

This is characteristic of the Zeno phase in extended systems [19]: at strong enough dissipation transport across the dissipative impurity is impeded as a result of the frequent measurement of

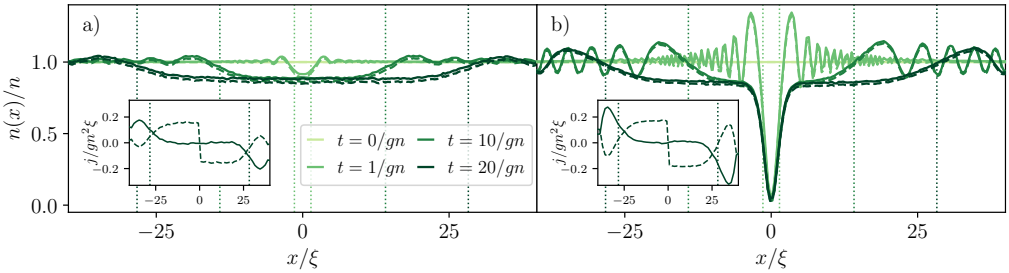

Figure 2: **Snapshots of density close to a static noisy point contact** in a) the linear-response phase $\sigma = 0.2gn\xi$ and b) in the Zeno phase $\sigma = 8gn\xi$. Solid lines are total densities $\overline{|\phi(x,t)|^2}$ while dashed lines are the coherent ones $|\overline{\phi(x,t)}|^2$. The density of incoherent particles is low. The insets show the coherent (dashed) and total (solid) particle current. The point contact scatters particles out of the coherent state, leading to a coherent current towards the noise contact and an incoherent counterflow, which exactly balances the coherent flow. The dotted vertical lines mark the size of the 'sound' cone, moving at the average speed of sound $c = \sqrt{gn/m}$. Colors match the ones of the related density profiles evaluated at the same time.

the observable to which the noise couples at $x = 0$. Outside the depleted area (which travels at the sound speed) the density $n_0 < n$ remains constant.

In contrast to the case of local loss, the noisy potential conserves the total particle number, which at first glance seems at odds with a current of particles flowing towards the point contact, while the particle density remains constant over time. Simulating the dynamics of the total SGPE Eq. (2) one finds, however, that the total current vanishes in the area of constant density, see insets of Fig. 2. This shows that the noisy point contact scatters particles out of the condensate state, causing a coherent inward flow. At the same time it is a source of particles in excited modes of the Bose field leading to an incoherent outward flow of particles. Since these particles are removed from the coherent state, the noise affects the coherent amplitude of the Bose gas similarly to a local loss. This means that a local non-unitary rearrangement of the system generates a coherent superfluid flow. In the next Sections, we harness this mechanism to engineer the coherent transport properties of the Bose gas by using purely incoherent point contacts.

4 Noisy point contact in a moving BEC

In this section we generalize our results to a noisy point contact in an externally imposed coherent current or equivalently to a noisy impurity moving at a constant velocity v relative to the condensate. An important difference with respect to a static point contact is the emergence of a third dynamical phase (which we label 'phase III' in the following), that is characterized by the absence of stationary particle flows at the point contact. This phase occurs in addition to the linear-response I and Zeno phases II. We characterize the phases by evaluating the coherent current on the left and on the right of the noisy point contact; their difference is equal to the change in the number of particles of the coherent fraction of the field and therefore proportional to the scattering rate of particles off the dissipative impurity, cf. Appendix B Since we work in the frame in which the point contact is stationary there appears an additional term

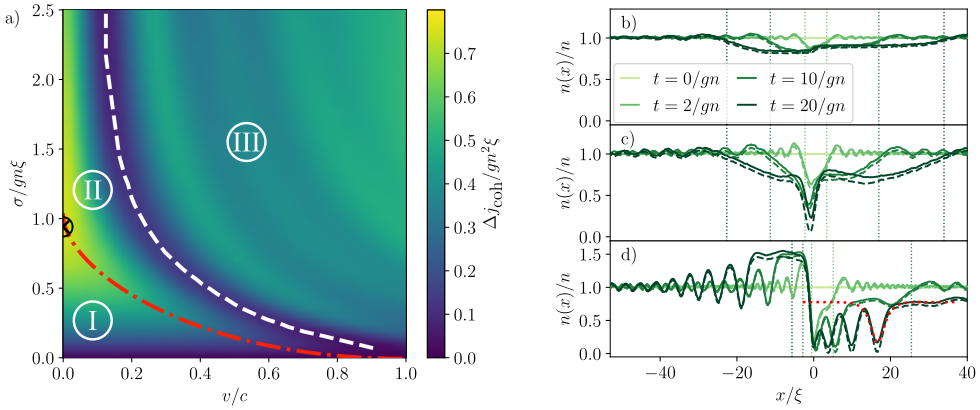

Figure 3: a) **Phase diagram of a noisy point contact** of strength σ in a BEC moving with velocity v. We plot the total coherent current flowing towards the impurity on the left and on the right of the point contact, which equals the scattering rate of the dissipative impurity. We average in space over the interval $x \in \pm[2,5]\xi$ and in time over $t \in [10,20]/gn$, where the intervals are chosen to be within the 'sound' cone, but large enough to average over multiple oscillations in the dynamically unstable phase III. The red line marks the estimated transition between linear response and Zeno regime which agrees well with the local maximum for fixed v, see Appendix C for details. The white dashed line marks the transition form the Zeno to the soliton regime. The analytical result $\sigma_c = 2c/3$ of the transition form normal to Zeno phase at $v = 0$ [64] is shown by the black circle. b)-d) Density close to the noisy point contact at different times. Shown are in b) the normal phase I for $\sigma = 0.2gn\xi$ and $v = 0.2c$, in c) the Zeno phase II for $\sigma = 0.7gn\xi$ and $v = 0.2c$; and in d) the soliton phase III for $\sigma = 2gn\xi$ and $v = 0.8c$. The times marked in color are the same in all three plots. Solid, dashed and dotted lines are chosen as in Fig. 3. The red dotted line in d) is the profile of a grey soliton fitted to the simulated density.

in the expression of $j_{\rm coh}$

$$j_{\rm coh} = \frac{1}{m}\,\mathrm{Im}\big(\bar{\phi}^*\partial_x\bar{\phi}\big) + v\,\bar{\phi}^*\,\bar{\phi}\,. \tag{10}$$

The scattering rate of particles out of the condensate and thus the total coherent current flowing towards the impurity depends both on the velocity v of the point contact and on the noise strength σ as shown in Fig. 3a. We distinguish the three phases, depending on whether this current increases or decreases as the noise strength changes.

4.1 Linear-response regime

Phase I, cf. with Fig. 3b, is akin to the linear-response phase of a static noisy point contact, since the scattering rate increases with increasing dissipation strength, inducing an increasing coherent current flowing towards the noise source. Due to the motion of the condensate relative to the contact, the coherent currents on the left and on the right side are unequal in magnitude. This results also in a different density on the left n_l and on the right n_r of the point contact. Our numerical simulations show that, like in the static case, a quasi-stationary state is established in an area growing over time, but with different velocities $(c_l - v)$ for $x < 0$ and $(c_r + v)$ for $x > 0$. The two halves of the system are characterized by different velocities for two distinct reasons: the speed of sound $c_{l,r} = \sqrt{gn_{l,r}/m}$ is different as a result of density

differences on the two sides of the dissipative impurity, and the velocity v breaks the directional symmetry in the 1D gas.

4.2 Zeno regime

Upon increasing the dissipation strength, the system undergoes a transition into the Zeno phase II (Fig. 3c), however this occurs at a smaller critical value as in the static case. An estimate for the crossover point can be obtained as follows: The transition to the Zeno regime occurs when the local speed of sound $c(x)$ and the velocity of the coherent current u become equal

$$c(x) \equiv \sqrt{\frac{gn(x)}{m}} = u(x) \equiv \frac{j_{\mathrm{coh}}(x)}{n(x)}, \tag{11}$$

at any point in the system. The reduction of the critical noise strength in a moving condensate can then be traced back to two effects. First the coherent current is modified by to the background flow at velocity v. Second the local speed of sound is smaller on one side of the contact when compared to the stationary case, because of the reduced density. The overall coherent current in the system can therefore become supersonic already at a smaller critical dissipation strength. As explained in detail in Appendix C one can derive an approximate expression for the transition point by utilizing Eq. (11). The result is marked by the red line in Fig. 3a and agrees very well with the observed local maximum of the current. As in the static case a grey soliton forms in the Zeno phase II at the position of the point contact and the smaller density leads to a decrease of the scattering rate with increasing dissipation strength. However, due to the motion of the condensate relative to the point contact the coherent current cannot go to zero but must always stays finite, allowing for the onset of a new phase III.

4.3 Soliton-emission regime

The minimum density of the grey soliton close to the point contact would drop to zero for strong dissipation $\sigma \gg gn\xi$ obstructing any particle current at $x = 0$. However, the external flow forces particles to pass the noise contact, which can no longer be facilitated by a grey solition solution if σ increases. This then leads to instabilities and a continuous train of solitons is formed moving in the direction of the external current, see Fig. 3d. The system becomes dynamically unstable, when the external current becomes so large that the condition for the self-consistent formation of a grey soliton can not be fulfilled any more. The minimum density in a stable grey soliton is related to the velocity u of the total coherent current passing it by $n_{\mathrm{min}}/n_0 = u^2/c_0^2$ [59]. A similar effect of a continuous creation of solitons also occurs in the case of a constant repulsive potential in a moving condensate [66]. It happens when the Bose gas density is locally reduced to an extent that a constant coherent current (superfluid flow) cannot be sustained anymore. To verify that the moving density oscillations are indeed soliton trains, we fit the analytic expression for a grey soliton wave function [59] to it, which agrees well with the observed density, see red dotted line in Fig. 3d.

In summary, a moving Bose gas responds to a local noisy impurity like a stationary Bose gas, resulting in a linear response I and a Zeno phase II with renormalized transition points between the phases. The key difference is the formation of a soliton phase III, which only exists in the presence of an external current, preventing the formation of a quasi stationary state close the impurity and a constant current flow. Different from the Zeno regime the "shooting" of solitons leads again to an increase in the time-averaged number of scattered particles with growing dissipation strength.

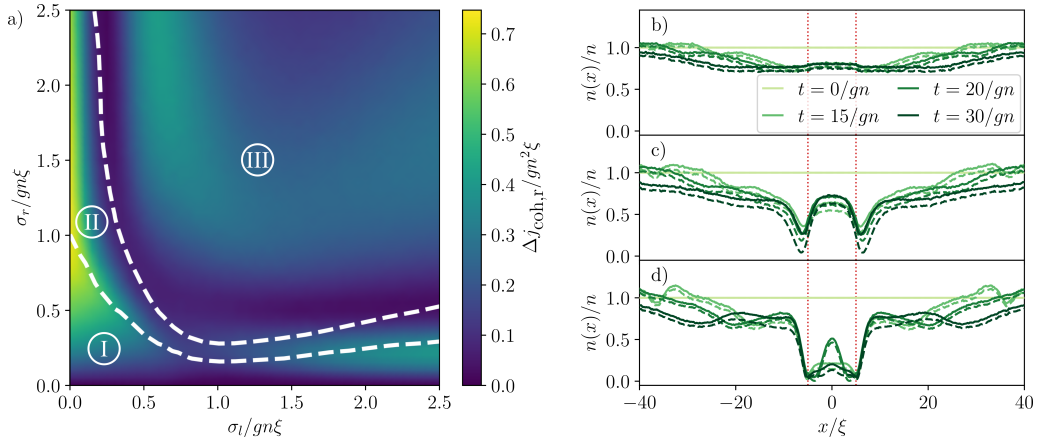

Figure 4: **Phase diagram of a configuration of two noisy point contacts.** a) Scattering rate out of the condensate at the right point contact for impurity separation $r = 10\xi$, plotted for different noise strengths σ_l and σ_r. The current is averaged over time $t \in [25-35]/gn$ and space $x \in [-4.5, 4.5]\xi$; intervals are chosen as in Fig. 3a. The dashed lines mark the border between different phases as in Fig. 3, calculated by assuming a single contact in motion, see main text. b)-d) Density in the vicinity of two dissipative point contacts at distance $r = 10$ at equal dissipation strength $\sigma_r = \sigma_l = \sigma$. Their positions are marked with the red dotted lines. Parameters are chosen for both contacts to be in b) the normal phase $\sigma = 0.2gn\xi$, c) the Zeno phase $\sigma = .5gn\xi$ and d) the soliton phase $\sigma = 2.2gn\xi$. Solid and dashed lines are chosen as in Fig. 3.

5 Controlling superfluid flow with two noisy contacts

In this section we show how superfluid flow can be controlled using a pair of noisy point contacts. Each contact creates a coherent current of particles flowing towards it, which is balanced out by an incoherent one. After a time $t = r/c$, where r is the distance between the contacts, the coherent current created by one reaches the other contact. Each of the two dissipative impurities thus experiences an effective coherent flow generated by the other impurity, and thus can sustain one of the three previously discussed phases. In the following we determine the phase diagram of the wire depending on the noise strength of the left (σ_l) and right (σ_r) noisy contacts. Evaluating the resulting currents in between the contacts we will demonstrate that a segment with two noisy defects at its edges, can act as a current shunt.
We assume the noises $\mathrm{d}W_r$ and $\mathrm{d}W_l$ acting on the left and right impurity to be uncorrelated $\overline{\mathrm{d}W_r\,\mathrm{d}W_l} = 0$, such that the time evolution is determined by the SGPE

$$\begin{aligned}\mathrm{d}\phi(x,t) = -i\Big[-\frac{\partial_x^2}{2m} + g|\phi(x,t)|^2\Big]\phi(x,t)\,\mathrm{d}t - i\,\sqrt{2\sigma_l\,\delta(x+r/2)}\,\phi(x,t)\circ\mathrm{d}W_l \\ - i\,\sqrt{2\sigma_r\,\delta(x-r/2)}\,\phi(x,t)\circ\mathrm{d}W_r\,.\end{aligned} \tag{12}$$

We consider, in the following, a separation of the contacts larger than the healing length $r \gg \xi$; the latter is, in fact, the minimum length over which a coherent current can be established [59], and therefore a necessary requirement to apply the tools developed in the previous Sections. The scattering out of the condensate at the right noisy contact is plotted in Fig. 4a for different noise strengths. For a fixed noise strength of the left contact (σ_l), the number of scattered particles at the right impurity grows upon increasing the noise strength σ_r in the linear-response phase Fig. 4b, and then it shows Zeno physics above a critical value of σ_r, see Fig. 4c. Upon

further increasing the noise strength on the right point contact, the effect of solitons 'shooting' discussed in the previous Section sets in, leading again to an increase of scattered particles when averaged over time; solitons move downstream towards the other point contact resulting in an oscillatory density patter in space and time between them (cf. Fig. 4d). We now show that the critical thresholds for the dissipation strength of two contacts can be approximated using the results for a single moving defect. Let us assume that the left contact is placed into a initially static gas. This then leads to an onset of a coherent current, as discussed in Sec. 3. We determine the velocity of this current by interpolating the results in Fig. 3a at zero velocity ($v = 0$). The right contact is then placed into this background current; we further assume that its presence will not affect the scattering rate at the left impurity and that the system near the right impurity is determined by its own dissipation strength σ_r and the velocity of the coherent background current. Under these assumption we can determine the system response following the lines of Sec 4, and estimate the crossovers in the setup of a pair of noise contacts. These crossover points are marked with the white dashed lines in Fig. 4a and we recognize that they agree well with the observed extrema especially for small values of $\sigma_l/gn\xi$. This shows that only the coherent current is relevant for characterizing the steady state of the system under the noisy drive of the two impurities. For larger values of σ_l the assumption of a constant coherent background current created by the left impurity no longer holds and the scattering rate out of the condensate at the left contact depends also on the noise strength of the right one. This explains the poorer agreement of the numerical results with the above physical picture for larger values of σ_l.

A possible application of the system of two noise contacts is the creation of a coherent current in the space between them. We note that in the proposed scheme the current is controlled directly and not via differences in chemical potentials. In Fig. 5 the coherent current between the contacts, averaged over space and a finite time interval, is plotted as function of the two noise strengths. Note that it is anti-symmetric since the exchange of the two interaction strengths leads to a reversal of the current. For a small sum $\sigma_+ = \sigma_r + \sigma_l \ll gn\xi$ both contacts are in the normal phase and the scattering rate of each contact is independent from the noise strength of the other. The coherent current in between the contacts is therefore the sum of two independent contacts. This is shown in the inset of Fig. 5, were the coherent current is normalized to $gn_0^2\xi_0$, with n_0 being the average density between the contacts, depending weakly on $\sigma_{l,r}$, and $\xi_0 = 1/\sqrt{2gmn_0}$ is the corresponding healing length. For small $\sigma_+ \equiv \sigma_l + \sigma_r$ the normalized current depends only on the difference $\sigma_- = \sigma_r - \sigma_l$ and it is equal to the current created by a single contact at dissipation strength σ_-. For larger σ_+ at least one of the two contacts is not in the linear response phase, which results in a different slope and a non monotonous dependency on σ_-.

6 Experimental implementation and perspectives

In this work we have revisited the Zeno crossover for particle currents traversing a moving noisy defect. We have shown that the speed of the impurity can be used as a knob to boost transport suppression. As a possible experimental implementation we envisage the use of noisy in-situ potentials, to control superfluid flows. Such potentials can be realized with two-color time-dependent optical potentials and tailored conservative potentials. We first note that it is crucial to have a vanishing mean of $V(x)$ for all positions x (see section 2. This is important in order to avoid residual repulsive or attractive potentials, which interfere with the effect of the dephasing. This condition can be fulfilled by using two laser beams, which are red- and blue-detuned with respect to an atomic transition [67]. Both beams have to share the same spatial mode, which can be ensured by guiding them through the same optical fiber. For the defect

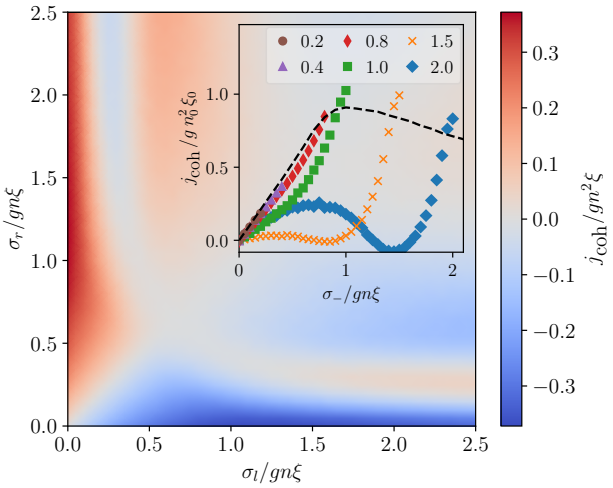

Figure 5: **Coherent current between two noisy impurities** as a function of the individual noise strengths σ_r and σ_l. The current is averaged over time $t \in [25-35]/gn$ and space $x \in [-4.5, 4.5]\xi$. The inset shows the coherent current as a function of the difference σ_- and sum $\sigma_+/gn\xi$ (different colors) of the two noise strengths. The current is rescaled to the density n_0 and the healing $\xi_0 = 1/\sqrt{2gn_0m}$ of the Bose gas inbetween the two contacts. The plot shows that the current does not depend on σ_+, for small $\sigma_+ \leq gn\xi$. The black dashed line is the coherent current created by a single stationary point contact at noise strength σ_-, which agrees well with the two-contacts result at small σ_+.

considered in this work, it is sufficient to use Gaussian beams, which are focues onto the atoms with a high numerical aperture objective. To achieve a defect size, which is smaller than the healing length (as assumed in this work), one has to find a proper combination of numerical aperture (NA=0.4 or higher is necessary for most parameter settings), a short wavelength (higher energy atomic transitions are the better choice as not much optical power is needed to create the necessary potential height) and atomic density and interaction in order to enlarge the healing length. In 1D (as considered here) or 2D configurations, the Rayleigh length should be larger than the thickness of the sample in order to treat the impurity as independent of the perpendicular direction.

Regarding the time dependence of the optical potential, a large bandwidth of the modulation is another necessity. Modulating the intensity with acousto-optical modulators typically results in a bandwidth of more than 1 MHz. This is much faster than any intrinsic timescale (interaction energy, kinetic energy, potential energy, transverse confinement) of a typical experimental setting. The corresponding correlation time of less than 1µs is therefore short enough to provide an effective δ-correlated noise potential. In order to provide white or colored noise in the defect, both laser beams have to be driven with an arbitrary waveform generator, whose temporal signals are either inherently provided by the function generator or are computer generated, providing the required correlation functions. We note that experimentally, it is straightforward to generate much more complex correlation functions for the defect potential, thus bridging noisy defects and Floquet driven defects.

Measurements of the superfluid density in a quantum gas experiment are always challenging since in most schemes it is the total atomic density which is imaged. In the case of 1D systems, heterodyning with a twin system is the method of choice in order to access the motion of the superfluid as well as its amplitude [68]. To this end, one has to prepare a twin

1D system aside with the system under investigation. Upon measuring, one lets both systems interfere with each other and the fringe distance encodes the local velocity of the atoms, while the fringe contrast encodes the amplitude of the superfluid density.

From the theory side, it would be interesting to extend the control of transport properties through the segment in systems without a macroscopic condensate occupation. For instance, studying the effect of two Markovian time-dependent noisy fields coupled to local densities in an interacting fermionic wire. The non-interacting case could be solved exactly as for the single impurity [69], while the RG-scattering theory of Refs. [70] could be used to assess the role of strong quantum fluctuations in enhancing or eradicating the semi-classical effect discussed in this paper. We expect that studying real time dynamics of the problem with bosonization could serve equally well for this purpose. For what concerns the results disussed in our work, we expect that adding quantum fluctuations on top of the macroscopic occupation of the Bose gas, would not significantly alter the dynamics discussed in the paper. On one hand, quantum effects would become sizeable only on times that are parametrically large in the condensate occupation. On the other hand, the region traversed by the density waves produced by the impurity can be regarded effectively as a driven-open systems and therefore subject to decoherence: the energy is pumped into the system via the noisy contact (which is held at infinite temperature) and dissipated by the 'bath' given by the rest of the system which stays at zero temperature, till the heat front will reach it. The dynamics within the 'sound' cone will therefore wash out quantum fluctuations through decoherence as any other open quantum system would. In a semi-classical quantum trajectory description it is in fact impossible to distinguish the noise averaging used to derive the dynamics in our work, from sampling over a probability distribution function given by the quantum fluctuations inherent in the initial state: the trajectories sampled from the classical noise imprinted by the impurity would quickly dephase those arising from quantum fluctuations.

Another interesting direction would consist in generalizing the setup of our work to interacting quantum spin chains in view of applications to spintronics.

Acknowledgements

We thank R. Barnett, J. Jager, S. Kelly and D. Sels for fruitful discussions. M.W., H.O. and M.F. acknowledge financial support by the DFG through SFB/TR 185, Project No.277625399. J. M. acknowledges financial support by the DFG through the grant HADEQUAM-MA7003/3-1. J.M. and M.F acknowledge support from the Dynamics and Topology Centre funded by the State of Rhineland Palatinate. M.W. is supported by the Max Planck Graduate Center with the Johannes Gutenberg-Universität Mainz.

A Derivation of the noise averaged SGPE

In the following we derive the noise average of the SGPE Eq. (12), which can be written as

$$d\phi(x,t) = A[\phi,\phi^*]\,\mathrm{d}t + B[\phi]\circ \mathrm{d}W\,, \tag{13}$$

where

$$\begin{aligned} A[\phi,\phi^*] &= -i\Big[-\frac{\partial_x^2}{2m} - iv\,\partial_x + g|\phi(x,t)|^2\Big]\phi(x,t)\,,\\ B[\phi] &= -i\,V(x)\phi(x,t)\,. \end{aligned} \tag{14}$$

This equation is a Stratonovich stochastic differential equation, where the noise is correlated with $\phi(x,t)$, so that $\overline{B[\phi]\circ \mathrm{d}W} \neq 0$. To evaluate the noise average we transform the

Stratonovich into an Ito equation, where the noise and field are not correlated $\overline{B[\phi]\mathrm{d}W} = 0$, see [60]. The Ito equation is then given by

$$d\phi(x,t) = \Big\{A[\phi,\phi^*] + \frac{1}{2}B[\phi]\frac{\delta}{\delta\phi(x,t)}B[\phi]\Big\}\mathrm{d}t + B[\phi]\mathrm{d}W\,. \tag{15}$$

The noise average results in the Gross-Pitaevskii equation for the coherent state $\overline{\phi(x,t)}$

$$\frac{\mathrm{d}}{\mathrm{d}t}\overline{\phi} = -i\Big[-\frac{\partial_x^2}{2m} - iv\,\partial_x - \frac{i}{2}V(x)^2\Big]\overline{\phi} - i\,g\,\overline{|\phi|^2\phi}\,. \tag{16}$$

The complex potential shows that the local noise scatters particles out of the coherent state $\overline{\phi}$, resulting in the incoherent current flowing away form the noise source.

B Coherent particle number

In this section we show that the jump in the coherent current between the left and right sides of a noise contact is equal to the change in the number of particles of the coherent fraction of the field. We start by deriving a continuity equation for the modulus of the average field $n_{\mathrm{coh}}(x,t) = \overline{\phi}^*\,\overline{\phi}$ from the noise averaged mean-field equation Eq. (16)

$$\partial_t n_{\mathrm{coh}}(x,t) + \partial_x j_{\mathrm{coh}}(x,t) = -2\sigma\,\delta(x)\,n_{\mathrm{coh}}(x,t)\,. \tag{17}$$

Note that since the left hand side of this equation is nonzero $N_{\mathrm{coh}} = \int_{-L/2}^{L/2} dx\, n_{\mathrm{coh}}(x,t)$ is not conserved. The local noise scatters particles out of the coherent state. This is follows from integrating Eq. (17) over the whole system

$$\dot{N}_{\mathrm{coh}} = \int_{-L/2}^{L/2} \mathrm{d}x\,\partial_t\, n_{\mathrm{coh}}(x,t) = -\sigma\, n_{\mathrm{coh}}(0,t)\,, \tag{18}$$

where the current term vanishes because we use periodic boundary conditions. Integrating Eq. (17) again, but over a small interval around the impurity shows

$$\Delta j_{\mathrm{coh}} = \int_{-\epsilon}^{\epsilon} \mathrm{d}x\,\partial_x j_{\mathrm{coh}} = -2\sigma\, n_{\mathrm{coh}}(0,t)\,, \tag{19}$$

where we used that $n_{\mathrm{coh}}(x,t)$ is constant close to the impurity in the long time limit, which we showed by simulating the dynamics of the total SGPE Eq. (2). This yields

$$\dot{N}_{\mathrm{coh}} = \Delta j_{\mathrm{coh}}\,. \tag{20}$$

C Estimate of the transition point between linear response and Zeno regimes

In the following we estimate the linear response to Zeno transition of a noisy point contact in an external driven current of velocity v. We do so by deriving four equations containing the local speeds of sound $c_i = \sqrt{g n_i/m}$ and current velocities $u_i = j_{\mathrm{coh},i}/n_i$ at the left ($i = l$) and right side ($i = r$) of the noise contact, which determine the crossover point.
The system undergoes a transition, once the current velocity is equal to the speed of sound

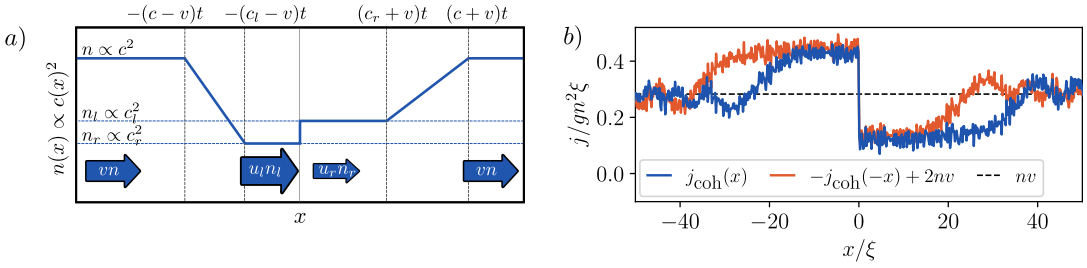

Figure 6: a) Qualitative sketch of the density profile (i.e. local speed of sound) at a dissipative point contact in a constant background current vn, within the linear response regime. The size of the blue arrows indicates the strength of the current at their position. b) Simulation of the coherent current in the linear response regime ($\sigma = 0.2gn\xi$, $v = 0.2c$ and $t = 20/gn$). The two lines agree close to the contact, since it induces equally strong currents on both sides.

$c_i = |u_i|$ on either of the two sides of the contact. For $v > 0$ the simulation show $c_l < c_r$ and $|u_l| > |u_r|$, see Fig. 6, causing the critical condition to be fulfilled first on the left side

$$c_l = u_l\,, \tag{21}$$

which is the first equation we use. We determine the other three by analyzing the system in the linear response regime and assuming that the conditions are still valid at the critical point. Since the state in the depleted area is quasi stationary, the chemical potential

$$\mu = gn_i + \frac{1}{2}mu_i^2 - \frac{1}{2}mv^2\,, \tag{22}$$

on both sides of the contact must be equal, from which the second equation is derived

$$c_l^2 + \frac{1}{2}u_l^2 = c_r^2 + \frac{1}{2}u_r^2\,. \tag{23}$$

For the third equation we utilize the numerical evidence, that the contact induces equally strong currents on both sides, which is either added to or subtracted form the background current vn, see Fig. 6b. This symmetry can be written as

$$j_{\mathrm{coh},r} + j_{\mathrm{coh},l} = 2vn \;\Rightarrow\; c_l^2 u_l + c_r^2 u_r = 2vc^2\,. \tag{24}$$

At last we derive an equation for the difference of the currents, which is equal to the change in the number of particles of the coherent fraction of the field $\dot{N}_{\mathrm{coh}}$, see Eq. (20). We assume that these particles are only removed from the "transition area" in between the quasi stationary state at density n_i and the unperturbed area at density n. To estimate it we approximate the density profile as being linear, as illustrated in Fig. 6a. This results in

$$\dot{N}_{\mathrm{coh}} = -\frac{1}{2}(n-n_l)(c_l+c-2v) - \frac{1}{2}(n-n_r)(c_r+c+2v)\,. \tag{25}$$

The fourth equation is then given by

$$2c_l^2 u_l - 2c_r^2 u_r \;=\; (c^2-c_l^2)(c_l+c-2v) + (c^2-c_r^2)(c_r+c+2v)\,. \tag{26}$$

To determine the critical values we solve Eqs. (21), (23), (24) and (26) numerically and in order to calculate the corresponding critical noise strength σ_c we use Eq. (19), with the approximation $n_{\mathrm{coh}}(0,t) = (n_r+n_l)/2$. This eventually yields

$$\sigma_c = \frac{c_l^2 u_l - c_r^2 u_r}{c_l^2 + c_r^2}\,. \tag{27}$$

The critical dissipation strength derived in this way agrees very well with the local maximum in the coherent current, which we calculated numerically, see Fig. 3a. In the stationary case ($v = 0$) we get $\sigma_c = 0.74c$, which is only slightly larger as the exact value $\sigma_c = 2c/3$ [64].

References

[1] C. W. J. Beenakker and H. van Houten, *Quantum transport in semiconductor nanostructures*, Solid State Phys. **4**, 1 (1991), doi:10.1016/S0081-1947(08)60091-0.

[2] S. Datta, *Electronic transport in mesoscopic systems*, Cambridge University Press, UK, ISBN 9780521416047 (1995), doi:10.1017/CBO9780511805776.

[3] Y. V. Nazarov and Y. M. Blanter, *Quantum transport*, Cambridge University Press, UK, ISBN 9780521832465 (2009), doi:10.1017/CBO9780511626906.

[4] C.-C. Chien, S. Peotta and M. Di Ventra, *Quantum transport in ultracold atoms*, Nat. Phys. **11**, 998 (2015), doi:10.1038/nphys3531.

[5] B. T. Seaman, M. Krämer, D. Z. Anderson and M. J. Holland, *Atomtronics: Ultracold-atom analogs of electronic devices*, Phys. Rev. A **75**, 023615 (2007), doi:10.1103/PhysRevA.75.023615.

[6] R. A. Pepino, J. Cooper, D. Z. Anderson and M. J. Holland, *Atomtronic circuits of diodes and transistors*, Phys. Rev. Lett. **103**, 140405 (2009), doi:10.1103/PhysRevLett.103.140405.

[7] M. B. Dahan, E. Peik, J. Reichel, Y. Castin and C. Salomon, *Bloch oscillations of atoms in an optical potential*, Phys. Rev. Lett. **76**, 4508 (1996), doi:10.1103/PhysRevLett.76.4508.

[8] O. Morsch, J. H. Müller, M. Cristiani, D. Ciampini and E. Arimondo, *Bloch oscillations and mean-field effects of Bose-Einstein condensates in 1D optical lattices*, Phys. Rev. Lett. **87**, 140402 (2001), doi:10.1103/PhysRevLett.87.140402.

[9] J.-P. Brantut, J. Meineke, D. Stadler, S. Krinner and T. Esslinger, *Conduction of ultracold Fermions through a mesoscopic channel*, Science **337**, 1069 (2012), doi:10.1126/science.1223175.

[10] S. Krinner, D. Stadler, D. Husmann, J.-P. Brantut and T. Esslinger, *Observation of quantized conductance in neutral matter*, Nature **517**, 64 (2014), doi:10.1038/nature14049.

[11] M. Lebrat, S. Häusler, P. Fabritius, D. Husmann, L. Corman and T. Esslinger, *Quantized conductance through a spin-selective atomic point contact*, Phys. Rev. Lett. **123**, 193605 (2019), doi:10.1103/PhysRevLett.123.193605.

[12] R. Onofrio, C. Raman, J. M. Vogels, J. R. Abo-Shaeer, A. P. Chikkatur and W. Ketterle, *Observation of superfluid flow in a Bose-Einstein condensed gas*, Phys. Rev. Lett. **85**, 2228 (2000), doi:10.1103/PhysRevLett.85.2228.

[13] R. Desbuquois, L. Chomaz, T. Yefsah, J. Léonard, J. Beugnon, C. Weitenberg and J. Dalibard, *Superfluid behaviour of a two-dimensional Bose gas*, Nat. Phys. **8**, 645 (2012), doi:10.1038/nphys2378.

[14] C. Ryu, M. Andersen, P. Cladé, V. Natarajan, K. Helmerson and W. Phillips, *Observation of persistent flow of a Bose-Einstein condensate in a toroidal trap*, Phys. Rev. Lett. **99**, 260401 (2007), doi:10.1103/PhysRevLett.99.260401.

[15] A. Ramanathan, K. C. Wright, S. R. Muniz, M. Zelan, W. T. Hill, C. J. Lobb, K. Helmerson, W. D. Phillips and G. K. Campbell, *Superflow in a toroidal Bose-Einstein condensate: An atom circuit with a tunable weak link*, Phys. Rev. Lett. **106**, 130401 (2011), doi:10.1103/PhysRevLett.106.130401.

[16] S. Levy, E. Lahoud, I. Shomroni and J. Steinhauer, *The a.c. and d.c. Josephson effects in a Bose-Einstein condensate*, Nature **449**, 579 (2007), doi:10.1038/nature06186.

[17] C. Ryu, P. W. Blackburn, A. A. Blinova and M. G. Boshier, *Experimental realization of Josephson junctions for an atom SQUID*, Phys. Rev. Lett. **111**, 205301 (2013), doi:10.1103/PhysRevLett.111.205301.

[18] J.-P. Brantut, C. Grenier, J. Meineke, D. Stadler, S. Krinner, C. Kollath, T. Esslinger and A. Georges, *A thermoelectric heat engine with ultracold atoms*, Science **342**, 713 (2013), doi:10.1126/science.1242308.

[19] B. Misra and E. C. G. Sudarshan, *The Zeno's paradox in quantum theory*, J. Math. Phys. **18**, 756 (1977), doi:10.1063/1.523304.

[20] Q. Bouton, J. Nettersheim, D. Adam, F. Schmidt, D. Mayer, T. Lausch, E. Tiemann and A. Widera, *Single-atom quantum probes for ultracold gases boosted by nonequilibrium spin dynamics*, Phys. Rev. X **10**, 011018 (2020), doi:10.1103/PhysRevX.10.011018.

[21] C. Weber, S. John, N. Spethmann, D. Meschede and A. Widera, *Single Cs atoms as collisional probes in a large Rb magneto-optical trap*, Phys. Rev. A **82**, 042722 (2010), doi:10.1103/PhysRevA.82.042722.

[22] M. Hohmann, F. Kindermann, T. Lausch, D. Mayer, F. Schmidt and A. Widera, *Single-atom thermometer for ultracold gases*, Phys. Rev. A **93**, 043607 (2016), doi:10.1103/PhysRevA.93.043607.

[23] V. Alba, *Unbounded entanglement production via a dissipative impurity*, SciPost Phys. **12**, 011 (2022), doi:10.21468/SciPostPhys.12.1.011.

[24] P. W. Anderson, *Infrared catastrophe in Fermi gases with local scattering potentials*, Phys. Rev. Lett. **18**, 1049 (1967), doi:10.1103/PhysRevLett.18.1049.

[25] R. Schmidt, M. Knap, D. A. Ivanov, J.-S. You, M. Cetina and E. Demler, *Universal many-body response of heavy impurities coupled to a Fermi sea: A review of recent progress*, Rep. Prog. Phys. **81**, 024401 (2018), doi:10.1088/1361-6633/aa9593.

[26] L. Landau, *Über die Bewegung der Elektronen in Kristalgitter*, Phys. Z. Sowjetunion **3**, 644 (1933).

[27] S. I. Pekar, *Effective mass of a polaron*, Zh. Eksp. Teor. Fiz. **16**, 335 (1946).

[28] A. Schirotzek, C.-H. Wu, A. Sommer and M. W. Zwierlein, *Observation of Fermi polarons in a tunable Fermi liquid of ultracold atoms*, Phys. Rev. Lett. **102**, 230402 (2009), doi:10.1103/PhysRevLett.102.230402.

[29] J. Jager, R. Barnett, M. Will and M. Fleischhauer, *Strong-coupling Bose polarons in one dimension: Condensate deformation and modified Bogoliubov phonons*, Phys. Rev. Res. **2**, 033142 (2020), doi:10.1103/PhysRevResearch.2.033142.

[30] C. Kohstall, M. Zaccanti, M. Jag, A. Trenkwalder, P. Massignan, G. M. Bruun, F. Schreck and R. Grimm, *Metastability and coherence of repulsive polarons in a strongly interacting Fermi mixture*, Nature **485**, 615 (2012), doi:10.1038/nature11065.

[31] J. Catani, G. Lamporesi, D. Naik, M. Gring, M. Inguscio, F. Minardi, A. Kantian and T. Giamarchi, *Quantum dynamics of impurities in a one-dimensional Bose gas*, Phys. Rev. A **85**, 023623 (2012), doi:10.1103/PhysRevA.85.023623.

[32] M.-G. Hu, M. J. Van de Graaff, D. Kedar, J. P. Corson, E. A. Cornell and D. S. Jin, *Bose polarons in the strongly interacting regime*, Phys. Rev. Lett. **117**, 055301 (2016), doi:10.1103/PhysRevLett.117.055301.

[33] N. B. Jørgensen, L. Wacker, K. T. Skalmstang, M. M. Parish, J. Levinsen, R. S. Christensen, G. M. Bruun and J. J. Arlt, *Observation of attractive and repulsive polarons in a Bose-Einstein condensate*, Phys. Rev. Lett. **117**, 055302 (2016), doi:10.1103/PhysRevLett.117.055302.

[34] F. Scazza et al., *Repulsive Fermi polarons in a resonant mixture of ultracold* ^{6}Li *atoms*, Phys. Rev. Lett. **118**, 083602 (2017), doi:10.1103/PhysRevLett.118.083602.

[35] T. Müller, M. Gievers, H. Fröml, S. Diehl and A. Chiocchetta, *Shape effects of localized losses in quantum wires: Dissipative resonances and nonequilibrium universality*, Phys. Rev. B **104**, 155431 (2021), doi:10.1103/PhysRevB.104.155431.

[36] T. Wasak, R. Schmidt and F. Piazza, *Quantum-Zeno Fermi polaron in the strong dissipation limit*, Phys. Rev. Res. **3**, 013086 (2021), doi:10.1103/PhysRevResearch.3.013086.

[37] F. Tonielli, N. Chakraborty, F. Grusdt and J. Marino, *Ramsey interferometry of non-Hermitian quantum impurities*, Phys. Rev. Res. **2**, 032003 (2020), doi:10.1103/PhysRevResearch.2.032003.

[38] P. L. Krapivsky, K. Mallick and D. Sels, *Free bosons with a localized source*, J. Stat. Mech.: Theory Exp. 063101 (2020), doi:10.1088/1742-5468/ab8118.

[39] D. A. Zezyulin and V. V. Konotop, *Perfectly absorbed and emitted currents by complex potentials in nonlinear media*, Phys. Rev. A **104**, 053527 (2021), doi:10.1103/PhysRevA.104.053527.

[40] P. Barmettler and C. Kollath, *Controllable manipulation and detection of local densities and bipartite entanglement in a quantum gas by a dissipative defect*, Phys. Rev. A **84**, 041606 (2011), doi:10.1103/PhysRevA.84.041606.

[41] W. Berdanier, J. Marino and E. Altman, *Universal dynamics of stochastically driven quantum impurities*, Phys. Rev. Lett. **123**, 230604 (2019), doi:10.1103/PhysRevLett.123.230604.

[42] K. Seetharam, Y. Shchadilova, F. Grusdt, M. B. Zvonarev and E. Demler, *Dynamical quantum Cherenkov transition of fast impurities in quantum liquids*, Phys. Rev. Lett. **127**, 185302 (2021), doi:10.1103/PhysRevLett.127.185302.

[43] H. Fröml, A. Chiocchetta, C. Kollath and S. Diehl, *Fluctuation-induced quantum zeno effect*, Phys. Rev. Lett. **122**, 040402 (2019), doi:10.1103/PhysRevLett.122.040402.

[44] L. Corman, P. Fabritius, S. Häusler, J. Mohan, L. H. Dogra, D. Husmann, M. Lebrat and T. Esslinger, *Quantized conductance through a dissipative atomic point contact*, Phys. Rev. A **100**, 053605 (2019), doi:10.1103/PhysRevA.100.053605.

[45] T. Yoshimura, K. Bidzhiev and H. Saleur, *Non-Hermitian quantum impurity systems in and out of equilibrium: Noninteracting case*, Phys. Rev. B **102**, 125124 (2020), doi:10.1103/PhysRevB.102.125124.

[46] M. Schiro and O. Scarlatella, *Quantum impurity models coupled to Markovian and non-Markovian baths*, J. Chem. Phys. **151**, 044102 (2019), doi:10.1063/1.5100157.

[47] V. Alba and F. Carollo, *Noninteracting fermionic systems with localized losses: Exact results in the hydrodynamic limit*, Phys. Rev. B **105**, 054303 (2022), doi:10.1103/PhysRevB.105.054303.

[48] F. Tarantelli and E. Vicari, *Quantum critical systems with dissipative boundaries*, Phys. Rev. B **104**, 075140 (2021), doi:10.1103/PhysRevB.104.075140.

[49] A. P. Chaudhari, S. P. Kelly, R. J. V. Tortora and J. Marino, *Zeno crossovers in the entanglement speed of spin chains with noisy impurities*, J. Stat. Mech.: Theory Exp. 103101 (2022), doi:10.1088/1742-5468/ac8e5d.

[50] A. Khedri, A. Štrkalj, A. Chiocchetta and O. Zilberberg, *Luttinger liquid coupled to Ohmic-class environments*, Phys. Rev. Res. **3**, L032013 (2021), doi:10.1103/PhysRevResearch.3.L032013.

[51] V. Alba and F. Carollo, *Noninteracting fermionic systems with localized losses: Exact results in the hydrodynamic limit*, Phys. Rev. B **105**, 054303 (2022), doi:10.1103/PhysRevB.105.054303.

[52] U. Javed, J. Marino, V. Oganesyan and M. Kolodrubetz, *Counting edge modes via dynamics of boundary spin impurities*, (arXiv preprint) doi:10.48550/arXiv.2111.11428.

[53] A.-M. Visuri, T. Giamarchi and C. Kollath, *Symmetry-protected transport through a lattice with a local particle loss*, Phys. Rev. Lett. **129**, 056802 (2022), doi:10.1103/PhysRevLett.129.056802.

[54] V. A. Brazhnyi, V. V. Konotop, V. M. Pérez-García and H. Ott, *Dissipation-induced coherent structures in Bose-Einstein condensates*, Phys. Rev. Lett. **102**, 144101 (2009), doi:10.1103/PhysRevLett.102.144101.

[55] G. Barontini, R. Labouvie, F. Stubenrauch, A. Vogler, V. Guarrera and H. Ott, *Controlling the dynamics of an open many-body quantum system with localized dissipation*, Phys. Rev. Lett. **110**, 035302 (2013), doi:10.1103/PhysRevLett.110.035302.

[56] C. Baals, A. Gil Moreno, J. Jiang, J. Benary and H. Ott, *Stability analysis and attractor dynamics of three-dimensional dark solitons with localized dissipation*, Phys. Rev. A **103**, 043304 (2021), doi:10.1103/PhysRevA.103.043304.

[57] R. Labouvie, B. Santra, S. Heun and H. Ott, *Bistability in a driven-dissipative superfluid*, Phys. Rev. Lett. **116**, 235302 (2016), doi:10.1103/PhysRevLett.116.235302.

[58] C. Mink, A. Pelster, J. Benary, H. Ott and M. Fleischhauer, *Variational truncated Wigner approximation for weakly interacting Bose fields: Dynamics of coupled condensates*, SciPost Phys. **12**, 051 (2022), doi:10.21468/SciPostPhys.12.2.051.

[59] C. J. Pethick and H. Smith, *Bose-Einstein condensation in dilute gases*, Cambridge University Press, UK, ISBN 9780521846516 (2008), doi:10.1017/CBO9780511802850.

[60] C. Gardiner, *Handbook of stochastic methods for physics, chemistry, and the natural sciences*, Springer, Berlin, Germany, ISBN 9780387156071 (1985).

[61] H. T. C. Stoof and M. J. Bijlsma, *Dynamics of fluctuating Bose-Einstein condensates*, J. Low Temp. Phys. **124**, 431 (2001), doi:10.1023/A:1017519118408.

[62] S. P. Cockburn and N. P. Proukakis, *The stochastic Gross-Pitaevskii equation and some applications*, Laser Phys. **19**, 558 (2009), doi:10.1134/S1054660X09040057.

[63] C. W. Gardiner and M. J. Davis, *The stochastic Gross-Pitaevskii equation: II*, J. Phys. B: At. Mol. Opt. Phys. **36**, 4731 (2003), doi:10.1088/0953-4075/36/23/010.

[64] D. Sels and E. Demler, *Thermal radiation and dissipative phase transition in a BEC with local loss*, Ann. Phys. **412**, 168021 (2020), doi:10.1016/j.aop.2019.168021.

[65] D. A. Zezyulin, V. V. Konotop, G. Barontini and H. Ott, *Macroscopic Zeno effect and stationary flows in nonlinear waveguides with localized dissipation*, Phys. Rev. Lett. **109**, 020405 (2012), doi:10.1103/PhysRevLett.109.020405.

[66] V. Hakim, *Nonlinear Schrödinger flow past an obstacle in one dimension*, Phys. Rev. E **55**, 2835 (1997), doi:10.1103/PhysRevE.55.2835.

[67] J. Jiang, E. Bernhart, M. Röhrle, J. Benary, M. Beck, C. Baals and H. Ott, *A Kapitza pendulum for ultracold atoms*, (arXiv preprint) doi:10.48550/arXiv.2112.10954.

[68] S. Hofferberth, I. Lesanovsky, B. Fischer, T. Schumm and J. Schmiedmayer, *Non-equilibrium coherence dynamics in one-dimensional Bose gases*, Nature **449**, 324 (2007), doi:10.1038/nature06149.

[69] P. E. Dolgirev, J. Marino, D. Sels and E. Demler, *Non-Gaussian correlations imprinted by local dephasing in fermionic wires*, Phys. Rev. B **102**, 100301 (2020), doi:10.1103/PhysRevB.102.100301.

[70] H. Fröml, C. Muckel, C. Kollath, A. Chiocchetta and S. Diehl, *Ultracold quantum wires with localized losses: Many-body quantum Zeno effect*, Phys. Rev. B **101**, 144301 (2020), doi:10.1103/PhysRevB.101.144301.

5 Dynamics of polaron formation in 1D Bose gases in the strong-coupling regime

Martin Will and Michael Fleischhauer
New J. Phys. **25**, 083043 (2023).

In this publication, we extended the methodology used to investigate the ground state polaron properties in Chapter 2 [P1] to explore the system's dynamical properties. This is accomplished through simulations of the generalized GPE (1.24).

Before doing this, we extend the analytical expression for the stationary polaron state to encompass an arbitrary total momentum p. The system is stable only if the polaron velocity v is below a critical value, which depends on the impurity-Bose coupling constant. In the case of a weak coupling $g_{\mathrm{IB}} \ll gn\tilde{\xi}$, the critical velocity agrees with the Landau criterion and equals the speed of sound $\tilde{c} = \sqrt{gn/\tilde{m}}$. Here, $\tilde{\xi} = 1/\sqrt{2gn\tilde{m}}$ is the rescaled healing length, and $\tilde{m}$ is the reduced mass. Nevertheless, when the impurity interacts strongly with the Bose gas, it induces significant deformations in the condensate, resulting in a monotonic decrease in the critical velocity with g_{IB}. Furthermore, we demonstrate that the polaron's energy and velocity v exhibit periodic dependencies on the momentum p, with a period length of $2\pi n$. This includes regions where the signs of v and p differ.

Next, we investigate the time evolution following either an adiabatic turn-on or a sudden quench of the impurity-boson coupling constant. We observe that the impurity is decelerated until its velocity is at least below the critical value, illustrated in Figure 5.1. Yet the specific mechanism governing this deceleration varies, giving rise to various dynamical regimes. In the scenario of a quasi-adiabatic increase in the coupling constant, impurities with velocities exceeding the critical value undergo a non-reversible slowdown due to the emission of density waves. Otherwise, impurities with velocities below this threshold experience reversible deceleration due to the increasing effective mass during the polaron formation. This is depicted in Figure 5.1a), where the coupling constant is gradually ramped up and then down again. Initially, the impurity slows down as the coupling increases and subsequently accelerates as the coupling is reduced. However, the impurity can only return to its initial velocity if it is always sub-critical. In the case of a sudden quench of the coupling constant, as depicted in Figure 5.1b), we observe a rather unusual motion of the impurity for heavy impurity masses. This includes oscillations of its velocity and even instances of backscattering before stabilizing at a finite velocity. These peculiar effects cannot be solely attributed to the frictional force resulting from density waves or the increase in the polaron mass. Instead, we find this to result from the emission of solitons.

The dynamical polaron properties were also studied using the Fröhlich model [35–44]. It includes the deceleration caused by the increase in polaron mass as a dressing of the impurity by Bogoliubov phonons. The friction force, generated in the MF model by density waves, arises in the Fröhlich model from the emission of Cherenkov radiation of phonons. It is worth noting that the deformed MF model minimizes the emission of (deformed) phonons, so unlike the Fröhlich model, it is a good approximation to neglect them in our model. Because of the

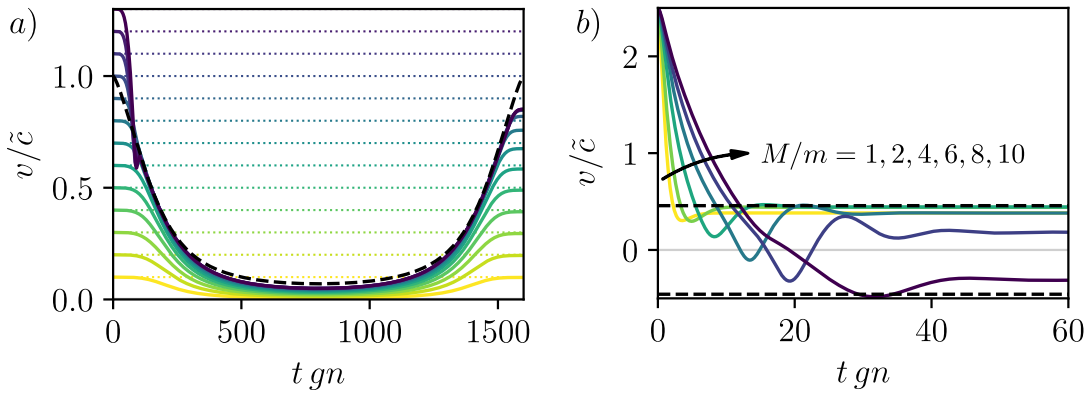

Figure 5.1: a) Time evolution of the impurity velocity when the impurity coupling constant is quasi-adiabatically switched on and off again for different initial velocities. The mass ratio $M = 3m$ and Tonks parameter $\gamma = 0.1$ are constant, but the impurity-boson coupling strength is time dependent $g_{\mathrm{IB}}(t) = 10gn\tilde{\xi}\,\sin^2(\pi\, t\, gn/1600)$. The black dashed line marks the instantaneous critical velocity, and the dotted lines mark the initial velocities. b) Impurity velocity after a quench of the coupling constant to $g_{\mathrm{IB}} = gn\tilde{\xi}$ for different mass ratios and with the Tonks parameter $\gamma = 0.1$. The absolute value of the final velocity is always subcritical (dashed lines represent $\pm$ of the critical velocity).

higher phonon density, the Fröhlich model leads to incorrect results when the condensate is substantially deformed. Especially the effects arising from the emission of solitons are beyond the scope of the Fröhlich model.
Lastly, we investigate the impact of quantum fluctuations on the motion of the impurity to assess the validity of the MF approximation using a Truncated Wigner simulation [108–110]. This approach fully accounts for the influence of (deformed) Bogoliubov phonons in the condensate, similar to the model used in Chapter 2 [P1]. However, the absence of a true BEC in homogenous 1D systems, as stated by the Mermin-Wagner-Hohenberg theorem [92, 93], leads to infrared divergences in the lowest-order quantum fluctuations. We consider a gas trapped within a harmonic potential to avoid these divergences. This adds complexity to the theory, as the LLP transformation no longer decouples the center-of-mass motion. Nevertheless, when the impurity is also trapped, the center-of-mass momentum follows a simple equation of motion.

Author contributions

In this study, I analytically extended the stationary solutions from Chapter 2 to arbitrarily large total momenta. Additionally, I conducted numerical simulations to explore the system's dynamical properties using a similar approach as described in Chapter 4 [P3]. The detailed methodology for these simulations can be found in Appendix B. Furthermore, I extended the MF approximation within the LLP frame, initially discussed for a homogeneous system in Section 1.3, to encompass a harmonically trapped gas incorporating quantum fluctuations. Michael Fleischhauer supervised the project and was engaged in discussions with me about the obtained results. Both authors contributed to the preparation of the manuscript and participated in the review process.

Copyright

IOP Publishing New J. Phys. 25 (2023) 083043 https://doi.org/10.1088/1367-2630/acf06a

New Journal of Physics
The open access journal at the forefront of physics

Deutsche Physikalische Gesellschaft DPG
IOP Institute of Physics

Published in partnership with: Deutsche Physikalische Gesellschaft and the Institute of Physics

OPEN ACCESS

RECEIVED
9 May 2023

REVISED
31 July 2023

ACCEPTED FOR PUBLICATION
15 August 2023

PUBLISHED
29 August 2023

PAPER

Dynamics of polaron formation in 1D Bose gases in the strong-coupling regime

Martin Will and Michael Fleischhauer*

Department of Physics and Research Center OPTIMAS, University of Kaiserslautern-Landau, 67663 Kaiserslautern, Germany
* Author to whom any correspondence should be addressed.

E-mail: mfleisch@rhrk.uni-kl.de

Keywords: Bose polaron formation, mobile impurity, truncated Wigner, nonlinear dynamics, one-dimensional Bose gas

Abstract

We discuss the dynamics of the formation of a Bose polaron when an impurity is injected into a weakly interacting one-dimensional Bose condensate. While for small impurity-boson couplings this process can be described within the Froehlich model as generation, emission and binding of Bogoliubov phonons, this is no longer adequate if the coupling becomes strong. To treat this regime we consider a mean-field approach beyond the Froehlich model which accounts for the backaction to the condensate, complemented with Truncated Wigner simulations to include quantum fluctuation. For the stationary polaron we find a periodic energy-momentum relation and non-monotonous relation between impurity velocity and polaron momentum including regions of negative impurity velocity. Studying the polaron formation after turning on the impurity-boson coupling quasi-adiabatically and in a sudden quench, we find a very rich scenario of dynamical regimes. Due to the build-up of an effective mass, the impurity is slowed down even if its initial velocity is below the Landau critical value. For larger initial velocities we find deceleration and even backscattering caused by emission of density waves or grey solitons and subsequent formation of stationary polaron states in different momentum sectors. In order to analyze the effect of quantum fluctuations we consider a trapped condensate to avoid 1D infrared divergencies. Using Truncated Wigner simulations in this case we show under what conditions the influence of quantum fluctuations is small.

1. Introduction

The dynamics of a quantum impurity coupled to an interacting many-body environment is one of the most fundamental problems of many-body physics. Of particular interest is the dressing of the impurity with elementary excitations of the host systems leading to the formation of a quasiparticle. A paradigmatic model of such a quasiparticle in condensed matter physics is the polaron, introduced by Landau and Pekar [1, 2] to describe the interaction of an electron with lattice vibrations in a solid, and which is key for understanding transport, response and induced interactions in many systems. In recent years ultra-cold quantum gases have become a versatile experimental testing ground for studying polaron physics with high precision and in novel regimes. For example, employing Feshbach resonances [3] for neutral atoms, the impurity-bath interaction can be tuned from weak to strong coupling. Furthermore many-body environments of different quantum statistics and with different interactions can be considered. While impurities in a degenerate Fermi gas, called Fermi-polarons, have been studied in a number of experiments only a small number of experiments exist on Bose polarons [4–7]. Here due to the large compressibility of the Bose gas a larger amount of excitations can be created by the impurity and interactions among the environment particles become increasingly important.

While much theoretical work exists addressing the ground state properties of Bose polarons [8–16] there is still little understanding of finite temperature properties [7, 17–19] and even more so of its

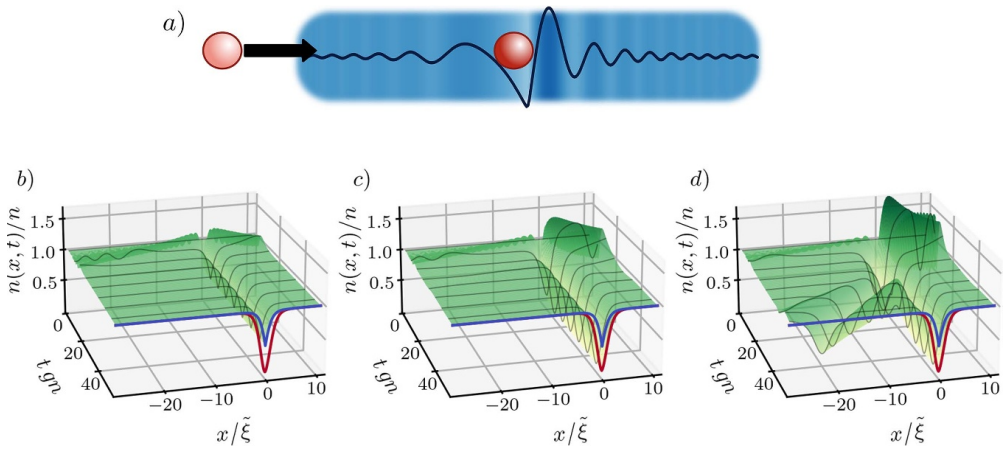

Figure 1. Formation of a polaron when an impurity is injected into a weakly interacting Bose gas (a). (b)–(d) Evolution of the Bose gas density $n(x,t)$ for different total momenta ($p/M\tilde{c} = 0.3, 1.0, 1.6$), where M is the impurity mass, n the average boson density, $\tilde{c}$ the speed of sound and $\tilde{\xi}$ the healing length (see text). The impurity emits density waves before converging into on of two stationary states, marked in red and blue. For large momenta (d) also solitons are created which can lead to a change in the direction of motion of the impurity. The evolution is shown for an impurity-Bose mass ratio $M = 10$ m, Tonks parameter $\gamma = 0.1$ and impurity-Bose coupling constant $g_{IB} = gn\tilde{\xi}$.

non-equilibrium dynamics [4, 20–23]. What happens when an impurity is injected into a weakly interacting Bose condensate? What is the dynamics of the formation of a polaron and under what conditions and on what time scales can a stable quasiparticle form at all? We will address these questions in the present paper considering a point impurity interacting with a weakly interacting, one-dimensional Bose condensate in the full range of impurity-boson coupling strength, see figure 1. The limit of weak impurity-boson interaction can be well described by the generation and subsequent binding or emission of Bogoliubov phonons from the impurity [24] in terms of a Hamiltonian similar to that of the Froehlich model used in solid state systems [25]. Most existing studies of the non-equilibrium dynamics of Bose polarons is based on this model [8, 26–31]. It is however no longer well suited in the limit of strong impurity-boson coupling and thus we here follow a different approach. Starting from a full quantum description of the interaction of a mobile impurity with the condensate we employ a mean-field approach that takes the backaction of the impurity onto the condensate into account as in [32–34], but keeps the entanglement between impurity and BEC by working in a co-moving frame. This approach was shown to be very accurate for the prediction of ground state properties of Bose-polarons [35] and bi-polarons [36] even for very strong impurity-boson couplings as long as the Bose–Bose interaction is weak. Quantum effects are then taken into account by considering Bogoliubov excitations on top of the deformed condensate, which are here treated within a Truncated Wigner approximation [37–39]. The advantage of this approach as compared to the Froelich model and its extensions [12, 14, 28] is the substantially reduced number of deformed Bogoliubov phonons created by the impurity in such a description. As we will show the effect of these modified phonons can be neglected even in the non-equilibrium dynamics in many situations allowing for a comprehensive study of the polaron dynamics in terms of non-linear c-number differential equations.

2. Energy-momentum relation in a homogeneous 1D Bose gas

Before considering the time evolution of an impurity injected into a 1D Bose gas of neutral atoms, let us discuss the stationary properties of a polaron at finite momentum relative to the Bose gas. A widely used approach to describe Bose-polarons for weak boson-boson and impurity-boson couplings is to consider the interaction of the impurity with Bogoliubov excitations of the unperturbed condensate. The resulting model is reminiscent of the Froehlich model in condensed matter physics. Due to the large compressibility of the Bose condensate, this model is however no longer adequate if the impurity-boson coupling becomes large. In the latter case a growing number of phonons is generated at the location of the impurity and boson-boson interactions become relevant. For this reason we here start from the full quantum model and apply a different approximation scheme.

2.1. Model and modified mean-field approach

A single mobile impurity coupled to a Bose gas in a homogeneous one-dimensional system is described by the Hamiltonian

$$\hat{H} = \frac{\hat{p}^2}{2M} + \int \mathrm{d}x \hat{\phi}^\dagger(x) \left[-\frac{\partial_x^2}{2m} + \frac{1}{2} g \hat{\phi}^\dagger(x)\hat{\phi}(x) + g_{\mathrm{IB}} \delta(x - \hat{r}) \right] \hat{\phi}(x), \tag{1}$$

for $\hbar = 1$. Here m (M) is the boson (impurity) mass, g_{IB} (g) the impurity-Bose (Bose–Bose) interaction constant, $\hat{\phi}(x)$ the bosonic field operator and $\hat{r}$ ($\hat{p}$) the impurity position (momentum) operator. In the following we consider the case of repulsive coupling between all particles, i.e. $g, g_{\mathrm{IB}} > 0$.

Since the system is homogeneous, its total momentum $\hat{p} + \hat{P}_{\mathrm{B}}$ is conserved, where $\hat{P}_{\mathrm{B}} = -i \int \mathrm{d}x \hat{\phi}^\dagger(x) \partial_x \hat{\phi}(x)$ is the momentum of the Bose gas. The infinite homogeneous system is treated here as the limit of a finite system of length L with periodic boundary conditions with $L \to \infty$. In order to exploit the translational invariance we apply the Lee–Low–Pines (LLP) transformation [40] $\hat{U}_{\mathrm{LLP}} = \exp(-i\hat{r}\hat{P}_{\mathrm{B}})$, leading to the transformed Hamiltonian

$$\begin{aligned} \hat{H}_{\mathrm{LLP}} &= \hat{U}_{\mathrm{LLP}}^\dagger \hat{H} \hat{U}_{\mathrm{LLP}} \\ &= \frac{1}{2M}\left(p - \hat{P}_{\mathrm{B}}\right)^2 + \int \mathrm{d}x \hat{\phi}^\dagger(x) \left[-\frac{\partial_x^2}{2m} + \frac{1}{2} g \hat{\phi}^\dagger(x)\hat{\phi}(x) + g_{\mathrm{IB}} \delta(x) \right] \hat{\phi}(x). \end{aligned} \tag{2}$$

Due to translation invariance, $\hat{H}_{\mathrm{LLP}}$ no longer depends on $\hat{r}$, and $\hat{p} = \hat{U}_{\mathrm{LLP}}^\dagger(\hat{p} + \hat{P}_{\mathrm{B}})\hat{U}_{\mathrm{LLP}}$ is the conserved total momentum in this frame and can be replaced by a c-number p. We note that due to the LLP transformation, $\hat{\phi}^{(\dagger)}(x)$ describes the creation/annihilation of a boson in a frame co-moving with the impurity, such that $n(x) = \langle \hat{\phi}^\dagger(x)\hat{\phi}(x) \rangle$ is the Bose gas density relative to the position of the impurity, or rather the relative impurity-boson density-density correlation function, to which we refer from now on for simplicity as the Bose gas density.

Since $\hat{H}_{\mathrm{LLP}}$ is an interacting many-body Hamiltonian, a complete solution of the dynamics is difficult without further approximations. In [35, 36] we have shown that for a weak boson-boson interaction, indicated by a small Tonks parameter $\gamma = gm/n$, the ground state properties of a single or a pair of Bose polarons at rest is very well captured by a mean-field approximation that takes the backacktion of the impurity to the condensate into account and goes beyond the standard Froehlich model, which fails if $g_{\mathrm{IB}} \gg g n \tilde{\xi}$. Here $\tilde{\xi} = 1/\sqrt{2gn\tilde{m}}$ is the rescaled healing length with the reduced mass $\tilde{m} = (1/m + 1/M)^{-1}$. This motivates us to use this mean-field approximation also for the case of a moving impurity. We will test its validity by taking into account quantum fluctuations within a Truncated Wigner approach in section 4. The mean-field approximation amounts to replacing the field operator $\hat{\phi}(x)$ by a complex order parameter $\phi(x)$, whose time evolution is determined by the non-linear Schrödinger equation [32]

$$i\partial_t \phi(x,t) = \left[-\frac{\partial_x^2}{2\tilde{m}} + i v(t) \partial_x + g|\phi(x,t)|^2 + g_{\mathrm{IB}} \delta(x) \right] \phi(x,t). \tag{3}$$

Here $v(t) = \left(p - P_{\mathrm{B}}(t)\right)/M$ is the impurity velocity.

Since we are interested in the formation dynamics of polarons either after a sudden quench or an adiabatic turn-on of the impurity-Bose coupling constant g_{IB}, the Bose gas is assumed to be initially in its ground state $\phi(x, t = 0) = \sqrt{n}$ at $t = 0$, where n is the average density of bosons. As the Bose gas carries no initial momentum, the conserved total momentum is equal to the initial impurity momentum $p = Mv(t = 0)$. We simulate the time evolution with periodic boundary conditions numerically using a Fourier split-step method [41]. If not stated otherwise we choose the system size L large enough such that signals are not able to reach the boundary for all times t considered, i.e. $L \gg \tilde{c}t$, where $\tilde{c} = \sqrt{gn/\tilde{m}}$ is the rescaled speed of sound.

2.2. Stationary state and energy-momentum relation

We proceed by discussing the stationary properties of a polaron moving with non-zero total momentum p by characterizing the steady-state solutions of equation (3) [23]. Since the solution has a simpler form if the impurity velocity v is used as a parameter, rather than the conserved momentum p, it is useful to derive the stationary state as a function of v as in [32], and then calculate the corresponding momentum by $p = Mv + P_{\mathrm{B}}[\phi]$. This is possible since $v(t) = v$ is constant in the stationary state. The analytical expression of the state for a fixed v was derived in [16, 32, 35, 42], see appendix A. for technical details and analytical expressions.

As shown in [32], below a critical impurity velocity v_c the system has two stationary states for every given value of v, see figure 2(b) for the corresponding density profiles. Above the critical value no stationary

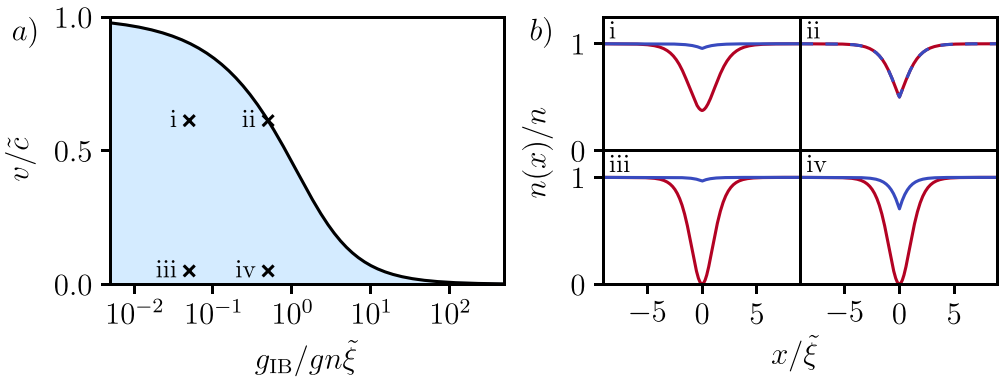

Figure 2. (a) The black line shows the critical impurity velocity v_c. Only in the blue-shaded area, the system has two stationary states for each velocity v and none otherwise. (b) Density profile of the stationary states for different parameters, marked by crosses in (a). At the critical velocity (ii) the two states are equal.

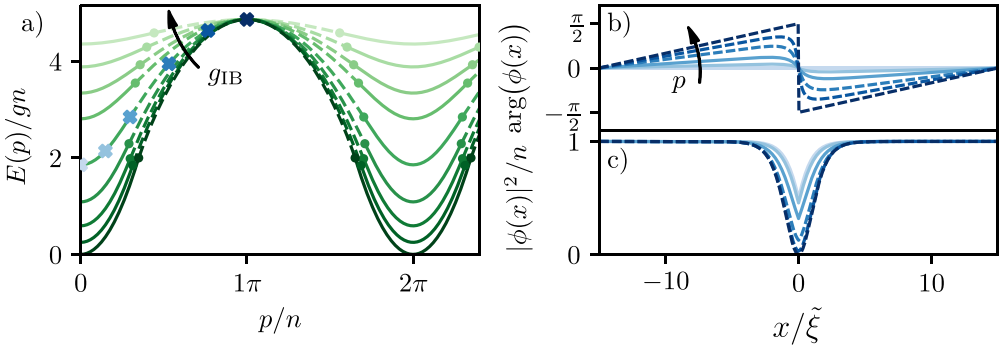

Figure 3. (a) Energy momentum relation of the Bose polaron for different coupling constants $g_{\mathrm{IB}}/gn\tilde{\xi} = 0, 0.1, 0.25, 0.5, 1, 2, 3, 5, 10$, the direction of the arrow points from weak to strong coupling. The mass ratio is $M = 3$ m and Tonks parameter $\gamma = 0.1$. The phase/density of the Bose gas is shown in (b) and (c) for $g_{\mathrm{IB}} = gn\tilde{\xi}$ and different total momenta p, below $p/n = \pi$ indicated by the blue crosses in (a). Other parameters are as in (a) except a finite system size $L = 30\tilde{\xi}$. For $\nu\pi \leqslant p/n \leqslant (\nu+1)\pi$ and integer ν the condensate picks up a constant phase gradient of $\nu\pi$ over its total length.

solution exists. Exactly at the critical velocity, the two states are equal two each other. v_c depends on the coupling constant and can be found from the solution of [16, 32]

$$\frac{g_{\mathrm{IB}}}{gn\tilde{\xi}} \stackrel{!}{=} \frac{1}{2a_c}\sqrt{1 - 20a_c^2 - 8a_c^4 + (1+8a_c^2)^{3/2}}, \quad \text{where } a_c = v_c/\tilde{c}\,. \tag{4}$$

It is plotted in figure 2(a). For small interaction $g_{\mathrm{IB}} \ll gn\tilde{\xi}$, it agrees with the prediction of the Froehlich model $v_c = \tilde{c}$ [24, 43]. However in the limit of strong interactions $g_{\mathrm{IB}} \gg gn\tilde{\xi}$ the condensate is strongly depleted at the impurity position, resulting in a vanishing critical velocity $v_c \to 0$.

The polaron energy is given by the difference in energy of the full system with and without the impurity $E_{\mathrm{pol}} = E(g_{\mathrm{IB}}, p) - E(g_{\mathrm{IB}} = 0, p = 0)$, where $E(g_{\mathrm{IB}}, p)$ is the expectation value of the LLP Hamiltonian equation (2) in a coherent state with amplitude $\phi(x,t)$. E_{pol} is shown as a function of the polaron momentum in figure 3(a), where the two stationary states are distinguished by solid and dashed lines. It becomes clear that the polaron state is unique for every momentum p and the two different states only refer to different parts of the energy-momentum relation. For the lower momentum state the energy-momentum relation was derived in [15].

From the existence of a critical velocity one might conclude that a Bose polaron exists only up to maximum polaron momentum p_{max} depending on g_{IB}, and the energy momentum relation $E_{\mathrm{pol}}(p)$ would terminates at some value of momentum. This is not the case. Instead when increasing p further the solution smoothly crosses over into the second steady state with smaller kinetic velocity and larger condensate depletion. As can be seen from figure 3(c) the condensate depletion grows with increasing momentum. As a consequence the kinetic mass of the polaron, defined as the ratio of polaron momentum and velocity

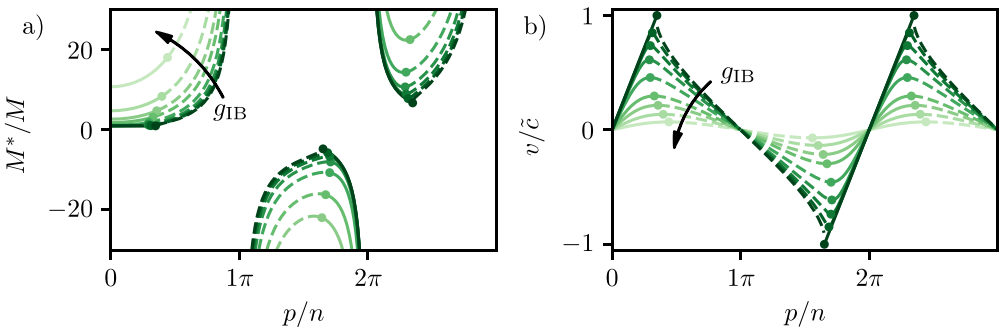

Figure 4. (a) Kinetic polaron mass $M^* = p/v$ and (b) velocity v as a function of the momentum p/n and for increasing coupling constants g_{IB} as in figure 3(a). The direction of the arrow indicates increasing g_{IB} in (a) and (b) for the different lines.

$M^* = p/v$, increases with p as shown in figure 4(a). When crossing from the momentum regime of the first solution of equation (3) to the second solution, the increase of the mass with momentum becomes larger than linear. This leads to a non-monotonous relation between polaron velocity v and momentum p, plotted in figure 4(b). Note that the polaron velocity always stays below the weak-coupling critical value v_c.

When the momentum reaches the value $p_{max} = n\pi$, the state of the condensate is exactly equal to a dark soliton, such that the energy is $E(p_{max}) = \frac{4}{3}n\tilde{c}$ and the impurity velocity goes to zero $v(p_{max}) = 0$. In this case the condensate phase winds by π over its entire length, which for periodic boundary conditions corresponds to half a flux quantum piercing through the ring. Since the density is fully depleted the kinetic polaron mass $M^*(p_{max})$ diverges at this point.

We note that the relation between momentum, energy, and velocity of the polaron has already been found for momenta $|p| < n\pi$ [23]. A peculiar behavior of $E(p)$ is however seen when the total momentum is increased further. The energy starts to decrease with increasing momentum, corresponding to a negative group velocity $\partial E/\partial p$ and consequently a negative impurity velocity. In fact, as can be seen from figure 3(a), $E(p)$ is a periodic function of p/n with period 2π. This is because the properties of the polaron are determined by collective excitations of the Bose gas, whose energy-momentum relation in 1D is periodic with period $2\pi n$ due to Luttingers theorem. Here it can be interpreted as follows: If the total momentum is in the range $(\nu - 1)\pi \leqslant p/n \leqslant \nu\pi$, with ν being an integer, the condensate picks up an integer winding of its phase over its whole length (period) in the stationary state. If ν is even, the momentum picked up by the background condensate exceeds the total momentum and the excess must be compensated by a relative motion of the impurity against the condensate, corresponding to negative values of v.

We will see in the following that the periodic behavior of the energy-momentum relation can give rise to negative asymptotic impurity velocities after injecting it into the condensate with large positive initial velocity. We note that the reversal of the impurity velocity has already been seen in experiments with a strongly interacting Bose gas ($\gamma \gg 1$), where Bloch oscillations of an impurity subject to a constant force have been observed [20].

3. Mean-field description of polaron formation

We now discuss the dynamics when an impurity is injected into a homogeneous condensate with finite initial momentum. First we consider a quasi-adiabatic turn-on of the impurity-boson coupling and subsequently discuss a sudden quench.

3.1. Quasi-adiabatic evolution

Let us first investigate the dynamical properties of the system when the impurity-boson coupling constant $g_{IB}(t)$ is turned on slowly compared to the other time scales of the system. We will show that even though the energy spectrum of the full system is gapless in the thermodynamic limit, a local adiabatic following of the polaron ground state is possible if the initial velocity of the impurity is subsonic.

In order to achieve a smooth turn-on protocol, we choose a time dependence of the coupling according to:

$$g_{IB}(t) = g_{IB}\tanh(t/T). \tag{5}$$

g_{IB} is the final coupling constant and T the turn-on timescale, which we chose large compared to the inverse chemical potential $1/gn$. Since the critical velocity v_c, below which stationary states exist, depends on g_{IB} it is

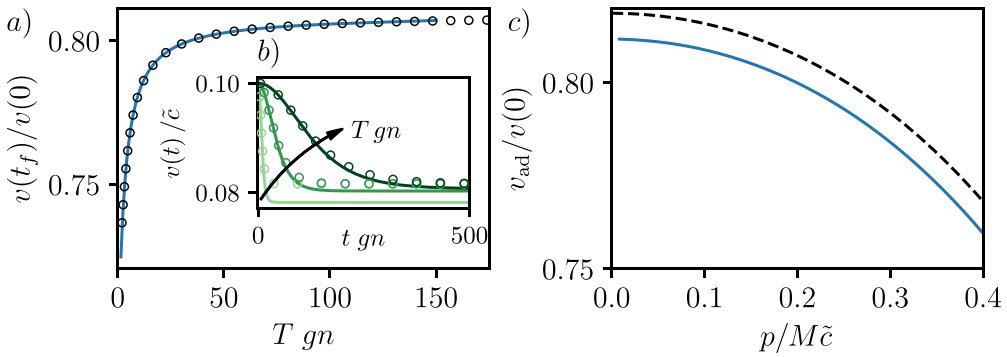

Figure 5. (a) Final impurity velocity $v(t_f)$ after the turn-on with timescale T of the impurity-Bose coupling constant. The initial velocity is $v(0) = p/M = 0.1\tilde{c}$ and we choose a mass ratio of $M = 3$ m, Tonks parameter $\gamma = 0.1$ and $g_{IB} = gn\tilde{\xi}$. The numerical result (blue line) agrees very well with the exponential fit (black circle) of $\alpha_1 e^{-\alpha_2/T} + \alpha_3$, where α_i are fitting parameters. The simulation is performed up to $t_f = 600/gn$. (b) Time evolution of the impurity velocity for $Tgn = 10, 50, 150$, indicated by the black arrow. Lines are simulated results and circles are analytically calculated from the instantaneous stationary state. (c) Final impurity velocity v_{ad} in the adiabatic limit $T \gg 1/gn$ for different total momenta $p = Mv(0)$. Simulated result (blue solid) differ only slightly from the analytical prediction (black dashed). The deviations are caused by the system not being gaped, see appendix B.

also time-dependent and the time evolution differs qualitatively whether the impurity momentum is below or above v_c at any time. The time evolution of the condensate for the two cases is shown exemplarly in figure 6, where the blue and red lines indicate the two stationary states corresponding to the final velocity of the impurity.

First, we focus on the case of a slow impurity $v(t) < v_c(t)$ for all t, such that equation (3) has a stationary solution for all $v(t)$. The evolution of the impurity velocity is exemplary shown for different T in figure 5(b). Even though the impurity is always subsonic it is decelerated to a finite value $v(t_f) < v(0)$, which increases monotonously with T, see figure 5(a). Notably also in the limit $T \to \infty$ the impurity is still slowed down and $v(t_f)$ does not converge to $v(0)$. This is caused by the formation of the polaron. In the instantaneous ground state, the total conserved momentum p is the polaron momentum and is related to the impurity velocity by the effective mass m^* off the polaron

$$v(t) = \frac{p}{m^*(t)}. \tag{6}$$

Since the effective mass increases monotonously with the coupling constant g_{IB} [35], the impurity must decelerate when the impurity-Bose coupling constant is turned on. For finite turn-on times T, density waves are created during the formation of the polaron leading to an additional friction force.

To quantify the quasi-adiabatic slow-down we fit an exponential $\alpha_1 e^{-\alpha_2/T} + \alpha_3$ to the simulated impurity velocity (see figure 5(a)). From the fit the final impurity velocity in the adiabatic limit is determined by $v_{ad} = \alpha_1 + \alpha_3$. It is shown as a function of the conserved total momentum $p = Mv(0)$ in figure 5(c), where it becomes apparent that the deceleration occurs for all p. Due to the gaplessness of the system to collective excitations the simulated final velocity is always slightly below the quasi-adiabatic value, following from equation (6) with m^* replaced by the effective mass of the stationary solution, see figure 4. This is because the adiabatic theorem [44] strictly does not hold. Assuming strict adiabatic following we can derive the relation between $v(t)$ and p as a function of the instantaneous coupling constant $g_{IB}(t)$ in the polaron ground state (see appendix A.). Figure 5(a) shows that the simulated time evolution follows the instantaneous ground state reasonably well for large T except for the small difference shown in figure 5(c), see appendix B.

We now consider an impurity that is initially faster than the critical momentum $v(0) > \tilde{c}$. In that case, equation (3) does not have a stationary solution in the initial phase, which leads to the creation of density waves figure 6(b) and a friction force acting on the impurity. Figure 7(a) shows that the impurity is quickly decelerated until its velocity is below the critical $v_c(g_{IB})$. Afterward, the system again follows the instantaneous ground state quasi-adiabatically, resulting in a slower deceleration.

An important difference between these two processes is, that the second slow deceleration, related to the adiabatic formation of the polaron, is reversible, while the other one is not. This can be seen in figure 7(b), where the impurity-Bose coupling constant is turned on and off again by $g_{IB}(t) = g_{IB} \sin^2(\frac{1}{2}\pi\, t/T)$. Here impurities that are initially below the critical momentum are almost brought to a standstill when the coupling constant is at a maximum but accelerate again to the initial velocity when g_{IB} is turned off again. In

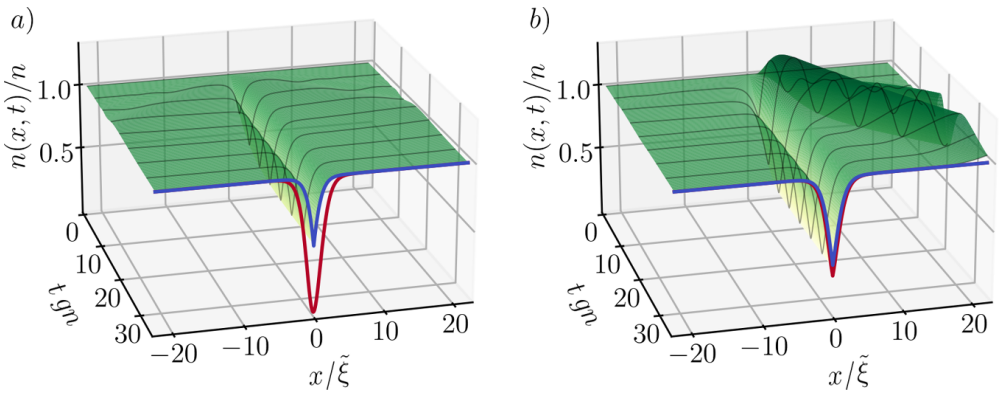

Figure 6. Evolution of the Bose gas density close to the impurity for an (a) initially slow $v(0) = 0.1\,\tilde{c}$ and (b) fast $v(0) = 1.1\,\tilde{c}$ impurity. The impurity Bose coupling constant of strength $g_{IB} = gn\tilde{\xi}$ is turned with the timescale $T = 10/gn$. The mass ratio is constant at $M = 3$ m and the Tonks parameter is $\gamma = 0.1$. The blue and red lines are the two analytically derived stationary states evaluated at the final impurity velocity $v(t)$. The system converges locally in either one of the two states, dissipating the energy as density waves.

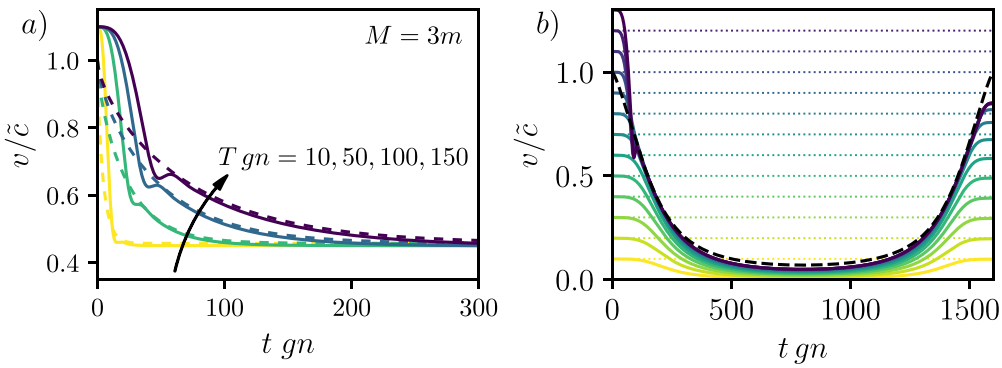

Figure 7. (a) Time evolution of the impurity velocity (solid line) for a supersonic impurity $v(0) = 1.1\tilde{c}$ and different turn-on times T. The initial fast deceleration slows down as soon the impurity is below the critical velocity $v_c(g_{IB}(t))$ (dashed lines). The mass ratio is $M = 3$ m, the Tonks parameter $\gamma = 0.1$, and the final impurity coupling is $g_{IB} = gn\tilde{\xi}$. (b) Evolution of the impurity velocity for different initial velocities. The coupling constant is switched on and off again by $g_{IB}(t) = g_{IB}\sin^2(\frac{1}{2}\pi\, t/T)$, with $g_{IB} = 10gn\tilde{\xi}$, $T = 800$ and otherwise parameters as in (*a*). The black dashed line is the instantaneous critical velocity and the dotted lines mark the initial velocity. The deceleration of subsonic impurities is reversible, but not for supersonic ones.

contrast, impurities starting above criticality are not reaching their initial momentum again after the sweep. The small deviation in the final velocity for sub-critical trajectories is again caused by the system not being gaped in the thermodynamic limit.

3.2. Quench

Here we examine the evolution of the system when the coupling constant is abruptly quenched at $t = 0$.

The time evolution of the impurity velocity after a sudden turn-on of the interaction with the condensate is shown in figures 8(a) and (b) for different initial velocities and different ratios of bare impurity mass M to boson mass m. The quench leads to radiation of density waves until the system reaches a steady state. For all initial conditions and parameters, a friction force [23] is exerted on the impurity and slows it down until the final velocity is reached smaller than the critical v_c. This agrees again with the analytic prediction, that the system has a stationary state only below v_c. However, for a large initial momentum, the impurity velocity is non-monotonic, which cannot be explained by a frictional force alone.

If the impurity is heavy a rather unexpected behavior is found for sufficiently large initial momentum, see figure 8(b). First, as expected the deceleration is slower in the case of heavier impurities. However for a sufficiently large mass, the impurity is not only slowed down, but the velocity can change its direction before converging to a constant velocity. In this case, the background condensate attains an additional momentum

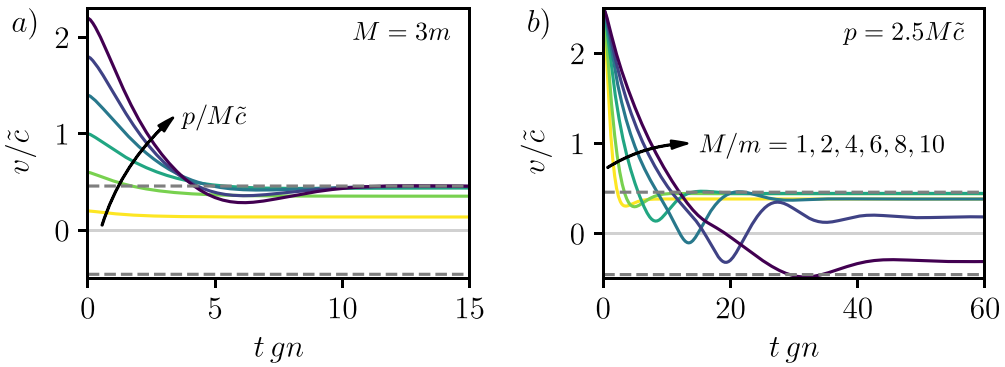

Figure 8. Polaron quench dynamic for (a) different initial impurity velocities and (b) different mass ratios. We choose a coupling constant of $g_{IB} = gn\tilde{\xi}$ and $\gamma = 0.1$. The horizontal dashed grey lines are $\pm v_c$. The impurity velocity always converges to a value $|v(t)| < v_c$.

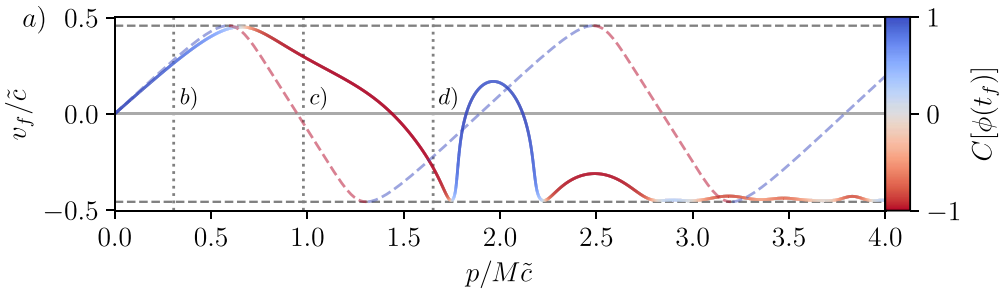

Figure 9. (a) Final velocity v_f after a quench of the impurity-Bose coupling constant to $g_{IB} = gn\tilde{\xi}$ for different total momenta $p = Mv(0)$. For the mass ratio we choose $M = 10$ m and the Tonks parameter $\gamma = .1$. The final velocity is always in an interval $[-v_c, v_c]$, marked by grey vertical lines. The color code indicates the generalized contrast equation (7). The evolution of the Bose gas densities at the marked positions is shown in figures 1(b)–(d). The colored dashed line shows the velocity-momentum relation of the stationary state. It agrees well with the simulated result for sub-critical initial velocities $v(0) < v_c$. For higher total momenta emission of density waves or solitons leads to initial friction forces, causing the deviation.

by building up a finite phase gradient away from the impurity locally approaching a stationary polaron solution with negative impurity velocity as discussed in the previous section.

This effect is examined in more detail in figure 9(a). It shows the final impurity velocity as a function of the conserved momentum $p = Mv(0)$ of a heavy impurity $M = 10$ m. Again the final velocity is for all initial conditions in the interval $[-v_c, v_c]$. However, as mentioned in section 2.2 the system has two stationary states for each velocity and we examine which of these states are populated. For this we first focus on figures 1(b)–(d), showing the evolution of the Bose gas density for different total momenta. The red and blue lines are the analytically calculated stationary states, where we used the final impurity velocity from the simulation as a parameter, rather than the total momentum. Depending on the initial conditions the system converges in either of these two states. In order to quantify the overlap of the final polaron state with either of the two stationary states we determine the generalized contrast

$$C[\phi(t)] = \frac{|\langle\phi(t)|\phi_1\rangle| - |\langle\phi(t)|\phi_2\rangle|}{|\langle\phi(t)|\phi_1\rangle| + |\langle\phi(t)|\phi_2\rangle| - 2|\langle\phi_1|\phi_2\rangle|}$$
$$\langle\phi_a|\phi_b\rangle = \int_{-l/2}^{l/2} \mathrm{d}x\, \phi_a(x)^* \phi_b(x). \tag{7}$$

Here $|\phi(t)\rangle$ is the simulated state of the system and $|\phi_i\rangle$ the steady states, evaluated at the simulated final velocity. The contrast is 1 if the system converges into the first state and -1 for the second. This definition differs from the standard expression of contrast by the term $\langle\phi_1|\phi_2\rangle$ in the denominator, which we need since the stationary states are not orthogonal. We evaluate the scalar products over an interval l which we choose such that the time evolution is properly converged within it. The contrast is depicted in figure 9(a) by the color code and it becomes apparent that the polaron changes its state when its velocity intersects with the critical value v_c. This is explained by the states being equal at the critical velocity.

The explanation for the non-monotonic impurity velocity and the change in the movement direction at larger total momenta can be seen in figure 1(d). At large momenta, the impurity carries enough energy that a grey soliton is created besides density waves which carry additional momentum. This is visible as the local depletion moving away from the impurity at a slower speed as the initially created density waves in figure 1(d). Note, however, that this interpretation is based on numerical evidence only where a non-trivial behaviour of the impurity velocity always coincided with soliton emission.

4. Truncated-Wigner approximation of a harmonically trapped polaron

The above mean-field analysis has neglected quantum fluctuations. Although it has been shown in [35, 36] that the ground state properties of Bose polarons and bi-polarons are well described by the modified mean-field approach even in the limit of strong boson-impurity coupling $g_{\rm IB} \gg gn\tilde{\xi}$, provided the Bose–Bose interaction is weak, i.e. if $\gamma \ll 1$, it is not clear if this still holds in the non-equilibrium case. For this reason we now consider the effect of small quantum fluctuations using a truncated Wigner approach [37–39]. This approach fully captures the influence of (deformed) Bogoliubov phonons on top of the condensate in quadratic (Bogoliubov) approximation. However, as stated by the Mermin–Wagner–Hohenberg theorem [45, 46] there is no true Bose condensation in homogeneous 1D gases, which manifests itself by infrared divergencies when considering lowest-order quantum fluctuations. The latter also holds for finite systems with periodic boundary conditions. Thus in order to describe quantum fluctuations we can no longer approximate the one-dimensional gas as being homogeneous and have to take into account the presence of a harmonic trapping potential. (The different regimes of quantum degeneracy in trapped 1D Bose gases are discussed e.g. in [47].) This complicates the theoretical description as the LLP transformation, conveniently used in homogeneous systems, no longer leads to a decoupling of the total momentum of the polaron. We will show however that the total momentum obeys a simple equation of motion if also the impurity is trapped.

4.1. LLP Hamiltonian of a trapped 1D Bose gas

We start by adding a harmonic potential with frequency ω for bosons and Ω for the impurity to the Hamiltonian equation (1) to avoid infrared divergencies in the Bogoliubov theory of boson-boson interactions. Since these potentials break the translation invariance of the system the total momentum of the system is no longer conserved. Therefore, the transformation into a relative and a center of mass coordinate by the LLP transformation does not eliminate the impurity operators. Nevertheless, it is useful to apply the transformation, since $\hat{p}$ and $\hat{r}$ only appear up to quadratic order in the LLP Hamiltonian

$$\hat{H}_{\rm LLP} = \frac{1}{2M}\left(\hat{p}-\hat{P}_{\rm B}\right)^2 + \frac{1}{2}M\Omega^2\hat{r}^2 + \int \mathrm{d}x\,\hat{\phi}^\dagger(x)\left[-\frac{\partial_x^2}{2m} + \frac{1}{2}m\omega^2(x+\hat{r})^2 + \frac{1}{2}g\hat{\phi}^\dagger(x)\hat{\phi}(x) + g_{\rm IB}\delta(x)\right]\hat{\phi}(x). \tag{8}$$

To simulate the time evolution of the system we derive the Heisenberg equation of motion $\partial_t \bullet = i\,[\hat{H}_{\rm LLP}\,, \bullet]$ for $\hat{p}(t)$, $\hat{r}(t)$ and $\hat{\phi}(x,t)$. The advantage of the LLP transformation even in the case of harmonic trapping becomes clear here since the equations for $\hat{p}(t)$ and $\hat{r}(t)$ are formally solvable and we get

$$\hat{p}(t) = \hat{p}(0)\cos\Omega t + \frac{1}{\Omega}\dot{\hat{p}}(0)\sin\Omega t + \frac{\Omega^2-\omega^2}{\Omega}\int_0^t \mathrm{d}t'\sin\Big(\Omega(t-t')\Big)\hat{P}_{\rm B}(t'), \tag{9}$$

$$\hat{r}(t) = -\frac{\dot{\hat{p}}(t) + Nm\omega^2\hat{X}_{\rm B}(t)}{M\Omega^2 + Nm\omega^2}. \tag{10}$$

Here N is the particle number of bosons and $\hat{X}_{\rm B}(t) = \int \mathrm{d}x\,x\hat{\phi}^\dagger(x,t)\,\hat{\phi}(x,t)/N$ their center of mass position. In the case of equal trapping frequencies $\omega = \Omega$, the last term in the solution of the total momentum $\hat{p}(t)$, equation (9), vanishes, and its time evolution corresponds to that of an uncoupled harmonic oscillator

$$\hat{p}(t) = \hat{p}(0)\cos\Omega t + \frac{1}{\Omega}\dot{\hat{p}}(0)\sin\Omega t, \qquad \text{for} \quad \Omega = \omega. \tag{11}$$

The remaining equation for the bosonic field $\hat{\phi}(x,t)$ then reads:

$$i\partial_t\hat{\phi}(x,t) = \left\{-\frac{\partial_x^2}{2m} + \frac{i}{M}\left[\hat{p}(t)-\hat{P}_{\rm B}(t)\right]\partial_x + g\hat{\phi}^\dagger(x,t)\hat{\phi}(x,t) + g_{\rm IB}\delta(x) + \frac{1}{2}m\omega^2\left[x+\hat{r}(t)\right]^2\right\}\hat{\phi}(x,t). \tag{12}$$

4.2. Truncated Wigner simulation of the boson field

We now solve the system of equations (9), (10) and (12) in a limit where quantum fluctuation of the impurity position and momentum are negligible, but include fluctuation of the Bose field using a truncated Wigner phase space approach (TWA). For reviews on the TWA methods see [38, 39]. To be able to apply a TWA we have to first treat the quantum evolution of $\hat{r}(t)$ and $\hat{p}(t)$. For this we apply another approximation and replace the total momentum and position operator of the Bose field in the dynamical equations of the impurity by expectation values

$$\hat{P}_{\rm B} \to \langle \hat{P}_{\rm B} \rangle := P_{\rm B}, \quad \text{and} \quad \hat{X}_{\rm B} \to \langle \hat{X}_{\rm B} \rangle := X_{\rm B}. \tag{13}$$

This approximation is reasonable since the number of bosons is large $N \gg 1$ such that fluctuations of their center of mass coordinate are small. From equations (9) and (10) then follows, that the fluctuation of $\hat{p}$ and $\hat{r}$ do not grow in time. It is possible to prepare the impurity in a state where fluctuation are small as long as its harmonic oscillator length scale $l_I = 1/\sqrt{\Omega M}$ is small when compared to all other length scales of the system, especially the healing length of the condensate $\xi = 1/\sqrt{2gnm}$, where n is the peak density of the ground state of the trapped Bose gas without an impurity. The semiclassical treatment of impurity position and total momentum is therefore justified only in the regime where $\frac{gnm}{\Omega M} \ll 1$. Under this condition the operators

$$\hat{r} \to \langle r \rangle := r, \quad \text{and} \quad \hat{p} \to \langle p \rangle := p \tag{14}$$

are replaceable by expectation values.

In order to calculate the time evolution of the Bose field in a Wigner phase space description, an expression for the initial ground state of the Bose gas including quantum fluctuation is needed. Since we consider a weakly interacting Bose gas, it suffices to do this by replacing the field operators $\hat{\phi}(x, t = 0)$ by the mean-field ground state $\phi_0(x)$ of a trapped Bose gas and add quantum fluctuation within Bogoliubov–de Gennes (BdG) approximation

$$\hat{\phi}(x,t) = \phi_0(x+r) + \sum_n \Big[u_n(x+r)\hat{b}_n(t) + v_n(x+r)^* \hat{b}_n^\dagger(t) \Big]. \tag{15}$$

Here $u_n(x)$ and $v_n(x)$ are the BdG coefficients of the trapped Bose gas and $\hat{b}_n^{(\dagger)}$ the phonon operators of the respective modes, see appendix C. for more details. The position r appears in this expression since the Bose gas ground state is transformed into the LLP frame, corresponding to the shift by r. In the Wigner phase-space description, the phonon operators are replaced by stochastic c-numbers $\hat{b}_n^{(\dagger)}(t) \to \beta_n^{(*)}(t)$ where all stochasticity is in the initial state. Since this state is the phonon vacuum they are set to Gaussian random variables with mean and variance given by $\langle \beta_n(0) \rangle = 0$ and $\langle \beta_n(0)\beta_m^*(0) \rangle = \frac{1}{2}\delta_{n,m}$, corresponding to a virtual occupation of half a phonon per mode on average. By symmetric ordering of the Heisenberg equation (12) and replacing the operators by c-numbers $\hat{\phi} \to \phi$ we get the c-number equation of motion

$$\begin{aligned} i\partial_t \phi(x,t) = \Big\{ -\frac{\partial_x^2}{2m} + \frac{i}{M}\big[p(t) - P_{\rm B}(t)\big]\partial_x + g|\phi(x,t)|^2 - 2g n^w\big(x + r(t)\big) + g_{\rm IB}\delta(x) \\ + \frac{1}{2} m\omega^2 \big[x + r(t)\big]^2 \Big\} \phi(x,t). \end{aligned} \tag{16}$$

Here $n^w(x)$ is the virtually occupied particle density due to the Wigner description and is given by

$$n^w(x) = \frac{1}{2}\sum_n^{n_{\rm max}} |u_n(x)|^2 - |v_n(x)|^2. \tag{17}$$

Note that we have truncated the number of modes taken into account, which is necessary in TWA, since if all BdG modes are included $n^w(x)$ would diverge $n^w(x) = \frac{1}{2}\delta(0)$. The truncation of higher modes is commonly used in TWA simulations of trapped gases [37, 38] and is physically justified as quantum fluctuations of high frequency modes can be neglected. We simulate equation (16) multiple times for different initial conditions and average about the different realization. In order to obtain expectation values all operators need to be symmetrically ordered first, e.g. the Bose gas density is given by

$$n(x,t) = \Big\langle \big|\phi(x - r(t), t)\big|^2 - n^w(x) \Big\rangle, \tag{18}$$

where $r(t)$ appears, such that the expression describes the density in the laboratory and not LLP frame.

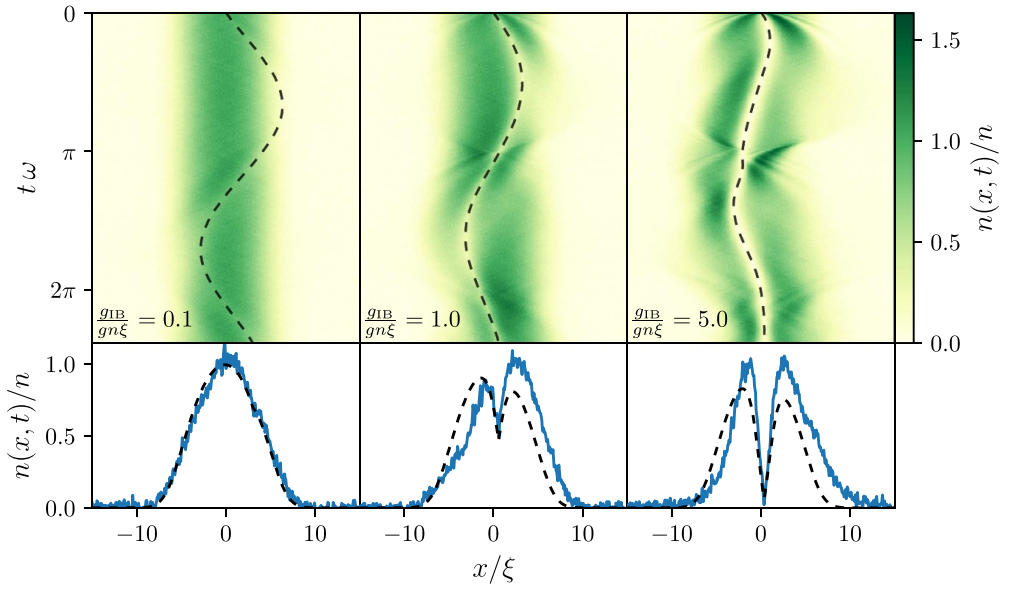

Figure 10. TWA simulation of a trapped system for different impurity-Bose coupling constants. Here trapping frequencies for bosons and impurity are equal $\Omega = \omega = 0.3gn$, the Tonks parameter is $\gamma = 0.1$, the mass ratio is $M/m = 10$ and the initial impurity momentum is $p = 0.75Mc$. The upper panels show the time evolution up to $t = 25/gn = 7.5/\omega$, where the dashed line marks the position of the impurity. The lower panels show the final density (blue) and compare it to the stationary state of the homogeneous system (dashed) modulated by the initial mean-field density of the trapped gas. The TWA simulation is averaged over 5000 noise realizations.

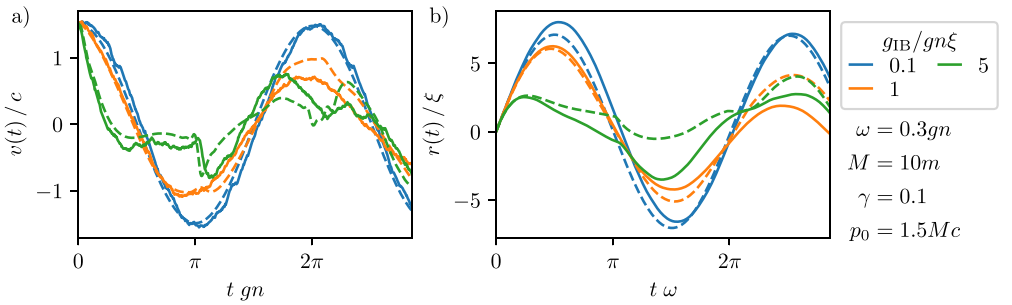

Figure 11. (a) Impurity velocity and (b) impurity position in a trapped system with equal trapping frequencies $\Omega = \omega$. Solid lines show the TWA simulation, dashed lines the classical mean-field approximation. The TWA simulation is averaged over 5000 noise realizations.

The time evolution of the trapped system is illustrated in figure 10. A problem of this approach is that the system is finite, so that density waves created by the impurity oscillate in the trap and return back to the impurity. The system does therefore only reach locally a stationary state in very shallow traps with very small trapping frequency $\omega \ll gn$. This however conflicts with the condition of a classical impurity $\frac{gnm}{\Omega M} \ll 1$ for reasonably heavy impurities and equal trapping potential. However, although the system is not in a stationary state the stationary solution described in section 2.2 agrees reasonably well with the observed density distribution, see figure 10 when applying a local density approximation.

Next, in order to test the validity of the mean-field approach used in sections 2 and 3, we compare the time evolution of the trapped system obtained from TWA calculations to a mean-field simulation. For the latter, we set the initial virtual particle occupation to zero $\beta_n = 0$. The impurity velocity $v(t) = (p(t) - P_B(t))/M$ and position $r(t)$ obtained in that way are shown in figure 11. For a small coupling constant $g_{IB} \ll gn\xi$ the evolution remains sinusoidal, however, at large coupling it deviates strongly from an harmonic motion. The agreement between TWA and mean-field is reasonably well, given that we consider a quite strongly interacting gas with $\gamma = 0.1$. The impurity position figure 11(b) gets in some cases an overall shift between TWA and mean-field, the motion is however qualitatively similar. Especially the deviation in

the impurity velocity is small, see figure 11(a). From this, we conclude that the mean-field simulation is sufficient to predict the time evolution at least qualitatively.

5. Summary

In the present paper we have discussed the dynamics of the formation of a Bose polaron when an impurity is injected into a 1D weakly-interacting Bose gas by performing time-dependent simulations of mean-field equations of the condensate amplitude complemented by truncated Wigner simulations to include quantum fluctuations. In a homogeneous gas with periodic boundary conditions the total momentum p of the system is conserved and can be used as independent parameter to characterize different dynamical regimes. Analyzing steady state solutions of the mean-field equations first, we showed that stationary solutions exist only for impurity velocities below a critical value, which in the limit of weak impurity-boson couplings $g_{\rm IB}$ agrees with the Landau critical velocity, as predicted by the Froehlich model, but monotonously decreases with increasing interaction and eventually approaches zero. This is because with growing values of $g_{\rm IB}$ the condensate is more and more depleted in the vicinity of the impurity, which leads to a reduced local speed of sound. While, as first shown in [32] for a given velocity of the impurity below the critical value, there are always two stationary solutions of the condensate equations, the solution is unique when fixing the total momentum. For momentum values with a convex energy-momentum relation, $\partial^2 E/\partial p^2 > 0$, one of the two solutions applies and in regions with $\partial^2 E/\partial p^2 < 0$ the other solution holds. We showed moreover that the stationary energy-momentum relation is periodic in p as the background condensate away from the impurity can pick up additional quantized amounts of momentum corresponding to integer windings of the condensate phase over its length. As a consequence the relation between impurity velocity v and polaron momentum p is also periodic and includes regions of momentum where the impurity velocity is negative. In these regions the Bose gas stabilizes only a steady state with momentum exceeding the total momentum which must then be compensated by an opposite motion of the impurity. While a direct measurement of the energy-momentum relation of the polaron is challenging, its non-monotonous form can have interesting experimental consequences. E.g. injecting impurities with finite velocity into a small ring condensate can induce a finite circular current corresponding to a finite number of enclosed flux quanta.

To study the formation of the polaron we considered two cases, a slow, quasi-adiabatic turning on of the Bose-impurity coupling and a sudden quench. If in the quasi-adiabatic situation the initial velocity is chosen small enough such that it stays below the critical value at all times, the impurity is decelerated only due to the increase in its effective mass, associated with the formation of the polaron. As the system evolves quasi-adiabatic this reduction in velocity is reversible. We find that the polaron quasiparticle is formed on the timescale of the inverse chemical potential $1/gn$ (see figure 8), which for parameters of a recent experiment in 1D gases [4] is on the order of 60 μs. If in the quasi-adiabatic scheme the initial velocity is above the critical value the impurity emits density waves irrespective how slowly the interaction is turned on leading to irreversible friction. Switching on the impurity-boson interaction suddenly a rich scenario of dynamical regimes is observed. Depending on the mass ratio of particles, the total momentum and the impurity-boson coupling strength the impurity is slowed down by emission of density waves or grey solitons. The latter happens for large momenta and large impurity masses and is specific for the regime of strong impurity-boson coupling. In this case asymptotic states can form where the impurity velocity changes its sign, i.e. backscattering occurs, which cannot occur in the weak coupling regime dominated by Cherenkov radiation of phonons. While an in-situ measurement of the impurity motion is difficult in an experiment, the emission of grey solitons can be directly observed by density measurements of the condensate. We here considered impurities in one-dimensional condensates. The modified mean-field approach including the backaction of the impurity to the condensate can however be applied also to higher dimensions. Theories predicting the polaron dynamics based on the Froehlich model, using e.g. a coherent variational ansatzes [28–30] or master equation [24, 31] are capable of capturing the evolution as long as the condensate deformation is not substantial. From a straightforward dimensional analysis of the mean-field equation in D dimension we estimate that the condensate deformation becomes significant for $g_{\rm IB}/g \gtrsim n\tilde{\xi}^D$. Some of the predicted effects are expected to carry over from one to higher dimensions to these cases. E.g. the reversible slowdown of a sub-sonic impurity due to the formation of a polaron and the friction forces experienced by a super-sonic impurity due to emission of density waves will be very similar. The emission of grey solitons and the dragging of the impurity towards the grey solitons, on the other hand, is an effect specific to one-dimensional gases. In two dimensions a heavy, supersonic impurity might instead emit vortex anti-vortex pairs.

To justify the validity of the mean-field approximation we performed truncated Wigner simulations of the full quantum problem in a trapped gas. The TWA accounts for quantum fluctuations due to Bogoliubov phonons on the deformed condensate background up to quadratic order. To avoid infrared divergencies

related to the one-dimensional setup, enforced by the Mermin–Wagner–Hohenberg theorem, we considered a harmonically trapped gas. Although the total momentum is no longer conserved it follows a simple equation of motion, which we solve in semiclassical approximation. The TWA simulations show that the mean-field description of the dynamics of polaron formation is well justified as long as the Tonks parameter of the Bose gas is small, i.e. for a weakly interacting gas. The case of strong boson-boson interactions requires different analytical and numerical tools and will be discussed elsewhere.

Data availability statements

The data that support the findings of this study are available upon reasonable request from the authors.

Acknowledgments

We would like to thank Artur Widera, Jonas Jager and Ryan Barnett for fruitful discussions. Financial support by the DFG through SFB/TR 185, Project No. 277625399 is gratefully acknowledged. M W was supported by the Max Planck Graduate Center with the Johannes Gutenberg-Universität Mainz.

Appendix A. Stationary mean-field solution

In the following, we briefly summarize the stationary solution of the Gross–Pitaevskii equation (GPE) equation (3), which are derived in more detail in [32, 35]. Since the equation explicitly depends on the impurity velocity v and not the conserved momentum p, it is convenient to use v as a parameter and then calculate the total momentum of the stationary state by

$$p = Mv + P_{\mathrm{B}} = Mv - i\int \mathrm{d}x\phi^*(x,t)\partial_x\phi(x,t). \tag{19}$$

This is possible since $v(t)$ is a constant in the steady state. As shown in [32, 35] the stationary solution of equation (3) is similar to a grey soliton, except at $x=0$, and given by

$$\phi(x,t) = \sqrt{n}e^{i(\varphi_1 x+\varphi_2\mathrm{sgn}(x)-gnt)}\left[a - ib\,\mathrm{sgn}(x)\tanh\left(\frac{b}{\sqrt{2}\tilde{\xi}}|x|+d\right)\right], \tag{20}$$

as long as the system size L is large compared to the rescaled healing length $\tilde{\xi} = 1/\sqrt{2gn\tilde{m}}$. Here $a = v/\tilde{c}$, $b = \sqrt{1-a^2}$ and the parameters φ_1 and φ_2 are chosen such that the phase of the solution is continuous at $x=0$ and fulfills periodic boundary condition. The parameter d shifts the grey soliton wave function such that the boundary condition generated by the delta distribution in equation (3)

$$\partial_x\phi(x,t)\Big|_{x=0^-}^{0^+} = 2g_{\mathrm{IB}}\tilde{m}\,\phi(0,t) \tag{21}$$

is fulfilled. From this, it can be deduced that $\tanh d$ must be the solution of a cubic equation

$$b^3\tanh d\left(1-\tanh^2 d\right) \overset{!}{=} \frac{g_{\mathrm{IB}}}{\sqrt{2}gn\tilde{\xi}}\left(1-b^2+b^2\tanh^2 d\right). \tag{22}$$

The three solutions of the equation are shown in figure 12(b). The one which is real for all parameters is always less than or equal -1, such that d is not a real number corresponding to a nonphysical state. The other two solutions are real and between 0 and 1, if the impurity velocity v is below the critical velocity $v_c = a_c\tilde{c}$, see figure 12(a). Here a_c can be determined by solving

$$\frac{g_{\mathrm{IB}}}{gn\tilde{\xi}} \overset{!}{=} \frac{1}{2a_c}\sqrt{1-20a_c^2-8a_c^4+(1+8a_c^2)^{3/2}}, \tag{23}$$

which is equivalent to a cubic equation in a_c^2. For a small coupling constant $g_{\mathrm{IB}} \ll gn\tilde{\xi}$ the critical velocity is $\tilde{c}$ and agrees with the prediction of the Froehlich model [24, 43]. However for strong repulsion $g_{\mathrm{IB}} \gg gn\tilde{\xi}$ the critical velocity converges to zero. Substituting the two physical solutions of equation (22) into equation (20) yields the two stationary states mentioned in the main part of this work. The two solutions are equal at the critical momentum, explaining why the stationary states merge at criticality.

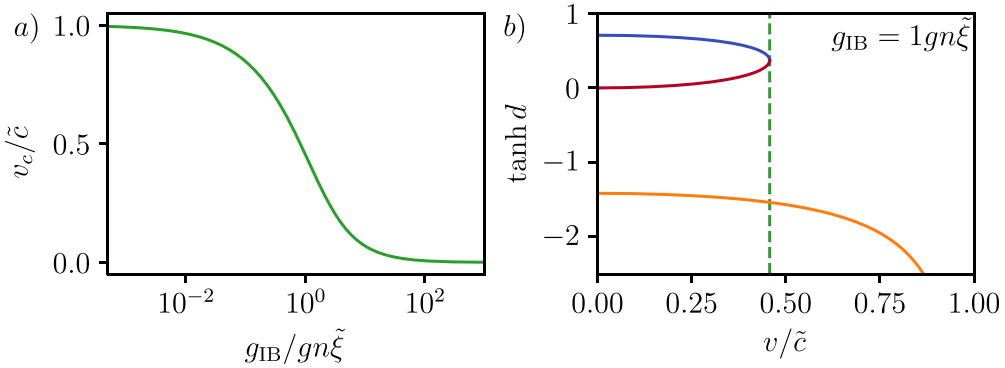

Figure 12. (a) Critical impurity velocity v_c. (b) Solutions of the cubic equation (22). The orange solution (lowest curve) is $\tanh d < -1$ for all v and therefore nonphysical. The red and blue solutions exist only below the critical velocity v_c (dashed green), yielding the two relevant states.

Next, since p and not v is conserved under time evolution it is important to derive an expression relating the parameters for the stationary solutions. It follows from equations (19) and (20) and is given by

$$p = Mv - 2nab\left(1 - \tanh d\right) + 2n\left[\arctan\left(\frac{a}{b}\right) - \arctan\left(\frac{a}{b}\tanh d\right)\right]. \tag{24}$$

In order to compare this analytic expression to the time-dependent simulation we solve it numerically for v.

The polaron energy is given by $E_{\mathrm{pol}} = E(g_{\mathrm{IB}}, p) - E(g_{\mathrm{IB}} = 0, v = 0)$, where $E(g_{\mathrm{IB}}, p)$ is the expectation value of the LLP Hamiltonian equation (2)

$$\begin{aligned} E_{\mathrm{pol}} = \sqrt{2}gn^2\tilde{\xi}\Big[2b\big(1 - \tanh(d)\big) - \frac{1}{3}b^3\big(2 - 3\tanh(d) + \tanh(d)^3\big)\Big] \\ + \frac{1}{2}Mv^2\Big[1 - 4\sqrt{2}\frac{\tilde{m}}{M}n\tilde{\xi}\big(1 - \tanh(d)\big)\Big]. \end{aligned} \tag{25}$$

In the approach described so far equation (24) results only in momentum values with $-\pi n \leqslant p \leqslant \pi n$. In order to reach higher momenta the stationary solution equation (20) must be modified by an additional phase gradient

$$\tilde{\phi}(x,t) = \mathrm{e}^{ix\frac{2\pi}{L}\nu}\phi(x,t) \quad \text{with } \nu \in \mathbb{Z}. \tag{26}$$

Except for the additional phase gradient, the stationary solution, all parameters in equation (20), and the energy equation (25) are not modified in the thermodynamic limit $L \gg \tilde{\xi}$. Only the total momentum

$$\tilde{p} = p + 2\pi n\nu \tag{27}$$

picks up an additional term, which explains why the observables in figures 3(a) and 4(b) are periodic in p, with a period length of $2\pi n$.

Appendix B. Gapless adiabaticity

In section 3.1 we showed that the system evolves quasi-adiabatic if the impurity-Bose coupling constant is turned on slowly compared to the other timescales. However, there always remains a small but finite difference to the instantaneous stationary state in figure 5(c). In this section we show, that this difference originates from the system not being energetically gaped in the thermodynamic limit. To this end, the time evolution of a large system $L \gg \tilde{c}T$ is compared to a small one $L \ll \tilde{c}T$, with otherwise equal parameters. The small system is gaped due to finite-size effects, such that the adiabatic theorem strictly holds. This is shown in figures 13(a)–(c), where the impurity momentum as well as the density and phase of the Bose gas agree with the instantaneous ground state. In contrast in the large system. Here in particular the phase disagrees at a large distance from the impurity $|x| \gg \tilde{\xi}$, see figure 13(d), explaining the small discrepancy of the impurity momentum figure 13(a). In the large system the stationary state is not reached globally, but only locally at the position of the impurity. This is however sufficient for the system to evolve quasi-adiabatic.

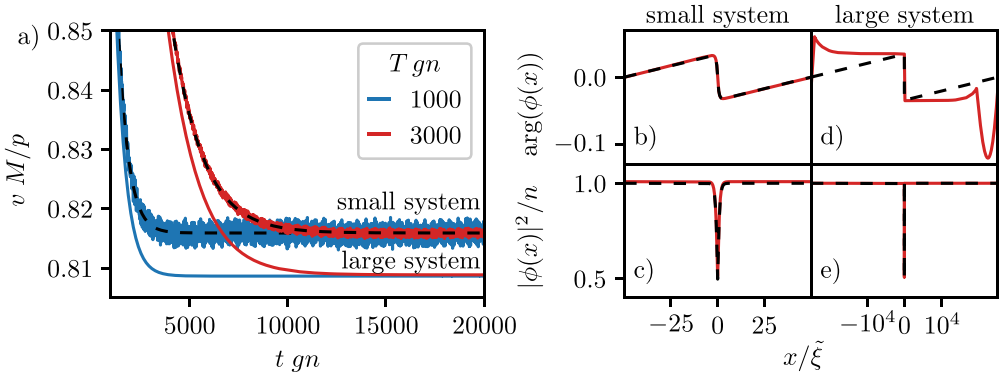

Figure 13. Comparison of the quasi-adiabatic (large system) to true-adiabatic (small system) evolution for $v(0) = p/M = 0.1\tilde{c}$, $g_{\mathrm{IB}} = gn\tilde{\xi}$, $\gamma = 0.1$ and $M = 3$ m. (a) Evolution of the impurity velocity for two turn-on timescales T. Dashed lines represent the instantaneous stationary state. (b)–(d) State at the end of the evolution at $tgn = 2 \cdot 10^4$ for $Tgn = 3 \cdot 10^3$. For a small system $L = 100\tilde{\xi}$, both phase (b) and density (c) agree with the instantaneous stationary state (dashed). For a large system $L = 5 \cdot 10^4\tilde{\xi}$ the phase (d) disagrees at a large distance from the center.

Appendix C. Bogoliubov–de Gennes in a trap

In order to express the initial ground state of the trapped Bose gas, before the interaction with the impurity, we diagonalize the Bose gas Hamiltonian

$$\hat{H}_{\mathrm{B}} = \int \mathrm{d}x\,\hat{\phi}^\dagger(x)\Big(-\frac{\partial_x^2}{2m} + \frac{1}{2}m\omega^2x^2 + \frac{1}{2}g\hat{\phi}^\dagger(x)\hat{\phi}(x)\Big)\hat{\phi}(x), \tag{28}$$

approximately using a BdG approach [48]. In the first step, the mean-field ground state is determined by the GPE

$$\Big(-\frac{\partial_x^2}{2m} + \frac{1}{2}m\omega^2x^2 + g|\phi_0(x)|^2 - \mu\Big)\phi_0(x) = 0, \tag{29}$$

which we solve numerically using imaginary time evolution. Here μ is the mean-field chemical potential. In case of a weakly interacting Bose gas, it is sufficient to only include small fluctuation on top of the mean-field solution, which is done by expressing the bosonic field operators by

$$\hat{\phi}(x) = \phi_0(x) + \sum_n \Big(u_n(x)\hat{b}_n + v_n(x)^*\hat{b}_n^\dagger\Big), \tag{30}$$

and only keep terms up to quadratic order in the operators $\hat{b}_n^{(\dagger)}$. Here $u_n(x)$ and $v_n(x)$ are the BdG coefficients. This Ansatz diagonalizes the Hamiltonian equation (28) if the coefficients fulfill the BdG equation

$$\begin{pmatrix} \hat{L} & g|\phi_0(x)|^2 \\ -g|\phi_0(x)|^2 & -\hat{L} \end{pmatrix}\begin{pmatrix} u_n(x) \\ v_n(x) \end{pmatrix} = \epsilon_n \begin{pmatrix} u_n(x) \\ v_n(x) \end{pmatrix}, \quad \text{where} \quad \hat{L} = -\frac{\partial_x^2}{2m} + \frac{1}{2}m\omega^2x^2 + 2g|\phi_0(x)|^2 - \mu, \tag{31}$$

where ϵ_n are the eigenenergies of the corresponding BdG modes. To solve this equation, we expand it in a finite number of eigenfunctions of the free harmonic oscillator and diagonalize the resulting matrix numerically.

ORCID iDs

Martin Will https://orcid.org/0000-0003-1490-8928
Michael Fleischhauer https://orcid.org/0000-0003-4059-7289

References

[1] Landau L 1933 *Phys. Z. Sowjetunion* **3** 644–5
[2] Pekar S I 1946 *Zh. Eksp. Teor. Fiz.* **16** 335
[3] Chin C, Grimm R, Julienne P and Tiesinga E 2010 *Rev. Mod. Phys.* **82** 1225–86

[4] Catani J, Lamporesi G, Naik D, Gring M, Inguscio M, Minardi F, Kantian A and Giamarchi T 2012 *Phys. Rev.* A **85** 023623
[5] Jørgensen N B, Wacker L, Skalmstang K T, Parish M M, Levinsen J, Christensen R S, Bruun G M and Arlt J J 2016 *Phys. Rev. Lett.* **117** 055302
[6] Hu M-G, Van de Graaff M J, Kedar D, Corson J P, Cornell E A and Jin D S 2016 *Phys. Rev. Lett.* **117** 055301
[7] Yan Z Z, Ni Y, Robens C and Zwierlein M W 2020 *Science* **368** 190–4
[8] Rath S P and Schmidt R 2013 *Phys. Rev.* A **88** 053632
[9] Levinsen J, Parish M M and Bruun G M 2015 *Phys. Rev. Lett.* **115** 125302
[10] Casteels W and Wouters M 2014 *Phys. Rev.* A **90** 043602
[11] Christensen R S, Levinsen J and Bruun G M 2015 *Phys. Rev. Lett.* **115** 160401
[12] Grusdt F, Astrakharchik G E and Demler E 2017 *New J. Phys.* **19** 103035
[13] Parisi L and Giorgini S 2017 *Phys. Rev.* A **95** 023619
[14] Ichmoukhamedov T and Tempere J 2019 *Phys. Rev.* A **100** 043605
[15] Panochko G and Pastukhov V 2019 *Ann. Phys., NY* **409** 167933
[16] Volosniev A G and Hammer H-W 2017 *Phys. Rev.* A **96** 031601
[17] Schmidt R, Sadeghpour H R and Demler E 2016 *Phys. Rev. Lett.* **116** 105302
[18] Levinsen J, Parish M M, Christensen R S, Arlt J J and Bruun G M 2017 *Phys. Rev.* A **96** 063622
[19] Dzsotjan D, Schmidt R and Fleischhauer M 2020 *Phys. Rev. Lett.* **124** 223401
[20] Meinert F, Knap M, Kirilov E, Jag-Lauber K, Zvonarev M B, Demler E and Nägerl H-C 2017 *Science* **356** 945–8
[21] Boyanovsky D, Jasnow D, Wu X-L and Coalson R C 2019 *Phys. Rev.* A **100** 043617
[22] Skou M G, Skov T G, Jørgensen N B, Nielsen K K, Camacho-Guardian A, Pohl T, Bruun G M and Arlt J J 2021 *Nat. Phys.* **17** 731–5
[23] Koutentakis G M, Mistakidis S I and Schmelcher P 2022 *Atoms* **10** 3
[24] Lausch T, Widera A and Fleischhauer M 2018 *Phys. Rev.* A **97** 023621
[25] Fröhlich H 1954 *Adv. Phys.* **3** 325–61
[26] Astrakharchik G E and Pitaevskii L P 2004 *Phys. Rev.* A **70** 013608
[27] Casteels W, Van Cauteren T, Tempere J and Devreese J T 2011 *Laser Phys.* **21** 1480–5
[28] Shchadilova Y E, Schmidt R, Grusdt F and Demler E 2016 *Phys. Rev. Lett.* **117** 113002
[29] Drescher M, Salmhofer M and Enss T 2019 *Phys. Rev.* A **99** 023601
[30] Ardila L A P 2021 *Phys. Rev.* A **103** 033323
[31] Nielsen K K, Ardila L A P, Bruun G M and Pohl T 2019 *New J. Phys.* **21** 043014
[32] Hakim V 1997 *Phys. Rev.* E **55** 2835–45
[33] Bruderer M, Bao W and Jaksch D 2008 *Europhys. Lett.* **82** 30004
[34] Blinova A A, Boshier M G and Timmermans E 2013 *Phys. Rev.* A **88** 053610
[35] Jager J, Barnett R, Will M and Fleischhauer M 2020 *Phys. Rev. Res.* **2** 033142
[36] Will M, Astrakharchik G E and Fleischhauer M 2021 *Phys. Rev. Lett.* **127** 103401
[37] Steel M J, Olsen M K, Plimak L I, Drummond P D, Tan S M, Collett M J, Walls D F and Graham R 1998 *Phys. Rev.* A **58** 4824–35
[38] Sinatra A, Lobo C and Castin Y 2002 *J. Phys. B: At. Mol. Opt. Phys.* **35** 3599
[39] Blakie P, Bradley A, Davis M, Ballagh R and Gardiner C 2008 *Adv. Phys.* **57** 363–455
[40] Lee T D, Low F E and Pines D 1953 *Phys. Rev.* **90** 297–302
[41] Geiser J and Nasari A 2019 *Math. Comput. Appl.* **24** 76
[42] Tsuzuki T 1971 *J. Low Temp. Phys.* **4** 441–57
[43] Landau L 1941 *Phys. Rev.* **60** 356–8
[44] Nenciu G 1980 *J. Phys. A: Math. Gen.* **13** L15
[45] Mermin N D and Wagner H 1966 *Phys. Rev. Lett.* **17** 1133–6
[46] Hohenberg P C 1967 *Phys. Rev.* **158** 383–6
[47] Petrov D S, Shlyapnikov G V and Walraven J T M 2000 *Phys. Rev. Lett.* **85** 3745–9
[48] Pethick C J and Smith H 2008 *Bose-Einsetin Condensation in Dilute Gases* (Cambridge University Press)

6 Ultracold Bose gases in dynamic disorder with tunable correlation time

Benjamin Nagler, Martin Will, Silvia Hiebel, Sian Barbosa, Jennifer Koch, Michael Fleischhauer, and Artur Widera
Phys. Rev. Lett. **128**, 233601 (2022).

This study presents an experiment involving a trapped three-dimensional gas of bosonic $^6Li_2$ Feshbach molecules, exposed to a spatiotemporal disorder potential. The disorder induces heating within the cloud, leading to evaporative particle loss. Depending on the correlation time of the disorder, the heating process is dominated either by the heating of background thermal atoms or by direct excitations of the superfluid to the thermal cloud. The latter process is theoretically estimated using particle-number conserving Bogoliubov theory [111]. The measured particle loss rates are compared to a theoretical rate model. The study illuminates the complex interplay between a superfluid gas and a time-dependent disorder. In the following, I summarize the model, focusing on the direct excitation process from the superfluid phase to thermal particles. The interplay between heating, evaporation, and cooling is described by a set of rate equations of the total particle-number N and temperature T

$$\dot{N} = \dot{N}|_{\mathrm{ev}} + \dot{N}|_{\mathrm{rel}} \tag{6.1}$$

$$\dot{T} = \dot{T}|_{\mathrm{ev}} + \dot{T}|_{N_{\mathrm{th}}} + \dot{T}|_{N_0}. \tag{6.2}$$

They account for the evaporation of the thermal component by $\dot{N}|_{\mathrm{ev}}$ and $\dot{T}|_{\mathrm{ev}}$. The molecular relaxation rate $\dot{N}|_{\mathrm{rel}}$ is the loss rate of molecules, which is present in the experiment without the speckle potential. Additionally, the rate equation includes the heating of the thermal component $\dot{T}|_{N_{\mathrm{th}}}$ and excitations from the superfluid fraction to the thermal gas $\dot{T}|_{N_0}$, both induced by the speckle potential. More details and expressions for the rates can be found in the supplementary material of the publication [P5]. To calculate the number of particles in the superfluid N_0, we assume that the system thermalizes rapidly compared to all other timescales. Thus, N_0 can be determined from the equilibrium expression of the superfluid fraction $n_c(T, N)$ by $N_0 = N\, n_c$. In leading order, assuming a noninteracting harmonically trapped gas, the superfluid fraction is $n_c = 1 - (T/T_c)^3$, where T_c is the critical BEC temperature. However, we also include an interaction and finite-size corrections to n_c [112].
To compute the excitation rate $\dot{T}|_{N_0}$, we adopt a local density approximation, treating the gas as a homogeneous BEC with Bogoliubov excitations. In order to quantify processes that change the superfluid fraction, we maintain the number of condensed particles $\hat{N}_0$ as an operator by employing total number conserving Bogoliubov theory [111]. To achieve this, we transform the creation operators of a particle $\hat{a}_{\mathbf{k}}$ into operators creating Bogoliubov phonons $\hat{b}_{\mathbf{k}}$ using

$$\hat{a}_0^\dagger \hat{a}_{\mathbf{k}}/\sqrt{N} = u_{\mathbf{k}} \hat{b}_{\mathbf{k}} + v_{-\mathbf{k}} \hat{b}_{-\mathbf{k}}^\dagger, \tag{6.3}$$

where $u_{\mathbf{k}}$ and $v_{\mathbf{k}}$ are the Bogoliubov coefficients [88, 111]. In this basis, the gas Hamiltonian becomes approximately diagonal $\hat{H}_0 = \sum_{\mathbf{k}\neq 0} \omega_k \hat{b}_{\mathbf{k}}^\dagger \hat{b}_{\mathbf{k}}$, where ω_k is the Bogoliubov dispersion

relation [88, 111]. The influence of the speckle potential is then given by the Hamiltonian

$$\hat{H}_s = \hat{N}_0 V_0(t) + \sqrt{N} \sum_{\mathbf{k}\neq 0} V_{\mathbf{k}}(t)\ (u_{\mathbf{k}} + v_{\mathbf{k}}) \left(\hat{b}_{\mathbf{k}} + \hat{b}^\dagger_{-\mathbf{k}}\right)\ + \mathcal{O}(\hat{b}^2_{\mathbf{k}}). \tag{6.4}$$

In this expression, we keep terms up to linear order in the phonon operators. This approach is similar to the Fröhlich model for polarons discussed in Section 1.2.1, in the limit of infinite impurity mass. Here $V_{\mathbf{k}}(t)$ is the Fourier transformed speckle potential $V(\mathbf{r}, t)$. We assume that the potential is a Gaussian random variable in space and time, with zero mean and variance given by

$$\overline{V(\mathbf{r}, t)V(0, 0)} = \overline{V}^2 \eta^2 \exp\left(-\mathbf{r}^2/\sigma^2 - \log(2)\, t^2/\tau^2\right), \tag{6.5}$$

where σ and τ are the correlation length and time and $\overline{V}$ the experimentally measured peak strength of the speckle potential. The parameter η is introduced to describe the trapped system using a theory designed for a homogeneous gas. We find a good agreement to the experiment for $\eta \simeq 0.05$. After solving the Heisenberg equation of motion for $\hat{N}_0$ and $\hat{b}_{\mathbf{k}}$ we find that the average condensed particle-number $N_0 = \overline{\langle \hat{N}_0 \rangle}$ decreases linear at late times $t \gg \tau$

$$N_0(t) - N_0(0) = -N\Gamma t. \tag{6.6}$$

The decay rate Γ is given analytically in Equation (A.31) of the supplementary material of the publication [P5]. Since we assume that the gas thermalizes quickly, the change in the number of condensed atoms can be directly related to a heating rate. We calculate it from the lowest order noninteracting part of the superfluid fraction and find

$$\dot{T}|_{N_0} = \frac{T_c^3}{3T^2}\Gamma. \tag{6.7}$$

Finally, we numerically solve the rate Equations (6.1) and (6.2), incorporating the other loss and heating rates. The Figures 3 b) and 4 in the publication [P5] demonstrate that the experimentally observed particle loss rates align closely with the predictions of the theoretical model across all measured parameters.

Author contributions

In the initial version, this manuscript was submitted to Phys. Rev. Lett. without Michael Fleischhauer and myself as authors. However, one of the reviewers highlighted the importance of a microscopic description of the excitation processes from the BEC into the thermal cloud. Michael Fleischhauer suggested using total particle-number conserving Bogoliubov theory to address this issue. I performed this calculation, which is discussed in detail in the supplemental material of [P5]. Benjamin Nagler derived the other excitation and particle loss rates. We both conducted the numerical simulation of the nonlinear rate equations. The experiment was mainly executed by Benjamin Nagler, who was supported by Silvia Hiebel, Sian Barbosa, and Jennifer Koch. Artur Widera supervised the project. Benjamin Nagler and Artur Widera prepared the initial version of the manuscript. In addition, Michael Fleischhauer and I contributed to the writing and review process of the final version.

Copyright

Ultracold Bose Gases in Dynamic Disorder with Tunable Correlation Time

Benjamin Nagler, Martin Will, Silvia Hiebel, Sian Barbosa, Jennifer Koch, Michael Fleischhauer, and Artur Widera*
Department of Physics and Research Center OPTIMAS, Technische Universität Kaiserslautern, 67663 Kaiserslautern, Germany

(Received 17 August 2020; revised 25 December 2021; accepted 4 May 2022; published 6 June 2022)

We study experimentally the dissipative dynamics of ultracold bosonic gases in a dynamic disorder potential with tunable correlation time. First, we measure the heating rate of thermal clouds exposed to the dynamic potential and present a model of the heating process, revealing the microscopic origin of dissipation from a thermal, trapped cloud of bosons. Second, for Bose-Einstein condensates, we measure the particle loss rate induced by the dynamic environment. Depending on the correlation time, the losses are either dominated by heating of residual thermal particles or the creation of excitations in the superfluid, a notion we substantiate with a rate model. Our results illuminate the interplay between superfluidity and time-dependent disorder and on more general grounds establish ultracold atoms as a platform for studying spatiotemporal noise and time-dependent disorder.

DOI: 10.1103/PhysRevLett.128.233601

Disorder is ubiquitous, and its impact on physical systems has been studied intensely in recent decades [1,2]. Most investigations were focused on static disorder, in which single-particle wave transport can be suppressed due to Anderson localization [3–8], and thermalization is absent in certain interacting systems [7–11]. Since phenomena like Anderson localization are based on interference, modulating disorder in time has dramatic effects. Recent studies of dynamic disorder in classical and quantum systems focusing on transport showed, in stark contrast to the static case, that it can be supported [12,13] and even accelerated beyond the ballistic regime [14,15]. However, the interplay between superfluidity and long-range coherence with time-dependent disorder, and dissipation induced by the dynamic environment, have not yet been investigated in experiments. The impact of dynamic disorder is of broad interest, for example, in the context of energy transfer in biological systems [16,17], the electrical conductivity of ionic polymers [18] and microemulsions [19], chemical reactions [20], wave propagation in the sea [21], superconductors [22], and quantum walks [23]. Theoretical works on spatiotemporal noise predict a nonequilibrium phase transition [24,25] which is induced by the random environment. For quantum systems, it seems natural to pose the question if there is an extention of preparing nonequilibrium states by spatiotemporal periodic drive [26,27] to the case of general broadband spatiotemporal noise. This novel regime is particularly complicated by the nonlinearity of interacting quantum systems as Bose-Einstein condensates (BECs), giving rise to collective phenomena such as superfluid flow. One potential challenge is the unfavorable heating of atomic systems due to energy absorption from the dynamic environment [26]. The role of dissipation is of general interest in the paradigm of open quantum systems [28], which is realized by, e.g., quantum gases coupled to environments with spatiotemporal noise.

Here, we study the nonequilibrium dynamics of ultracold molecular Li_2 gases in tunable dynamical disorder. We employ a novel scheme to realize a time-dependent optical speckle potential with variable correlation time, inspired by a method for the decorrelation of light fields [29]. For ultracold, thermal ensembles, we observe the microscopic onset of dissipation for decreasing correlation time, which is well described by a random-walk model in momentum space. For BECs, the disorder additionally creates direct excitations in the superfluid, depleting the superfluid fraction. We model the dissipative dynamics of the quantum gas by an open-system rate model, treating the superfluid excitations in two complementary ways. Importantly, comparison with experimental data suggests a window of correlation times having negligible superfluid excitations, well suited for studies of nonequilibrium dynamics of quantum fluids.

Experimentally, we prepare dilute gases of bosonic $^6Li_2$ Feshbach molecules in a cigar-shaped hybrid magnetic-optical trap [Fig. 1(a)]; for details see Refs. [30,31]. The magnetic field close to a magnetic Feshbach resonance at 832.2 G [32] sets the s-wave scattering length a between the molecules and thus their binding energy. Typical thermal (degenerate) samples contain $> 10^5$ molecules at a temperature of $T = 590$ nK (50 nK). A repulsive optical speckle potential [33] at a wavelength of 532 nm introduces the disorder. The typical size of the anisotropic speckle grains is $\sigma^2 \times \sigma_\parallel$ with $\sigma = 750$ nm and $\sigma_\parallel = 10.2$ μm the correlation lengths along the x/y and z direction. We characterize the strength of the disorder by the spatial average $\bar{V}$ of the speckle potential at the cloud position.

We create the rotated speckle pattern by transmitting a laser beam through two glass plates with random surface structures, i.e., diffusers, rotated against each other, and

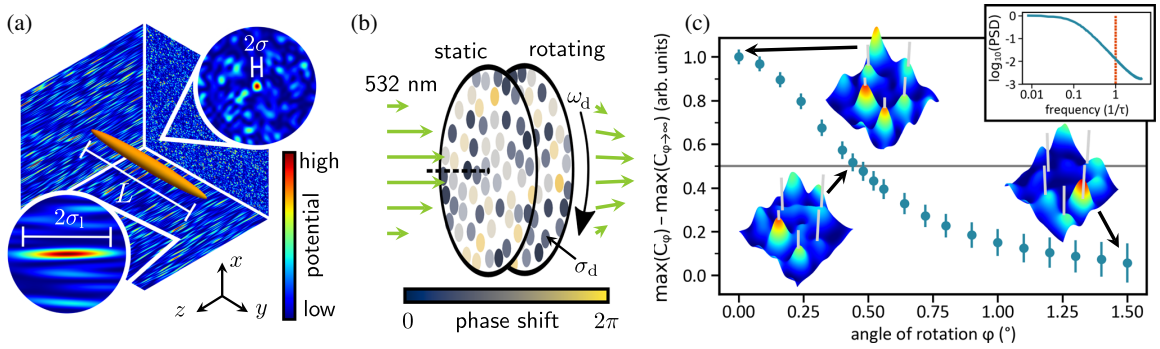

FIG. 1. (a) Sketch of experimental realization. Cigar-shaped clouds of $^6Li_2$ molecules with typical size $L \sim 300$ μm are exposed to an anisotropic speckle potential. (b) Creation of dynamic speckle. The dots with size σ_d represent the random surface of the diffusers, and their colors indicate the magnitude of the phase shift they imprint on incident light. The transmitted light is focused on the cloud. (c) Evolution of a dynamic speckle pattern. Maximum value of the cross-correlation function C_φ of the speckle intensity. Error bars mark the uncertainty of a fit that is used to extract the maximum value from C_φ. Insets: a section of a simulated speckle pattern with $\max(C_\varphi)$, as indicated by the arrows. Gray lines mark the positions of five distinct peaks in the initial speckle and simplify tracking the evolution of the intensity distribution. The inset plot shows the calculated temporal power spectral density (PSD) of a dynamic speckle (blue, solid line), where the inverse correlation time roughly coincides with the frequency at which PSD has dropped to $1/100$ of its maximum value at zero frequency. For comparison, we also show the PSD of a speckle whose mean potential is periodically modulated with frequency $1/\tau$ (red, dashed).

focusing the light field onto the atoms [Fig. 1(b)]. Upon rotation, the local phase imprints change significantly, causing the height and position of the interference pattern's speckle grains to change. We quantify the resemblance to the initial speckle intensity distribution $I_{\varphi=0^\circ}$ by the maximum value of the cross-correlation function [34], $\max(C_\varphi)$, with

$$C_\varphi(x,y) = \int dx'dy' I_{\varphi=0^\circ}(x',y') I_\varphi(x'+x, y'+y). \qquad (1)$$

$I_\varphi(x,y)$ are two-dimensional intensity distributions in the focal plane for rotation angle φ of the diffuser plate, independently measured in a test setup. We define the correlation angle φ_c at which $\max(C_\varphi)$ has dropped to half its initial value; see Fig. 1(c). For rotation at constant angular velocity ω_d, the correlation angle translates into a correlation time $\tau = \varphi_c/\omega_d$. In the experimental setup, $\omega_d \leq 2100\,^\circ\mathrm{s}^{-1}$ and $\varphi_c = 0.6^\circ$; hence $\tau > 285$ μs. Importantly, in contrast to a periodically driven potential, the temporal power-spectral density of this dynamic speckle comprises a broad distribution of frequencies, where low-frequency contributions dominate, and the inverse correlation time can be interpreted as a bandwidth or cutoff frequency [see inset of Fig. 1(c)].

To study the response of thermal clouds to the dynamic disorder, we prepare samples with 3.4×10^5 molecules with $a = 1524\,a_0$ (a_0 is the Bohr radius) in a trap with harmonic frequencies $\omega_x, \omega_y, \omega_z = 2\pi \times (498, 22.1, 340)$ Hz at a temperature of $T = 590$ nK. Following the end of the evaporation ramp, the cloud is allowed to relax for 500 ms to ensure thermal equilibrium. In order to minimize excitations in the gas, we increase the potential of the dynamic speckle during a 50 ms linear ramp to its final value of $\bar{V}/k_B = 30.5$ nK $\ll T$, where k_B is the Boltzmann constant. After a variable hold time $d_s \leq 180$ ms, the speckle is extinguished during 50 ms, and we take an absorption image of the trapped cloud. We extract the temperature by fitting a Bose-enhanced Gaussian function [35] to the integrated column-density distribution. We observe that the cloud temperature T is proportional to the hold time d_s and the slope, i.e., the heating rate $P = dT/dd_s$, grows with increasing $1/\tau$; see Fig. 2(a). The heating rate is extracted by fitting a linear function to the data. We compare these results to a numerical simulation of classical, non-interacting point particles with thermal velocity distribution in a dynamic, homogeneous speckle in two dimensions [36]. The dimensional reduction is facilitated by the anisotropic speckle, which allows one to neglect the much weaker potential gradients along the z axis as compared with the xy plane. The heating rates from this simulation [Fig. 2(b)] yield good agreement with the experimental data. We conclude that the heating is intrinsically a single-particle effect, not modified by the elastic molecule-molecule scattering at a rate of 11 ms^{-1} or inelastic collisions. Moreover, we develop a microscopic heating model based on a random walk in momentum space for the limiting case $k_BT \gg \bar{V}$, which is realized in the experiment. Single particles travel on almost straight trajectories, and experience "kicks" with momentum change $\Delta p \ll p$ from the time-dependent potential. The resulting heating rate is given by

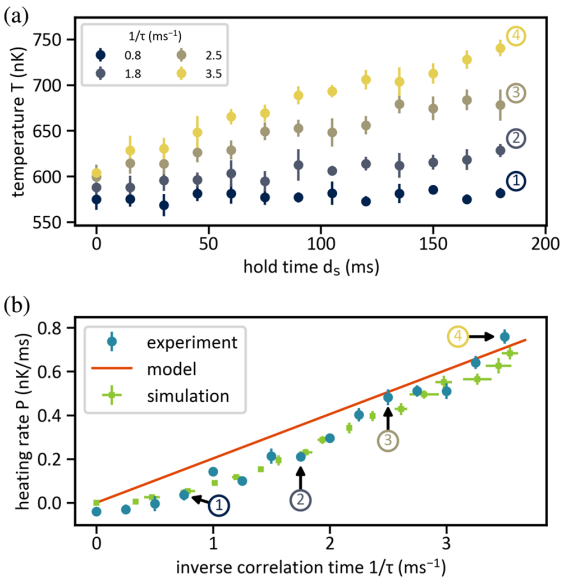

FIG. 2. Heating of a thermal ensemble with initial temperature $T = 590$ nK in dynamic speckle disorder with $\bar{V} = 30.5\ \mathrm{nK} \times k_B$. (a) Cloud temperature T versus hold time d_s for various values of $1/\tau$. (b) Heating rate P versus inverse correlation time $1/\tau$. Squares result from the numerical simulation, solid line from the microscopic model. Error bars of experimental data in (b) denote uncertainty of the fit, other errors the standard deviation of 5 repetitions.

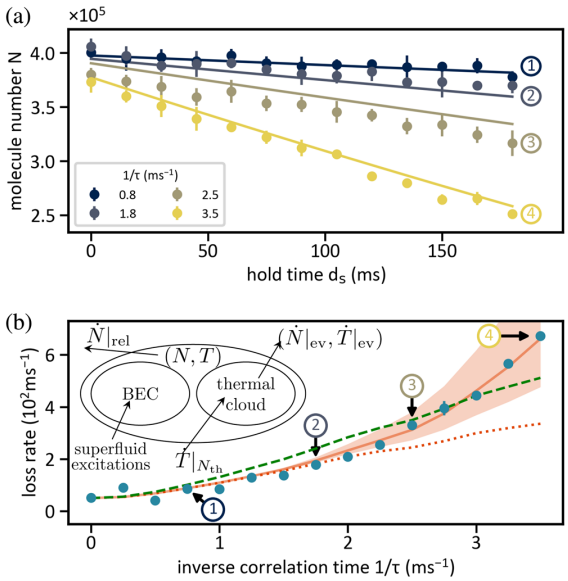

FIG. 3. Dissipation of a BEC in dynamic disorder. (a) Total molecule number N versus hold time d_s for various values of $1/\tau$. Error bars denote the standard deviation of 5 repetitions. Solid lines are from the rate model. (b) Loss rates versus inverse correlation time $1/\tau$. Error bars of experimental data points (blue) show the error estimation of the linear fit and are smaller than the marker size for most data points. Lines indicate results from the rate model, including thermal heating and phenomenologically superfluid excitations in the inhomogeneous gas (solid), thermal heating and microscopic particle loss from the homogeneous condensate (dashed green), or only heating of the thermal cloud (dotted). The shaded area represents a $\pm 20\%$ variation of v_s. Inset: the processes included in the open-system rate model.

$$P = \frac{\bar{V}^2}{2k_B^2 T\tau}\gamma, \tag{2}$$

where the constant γ corrects for the dimensionality and the trapping potential in each dataset independently [36]. The model matches the measured heating rates for sufficiently large inverse correlation times [Fig. 2(b)] [37].

In order to study quantum gases in dynamical disorder, we cool samples with $N = 4 \times 10^5$ molecules and scattering length $a = 2706\,a_0$ to $T = 50$ nK, far below the noninteracting critical temperature of condensation $T_c = 245$ nK. Hence, we expect a condensate fraction > 0.8 and a BEC with chemical potential $\mu = 250\ \mathrm{nK} \times k_B = 5.2\ \mathrm{kHz} \times h$, where h is Planck's constant. The corresponding timescale $h/\mu = 190\ \mu$s is smaller than the experimentally accessible correlation times, and the healing length at the trap center $\xi = 380$ nm [41] falls below the correlation lengths. Thus, for these maximum values, the condensate can temporally react to and spatially resolve all changes and details of the speckle potential. The experimental sequence for the exposure to the dynamic speckle is the same as for thermal clouds. Instead of the temperature, we monitor the total molecule number N of the sample, because the large condensed fraction does not allow one to extract a temperature from absorption images reliably. We find that the molecule number decreases linearly with d_s, and the loss rate $-dN/dd_s$ grows with $1/\tau$ (see Fig. 3). We distinguish two main processes contributing to the loss of molecules from the trap. On the one hand, as described before, the dynamic speckle heats the residual thermal component of the gas. The rising temperature causes molecules to transfer from the BEC to the thermal fraction, from which molecules with sufficient energy can evaporate, which in turn cools the sample. On the other hand, the motion of the dynamic speckle creates excitations in the BEC, which again diminishes the condensate fraction because of Landau damping [42]. We model the underlying dynamics by two approaches. The first takes into account the trap but treats superfluid damping in a phenomenological way, whereas the second provides analytic expressions for the particle loss from the condensate fraction in a homogeneous superfluid.

Due to the BEC being superfluid, excitations are mainly expected if the typical velocity v_s of the speckle exceeds the local Landau critical velocity $v_c(\boldsymbol{r}) = \sqrt{g n_0(\boldsymbol{r})/m}$ in the condensate, where n_0 is the condensate density distribution and g the coupling constant [41]. These local

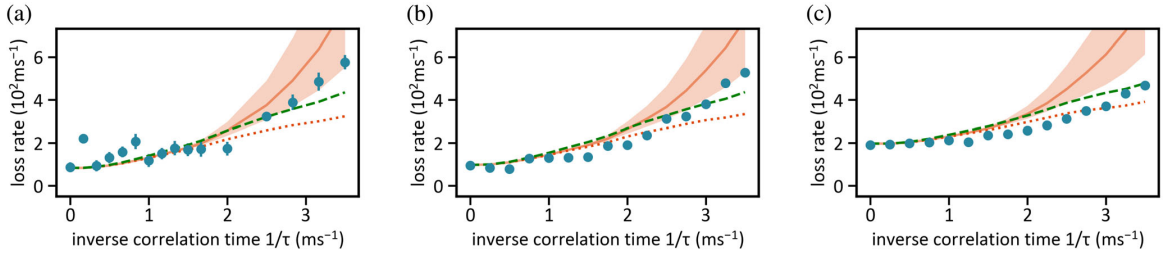

FIG. 4. Loss rates of BECs in dynamic speckle for various values of the s-wave scattering length a. The allocation of colors and line styles is the same as in Fig. 3(b). (a) $a = 1524a_0$, $\mu = 187$ nK $\times k_B = 3.9$ kHZ $\times h$; (b) $a = 1310a_0$, $\mu = 173$ nK $\times k_B = 3.6$ kHz $\times h$; (c) $a = 982a_0$, $\mu = 144$ nK $\times k_B = 3.0$ kHz $\times h$. The range of interaction strengths explored is limited for lower interactions by the decreasing collisional lifetime of molecules and for higher interactions by the emergence of free atoms as the binding energy decreases.

quantities are well defined because, for our parameters, the local-density approximation is valid [43]. We can estimate the largest velocity scale of the speckle from the correlation lengths and time to be $v_s = \sqrt[3]{\sigma^2\sigma_l}/\tau < 6.3$ mm s^{-1}, which is below the maximum critical velocity $v_c(\mathbf{0}) = 13.2$ mm s^{-1} at the center of the condensate. However, because of the Thomas-Fermi density profile [44], there are always regions with $v_c(\boldsymbol{r}) < v_s$ where excitations are possible. Additionally, inelastic collisions between molecules cause losses, even in the absence of any speckle potential [45]. We capture this interplay between heating, evaporation, and cooling by a set of rate equations

$$\dot{N} = \dot{N}|_{\mathrm{ev}} + \dot{N}|_{\mathrm{rel}} \tag{3}$$

$$\dot{T} = \dot{T}|_{N_{\mathrm{th}}} + \dot{T}|_{\mathrm{ev}} + (\dot{T}|_{N_0}) \tag{4}$$

modeling the open quantum system (for details see the Supplemental Material [36]), which includes the processes evaporation from the thermal component $(\dot{N}|_{\mathrm{ev}}, \dot{T}|_{\mathrm{ev}})$, molecular relaxation $\dot{N}|_{\mathrm{rel}}$, and heating of the thermal component by the dynamic speckle $\dot{T}|_{N_{\mathrm{th}}}$ [see inset of Fig. 3(b)]. We calculate the number of superfluid molecules $N_0 = N \times n_c(T/T_c, N, a)$ using an expression for the condensate fraction n_c, which incorporates the intermolecular interaction and finite size of the system [36,46]. We neglect effects of the relatively strong quantum depletion [46], because the depleted density remains superfluid [47]. The number of thermal molecules is given by $N_{\mathrm{th}} = N - N_0$ and we assume the system to be in thermal equilibrium at all times. In order to include the effect of the speckle potential onto the superfluid molecules, in a first approach, we calculate the fraction f of the ones located in regions of the condensate where $v_c(\boldsymbol{r}) < v_s$. We assume that in addition to thermally excited molecules N_{th}, the condensed particles in the former mentioned area $f \times N_0$ are removed from the system by evaporation. Numerically, we find that f is close to zero below $v_s/v_c(\mathbf{0}) = 0.3$ [36], which roughly coincides with $1/\tau \approx 2$ ms^{-1}. This model phenomenologically including superfluid excitations in the inhomogeneous system is indicated as solid line in Figs. 3 and 4.

This approach obviously neglects the intricate dynamics, interactions, and spectrum of superfluid excitations [48]. Therefore, in a second approach, we compute the rate of particles transferred from the condensate to the thermal fraction using number-conserving Bogoliubov theory in a speckle with Gaussian-shaped spatiotemporal spectrum [36,49], contributing another heating term $\dot{T}|_{N_0}$ in Eq. (4). For a homogeneous condensate, we find [36]

$$\dot{T}|_{N_0} = \frac{\eta^2 \bar{V}^2 T_c^3 \pi\sigma^3}{6T^2\hbar^2 v_c \xi\sqrt{\sigma^2 + v_c^2\tilde{\tau}^2}} e^u \{2u[I_{5/4}(u) - I_{3/4}(u) + I_{1/4}(u) - I_{-1/4}(u)] + I_{1/4}(u)\}, \tag{5}$$

where $I_\nu(u)$ are an modified Bessel function of the first kind [50], u is defined as $u = (\sigma^2 + v_c^2\tilde{\tau}^2)^2/16\xi^2 v_c^2\tilde{\tau}^2$, and $\tilde{\tau} = \tau/\sqrt{\log 2}$. In order to adopt the homogeneous theory to the inhomogeneous experimental system, we use the parameter η, which we set to $\eta \approx 0.05$, effectively accounting for the experimental speckle anisotropy and effects of the speckle's inhomogeneity to roughly yield the experimental particle loss rate [36], and evaluate Eq. (5) with the mean superfluid density. This value of η has been obtained by calculating the loss rates for all experimental parameter sets and for several values of η. We solve Eqs. (3) and (4) numerically to obtain the time dependence of the particle number and compare the results to the experimental data in Fig. 3, where this model microscopically including particle loss in a homogeneous system is shown as a dashed line. Both models reproduce the measured loss rates closely. Molecular relaxation is included via the relaxation rate α such that the loss rate in the static speckle matches the measured one; we find agreement with previously reported values [36,51,52]. For relatively long correlation times $1/\tau \lesssim 2$ ms^{-1}, the losses due to superfluid excitations are negligible, and the loss rates are well captured merely by the heating of the thermal cloud [dotted line in Fig. 3(b)]. In the case of $1/\tau \gtrsim 2$ ms^{-1}, both loss mechanisms contribute significantly. Reducing the interaction strength, the

phenomenological rate model systematically overestimates the loss rate by assuming immediate depletion of condensate atoms in the region $v_c(\vec{r}) < v_s$ (see Fig. 4 and the Supplemental Material [36]), while the model computing the excitation rate from the condensate yields good agreement for all interaction strengths with one common fit parameter.

Our studies indicate a regime, where quantum fluids are shielded from direct superfluid excitations even for a broadband excitation, prevailing for a broad range of interaction strengths. The tight control over correlation times points toward future studies of transport in time-dependent disorder both for classical and quantum systems with strong interactions.

We thank Hans Kroha and Axel Pelster for fruitful discussions and Maximilian Kaiser for carefully reading the manuscript. This work was supported by the Deutsche Forschungsgemeinschaft (DFG, German Research Foundation) via the Collaborative Research Center SFB/TR185 (Project No. 277625399). J. K. and M. W. were supported by the Max Planck Graduate Center with the Johannes Gutenberg-Universität Mainz (MPGC).

*widera@physik.uni-kl.de

[1] T. Vojta, Disorder in quantum many-body systems, Annu. Rev. Condens. Matter Phys. **10**, 233 (2019).
[2] *50 Years of Anderson Localization*, edited by E. Abrahams (World Scientific, Singapore; London, 2010).
[3] P. W. Anderson, Absence of diffusion in certain random lattices, Phys. Rev. **109**, 1492 (1958).
[4] D. S. Wiersma, P. Bartolini, A. Lagendijk, and R. Righini, Localization of light in a disordered medium, Nature (London) **390**, 671 (1997).
[5] G. Roati, C. D'Errico, L. Fallani, M. Fattori, C. Fort, M. Zaccanti, G. Modugno, M. Modugno, and M. Inguscio, Anderson localization of a non-interacting Bose–Einstein condensate, Nature (London) **453**, 895 (2008).
[6] J. Billy, V. Josse, Z. Zuo, A. Bernard, B. Hambrecht, P. Lugan, D. Clément, L. Sanchez-Palencia, P. Bouyer, and A. Aspect, Direct observation of Anderson localization of matter waves in a controlled disorder, Nature (London) **453**, 891 (2008).
[7] S. S. Kondov, W. R. McGehee, W. Xu, and B. DeMarco, Disorder-Induced Localization in a Strongly Correlated Atomic Hubbard Gas, Phys. Rev. Lett. **114**, 083002 (2015).
[8] M. Schreiber, S. S. Hodgman, P. Bordia, H. P. Luschen, M. H. Fischer, R. Vosk, E. Altman, U. Schneider, and I. Bloch, Observation of many-body localization of interacting fermions in a quasirandom optical lattice, Science **349**, 842 (2015).
[9] J. Z. Imbrie, On many-body localization for quantum spin chains, J. Stat. Phys. **163**, 998 (2016).
[10] J. Smith, A. Lee, P. Richerme, B. Neyenhuis, P. W. Hess, P. Hauke, M. Heyl, D. A. Huse, and C. Monroe, Many-body localization in a quantum simulator with programmable random disorder, Nat. Phys. **12**, 907 (2016).
[11] K. X. Wei, C. Ramanathan, and P. Cappellaro, Exploring Localization in Nuclear Spin Chains, Phys. Rev. Lett. **120**, 070501 (2018).
[12] P. Hänggi and F. Marchesoni, Artificial Brownian motors: Controlling transport on the nanoscale, Rev. Mod. Phys. **81**, 387 (2009).
[13] S. Gopalakrishnan, K. R. Islam, and M. Knap, Noise-Induced Subdiffusion in Strongly Localized Quantum Systems, Phys. Rev. Lett. **119**, 046601 (2017).
[14] A. M. Jayannavar and N. Kumar, Nondiffusive Quantum Transport in a Dynamically Disordered Medium, Phys. Rev. Lett. **48**, 553 (1982).
[15] L. Levi, Y. Krivolapov, S. Fishman, and M. Segev, Hyper-transport of light and stochastic acceleration by evolving disorder, Nat. Phys. **8**, 912 (2012).
[16] P. Rebentrost, M. Mohseni, I. Kassal, S. Lloyd, and A. Aspuru-Guzik, Environment-assisted quantum transport, New J. Phys. **11**, 033003 (2009).
[17] A. W. Chin, A. Datta, F. Caruso, S. F. Huelga, and M. B. Plenio, Noise-assisted energy transfer in quantum networks and light-harvesting complexes, New J. Phys. **12**, 065002 (2010).
[18] M. A. Ratner and A. Nitzan, Conductivity in polymer ionics. Dynamic disorder and correlation, Faraday Discuss. **88**, 19 (1989).
[19] G. S. Grest, I. Webman, S. A. Safran, and A. L. R. Bug, Dynamic percolation in microemulsions, Phys. Rev. A **33**, 2842 (1986).
[20] I. Sendiña-Nadal, S. Alonso, V. Pérez-Muñuzuri, M. Gómez-Gesteira, V. Pérez-Villar, L. Ramírez-Piscina, J. Casademunt, J. M. Sancho, and F. Sagués, Brownian Motion of Spiral Waves Driven by Spatiotemporal Structured Noise, Phys. Rev. Lett. **84**, 2734 (2000).
[21] A. L. Virovlyansky, D. V. Makarov, and S. V. Prants, Ray and wave chaos in underwater acoustic waveguides, Phys. Usp. **55**, 18 (2012).
[22] A. G. Aronov and P. Wölfle, Effect of a fluctuating magnetic field on weak localization in a two-dimensional disordered system, Phys. Rev. B **50**, 16574 (1994).
[23] Y. Yin, D. E. Katsanos, and S. N. Evangelou, Quantum walks on a random environment, Phys. Rev. A **77**, 022302 (2008).
[24] C. Van den Broeck, J. M. R. Parrondo, and R. Toral, Noise-Induced Nonequilibrium Phase Transition, Phys. Rev. Lett. **73**, 3395 (1994).
[25] J. García-Ojalvo and J. M. Sancho, Colored noise in spatially extended systems, Phys. Rev. E **49**, 2769 (1994).
[26] A. Eckardt, Colloquium: Atomic quantum gases in periodically driven optical lattices, Rev. Mod. Phys. **89**, 011004 (2017).
[27] K. Singh, C. J. Fujiwara, Z. A. Geiger, E. Q. Simmons, M. Lipatov, A. Cao, P. Dotti, S. V. Rajagopal, R. Senaratne, T. Shimasaki, M. Heyl, A. Eckardt, and D. M. Weld, Quantifying and Controlling Prethermal Nonergodicity in Interacting Floquet Matter, Phys. Rev. X **9**, 041021 (2019).
[28] H.-P. Breuer and F. Petruccione, *The Theory of Open Quantum Systems* (Oxford University Press, New York, 2007).
[29] F. T. Arecchi, Measurement of the Statistical Distribution of Gaussian and Laser Sources, Phys. Rev. Lett. **15**, 912 (1965).
[30] B. Gänger, J. Phieler, B. Nagler, and A. Widera, A versatile apparatus for fermionic lithium quantum gases based on an

interference-filter laser system, Rev. Sci. Instrum. **89**, 093105 (2018).
[31] B. Nagler, M. Radonjić, S. Barbosa, J. Koch, A. Pelster, and A. Widera, Cloud shape of a molecular Bose–Einstein condensate in a disordered trap: A case study of the dirty boson problem, New J. Phys. **22**, 033021 (2020).
[32] G. Zürn, T. Lompe, A. N. Wenz, S. Jochim, P. S. Julienne, and J. M. Hutson, Precise Characterization of ^{6}Li Feshbach Resonances Using Trap-Sideband-Resolved RF Spectroscopy of Weakly Bound Molecules, Phys. Rev. Lett. **110**, 135301 (2013).
[33] J. W. Goodman, *Speckle Phenomena in Optics* (Roberts and Company Publishers, 2007).
[34] A. Papoulis and McGraw-Hill, *The Fourier Integral and Its Applications*, Classic Textbook Reissue Series (McGraw-Hill, New York, 1962).
[35] W. Ketterle, D. Durfee, and D. Stamper-Kurn, Making, probing and understanding Bose-Einstein condensates, in *Proceedings of the International School of Physics "Enrico Fermi"*, edited by M. Inguscio, S. Stringari, and C. E. Wieman (1999), Vol. 140, pp. 61–176.
[36] See Supplemental Material at http://link.aps.org/supplemental/10.1103/PhysRevLett.128.233601 for details of the experimental setup and of the numerical and analytical models used.
[37] For the complementary regime of high particle velocities, theoretical works on the transport of classical particles in dynamic disorder predict a universal time dependence of the average kinetic energy of a particle $E_{\mathrm{kin}} \propto t^{2/5}$ [38–40]. Numerical simulations of our system reproduce power-law behavior with different exponents for sufficiently long observation times.
[38] L. Golubović, S. Feng, and F.-A. Zeng, Classical and Quantum Superdiffusion in a Time-Dependent Random Potential, Phys. Rev. Lett. **67**, 2115 (1991).
[39] M. N. Rosenbluth, Comment on "Classical and Quantum Superdiffusion in a Time-Dependent Random Potential", Phys. Rev. Lett. **69**, 1831 (1992).
[40] Y. Krivolapov and S. Fishman, Universality classes of transport in time-dependent random potentials, Phys. Rev. E **86**, 030103(R) (2012).
[41] C. J. Pethick and H. Smith, *Bose–Einstein Condensation in Dilute Gases*, 2nd ed. (Cambridge University Press, Cambridge, England, 2008).
[42] L. Pitaevskii and S. Stringari, Landau damping in dilute Bose gases, Phys. Lett. A **235**, 398 (1997).
[43] Y. Kagan, G. V. Shlyapnikov, and J. T. M. Walraven, Bose-Einstein Condensation in Trapped Atomic Gases, Phys. Rev. Lett. **76**, 2670 (1996).
[44] L. Pitaevskii and S. Stringari, *Bose–Einstein Condensation and Superfluidity*, International Series of Monographs on Physics (Oxford University Press, New York, 2016).
[45] D. S. Petrov, C. Salomon, and G. V. Shlyapnikov, Weakly Bound Dimers of Fermionic Atoms, Phys. Rev. Lett. **93**, 090404 (2004).
[46] H. Xiong, S. Liu, G. Huang, Z. Xu, and C. Zhang, Critical temperature and condensate fraction of the trapped interacting Bose gas with finite-size effects, J. Phys. B **34**, 3013 (2001).
[47] A. Miller, D. Pines, and P. Nozières, Elementary excitations in liquid helium, Phys. Rev. **127**, 1452 (1962).
[48] A. J. Leggett, *Quantum Liquids: Bose Condensation and Cooper Pairing in Condensed-Matter Systems* (Oxford University Press, United States, 2008).
[49] Y. Castin, Bose-einstein condensates in atomic gases: Simple theoretical results, in *Coherent Atomic Matter Waves*, edited by R. Kaiser, C. Westbrook, and F. David (Springer Berlin Heidelberg, Berlin, Heidelberg, 2001), pp. 1–136.
[50] M. Abramowitz and I. A. Stegun, *Handbook of Mathematical Functions with Formulas, Graphs, and Mathematical Tables*, 9th dover printing, 10th gpo printing ed. (Dover, New York, 1964).
[51] J. Cubizolles, T. Bourdel, S. J. J. M. F. Kokkelmans, G. V. Shlyapnikov, and C. Salomon, Production of Long-Lived Ultracold Li_2 Molecules from a Fermi Gas, Phys. Rev. Lett. **91**, 240401 (2003).
[52] S. Jochim, M. Bartenstein, A. Altmeyer, G. Hendl, C. Chin, J. H. Denschlag, and R. Grimm, Pure Gas of Optically Trapped Molecules Created from Fermionic Atoms, Phys. Rev. Lett. **91**, 240402 (2003).

Supplementary Material

In the following, details on the experimental procedure, the theoretical models and additional data are given.

Experimental procedure

We prepare quantum gases in the BEC-BCS crossover regime by forced evaporative cooling of fermionic ^{6}Li atoms in an equal mixture of the two lowest-lying Zeeman substates of the electronic ground state $^2S_{1/2}$. Evaporation takes place in a hybrid magnetic-optical trap at a magnetic field of 763.6 G on the repulsive side of a Feshbach resonance centered at 832.2 G [32], where atoms of opposite spin form bosonic molecules that eventually condense into a BEC. After evaporation, the sample is held at constant trap depth for 300 ms to ensure thermal equilibrium before the magnetic field is linearly ramped to its final value during 200 ms. At this point, the dynamic speckle is introduced by ramping the laser power linearly during 50 ms to its final value (Fig. 5). The laser power is held constant for a variable time d_s and subsequently extinguished. After a waiting time of 30 ms, we employ resonant high-intensity absorption imaging [53] to extract the column density distribution in the y-z-plane. For thermal clouds, the temperature is determined by fitting a Bose-enhanced Gaussian function to the density distribution. In the case of BECs, we estimate the sample temperature to be $T = 50 \pm 25$ nK by ramping the magnetic field to 680 G prior to imaging and fitting a bimodal density distribution [54].

The hybrid trap consists of an optical dipole trap and a magnetic saddle potential, which provides weak (anti-) confinement in (z-) x- and y-direction, whereas the optical trap strongly constrains the cloud along x and z. Since the saddle potential is an accessory to the magnetic field used to address the Feshbach resonance, its curvature depends on the field magnitude. The trapping frequencies and other relevant parameters for all presented experimental data are listed in Tab. I.

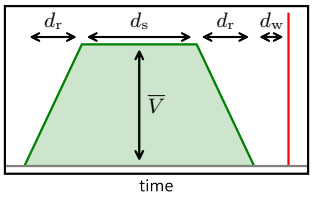

FIG. 5. Experimental sequence. Following the end of the evaporation ramp and a hold time of 500 ms, the dynamic speckle is ramped up linearly during $d_\mathrm{r} = 50$ ms. After a variable hold time $d_\mathrm{s} < 180$ ms, the speckle is slowly extinguished and we take an in-situ absorption image (red line) of the cloud after a waiting time $d_\mathrm{w} = 30$ ms.

The speckle potential is created by passing a laser beam of wavelength 532 nm through two diffusive plates (Edmund Optics 47-988 and 47-991) and focusing the light, using an objective with numerical aperture 0.29, onto the atoms. They experience a repulsive and spatially random dipole potential V, which we characterize by its spatial average $\overline{V}$ at the focal point of the objective. The typical grain size of the speckle is given by the Gaussian-shaped autocorrelation function of the potential with $1/e$ widths (correlation lengths) $\sigma = 750$ nm transversely to and $\sigma_\mathrm{l} = 10.2$ µm along the beam propagation direction. As the speckle beam has a Gaussian envelope with waist 440 µm, the average potential is inhomogeneous across the spatial extension of the cloud. We use a motorized rotation stage (OWIS DRTM 65-D35-HiDS) to rotate one of the circular diffusers around its principal axis. As a consequence, the rotation speed and hence the phase shift imprinted onto the light field depends on the distance from the rotation axis. This renders the correlation time k-vector dependent. However, the light-field distribution is imaged onto the plane of the atoms, which is deep in the Fraunhofer limit. Thus at every position of the atoms, all k-vectors contribute to the interference, yielding a Gaussian correlation in space and time with the correlation length and time as given in the manuscript.

Dynamical Speckle Potential

The static speckle potential is created by transmitting a laser beam through a glass plate with a random surface structure, i.e., a diffuser. The diffuser imprints a phase pattern whose spatial variation is characterized by the correlation length $\sigma_\mathrm{d} \approx 20$ µm of the surface structure (Fig. 1 (b)). By focusing the beam, all partial waves with random phases interfere and create a static speckle pattern with correlation length σ in the focal plane. The speckle is rendered dynamic by adding a second, similar diffuser directly after the first one, which is mounted in a motorized rotation stage. Upon rotation of the second diffuser, the details of the imprinted phase pattern are altered significantly once the local displacement of

magnetic field (G)	700.0	720.0	730.0	763.6
$\omega_y/2\pi$ (Hz)	21.7	22.0	22.1	22.6
a (a_0)	982	1310	1524	2706
$N(0)$ (10^3)	288	325	345	406
α (10^{-13}cm^3 s^{-1})	2.9	1.0	1.2	0.65

TABLE I. Overview of parameters for different magnetic fields. Scattering lengths taken from [32]. $N(0)$ is the initial molecule number used for the solution of Eqs. (A.34) and (A.35). α is the molecular relaxation rate.

the diffuser is comparable to σ_d. As a consequence, the height and position of the speckle grains change until the intensity distribution bears no resemblance to its initial state before rotation, see Fig. 1 (c).

Numerical simulation of classical particles in dynamic speckle

We simulate the motion of classical, noninteracting point particles in a dynamic, homogeneous speckle potential $V = V(x, y, t)$ in two spatial dimensions. To this end, we numerically solve Newton's equation of motion

$$m\boldsymbol{a} = -\boldsymbol{\nabla} V, \tag{A.6}$$

where $\boldsymbol{a}$ is the acceleration, using the explicit third-order Runge-Kutta method [55]. For the spatial and temporal discretization, we choose $\Delta x = \Delta y = 100\,\mathrm{nm}$ and $\Delta t = 1\,\mu\mathrm{s}$, which are far below all other relevant length and time scales. The simulation encompasses a rectangular region with size $22.5\,\mu\mathrm{m} \times 22.5\,\mu\mathrm{m}$ that is confined by hard walls. A typical simulation calculates the trajectories of $\sim 50\,000$ particles which start at random positions with velocities drawn from a thermal distribution. Our main observable is the growth rate of the ensemble-averaged kinetic energy, from which we get the heating rate.

We use a simple numerical approach to simulate a homogeneous two-dimensional speckle pattern. The scalar electric field distribution of a speckle is readily obtained from the discrete fast Fourier transform $\mathcal{F}(R)$ of a two-dimensional square array R filled with random phase factors [33]. Thus, each entry (k, l) of R is given by $R_{k,l} = \exp(2\pi i Q)$, where Q is a continuous random variable being uniformly distributed in the interval $[0, 1)$. R represents the electric field of the light after passing through the diffusers. In order to increase the smoothness of the output of $\mathcal{F}$, R is zero-padded. Since we are interested in the speckle intensity distribution S, we calculate $S = |\mathcal{F}(R)|^2$.

Such a static speckle is rendered dynamic by the following procedure. We call $R(t)$ and $S(t)$ the random phase array and corresponding intensity distribution at time t. $R(t)$ is propagated in time by adding a small phase $2\pi i Q\sqrt{\Delta t_\mathrm{s}/\tau}$ to each entry, where $\Delta t_\mathrm{s} < \tau$ is the time step. This simulates the continuous phase evolution on a time scale τ that is caused by the rotating diffuser. It is captured by the iteration formula

$$R_{k,l}(t + \Delta t_\mathrm{s}) = R_{k,l}(t) \times \exp\left(2\pi i Q\sqrt{\frac{\Delta t_\mathrm{s}}{\tau}}\right). \tag{A.7}$$

In order to minimize computational effort, we choose $\Delta t_\mathrm{s} = \tau/10 \gg \Delta t$ and use pointwise linear interpolation between $S(t)$ and $S(t + \Delta t_\mathrm{s})$ for intermediate times. It is important to note that Eq. (A.7) does not produce a sequence of speckle patterns $S(t)$ with a correlation time that is precisely given by τ. The exact value depends on the size of R, the zero-padding of R, and the choice of Δt_s and typically misses τ by several 10 %. Hence, we extract the correlation time from each sequence $S(t)$ by evaluating the auto-correlation function [56] of $S(t)$.

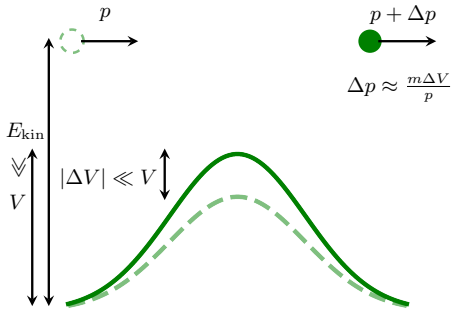

FIG. 6. Schematic illustration of a particle traversing a single grain of the dynamic speckle.

Derivation of Eq. (2)

To compute the heating rate in the thermal case, we assume the limiting case $k_\mathrm{B}T \gg \overline{V}$, which is realized in the experiment. Here, single particles in two dimensions travel on almost straight trajectories through the time-dependent potential. Each time a particle with momentum p traverses a speckle grain, it experiences a "kick", changing its momentum by an amount $\Delta p \ll p$ that is proportional to the change in potential height during flyby [36]. Due to the random spatial distribution and height of the grains, the particle experiences a series of kicks in random directions, performing a random walk [57].

Quantitatively, consider a particle with mass m and momentum p traveling through the dynamic speckle potential. We make two assumptions concerning the magnitude of p.

1. The kinetic energy $E_\mathrm{kin} = p^2/(2m)$ of the particle greatly exceeds the average disorder potential $\overline{V}$. This means that $k_\mathrm{B}T \gg \overline{V}$ for a thermal ensemble.

2. The velocity $v = p/m$ of the particle is much larger than the largest velocity scale $v_\mathrm{s} = \sigma/\tau$ of the dynamic speckle.

First, we investigate the particle traversing a single speckle grain with potential height V (Fig. 6). Since the grain has the width σ, it takes the time $\Delta t = \sigma/v$ to traverse it. Due to the dynamics, the potential height

changes by a small amount ΔV. Because of assumption 2, we know that $|\Delta V| \ll V$. Hence, the particle gains or loses the kinetic energy $\Delta E_{\mathrm{kin}} = \Delta V$ and the momentum Δp. The connection between ΔE_{kin} and Δp turns out to be

$$\Delta E_{\mathrm{kin}} = \frac{(p+\Delta p)^2}{2m} - \frac{p^2}{2m} = \frac{2p\Delta p + (\Delta p)^2}{2m}. \quad \text{(A.8)}$$

Since $|\Delta E_{\mathrm{kin}}| = |\Delta V| \ll V \ll E_{\mathrm{kin}}$ and thus $\Delta p \ll p$, we can neglect $(\Delta p)^2$ and write

$$\Delta p \approx \frac{m\Delta V}{p}. \quad \text{(A.9)}$$

Now, we have the change in particle momentum at a single grain of the speckle potential. Since the speckle is random, we have to calculate the disorder average of the change in momentum or kinetic energy. Therefore, we introduce the disorder average $\langle\cdot\rangle$ and apply it to the change in kinetic energy to get

$$\langle \Delta E_{\mathrm{kin}} \rangle = \frac{1}{2m}(\langle 2p\Delta p \rangle + \left\langle (\Delta p)^2 \right\rangle). \quad \text{(A.10)}$$

$\langle \Delta E_{\mathrm{kin}} \rangle$ is the disorder-averaged change in kinetic energy of a single particle passing by a single speckle grain. Because the two-dimensional disorder is isotropic, the same holds for the direction of Δp. Hence, the first term in Eq. (A.10) vanishes and we are left with

$$\langle \Delta E_{\mathrm{kin}} \rangle = \frac{1}{2m}\left\langle (\Delta p)^2 \right\rangle. \quad \text{(A.11)}$$

We plug in Δp from Eq. (A.9) to get

$$\langle \Delta E_{\mathrm{kin}} \rangle = \frac{m}{2p^2}\left\langle (\Delta V)^2 \right\rangle. \quad \text{(A.12)}$$

Now, we have to evaluate $\left\langle (\Delta V)^2 \right\rangle$. For a given grain with height V, the change in height ΔV during Δt is

$$|\Delta V| = \frac{\Delta t}{\tau} V \quad \text{(A.13)}$$

and Eq. (A.12) reduces to

$$\langle \Delta E_{\mathrm{kin}} \rangle = \frac{m\Delta t^2}{2p^2\tau^2}\left\langle V^2 \right\rangle. \quad \text{(A.14)}$$

Due to the exponential potential probability distribution of the speckle, we find $\left\langle V^2 \right\rangle = 2\overline{V}^2$. This leads to

$$\langle \Delta E_{\mathrm{kin}} \rangle = \frac{m\Delta t^2}{2p^2\tau^2}\bar{V}^2 = \frac{\sigma^2}{\tau^2 v^4 m}\bar{V}^2. \quad \text{(A.15)}$$

Now, we have the disorder-averaged change in kinetic energy at a single speckle grain. The particle passes grains with a rate $1/(2\Delta t)$, hence

$$P(v) = \frac{\mathrm{d}T}{\mathrm{d}t} = \frac{1}{k_{\mathrm{B}}}\frac{\mathrm{d}E_{\mathrm{kin}}}{\mathrm{d}t} \approx \frac{\langle \Delta E_{\mathrm{kin}} \rangle}{2\Delta t k_{\mathrm{B}}} = \frac{\sigma \bar{V}^2}{2\tau^2 v^3 m k_{\mathrm{B}}}. \quad \text{(A.16)}$$

Here, we have made the assumption that two speckle grains are separated by a typical distance σ. As to get the temperature dependence of P we integrate $P(v)$

$$P(T) = \int_0^\infty P(v)p(v)\mathrm{d}v. \quad \text{(A.17)}$$

over the two-dimensional Maxwell-Boltzmann distribution $p(v) = 2xv\exp\left(-xv^2\right)$, with $x = m/(2k_{\mathrm{B}}T)$. Unfortunately, the integrand diverges at $v = 0$ because $P(v)p(v) \propto v^{-2}$. Due to assumption 2, we can cut off the integral at v_{s} without making too big a mistake. We get

$$\int_{v_{\mathrm{s}}}^\infty \frac{\exp\left(-xv^2\right)}{v^2}\mathrm{d}v = \frac{1}{2}\sqrt{x}\Gamma\left(-\frac{1}{2}, xv_{\mathrm{s}}^2\right), \quad \text{(A.18)}$$

where $\Gamma(s,q) = \int_q^\infty t^{s-1}\exp(-t)\mathrm{d}t$ is the incomplete gamma function. From assumption 2 it follows that $xv_{\mathrm{s}}^2 \ll 1$ and we can approximate $\Gamma(s,q) \approx -q^s/s$ [58] to find

$$\frac{1}{2}\sqrt{x}\Gamma\left(-\frac{1}{2}, xv_{\mathrm{s}}^2\right) \approx \frac{1}{v_{\mathrm{s}}} \quad \text{(A.19)}$$

Finally, we get

$$P(T) = \frac{\sigma\bar{V}^2}{2k_{\mathrm{B}}\tau^2 m}\int_{v_{\mathrm{s}}}^\infty \frac{p(v)}{v^3}\mathrm{d}v = \frac{\bar{V}^2}{2k_{\mathrm{B}}^2 T\tau}. \quad \text{(A.20)}$$

Adaptions between experimental and theoretical data

To ensure that the experimental and theoretical data are comparable, we have to make two adaptions.

Inhomogeneous distribution of average speckle potential Both the numerical simulation and microscopic model assume a homogeneous speckle. In the experiment, a Gaussian envelope with waist $w \approx 440\,\mu\mathrm{m}$ modulates the local average of the speckle potential. The cloud is located in the center of this envelope. The inhomogeneity is most pronounced along the long (y-) axis of the cloud with density distribution $n(y)$. Locally, the heating rate P is proportional to $\overline{V}^2(y) = \overline{V}^2(0)\exp\left(-y^2/w^2\right)$. Hence, in the experiment, P is reduced by a factor of

$$\gamma_1 = \frac{\int n(y)\overline{V}^2(y)\mathrm{d}y}{\overline{V}^2(0)\int n(y)\mathrm{d}y} \quad \text{(A.21)}$$

as compared to the homogeneous case. Since γ_1 depends on the precise shape of the density distribution, which is different for the individual data sets, it is computed for each data set independently; it takes on values between 0.77 and 0.93.

Dimensionality and degrees of freedom As the numerical simulation and microscopic model employ two-dimensional systems and do not include the harmonic trapping potential, the number of degrees of freedom is different from the experiment. In the theory calculations, we have $d_{\mathrm{theo}} = 2$ degrees of freedom, assuming we can neglect the weak speckle potential. In the experiment, however, there are $d_{\mathrm{exp}} = 6$, two for the harmonic trapping potential and kinetic energy in each dimension. Therefore the additional kinetic energy, as extracted from the numerical simulation and microscopic model, must be equally distributed across d_{exp} degrees of freedom. Since the temperature of an ideal gas is $T = 2E_{\mathrm{kin}}/(k_{\mathrm{B}}d)$, the heating rates of theory and experiment are connected by

$$\left(\frac{\mathrm{d}T}{\mathrm{d}t}\right)_{\mathrm{exp}} = \gamma_2 \left(\frac{\mathrm{d}T}{\mathrm{d}t}\right)_{\mathrm{theo}}, \tag{A.22}$$

where $\gamma_2 = \frac{d_{\mathrm{theo}}}{d_{\mathrm{exp}}} = 1/3$.

All plotted heating rates from the numerical simulation are corrected by the factor $\gamma = \gamma_1\gamma_2$.

Direct excitation of superfluid atoms

In the following we present a theoretical model, which enables us to quantify a direct excitation rate from the superfluid ground state into the thermal cloud due to the speckle potential. We model the gas in local density approximation as a homogeneous ground state with Bogoliubov excitations. Using total number conserving Bogoliubov theory [46] enables us to keep the number of condensed atoms $\hat{N}_0 = \hat{a}_0^\dagger \hat{a}_0$ as an operator, and therefore quantify a process which changes the superfluid fraction. To do so we transform the annihilation (creation) operator $\hat{a}_{\boldsymbol{k}}^{(\dagger)}$ of an atom with momentum $\boldsymbol{k}$ into operators $\hat{b}_{\boldsymbol{k}}^{(\dagger)}$ describing the annihilation (creation) of a Bogoliubov phonon, via

$$\hat{a}_0^\dagger\, \hat{a}_{\boldsymbol{k}}/\sqrt{N} = u_k \hat{b}_{\boldsymbol{k}} + v_{-k}\hat{b}_{-\boldsymbol{k}}^\dagger, \tag{A.23}$$

where u_k and v_k are the Bogoliubov eigenvectors [46] and N is the total number of atoms. The Hamiltonian describing the gas is approximately diagonal in this bases $\hat{H}_0 = \sum_{k\neq 0} \hbar\omega_k \hat{b}_{\boldsymbol{k}}^\dagger \hat{b}_{\boldsymbol{k}}$, where $\omega_k = ck\sqrt{1+k^2\xi^2/2}$ is the Bogoliubov dispersion, with the healing length ξ and the speed of sound c. The influence of the speckle potential is given by the term

$$\begin{aligned}\hat{H}_s &= \sum_{\boldsymbol{k},\boldsymbol{k}'} V_{\boldsymbol{k}-\boldsymbol{k}'}(t)\, \hat{a}_{\boldsymbol{k}'}^\dagger \hat{a}_{\boldsymbol{k}} \\ &= \hat{N}_0 V_0(t) + \sqrt{N}\sum_{\boldsymbol{k}\neq 0} V_{\boldsymbol{k}}(t) W_k \left(\hat{b}_k + \hat{b}_{-k}^\dagger\right) + \mathcal{O}\left(\hat{b}_k^2\right),\end{aligned} \tag{A.24}$$

where $W_k = u_k + v_k$ is a structure factor and $V_{\boldsymbol{k}}(t) = \int \frac{d^3r}{L^3} V(\boldsymbol{r},t)\, e^{i\boldsymbol{k}\boldsymbol{r}}$ the Fourier transformed speckle potential. We assume that the potential is a Gaussian random variable in space and time, with mean and variance

$$\overline{V(\boldsymbol{r},t)} = 0 \tag{A.25}$$

$$\overline{V(\boldsymbol{r},t)V(0,0)} = \eta^2 \bar{V}^2 \exp\left(-\frac{\boldsymbol{r}^2}{\sigma^2} - \frac{t^2}{\tilde{\tau}^2}\right), \tag{A.26}$$

where η is a factor which we need to describe the trapped system with a theory of a homogeneous gas and $\tilde{\tau} = \tau/\sqrt{\log 2}$. Here, η rescales the relation between the speckle potential and resulting correlations of the homogeneous disorder potential to account for the experimental speckle anisotropy and the effect of the speckles' envelope. We chose a value of $\eta \approx 0.05$ yielding roughly the same particle-loss rate compared to the experiment in Figs. 3(b) and 4. The Heisenberg equation of motion of $\hat{b}_{\boldsymbol{k}}$ and $\hat{N}_0$ are given by

$$\frac{d}{dt}\hat{b}_{\boldsymbol{k}} = -i\left(\omega_k \hat{b}_{\boldsymbol{k}} + \frac{1}{\hbar} V_{-\boldsymbol{k}}(t) W_k \sqrt{N}\right) \tag{A.27}$$

$$\frac{d}{dt}\hat{N}_0 = \frac{i}{\hbar}\sqrt{N}\sum_{\boldsymbol{k}\neq 0} V_{\boldsymbol{k}}(t) W_k^{-1}\left(\hat{b}_{-\boldsymbol{k}}^\dagger - \hat{b}_{\boldsymbol{k}}\right), \tag{A.28}$$

where terms which do not scale with $\sqrt{N}$ where neglected. These equations can be integrated out exactly and we find for the averaged expectation value of condensed particle number $N_0 = \overline{\langle \hat{N}_0 \rangle}$

$$\begin{aligned}&N_0(t) - N_0(0) \\ &= -2\frac{N}{\hbar^2}\,\mathrm{Re}\Big(\sum_{k\neq 0}\int_0^t dt' \int_0^{t'} dt''\, e^{i\omega_k(t'-t'')} \\ &\qquad \cdot \overline{V_{\boldsymbol{k}}(t') V_{-\boldsymbol{k}}(t'')}\Big).\end{aligned} \tag{A.29}$$

This simplifies for late times $t \gg \tau$ to a linear excitation rate of ground state atoms

$$N_0(t) - N_0(0) = -N\,\Gamma\, t, \tag{A.30}$$

where the transition rate is given by

$$\begin{aligned}\Gamma =& \frac{\eta^2 \bar{V}^2\, \pi\sigma^3}{3\hbar^2 v_c \xi\, \sqrt{\sigma^2 + v_c^2\tilde{\tau}^2}} e^u \Big\{ 2u\Big[I_{5/4}(u) \\ &- I_{3/4}(u) + I_{1/4}(u) - I_{-1/4}(u)\Big] + I_{1/4}(u)\Big\},\end{aligned} \tag{A.31}$$

Here $I_\nu(u)$ are modified Bessel function of the first kind [47] and u is defined as

$$u = \frac{(\sigma^2 + v_c^2\tilde{\tau}^2)^2}{16\xi^2 v_c^2 \tilde{\tau}^2}. \tag{A.32}$$

At this point we assume, that the gas thermalized quickly via internal scattering, such that the decrease of condensed atoms directly leads to an increase in temperature. This results in an additional heating rate, which we calculate from the leading order non interacting part of the superfluid fraction $N_0/N = 1 - (T/T_c)^3$ and find

$$\dot{T}|_{N_0} = \frac{T_c^3}{3T^2}\Gamma. \tag{A.33}$$

Rate model for the dissipation of BECs

In the following we give a detailed description of the rate model

$$\dot{N} = \dot{N}|_{\mathrm{ev}} + \dot{N}|_{\mathrm{rel}} \tag{A.34}$$

$$\dot{T} = \dot{T}|_{N_{\mathrm{th}}} + \dot{T}|_{\mathrm{ev}}, \tag{A.35}$$

for the total particle number $N = N_0 + N_{\mathrm{th}}$ and the temperature T. The number of particles in the superfluid $N_0 = N \times n_{\mathrm{c}}$ is given by the superfluid fraction n_{c}. n_{c} coincides with the condensate fraction, provided that quantum depletion is negligible. Otherwise, n_{c} exceeds the condensate fraction. In order to account for the interaction between particles and the finite size of the system, we solve the transcendental equation

$$n_{\mathrm{c}} = \overbrace{1 - \left(\frac{T}{T_{\mathrm{c}}}\right)^3}^{\text{noninteracting}} - \overbrace{\frac{\zeta(2)}{\zeta(3)}\left(\frac{T}{T_{\mathrm{c}}}\right)^2 \left(\left(1 + 0.16\eta^3 n_{\mathrm{c}}^{1/5}\right)\eta n_{\mathrm{c}}^{2/5}\right)}^{\text{interaction corrections}} - \overbrace{\frac{3\omega_{\mathrm{a}}\zeta(2)}{2\omega_{\mathrm{g}}\zeta(3)^{2/3}}\left(\frac{T}{T_{\mathrm{c}}}\right)^2 N^{-1/3}}^{\text{finite-size correction}} \tag{A.36}$$

to determine n_{c} [43]. The first term of Eq. (A.36) is the well-known result for a noninteracting gas in a harmonic trap that only depends on T and the critical temperature

$$T_{\mathrm{c}} = \frac{\hbar\omega_{\mathrm{g}}}{k_{\mathrm{B}}}\left(\frac{N}{\zeta(3)}\right)^{1/3}, \tag{A.37}$$

where $\hbar$ is the reduced Planck constant, ω_{g} the geometric mean of the trapping frequencies, and ζ the Riemann zeta function. The second term includes a first-order correction due to interactions, quantified by the dimensionless parameter

$$\eta = \frac{1}{2}\zeta(3)^{1/3}\left(15N^{1/6}\frac{a}{a_{\mathrm{ho}}}\right)^{2/5} \tag{A.38}$$

with the oscillator length $a_{\mathrm{ho}} = \sqrt{\hbar/(m\omega_{\mathrm{g}})}$, and the Lee-Huang-Yang correction [59]. The third and last term is the finite-size correction with ω_{a} the arithmetic mean of the trapping frequencies. Disorder-induced depletion of the condensate fraction is negligible in our system, because the healing length ξ is roughly a factor two below the smallest correlation length [60]. After solving Eq. (A.36), n_{c} is reduced by the fraction f of particles that are located in a region of the condensate density $n_0(\boldsymbol{r})$ where the local critical velocity $v_{\mathrm{c}}(\boldsymbol{r})$ is below the largest velocity scale v_{s} of the dynamic speckle (see Fig. 7). Hence, $n_{\mathrm{c}} \to n_{\mathrm{c}} \times (1 - f)$ with

$$f = \frac{1}{N_0}\int_{v_{\mathrm{s}} > v_{\mathrm{c}}(\boldsymbol{r})} n_0(\boldsymbol{r})\mathrm{d}r^3, \tag{A.39}$$

where $n_0(\boldsymbol{r})$ is the Thomas-Fermi density distribution. The heating of the thermal fraction is described by $\dot{T}|_{N_{\mathrm{th}}} = P(t)\gamma$. We get the heating rate $P(t)$ from the numerical simulation and incorporate the time dependence of $\overline{V}$ as shown in Fig. 5. Evaporation from the thermal fraction is captured by

$$\dot{N}|_{\mathrm{ev}} = -\frac{N_{\mathrm{th}}}{\tau_{\mathrm{ev}}} \tag{A.40}$$

$$\dot{T}|_{\mathrm{ev}} = -\frac{1}{\tau_{\mathrm{ev}}}\left(\frac{U_0}{3k_{\mathrm{B}}} - T\right), \tag{A.41}$$

where $1/\tau_{\mathrm{ev}}$ is the evaporation rate and $U_0 = 438\,\mathrm{nK} \times k_{\mathrm{B}}$ the trap depth. The evaporation rate

$$\frac{1}{\tau_{\mathrm{ev}}} = \frac{1}{\tau_{\mathrm{coll}}}\frac{U_0}{\sqrt{2}k_{\mathrm{B}}T}\exp\left(-\frac{U_0}{k_{\mathrm{B}}T}\right) \tag{A.42}$$

depends on the elastic scattering rate $1/\tau_{\mathrm{coll}}$ and the probability of collision events which leave one of the particles in a state with energy $> U_0$ [38]. We calculate the scattering rate

$$\frac{1}{\tau_{\mathrm{coll}}} = \bar{v}_{\mathrm{rel}}\sigma_{\mathrm{coll}}\left(n_0^{\max} + n_{\mathrm{th}}^{\max}\right) \tag{A.43}$$

from the average relative velocity $\bar{v}_{\mathrm{rel}} = \sqrt{2}\sqrt{8k_{\mathrm{B}}T/(m\pi)}$ of a thermal gas in three dimensions, the scattering cross section $\sigma_{\mathrm{coll}} = 8\pi a^2/(1 + k_{\mathrm{dB}}^2 a^2)$ for indistinguishable particles with the thermal de Broglie wave vector $k_{\mathrm{dB}} = \sqrt{2\pi m k_{\mathrm{B}}T}/\hbar$, and the peak densities of the BEC $n_0^{\max} = \mu/g$ and the thermal cloud

$n_{\mathrm{th}}^{\mathrm{max}} = N_{\mathrm{th}} \left(m\omega_{\mathrm{g}}^2/(2k_{\mathrm{B}}T\pi)\right)^{3/2}$ [38]. At last, we include molecular relaxation $\dot{N}|_{\mathrm{rel}}$, which is a two-body process and hence described by the differential equation

$$\dot{n} = -\alpha n^2, \tag{A.44}$$

with the rate of molecular relaxation α. For simplicity, we treat the density of the thermal and condensed clouds separately by writing

$$\dot{n} \approx \dot{n}_0 + \dot{n}_{\mathrm{th}} = -\alpha(n_0^2 + n_{\mathrm{th}}^2) \tag{A.45}$$

Integration of Eq. (A.45) over all space yields

$$\dot{N}|_{\mathrm{rel}} = -\alpha \left(\frac{4}{7} n_0^{\mathrm{max}} N_0 + \frac{1}{2\sqrt{2}} n_{\mathrm{th}}^{\mathrm{max}} N_{\mathrm{th}} \right), \tag{A.46}$$

where we have assumed a Gaussian density distribution of the thermal molecules [38]. The determined loss rates α are given in Tab. I.

Employing Wolfram Mathematica, we solve Eqs. (A.34) and (A.35) numerically with initial conditions $T(0) = 35\,\mathrm{nK}$ for all measurement series and $N(0)$ as extracted from absorption images at $d_{\mathrm{s}} = 0$ and $\tau = \infty$ for each respective measurement series (see Tab. I). The initial temperature is adjusted such that evaporation is negligible during the experimental sequence (Fig. 5) with no speckle potential present and is well within the margin of error of the experimentally determined temperature of $50 \pm 25\,\mathrm{nK}$.

The failure of our phenomenological model to explain the experimental data for reduced interaction strength can be explained by the following argument. Exceeding the superfluid critical velocity, elementary excitations are created with energy $E < \mu$, which cannot remove particles from the trap. The decay of such excitations is possible only via interaction with other thermal or disorder-induced excitations, leading to the formation of a higher-energy excitation, which can eventually remove molecules from the trap. The corresponding damping rate of such excitations has been shown to scale with the interaction parameter as $(n_0 a^3)^{1/2}$ [61]. Thus, for large scattering length, the damping is sufficiently fast to justify the assumption of an immediate depletion of the superfluid density. For weaker interaction, by contrast, the damping rate does not suffice to cause immediate particle loss, and our model overestimates the loss rate. Furthermore, as the local density approaches zero in the outer regions of the condensate, the healing length grows, and the local chemical potential is diminished, effectively shielding the BEC against the disorder evolution on short time and length scales [62].

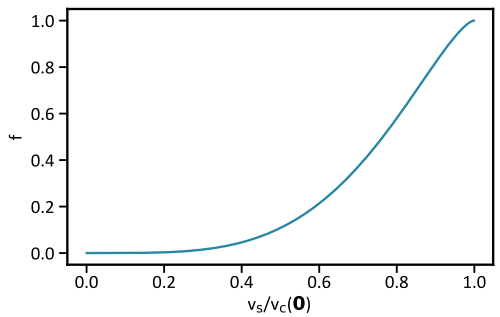

FIG. 7. Fraction f of particles located in regions of the condensate where $v_{\mathrm{c}}(\boldsymbol{r}) < v_{\mathrm{s}}$ versus $v_{\mathrm{s}}/v_{\mathrm{c}}(\boldsymbol{0})$.

7 Conclusion

7.1 Summary

Although the Bose polaron represents a fundamental problem in many-body physics, there remain unanswered questions, especially concerning impurities that exhibit strong coupling with the environment compared to other scales within the system. This thesis primarily focuses on this limit and discusses the characteristics of the Bose polaron within a one-dimensional system. Due to the strong coupling between the impurity and the Bose gas, the condensate is significantly deformed. Nevertheless, a MF approximation of the deformed condensate can accurately describe this phenomenon. To account for the correlations between the impurity and its surrounding environment, the system is described in the reference frame co-moving with the impurity by employing the LLP transformation[49]. By utilizing this novel technique, both equilibrium and non-equilibrium properties are examined.

In terms of the equilibrium properties, first, the stationary states of a single polaron are derived analytically. Notably, since the total momentum operator commutes with the Hamiltonian (1.3), the stationary states are distinguished by the total momentum p as a quantum number. For small momenta, the polaron energy-momentum relation is quadratic in p. It is entirely determined by the polaron energy and effective mass, as elaborated in Chapter 2 [P1] and the supplemental material of Chapter 3 [P2]. Both of these quantities are derived in MF approximation and exhibit excellent agreement with the results obtained from quasi-exact DMC simulations. As the impurity-boson coupling g_{IB} approaches infinity, the Bose gas is entirely pushed away from the impurity position. Consequently, the density profile and polaron energy become identical to those of a dark soliton. In this limit, particles can not bypass the impurity, which implies that the entire system must move along with the impurity once it is in motion. Consequently, the polaron mass equals the total mass of the system.
Extending the stationary solution to an arbitrary total momentum, as detailed in Chapter 5, offers insight into the critical impurity velocity below which it moves without experiencing friction within the condensate. For small coupling g_{IB}, the critical velocity agrees with the Landau criterion and is equal to the speed of sound. It monotonically decreases for larger coupling and eventually reaches zero. This can be understood as the Bose gas is increasingly depleted for large g_{IB}, thereby reducing the effective speed of sound at the impurity, which is proportional to $\sqrt{n}$. While there is an upper bound on the impurity velocity above which no stationary state exists, there is no such constraint on the total momentum. In fact, the energy-momentum relation is a periodic function in the total momentum p, with a periodicity of $2\pi n$, since the Bose gas, away from the impurity, can acquire integer windings of the condensate phase. Consequently, the impurity velocity v exhibits periodicity in the total momentum p, including regions where p and v have opposite signs.

To investigate the interaction between impurities mediated by the many-body environment, the approach is extended from a single to two impurities in Chapter 3 [P2]. In contrast to the single impurity case, the LLP transformation is unable to remove both impurity degrees of

freedom from the Hamiltonian. Therefore, a BO approximation is applied, which is reasonable for heavy impurity masses. The interaction potential derived through this method agrees excellently with results from DMC simulations. For strong repulsive polarons, the Bose gas is pushed out entirely from the space between the impurities if their distance is smaller than $\pi\tilde{\xi} = \pi\sqrt{(1/m + 1/2M)/(2gn)}$. Consequently, the impurities are pushed towards each other by a constant force, resulting in a linear interaction potential. To consider the impact of a finite impurity mass, the diagonal Born-Hunang correction to the BO approximation is derived, which causes the onset of a repulsive peak in the interaction potential. The bound states of the resulting interaction potential represent a bipolaron, and their corresponding binding energies are calculated. Notably, these binding energies agree excellent with the results obtained from DMC simulations for mass ratios as low as 3.

The formation dynamics of a single polaron is studied in Chapter 5 [P4]. The time evolution is simulated following a sudden quench or a quasi-adiabatic turn-on of the impurity-boson coupling constant. In the quasi-adiabatic situation, the impurity is decelerated even if the initial velocity is below the critical velocity derived from the stationary state. This deceleration arises due to the increase in the effective mass during polaron formation and is a reversible process in any finite system. If the initial velocity exceeds the critical value, the impurity emits density waves, leading to an irreversible frictional force. In the case of a sudden quench of the coupling constant, a diverse range of dynamic regimes can be observed. Alongside density waves, the impurity also emits solitons in specific parameter regimes. This results in unconventional impurity motion, including velocity oscillations and backscattering. To validate the accuracy of the MF treatment, quantum fluctuations are taken into account by a truncated Wigner simulation. In order to avoid infrared divergences related to the 1D setup, this simulation is conducted in a harmonically trapped system.

In addition to the coherent impurity-boson interaction, this thesis investigates the effects of a temporally fluctuating interaction. Chapter 4 [P3] demonstrates that noise can be utilized to control coherent currents within the Bose gas. The localized noise scatters particles from the condensate into highly excited modes, affecting the condensate similar to local particle loss. Consequently, it induces a coherent current directed towards the noise, counteracting the effective particle loss. Depending on the strength of the noise and the velocity of the impurity, three dynamical regimes are identified. First, a linear response regime where the induced current increases with the strength of the noise. However, because the local speed of sound limits the velocity of the coherent current, the system transitions into a Zeno regime at a critical noise strength. In this regime, a stationary soliton forms at the noise source, reducing the density and, consequently, the particle scattering rate and the strength of the induced current. At finite impurity velocity, a third regime emerges. The interplay between noise, finite impurity velocity, and the Bose-Bose interaction generates instabilities, resulting in the periodic emission of solitons. Generalizing this to two noisy point contacts reveals how noise tuning can be employed to control and stabilize the current in the segment between the contacts.

Finally, this thesis studies the impact of not only temporal but also spatiotemporal fluctuating noise on a cold Bose gas. This investigation was primarily conducted through an experiment within the group of Artur Widera. It was mainly carried out by Benjamin Nagler, with my involvement in the theoretical modeling of the experiment. The noise induces direct heating of the thermal cloud and excitation of particles out of the condensate state. Both of these

effects contribute to an evaporative loss of particles. This thesis contributes to this work by estimating the excitation rate of superfluid atoms into the thermal cloud.

7.2 Outlook

7.2.1 Generalization to higher dimensions

The main focus of this thesis is the description of the Bose polaron in one spatial dimension. However, it is important to note that most experiments conducted thus far have dealt with three-dimensional systems [17–19, 21]. This section discusses, therefore, the applicability of the MF approach within the LLP frame to higher dimensions.

The derivation of the MF equation, as presented in Section 1.3 for a one-dimensional system, can be straightforwardly generalized to arbitrary spatial dimensions d. The MF equation is given by

$$i\partial_t\, \phi(\vec{r},t) = \left[-\frac{1}{2\tilde{m}}\vec{\nabla}^2 + i\,\vec{v}(t)\cdot\vec{\nabla} + g|\phi(\vec{r},t)|^2 + g_{\mathrm{IB}}\delta^{(d)}(\vec{r})\right]\phi(\vec{r},t). \tag{7.1}$$

Here, $\tilde{m} = (1/m + 1/M)^{-1}$ represents the reduced mass of the boson m and the impurity mass M. The coupling constants are g for boson-boson interaction and g_{IB} for impurity-boson interaction. The impurity velocity is given by

$$\vec{v}(t) = \frac{1}{M}\left[\vec{p} + i\int \mathrm{d}^d r\; \phi(\vec{r},t)^*\;\vec{\nabla}\;\phi(\vec{r},t)\right]. \tag{7.2}$$

It depends on the conserved total momentum $\vec{p}$. Similarly to the analysis performed in this thesis, Equation (7.1) can be used to study both equilibrium and non-equilibrium properties of the d-dimensional Bose polaron. However, unlike the one-dimensional case, analytical solutions are unavailable in higher dimensions, and numerical simulations are computationally more demanding. Nevertheless, some studies have already been conducted, focusing on two- or three-dimensional systems using this technique. For instance, in a three-dimensional system, the ground state of the polaron was computed using a variational method in the study of Ref. [56]. Additionally, in Ref. [54], numerical simulations were conducted to determine the ground state in two and three dimensions. Furthermore, the method has been extended to study bipolarons in a three-dimensional system [58], similar to the approach used in Chapter 3 [P2]. Until now, non-equilibrium simulations of Equation (7.1) have only been conducted in one spatial dimension. Nevertheless, extending such simulations to higher dimensions is feasible, for example, by employing a time-splitting spectral method [107], as presented in Appendix B.

However, in cases where the impurity-boson coupling remains sufficiently weak, the Fröhlich model introduced in Section 1.2.1 also provides an adequate description of the Bose polaron. This model has been extensively explored in various publications, also in two and three dimensions [27–32, 35–44, 47]. In the following, a dimensional analysis of Equation (7.1) is performed to estimate whether the condensate is substantially deformed in realistic experiments. Only if this is the case, different results compared to the Fröhlich model can be expected from our theory. For this purpose, all parameters in the MF Equation (7.1) are expressed in dimensionless quantities

$$\tau = t\,gn, \quad \vec{\rho} = \vec{r}/\tilde{\xi}, \quad \tilde{\phi}(\vec{\rho},\tau) = \phi(\vec{r},t)/\sqrt{n}, \tag{7.3}$$

where n is the average particle density, gn the chemical potential and $\tilde{\xi} = 1/\sqrt{2gn\tilde{m}}$ the rescaled healing length. This results in the following equation

$$i\partial_\tau \, \tilde{\phi}(\vec{\rho},\tau) = \left[-\vec{\nabla}^2 + \frac{i\sqrt{2}}{\tilde{c}}\,\vec{v}(\tau)\cdot\vec{\nabla} + |\tilde{\phi}(\vec{\rho},\tau)|^2 + \frac{g_{\mathrm{IB}}}{g\,n\tilde{\xi}^d}\,\delta^{(d)}(\vec{\rho})\right]\tilde{\phi}(\vec{\rho},\tau). \tag{7.4}$$

From this representation, it is evident that the Bose gas experiences significant deformation for $g_{\mathrm{IB}}/g \gg n\tilde{\xi}^d$. Below, experimental values for the reduced gas parameter $n\tilde{\xi}^d$ are presented, allowing an assessment of whether the strongly interacting limit is achievable in current experiments.
The experiment discussed in Ref. [16] implements a one-dimensional system whose parameters are examined in detail in Section 1.4. The experiment realizes a gas parameter of $n\tilde{\xi} = 1.9$, signifying that the strong impurity-boson coupling limit is indeed reachable within this 1D system.
A three-dimensional realization is an experiment presented in Ref. [18]. The authors realize both the BEC and the impurity using ^{39}K atoms. The BEC density is $n = 2.3\times10^{14}\,\mathrm{cm}^{-3}$ and the boson-boson scattering length $a_{\mathrm{B}} = 9a_0$, where a_0 is the Bohr radius. The rescaled healing length $\tilde{\xi} = \sqrt{m/\tilde{m}}\,\xi$ is directly proportional to the conventional healing length $\xi = 1/\sqrt{8\pi n a_{\mathrm{B}}}$ [88]. This leads to a gas parameter of $n\tilde{\xi}^3 = 142$, indicating that reaching the strong coupling limit is much more challenging compared to the 1D experiment [16].
Another implementation of a three-dimensional system is presented in Ref. [19]. In this study, the authors employ ^{40}K to create impurities within a BEC of ^{87}Rb atoms, with a reported BEC density of $n = 1.8\times10^{14}\,\mathrm{cm}^{-3}$ and boson-boson scattering length $a_{\mathrm{B}} = 100a_0$. Consequently, the gas parameter is $n\tilde{\xi}^3 = 8.7$, making the attainment of the strong coupling limit considerably more feasible in this experiment.

In summary, extending this approach to higher dimensions is possible, and reaching the strong coupling limit in experiments is realistic. Therefore, further investigating this method in two and three spatial dimensions is worthwhile.

7.2.2 Beyond the mean-field approximation

The MF approximation employed in this thesis is suitable for a heavy impurity mass $M \gg m$ and weakly interacting Bose gases, characterized by a small Tonks parameter $\gamma = gm/n$, as discussed in Section 1.4. The commonly used Fröhlich model, derived in Section 1.2.1, shares these limitations. The following section explores alternative approaches that can be used to overcome these constraints.
One method that is applicable to arbitrary parameters is a DMC simulation, which has been used to determine ground-state properties of polarons and bipolarons [P2, 33, 34, 84]. Nevertheless, it is worth noting that this method cannot provide out-of-equilibrium properties and is computationally intensive. In the specific case of a 1D system with equal masses $M = m$ and interaction constants $g_{\mathrm{IB}} = g$, an exact analytical solution for the ground state is available using a Bethe ansatz [61].

Particularly in one-dimensional systems, tensor network methods, such as the density matrix renormalization group (DMRG) or time-evolving block decimation (TEBD), are accessible for calculating the properties of the quantum model over a wide range of parameters [113]. It is important to note that these techniques apply to lattice systems. Hence, the continuous

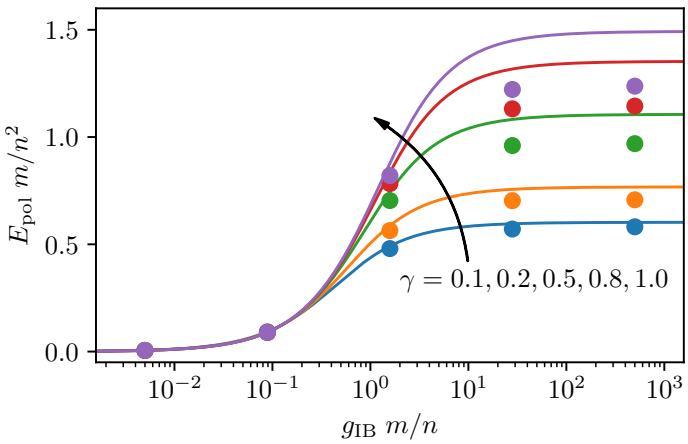

Figure 7.1: Polaron energy for different Tonks parameters $\gamma = gm/n$ derived using the MF approach (lines) and DMRG (dots). The DMRG simulation was conducted by Dennis Breu. Both theories are derived in a finite-size system of N=40 bosons within an infinite square well. The impurity is chosen to be heavy $M \to \infty$ and localized in the center of the square well.

Hamiltonian

$$\begin{aligned}\hat{H} = \int_{-L/2}^{L/2} \mathrm{d}x \Big\{ &\hat{\phi}^\dagger(x)\Big[-\frac{\partial_x^2}{2m} + \tfrac{1}{2}g\hat{\phi}^\dagger(x)\hat{\phi}(x)\Big]\hat{\phi}(x) \\ &+ \hat{\psi}^\dagger(x)\Big[-\frac{\partial_x^2}{2M} + g_{\mathrm{IB}}\hat{\phi}^\dagger(x)\hat{\phi}(x)\Big]\hat{\psi}(x)\Big\},\end{aligned} \tag{7.5}$$

needs to be discretized to a lattice with a small spacing Δx. The continuous field operators $\hat{\phi}(x)$ ($\hat{\psi}(x)$) for the bosons (impurity) are substituted with discrete operators, by

$$\begin{aligned}\hat{\phi}(x) &\to \hat{a}_i/\sqrt{\Delta x} \\ \hat{\psi}(x) &\to \hat{b}_i/\sqrt{\Delta x}.\end{aligned} \tag{7.6}$$

After replacing derivatives with finite differences, $\partial_x^2\hat{\phi}(x) = [\hat{a}_{i+1} + \hat{a}_{i-1} - 2\hat{a}_i]/\Delta x^2$, the resulting lattice Hamiltonian is

$$\begin{aligned}\hat{H} = \sum_i \Big\{ &\frac{1}{2m\,\Delta x^2}\left(\hat{a}_{i+1}^\dagger\hat{a}_i + \hat{a}_i^\dagger\hat{a}_{i+1} - 2\hat{a}_i^\dagger\hat{a}_i\right) + \frac{g}{2\,\Delta x}\hat{a}_i^\dagger\hat{a}_i^\dagger\hat{a}_i\hat{a}_i \\ &+ \frac{1}{2M\,\Delta x^2}\left(\hat{b}_{i+1}^\dagger\hat{b}_i + \hat{b}_i^\dagger\hat{b}_{i+1} - 2\hat{b}_i^\dagger\hat{b}_i\right) + \frac{g_{\mathrm{IB}}}{\Delta x}\hat{b}_i^\dagger\hat{a}_i^\dagger\hat{a}_i\hat{b}_i\Big\}.\end{aligned} \tag{7.7}$$

Using techniques such as DMRG and TEBD, it should be possible to extract both equilibrium and non-equilibrium polaron properties from this Hamiltonian in parameter regimes that are inaccessible via the MF approach.
At the time of writing, Dennis Breu is working on this approach as part of his master's thesis under the supervision of Michael Fleischhauer and supported by Julius Bohm and myself. A preliminary result obtained through a DMRG simulation is the polaron energy in the limit of a heavy impurity $M \to \infty$ and in a system confined in a box potential. This is compared to the results from the MF treatment in Figure 7.1. While the results agree for small γ, the DMRG

simulation can determine the energy in regimes where quantum fluctuations are no longer negligible, thus extending beyond the limitations of the MF approach. Further extending this approach, the effects of a small impurity mass M can also be investigated, which is not accessible using the MF treatment.
However, a disadvantage of this treatment is its limitation to finite-size systems, and it is difficult to implement PBCs efficiently [114]. This limitation is problematic because open boundary conditions exhibit edge effects like Friedel oscillations. PBCs would simplify finite-size scaling and provide direct access to a representation of finite momentum eigenstates [115–117]. This capability would be particularly valuable for studying the steady-state properties of polarons at finite momenta, such as the polaron energy-momentum relation or the critical impurity velocity for superfluid transport.
Nonetheless, tensor networks are a powerful technique to study the polaron properties beyond the MF limitation in the regime of a strong interacting Bose gas ($\gamma \gtrsim 1$) or a light impurity mass $M \lesssim m$.

7.2.3 Polaron Bloch oscillations

In certain quantum systems, particles subject to a constant external force undergo periodic oscillations. A prominent example of this phenomenon is observed in systems where particles are confined in periodic lattices, known as Bloch oscillations [118]. Here, the periodic motion is a consequence of the periodic band structure of the quantum particles in the lattice. Similar periodic motion phenomena have been observed in other systems, such as magnetic solitons in one-dimensional ferromagnets [119] and dark-bright solitons in weakly interacting Bose-Bose mixtures [120]. In the field of polaron physics, Bloch oscillations were experimentally measured in the motion of an impurity within a strongly interacting one-dimensional Bose gas (Tonks parameter $\gamma \gg 1$) in Ref. [20]. In this study, the authors attribute the emergence of oscillations to strong quantum correlations in the Tonks gas, leading to effective quasi-crystalline structures. However, as discussed in Chapter 5 [P4], the energy-momentum relation of a polaron, shown in Figure 7.2, exhibits periodicity in the total momentum even in the case of a weakly interacting Bose gas ($\gamma \ll 1$). This indicates that the impurity might still perform Bloch oscillations when subjected to a constant force without the quasi-crystalline structures of a Tonks gas.
To analyze the system under the influence of a constant force acting on the impurity, we modify the Hamiltonian (1.3) by adding a linear potential $-F\hat{r}$, where F represents the strength of the constant force. The total Hamiltonian is then expressed as:

$$\hat{H} = \frac{\hat{p}^2}{2M} - F\,\hat{r} + \int_{-L/2}^{L/2} \mathrm{d}x\, \hat{\phi}^\dagger(x)\Big[-\frac{\partial_x^2}{2m} + \tfrac{1}{2} g\, \hat{\phi}^\dagger(x)\hat{\phi}(x) + g_{\mathrm{IB}}\, \delta(x-\hat{r})\Big]\hat{\phi}(x). \tag{7.8}$$

Since this additional potential breaks the translational invariance of the system, the standard LLP transformation $\hat{U}_{\mathrm{LLP}} = \exp(-i\hat{P}_{\mathrm{B}}\hat{r})$ discussed in Section 1.3.1 cannot separate the center of mass coordinate from the other coordinates, as the total momentum is no longer conserved. Nonetheless, we can achieve a similar result by generalizing the LLP transformation to

$$\hat{U} = \exp\left[-i\left(F\,t + \hat{P}_{\mathrm{B}}\right)\hat{r}\right]. \tag{7.9}$$

The explicit time dependency of this transformation must be taken into account when transforming the Hamiltonian. The Heisenberg equations of motion $\partial_t \bullet = i[\hat{H}, \bullet]$ remain invariant

when defining the transformed Hamiltonian as

$$\hat{\tilde{H}} = \hat{U}^\dagger \hat{H} \hat{U} + i \hat{U}^\dagger \partial_t \hat{U}. \tag{7.10}$$

The transformation rule for all other operators $\hat{O}$ is given by $\hat{\tilde{O}} = \hat{U}^\dagger \hat{O} \hat{U}$. In the new frame of reference, the Hamiltonian is given by

$$\hat{\tilde{H}} = \frac{1}{2M} : \left(\hat{p} - F\,t - \hat{P}_\mathrm{B}\right)^2 : + \int_{-L/2}^{L/2} \mathrm{d}x\, \hat{\phi}^\dagger(x) \Big[-\frac{\partial_x^2}{2\tilde{m}} + \tfrac{1}{2} g \hat{\phi}^\dagger(x) \hat{\phi}(x) + g_\mathrm{IB} \delta(x) \Big] \hat{\phi}(x). \tag{7.11}$$

Here $\tilde{m} = (1/M + 1/m)^{-1}$ is the reduced mass. Since the Hamiltonian no longer depends on $\hat{r}$, the momentum $\hat{p}$ is conserved in this frame of reference and can again be replaced by a c-number p_0. The only difference of Equation (7.11) compared to the LLP Hamiltonian without an external force ($F = 0$), analyzed thoroughly in Chapters 2 and 5 [P1, P4], is the time-dependent term Ft. This corresponds to a time-dependent total momentum

$$p(t) = p_0 - F\,t. \tag{7.12}$$

Numerical simulations, e.g., based on a MF approximation of the Hamiltonian (7.11), are essential to investigate whether and under which conditions Bloch oscillations occur. Nevertheless, some initial insights can be gained from the study of the time evolution during a quasi-adiabatic turn-on of the impurity-boson coupling constant g_IB, discussed in Chapter 5[P4]. In this context, we show that the system is able to quasi-adiabatically follow the stationary state, even

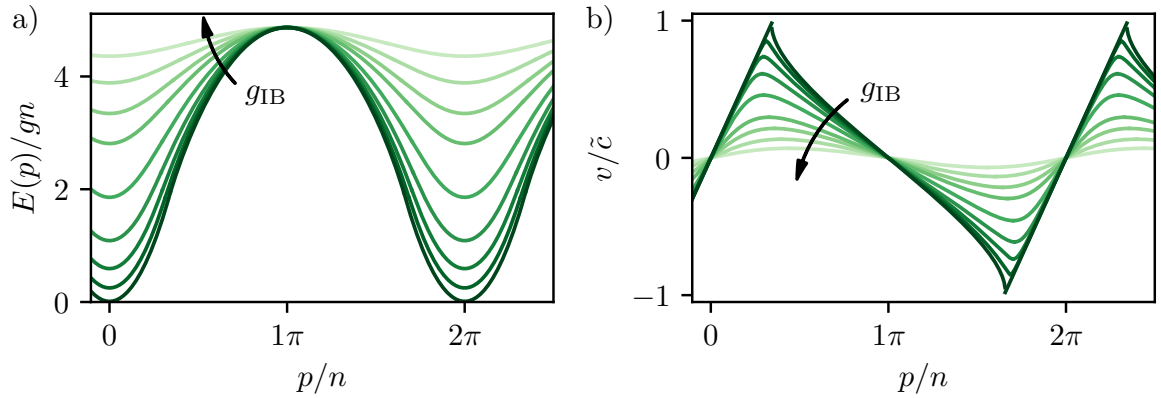

Figure 7.2: a) Energy and b) velocity of a polaron as a function of the total momentum without an external force ($F = 0$). Both quantities are periodic in p. They are plotted for various impurity-boson coupling constants $g_\mathrm{IB}/gn\tilde{\xi} = 0, 0.1, 0.25, 0.5, 1, 2, 3, 5, 10$. Here n is the density of bosons, $\tilde{\xi} = 1/\sqrt{2gn\tilde{m}}$ the rescaled healing length, and $\tilde{c} = \sqrt{gn/\tilde{m}}$ the speed of sound. When an external force acts on the impurity, the total momentum p changes linearly in time, given by Equation (7.12). If the system is able to adiabatically follow the stationary state, this force leads to an oscillatory motion of the impurity. The figures are published in Ref. [P4] under terms of the Creative Commons Attribution 4.0 International license (CC BY 4.0).

though the system is not gaped in the thermodynamic limit. Accordingly, it can be expected that the system is capable of following the stationary state when g_{IB} is constant, while the momentum $p(t)$ varies over time, at least for small forces F relative to other system scales. Since the stationary state is periodic in p, as depicted in Figure 7.2, this would imply the occurrence of Bloch oscillations. For large forces F, we expect that the system is no longer able to adiabatically follow the stationary state, resulting in a friction force and a motion without oscillations. It is important to emphasize that these are preliminary speculations, and a rigorous examination of these hypotheses requires thorough testing through appropriate numerical simulations.
Furthermore, if Bloch oscillations are indeed observable within a MF approximation, it becomes essential to explore the influence of quantum fluctuations. Phonon scattering processes could introduce effective dissipation mechanisms that might dampen or even entirely inhibit Bloch oscillations in the full quantum system. Tensor network techniques, as discussed in Section 7.2.2, could be employed to conduct such an investigation.

Appendices

A Experimental measurement of the polaron mass

In this section, results obtained in this thesis are compared to one of the few experimental realizations of the one-dimensional Bose polaron [16]. The experimental parameters of this study are provided in the main part of this thesis in Section 1.4. The main objective of the experiment is the measurement of the polaron mass from weak to strong impurity-boson coupling. In the following, their experimental procedure is briefly summarized.
The process begins by trapping and cooling a three-dimensional gas mixture of ^{87}Rb (bath) and ^{41}K (impurity) to the ultra-cold regime. After some further preparation steps, they realized the 1D limit by switching on a tight 2D optical lattice. Thus, an array of 1D tubes is created, each containing, on average, 180 Rb and 1.4 K atoms, such that the treatment as impurities is justified. Subsequently, the impurity atoms are centered in the cloud by a species-selective dipole potential. After switching this potential off again, they measure the axial size $\sigma(t)$ of the impurity trough in situ absorption imaging and derive the effective mass by using $\sigma(t) \propto 1/\sqrt{m^*}$. It is shown as a function of the impurity-Bose coupling constant g_{IB} in Figure A.1. The experimental result is compared to a quasi-exact DMC simulation from Ref. [33] for a finite system size of $N = 50$ bosons and to the MF value from this thesis for both finite system size [P2] and the thermodynamic limit [P1]. The theoretical results are obtained in a homogenous 1D system with PBC. It is noticeable that the theory results deviate from the experimental values for a coupling constant with $g_{\mathrm{IB}} \gtrsim gn\tilde{\xi}$. Here $\tilde{\xi} = 1/\sqrt{2\tilde{m}gn}$ is the rescaled healing length with respect to the reduced mass $\tilde{m} = (1/M + 1/m)^{-1}$, where m (M) is the boson (impurity) mass. As demonstrated in Chapters 2, 3 and 5[P1, P2, P4], the condensate deformation becomes significant at this particular value of the coupling constant. For large coupling, the DMC simulation saturates at a finite value since the polaron mass is bounded by the total mass of the system $N\,m + M$, which is captured well by the MF treatment [P2]. The deviations between DMC and MF are explained by the quite strongly

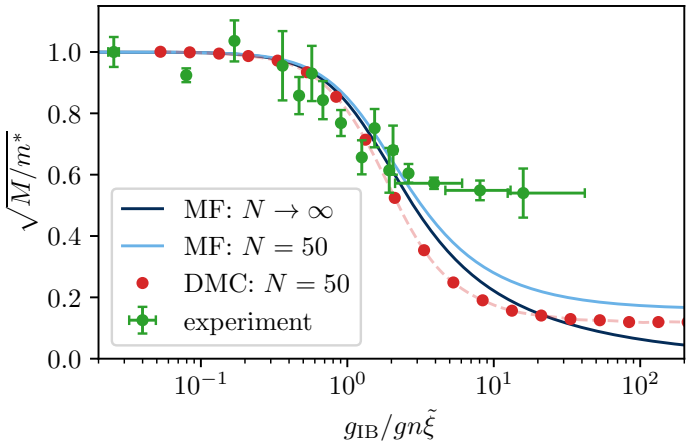

Figure A.1: Ratio of the bare impurity M to polaron mass m^* for different impurity-boson coupling constants g_{IB}. Shown is the experimental measurement of Ref. [16], the exact DMC simulation of Ref. [33] for $N = 50$ bosons and the MF results from this thesis for infinite system size [P1] and $N = 50$ bosons [P2]. The theoretical results are derived using the experimental parameters, see Section 1.4.

interacting gas $\gamma = 0.44$ and light impurity mass $M = 0.47m$, which are both not favorable for the MF treatment [P1]. The experimental value saturates, however, already at a much lower effective mass. The reason for this deviation is still unclear, but some possibilities are mentioned below.

Breaking of the 1D confinement
One possibility is that the transverse confinement in the experiment is not sufficiently tight, preventing the system from being treated strictly in the 1D limit. This becomes particularly significant when the impurity coupling is large since it would enable bosons in the experiment to bypass the impurity by moving around it rather than tunneling through it. To assess the potential impact of this effect, it is necessary to compare the length and energy scales of the polaron with the transverse confinement potential. In the case of a strong repulsive impurity, the MF polaron energy is equal to the energy of a dark soliton [P1], given by $E_{\mathrm{pol}} = \frac{4}{3}nc = 32\,\mathrm{kHz}$. The typical length scale of the polaron is the healing length $\xi = 150\,\mathrm{nm}$. In comparison, the transversal trapping frequency $\omega_\perp = 210(280)\,\mathrm{kHz}$ for Rb (K) is large, and the harmonic oscillator length of $\sqrt{\hbar/m\omega_\perp} = 58(74)\,\mathrm{nm}$ is small, which is favorable for the 1D regime. Nevertheless, the difference in length scales is only a factor of 2-3. This implies that the potential influence of higher dimensions cannot be definitively dismissed.

Inhomogeneity of the cloud
As discussed in the supplement material of Chapter 3[P2], finite-size effects significantly impact the polaron mass at high impurity-boson coupling, as it remains bounded by the total mass of the system. In the experiment, this upper bound is given by $m^* = 180m + M$, thus $\sqrt{M/m^*} = 0.05$. The measured polaron mass saturates at a significantly lower value, indicating that finite-size effects alone cannot account for the observed discrepancy. It is important to note that this upper bound is derived in a homogeneous system on a ring, utilizing PBCs. In contrast, the experimental setup involves a harmonic trapped system with a residual trapping frequency of $\omega = 390(550)\,\mathrm{Hz}$ for Rb(K). The common argument that both systems should be comparable is that the impurity is localized and interacts only on a finite range with the bath so that the gas can be treated in local density approximation. However, since the total mass of the system, which is not a local quantity, is relevant for the polaron mass in a homogeneous system, it can not be ruled out that the small trapping potential also influences the polaron mass. Given that the theoretical prediction is based on a homogeneous system, this could explain the observed discrepancy.

Thermal effects
The third discrepancy between theory and experiment arises from the fact that both theoretical models are formulated in the zero-temperature limit. In contrast, the experiment is carried out at a finite temperature of $T = 350\,\mathrm{nK}$. This temperature is related to the frequency $k_B T/\hbar = 46\,\mathrm{kHz}$, and is comparable to the polaron energy. This suggests that thermal effects might play a role and influence the measured polaron mass.

B Numerical simulation: the time-splitting spectral method

The following section presents the numerical method used in this thesis to predict the non-equilibrium polaron properties by simulating a generalized Gross–Pitaevskii equation (GPE). The method is used in Chapter 5 [P4] to solve the deterministic equation describing the polaron formation and in Chapter 4 [P3] generalized to stochastic equations to predict the effect of a noisy impurity. There are several methods known for simulating GPEs [107]; the one used in this work is a time-splitting spectral method, relying on the fast Fourier transformation [121]. There are different reasons why this algorithm is chosen:

- It is computationally fast compared to other methods [107].
- The algorithm naturally incorporates PBCs, which are essential as described in Section 1.3.
- The total particle-number is conserved exactly, besides floating-point errors.
- The unusual nonlinear and nonlocal coupling term in Equation (1.24) caused by the LLP transformation can be included very efficiently in this method.

In the following, the algorithm is first presented for solving a partial differential equation (PDE) and then generalized to a stochastic partial differential equation (SPDE).

Deterministic partial differential equations

This section outlines the algorithm employed to predict the time evolution of a single impurity interacting coherently with the surrounding Bose gas, as used in Chapter 5 [P4]. We solve the generalized GPE, as derived in Section 1.3 to achieve this. It is given by

$$i\,\partial_t\phi(x,t) = \left[\hat{T} + \hat{V}\right]\phi(x,t), \tag{B.1}$$

where $\hat{T}$ and $\hat{V}$ represent nonlinear operators

$$\hat{T} = -\frac{\partial_x^2}{2\tilde{m}} \;+\; \frac{i}{M}\left[p + i\int_{-L/2}^{L/2} \mathrm{d}y\; \phi(y,t)^*\;\partial_y\;\phi(y,t)\right]\partial_x \tag{B.2}$$

$$\hat{V} = g|\phi(x,t)|^2 \;+\; g_{\mathrm{IB}}\delta(x). \tag{B.3}$$

For a heavy impurity $M \to \infty$, Equation (B.1) is a standard GPE. However, for finite M, the kinetic operator $\hat{T}$ incorporates an unconventional nonlocal nonlinearity, which requires special attention in the simulations.
A conceptually simple algorithm for simulating this equation involves an iterative application of the exponential operator:

$$\phi(x, t + \mathrm{d}t) = e^{-i\mathrm{d}t(\hat{T}+\hat{V})}\phi(x,t). \tag{B.4}$$

This approximation remains valid for small time steps $\mathrm{d}t$, although $\hat{T}$ and $\hat{V}$ represent nonlinear operators. The nonlinear effects are incorporated by reevaluating $\hat{T}$ and $\hat{V}$ at each time step t, using the current value of $\phi(x,t)$. An option to numerically evaluate the exponential is to discretize both operators to a finite grid in real space and evaluate the exponential of the finite-dimensional matrix. However, this approach necessitates recalculating the matrix exponential

at each time step. Given that $\hat{T}$ and $\hat{V}$ do not commute, this numerical procedure becomes computationally costly.
To overcome this challenge, a time-splitting method is applied, which is equivalent to a Trotter-Suzuki decomposition [122, 123] of Equation (B.4)

$$\phi(x, t + \mathrm{d}t) = e^{-\frac{i}{2}\mathrm{d}t\,\hat{V}} e^{-i\mathrm{d}t\,\hat{T}} e^{-\frac{i}{2}\mathrm{d}t\,\hat{V}} \phi(x, t). \tag{B.5}$$

This represents a practicable algorithm for solving usual GPEs [107], which do not include the nonlocal coupling term in $\hat{T}$ ($M \to \infty$). In that case, $\hat{T}$ represents a linear operator and is constant in time. Consequently, its numerical complex matrix exponential must be computed only once, not in every time step. While $\hat{V}$ remains nonlinear, its diagonal form in the position basis allows for an efficient reevaluation of its matrix exponential in every time step.
In the case of finite M, so including the nonlocal coupling in $\hat{T}$, the previous method is no longer applicable due to the nonlinearity in $\hat{T}$, see Equation (B.2). To address this challenge, a Fourier transformation to the momentum basis is applied

$$\alpha_k(t) = \int_{-L/2}^{L/2} \frac{\mathrm{d}x}{L}\, e^{ikx} \phi(x, t), \quad \text{and} \quad \phi(x, t) = \sum_k e^{-ikx} \alpha_k(t). \tag{B.6}$$

The kinetic operator $\hat{T}$ is much simpler in momentum space, as it does not involve any derivatives, although it is still not diagonal:

$$\hat{T} = \frac{k^2}{2\tilde{m}} \; + \; \frac{k}{M} \left[p - \sum_q q\, |\alpha_q(t)|^2 \right]. \tag{B.7}$$

In this form, the time-evolution operator for a small step $\mathrm{d}t$ with respect to $\hat{T}$ can be efficiently evaluated. The process involves first calculating the expectation value of the total Bose gas momentum $\sum_q q\,|\alpha_q(t)|^2$. Subsequently, the time step generated by the kinetic energy term $\alpha_k(t + \mathrm{d}t) = \exp(-i\mathrm{d}t\hat{T})\ \alpha_k(t)$, is separately evaluated for every k mode. A complete time step can then be efficiently simulated using the following formula:

$$\phi(x, t + \mathrm{d}t) = e^{-\frac{i}{2}\mathrm{d}t\,\hat{V}}\ \mathscr{F}^{-1}\Big\{ e^{-i\mathrm{d}t\,\hat{T}}\ \mathscr{F}\Big[e^{-\frac{i}{2}\mathrm{d}t\,\hat{V}}\ \phi(x, t) \Big] \Big\}. \tag{B.8}$$

Here $\mathscr{F}^{(-1)}$ represents the (inverse) Fourier transformation. To simulate the time evolution over arbitrary large time steps, Equation (B.8) is applied iteratively to the initial condition. For the efficient computation of the Fourier transformation, the fast Fourier transformation algorithm is employed [121].
Lastly, it is important to mention that the system needs to be discretized in space for numerical implementation. Mainly, treating the delta function in $\hat{V}$ (see Equation (B.3)) requires special attention. This is addressed in this thesis by substituting the delta function with a Gaussian potential

$$\delta(x) \simeq \frac{1}{\sqrt{\pi l^2}} e^{-x^2/l^2}, \tag{B.9}$$

where the length l is chosen to be small compared to the other length scales of the system, particularly the healing length.

Stochastic partial differential equations

The subsequent section presents the generalization of the time-splitting spectral method to accommodate a stochastic impurity-boson interaction. As demonstrated in Chapter 4[P3], this involves generalizing the PDE (B.1) to an SPDE. It is important to note that this section will offer an overview of the numerical implementation rather than delving into the comprehensive foundations of stochastic equations. Readers should be familiar with the concept of Ito and Stratonovich calculus, which is elaborated, for example, in the book [106].
In order to simulate the impact of stochastic impurity coupling, we solve Equation (2) in Chapter 4[P3]. It is expressed as

$$i\mathrm{d}\phi(x,t) = \left[\hat{T} + \hat{V}\right]\phi(x,t)\ \mathrm{d}t + \hat{U}\phi(x,t) \circ \mathrm{d}W, \tag{B.10}$$

where $\hat{T}$, $\hat{V}$ and $\hat{U}$ are given by

$$\begin{aligned} \hat{T} &= -\frac{\partial_x^2}{2m} \ + \ iv\partial_x \equiv \frac{k^2}{2m} + vk \\ \hat{V} &= g|\phi(x,t)|^2 \\ \hat{U} &= \sqrt{2\sigma\delta(x)} \end{aligned} \tag{B.11}$$

Here v is the velocity of an external driven current and σ the strength of the noise. Equation (B.10) is a Stratonovich SPDE, denoted by the symbol $\circ$ and $\mathrm{d}W = \eta(t)\mathrm{d}t$ is a infinitesimal Wiener process [106]. The term $\eta(t)$ represents a delta-correlated white noise, characterized by its mean value $\overline{\eta(t)} = 0$ and variance $\overline{\eta(t)\eta(t')} = \delta(t-t')$.
Since besides $\hat{V}$ also $\hat{U}$ is diagonal in the position basis, a generalization of the time-splitting spectral method, as depicted in Equation (B.8), to this SPDE is possible. However, the Wiener process needs to be treated with special care. As the algorithm computes the subsequent time step $t + \mathrm{d}t$ using the preceding one t, it becomes necessary to convert Equation (B.10) into the Ito calculus:

$$i\mathrm{d}\phi(x,t) = \left[\hat{T} + \hat{V} - \tfrac{i}{2}\hat{U}^2\right]\phi(x,t)\ \mathrm{d}t + \hat{U}\phi(x,t)\ \mathrm{d}W. \tag{B.12}$$

It deviates from the Stratonovich form solely by the term proportional to $\hat{U}^2$. In this representation, the algorithm outlined in Equation (B.8) can be applied to derive the time evolution. However, as terms proportional to $\mathrm{d}W^2 = \mathrm{d}t$ cannot be neglected in the Ito formalism, special care must be taken when dealing with the exponential functions, as

$$\begin{aligned} \exp\left[-i\hat{U}\mathrm{d}W\right] &= 1 - i\hat{U}\mathrm{d}W - \tfrac{1}{2}\hat{U}^2\mathrm{d}W^2 \\ &= 1 - i\hat{U}\mathrm{d}W - \tfrac{1}{2}\hat{U}^2\mathrm{d}t. \end{aligned} \tag{B.13}$$

It is straightforward to show that the terms which are proportional to $\hat{U}^2$ in Equations (B.12) and (B.13) cancel each other out, so that no such term appears in the final expression of the utilized algorithm, given by

$$\phi(x, t+\mathrm{d}t) = e^{-\frac{i}{2}[\hat{V}\mathrm{d}t + \hat{U}\mathrm{d}W]}\ \mathscr{F}^{-1}\Big\{e^{-i\mathrm{d}t\,\hat{T}}\ \mathscr{F}\Big[e^{-\frac{i}{2}[\hat{V}\mathrm{d}t+\hat{U}\mathrm{d}W]}\ \phi(x,t)\Big]\Big\}. \tag{B.14}$$

Finally, in the numerical simulation, the infinitesimal $\mathrm{d}t$ must be discretized by a finite but small Δt. This is particularly intricate for the noise term $\mathrm{d}W = \eta(t)\mathrm{d}t$, since it also involves discretizing the delta-correlated $\eta(t)$, leading to

$$\overline{\eta(t)\eta(t')} = \delta(t-t') \;\Rightarrow\; \overline{\eta(t_1)\eta(t_2)} = \delta_{1,2}/\Delta t. \tag{B.15}$$

Simulating Equation (B.14) necessitates redrawing $\eta(t)$ in every time step form this Gaussian distribution. The time evolution must be computed from the same initial condition for multiple noise realizations to obtain any observables. Quantities, such as the boson density $n(x,t) = \overline{|\phi(x,t)|^2}$, are then calculated by averaging over these distinct realizations.

Bibliography

[1] L. Landau, *Electron motion in crystal lattices*, Phys. Z. Sowjetunion **3**, 644–645 (1933).

[2] S. I. Pekar, *Effective mass of a polaron*, Zh. Eksp. Teor. Fiz. **16**, 335 (1946).

[3] N. Mott, *Polaron models of high-temperature superconductivity*, Phys. C Supercond. **205**, 191–205 (1993).

[4] A. S. Alexandrov and J. T. Devreese, *Advances in Polaron Physics*, Vol. 159 (Springer-Verlag, Berlin, 2010).

[5] C. Zhang, J. Sous, D. R. Reichman, M. Berciu, A. J. Millis, N. V. Prokof'ev, and B. V. Svistunov, *Bipolaronic High-Temperature Superconductivity*, Phys. Rev. X **13**, 011010 (2023).

[6] A. Schirotzek, C.-H. Wu, A. Sommer, and M. W. Zwierlein, *Observation of Fermi Polarons in a Tunable Fermi Liquid of Ultracold Atoms*, Phys. Rev. Lett. **102**, 230402 (2009).

[7] Y. Zhang, W. Ong, I. Arakelyan, and J. E. Thomas, *Polaron-to-Polaron Transitions in the Radio-Frequency Spectrum of a Quasi-Two-Dimensional Fermi Gas*, Phys. Rev. Lett. **108**, 235302 (2012).

[8] C. Kohstall et al., *Metastability and coherence of repulsive polarons in a strongly interacting Fermi mixture*, Nature **485**, 615–618 (2012).

[9] M. Koschorreck, D. Pertot, E. Vogt, B. Fröhlich, M. Feld, and M. Köhl, *Attractive and repulsive Fermi polarons in two dimensions*, Nature **485**, 619–622 (2012).

[10] F. Scazza et al., *Repulsive Fermi Polarons in a Resonant Mixture of Ultracold* ^{6}Li *Atoms*, Phys. Rev. Lett. **118**, 083602 (2017).

[11] M. Cetina, M. Jag, R. S. Lous, J. T. M. Walraven, R. Grimm, R. S. Christensen, and G. M. Bruun, *Decoherence of Impurities in a Fermi Sea of Ultracold Atoms*, Phys. Rev. Lett. **115**, 135302 (2015).

[12] M. Cetina et al., *Ultrafast many-body interferometry of impurities coupled to a Fermi sea*, Science **354**, 96–99 (2016).

[13] M. M. Parish and J. Levinsen, *Quantum dynamics of impurities coupled to a Fermi sea*, Phys. Rev. B **94**, 184303 (2016).

[14] P. Massignan, M. Zaccanti, and G. M. Bruun, *Polarons, dressed molecules and itinerant ferromagnetism in ultracold Fermi gases*, Reports on Progress in Physics **77**, 034401 (2014).

[15] S. Palzer, C. Zipkes, C. Sias, and M. Köhl, *Quantum Transport through a Tonks-Girardeau Gas*, Phys. Rev. Lett. **103**, 150601 (2009).

[16] J. Catani et al., *Quantum dynamics of impurities in a one-dimensional Bose gas*, Phys. Rev. A **85**, 023623 (2012).

[17] M. Hohmann, F. Kindermann, B. Gänger, T. Lausch, D. Mayer, F. Schmidt, and A. Widera, *Neutral impurities in a Bose-Einstein condensate for simulation of the Fröhlich-polaron*, EPJ Quantum Technology **2**, 23 (2015).

[18] N. B. Jørgensen et al., *Observation of Attractive and Repulsive Polarons in a Bose-Einstein Condensate*, Phys. Rev. Lett. **117**, 055302 (2016).

[19] M. G. Hu, M. J. Van De Graaff, D. Kedar, J. P. Corson, E. A. Cornell, and D. S. Jin, *Bose Polarons in the Strongly Interacting Regime*, Phys. Rev. Lett. **117**, 055301 (2016).

[20] F. Meinert, M. Knap, E. Kirilov, K. Jag-Lauber, M. B. Zvonarev, E. Demler, and H.-C. Nägerl, *Bloch oscillations in the absence of a lattice*, Science **356**, 945–948 (2017).

[21] Z. Z. Yan, Y. Ni, C. Robens, and M. W. Zwierlein, *Bose polarons near quantum criticality*, Science **368**, 190–194 (2020).

[22] T. Giamarchi, *Quantum Physics in One Dimension* (Oxford University Press, Dec. 2003).

[23] B. L. Tolra, K. M. O'Hara, J. H. Huckans, W. D. Phillips, S. L. Rolston, and J. V. Porto, *Observation of Reduced Three-Body Recombination in a Correlated 1D Degenerate Bose Gas*, Phys. Rev. Lett. **92**, 190401 (2004).

[24] C. Chin, R. Grimm, P. Julienne, and E. Tiesinga, *Feshbach resonances in ultracold gases*, Rev. Mod. Phys. **82**, 1225–1286 (2010).

[25] M. Olshanii, *Atomic Scattering in the Presence of an External Confinement and a Gas of Impenetrable Bosons*, Phys. Rev. Lett. **81**, 938–941 (1998).

[26] H. Fröhlich, *Electrons in lattice fields*, Advances in Physics **3**, 325–361 (1954).

[27] J. Tempere, W. Casteels, M. K. Oberthaler, S. Knoop, E. Timmermans, and J. T. Devreese, *Feynman path-integral treatment of the BEC-impurity polaron*, Phys. Rev. B **80**, 184504 (2009).

[28] S. P. Rath and R. Schmidt, *Field-theoretical study of the Bose polaron*, Phys. Rev. A **88**, 053632 (2013).

[29] W. Casteels and M. Wouters, *Polaron formation in the vicinity of a narrow Feshbach resonance*, Phys. Rev. A **90**, 043602 (2014).

[30] R. S. Christensen, J. Levinsen, and G. M. Bruun, *Quasiparticle Properties of a Mobile Impurity in a Bose-Einstein Condensate*, Phys. Rev. Lett. **115**, 160401 (2015).

[31] J. Levinsen, M. M. Parish, and G. M. Bruun, *Impurity in a Bose-Einstein Condensate and the Efimov Effect*, Phys. Rev. Lett. **115**, 125302 (2015).

[32] T. Ichmoukhamedov and J. Tempere, *Feynman path-integral treatment of the Bose polaron beyond the Fröhlich model*, Phys. Rev. A **100**, 043605 (2019).

[33] F. Grusdt, G. E. Astrakharchik, and E. Demler, *Bose polarons in ultracold atoms in one dimension: beyond the Fröhlich paradigm*, New Journal of Physics **19**, 103035 (2017).

[34] L. A. Peña Ardila, G. E. Astrakharchik, and S. Giorgini, *Strong coupling Bose polarons in a two-dimensional gas*, Phys. Rev. Res. **2**, 023405 (2020).

[35] G. E. Astrakharchik and L. P. Pitaevskii, *Motion of a heavy impurity through a Bose-Einstein condensate*, Phys. Rev. A **70**, 013608 (2004).

[36] M. Will, T. Lausch, and M. Fleischhauer, *Rotational cooling of molecules in a Bose-Einstein condensate*, Phys. Rev. A **99**, 062707 (2019).

[37] W. Casteels, T. Van Cauteren, J. Tempere, and J. T. Devreese, *Strong coupling treatment of the polaronic system consisting of an impurity in a condensate*, Laser Physics **21**, 1480–1485 (2011).

[38] Y. E. Shchadilova, R. Schmidt, F. Grusdt, and E. Demler, *Quantum Dynamics of Ultracold Bose Polarons*, Phys. Rev. Lett. **117**, 113002 (2016).

[39] F. Grusdt, K. Seetharam, Y. Shchadilova, and E. Demler, *Strong-coupling Bose polarons out of equilibrium: Dynamical renormalization-group approach*, Phys. Rev. A **97**, 033612 (2018).

[40] M. Drescher, M. Salmhofer, and T. Enss, *Real-space dynamics of attractive and repulsive polarons in Bose-Einstein condensates*, Phys. Rev. A **99**, 023601 (2019).

[41] K. K. Nielsen, L. A. Peña Ardila, G. M. Bruun, and T. Pohl, *Critical slowdown of non-equilibrium polaron dynamics*, New Journal of Physics **21**, 043014 (2019).

[42] L. A. Peña Ardila, *Dynamical formation of polarons in a Bose-Einstein condensate: A variational approach*, Phys. Rev. A **103**, 033323 (2021).

[43] T. Lausch, A. Widera, and M. Fleischhauer, *Prethermalization in the cooling dynamics of an impurity in a Bose-Einstein condensate*, Phys. Rev. A **97**, 023621 (2018).

[44] T. Lausch, A. Widera, and M. Fleischhauer, *Role of thermal two-phonon scattering for impurity dynamics in a low-dimensional Bose-Einstein condensate*, Phys. Rev. A **97**, 033620 (2018).

[45] A. Klein and M. Fleischhauer, *Interaction of impurity atoms in Bose-Einstein condensates*, Phys. Rev. A **71**, 033605 (2005).

[46] A. Recati, J. N. Fuchs, C. S. Pe ça, and W. Zwerger, *Casimir forces between defects in one-dimensional quantum liquids*, Phys. Rev. A **72**, 023616 (2005).

[47] P. Naidon, *Two Impurities in a Bose–Einstein Condensate: From Yukawa to Efimov Attracted Polarons*, Journal of the Physical Society of Japan **87**, 043002 (2018).

[48] B. Reichert, A. Petkovi ć, and Z. Ristivojevic, *Field-theoretical approach to the Casimir-like interaction in a one-dimensional Bose gas*, Phys. Rev. B **99**, 205414 (2019).

[49] T. D. Lee, F. E. Low, and D. Pines, *The Motion of Slow Electrons in a Polar Crystal*, Phys. Rev. **90**, 297–302 (1953).

[50] M. Girardeau, *Relationship between Systems of Impenetrable Bosons and Fermions in One Dimension*, Journal of Mathematical Physics **1**, 516–523 (2004).

[51] E. H. Lieb and W. Liniger, *Exact Analysis of an Interacting Bose Gas. I. The General Solution and the Ground State*, Phys. Rev. **130**, 1605–1616 (1963).

[52] A. G. Volosniev and H.-W. Hammer, *Analytical approach to the Bose-polaron problem in one dimension*, Phys. Rev. A **96**, 031601 (2017).

[53] G. Panochko and V. Pastukhov, *Mean-field construction for spectrum of one-dimensional Bose polaron*, Annals of Physics **409**, 167933 (2019).

[54] O. Hryhorchak, G. Panochko, and V. Pastukhov, *Mean-field study of repulsive 2D and 3D Bose polarons*, Journal of Physics B: Atomic, Molecular and Optical Physics **53**, 205302 (2020).

[55] F. Brauneis, H.-W. Hammer, M. Lemeshko, and A. G. Volosniev, *Impurities in a one-dimensional Bose gas: the flow equation approach*, SciPost Phys. **11**, 008 (2021).

[56] R. Schmidt and T. Enss, *Self-stabilized Bose polarons*, SciPost Phys. **13**, 054 (2022).

[57] G. M. Koutentakis, S. I. Mistakidis, and P. Schmelcher, *Pattern Formation in One-dimensional Polaron Systems and Temporal Orthogonality Catastrophe*, Atoms **10**, 10.3390/atoms10010003 (2022).

[58] J. Jager and R. Barnett, *The effect of boson–boson interaction on the bipolaron formation*, New Journal of Physics **24**, 103032 (2022).

[59] A. Petković and Z. Ristivojevic, *Mediated interaction between polarons in a one-dimensional Bose gas*, Phys. Rev. A **105**, L021303 (2022).

[60] J. Jager and R. Barnett, *Stochastic-field approach to the quench dynamics of the one-dimensional Bose polaron*, Phys. Rev. Res. **3**, 033212 (2021).

[61] Z. Ristivojevic, *Exact result for the polaron mass in a one-dimensional Bose gas*, Phys. Rev. A **104**, 052218 (2021).

[62] L. N. Cooper, *Bound Electron Pairs in a Degenerate Fermi Gas*, Phys. Rev. **104**, 1189–1190 (1956).

[63] J. L. Bredas and G. B. Street, *Polarons, bipolarons, and solitons in conducting polymers*, Accounts of Chemical Research **18**, 309–315 (1985).

[64] S. Glenis, M. Benz, E. LeGoff, J. L. Schindler, C. R. Kannewurf, and M. G. Kanatzidis, *Polyfuran: a new synthetic approach and electronic properties*, Journal of the American Chemical Society **115**, 12519–12525 (1993).

[65] M. N. Bussac and L. Zuppiroli, *Bipolaron singlet and triplet states in disordered conducting polymers*, Phys. Rev. B **47**, 5493–5496 (1993).

[66] M. Fernandes, J. Garcia, M. Schultz, and F. Nart, *Polaron and bipolaron transitions in doped poly(p-phenylene vinylene) films*, Thin Solid Films **474**, 279–284 (2005).

[67] I. Zozoulenko, A. Singh, S. K. Singh, V. Gueskine, X. Crispin, and M. Berggren, *Polarons, Bipolarons, And Absorption Spectroscopy of PEDOT*, ACS Applied Polymer Materials **1**, 83–94 (2019).

[68] R. Onofrio, C. Raman, J. M. Vogels, J. R. Abo-Shaeer, A. P. Chikkatur, and W. Ketterle, *Observation of superfluid flow in a Bose-Einstein condensed gas*, Phys. Rev. Lett. **85**, 2228 (2000).

[69] R. Desbuquois, L. Chomaz, T. Yefsah, J. Léonard, J. Beugnon, C. Weitenberg, and J. Dalibard, *Superfluid behaviour of a two-dimensional Bose gas*, Nature Physics **8**, 645–648 (2012).

[70] C. Ryu, M. F. Andersen, P. Cladé, V. Natarajan, K. Helmerson, and W. D. Phillips, *Observation of persistent flow of a Bose-Einstein condensate in a toroidal trap*, Phys. Rev. Lett. **99**, 260401 (2007).

[71] A. Ramanathan et al., *Superflow in a toroidal Bose-Einstein condensate: An atom circuit with a tunable weak link*, Phys. Rev. Lett. **106**, 130401 (2011).

[72] G. Del Pace et al., *Imprinting Persistent Currents in Tunable Fermionic Rings*, Phys. Rev. X **12**, 041037 (2022).

[73] K. Sacha and E. Timmermans, *Self-localized impurities embedded in a one-dimensional Bose-Einstein condensate and their quantum fluctuations*, Phys. Rev. A **73**, 063604 (2006).

[74] F. M. Cucchietti and E. Timmermans, *Strong-Coupling Polarons in Dilute Gas Bose-Einstein Condensates*, Phys. Rev. Lett. **96**, 210401 (2006).

[75] A. A. Blinova, M. G. Boshier, and E. Timmermans, *Two polaron flavors of the Bose-Einstein condensate impurity*, Phys. Rev. A **88**, 053610 (2013).

[76] A. Boudjemâa, *Self-localized state and solitons in a Bose-Einstein-condensate–impurity mixture at finite temperature*, Phys. Rev. A **90**, 013628 (2014).

[77] M. Born and K. Huang, *Dynamical Theory of Crystal Lattices* (Oxford University Press, New York, 1954).

[78] F. M. Fernández, *Corrections to the Born-Oppenheimer approximation by means of perturbation theory*, Phys. Rev. A **50**, 2953–2959 (1994).

[79] V. A. Brazhnyi, V. V. Konotop, V. M. Pérez-García, and H. Ott, *Dissipation-Induced Coherent Structures in Bose-Einstein Condensates*, Phys. Rev. Lett. **102**, 144101 (2009).

[80] D. A. Zezyulin, V. V. Konotop, G. Barontini, and H. Ott, *Macroscopic Zeno Effect and Stationary Flows in Nonlinear Waveguides with Localized Dissipation*, Phys. Rev. Lett. **109**, 020405 (2012).

[81] G. Barontini, R. Labouvie, F. Stubenrauch, A. Vogler, V. Guarrera, and H. Ott, *Controlling the Dynamics of an Open Many-Body Quantum System with Localized Dissipation*, Phys. Rev. Lett. **110**, 035302 (2013).

[82] D. Sels and E. Demler, *Thermal radiation and dissipative phase transition in a BEC with local loss*, Ann. Phys. **412**, 168021 (2020).

[83] B. Misra and E. C. G. Sudarshan, *The Zeno's paradox in quantum theory*, J. Math. Phys **18**, 756–763 (1977).

[84] L. Parisi and S. Giorgini, *Quantum Monte Carlo study of the Bose-polaron problem in a one-dimensional gas with contact interactions*, Phys. Rev. A **95**, 023619 (2017).

[85] Y.-Q. Li, S.-J. Gu, Z.-J. Ying, and U. Eckern, *Exact results of the ground state and excitation properties of a two-component interacting Bose system*, Europhysics Letters **61**, 368 (2003).

[86] C. N. Yang, *Some Exact Results for the Many-Body Problem in one Dimension with Repulsive Delta-Function Interaction*, Phys. Rev. Lett. **19**, 1312–1315 (1967).

[87] M. Gaudin, *Un systeme a une dimension de fermions en interaction*, Physics Letters A **24**, 55–56 (1967).

[88] C. J. Pethick and H. Smith, *Bose-Einstein Condensation in Dilute Gases* (Cambridge University Press, 2008).

[89] L. P. Pitaevskii and S. Stringari, *Bose-Einstein Condensation and Superfluidity* (Oxford University Press, New York, 2016).

[90] E. Fermi, *Sul moto dei neutroni nelle sostanze idrogenate*, Ricerca scientifica **7**, 13–52 (1936).

[91] K. Huang and C. N. Yang, *Quantum-Mechanical Many-Body Problem with Hard-Sphere Interaction*, Phys. Rev. **105**, 767–775 (1957).

[92] N. D. Mermin and H. Wagner, *Absence of Ferromagnetism or Antiferromagnetism in One- or Two-Dimensional Isotropic Heisenberg Models*, Phys. Rev. Lett. **17**, 1133–1136 (1966).

[93] P. C. Hohenberg, *Existence of Long-Range Order in One and Two Dimensions*, Phys. Rev. **158**, 383–386 (1967).

[94] N. N. Bogoliubov, *On the theory of superfluidity*, J. Phys. (USSR) **11**, 23–32 (1947).

[95] V. Hakim, *Nonlinear Schrödinger flow past an obstacle in one dimension*, Phys. Rev. E **55**, 2835–2845 (1997).

[96] J. J. McClelland, A. V. Steele, B. Knuffman, K. A. Twedt, A. Schwarzkopf, and T. M. Wilson, *Bright focused ion beam sources based on laser-cooled atoms*, Applied Physics Reviews **3**, 011302 (2016).

[97] H. Hachisu et al., *Trapping of Neutral Mercury Atoms and Prospects for Optical Lattice Clocks*, Phys. Rev. Lett. **100**, 053001 (2008).

[98] A. H. Abbas, X. Meng, R. S. Patil, J. A. Ross, A. G. Truscott, and S. S. Hodgman, *Rapid generation of metastable helium Bose-Einstein condensates*, Phys. Rev. A **103**, 053317 (2021).

[99] H. Cayla, P. Massignan, T. Giamarchi, A. Aspect, C. I. Westbrook, and D. Clément, *Observation of $1/k^4$-Tails after Expansion of Bose-Einstein Condensates with Impurities*, Phys. Rev. Lett. **130**, 153401 (2023).

[100] R. Meinel, G. Neugebauer, and H. Steudel, *Solitonen Nichtlineare Strukturen* (Akademie-Verlag Berlin, 1991).

[101] J. S. Russell, *Report on waves, made to the meetings of the British Association in 1842-43* (London: John Murray. 311–390, 1845).

[102] D. D. J. Korteweg and D. G. de Vries, *XLI. On the change of form of long waves advancing in a rectangular canal, and on a new type of long stationary waves*, The London, Edinburgh, and Dublin Philosophical Magazine and Journal of Science **39**, 422–443 (1895).

[103] T. Tsuzuki, *Nonlinear waves in the Pitaevskii-Gross equation*, Journal of Low Temperature Physics **4**, 441–457 (1971).

[104] D. F. Lawden, *Elliptic Functions and Applications* (Applied Mathematical Sciences, 1989).

[105] J. N. Fuchs, A. Recati, and W. Zwerger, *Oscillating Casimir force between impurities in one-dimensional Fermi liquids*, Phys. Rev. A **75**, 043615 (2007).

[106] C. Gardiner, *Handbook of stochastic methods for physics, chemistry, and the natural sciences* (Springer, Berlin, Germany, 1985).

[107] J. Geiser and A. Nasari, *Comparison of Splitting Methods for Deterministic/Stochastic Gross–Pitaevskii Equation*, Math. Comput. Appl. **24**, 76 (2019).

[108] M. J. Steel et al., *Dynamical quantum noise in trapped Bose-Einstein condensates*, Phys. Rev. A **58**, 4824–4835 (1998).

[109] A. Sinatra, C. Lobo, and Y. Castin, *The truncated Wigner method for Bose-condensed gases: limits of validity and applications*[1], Journal of Physics B: Atomic, Molecular and Optical Physics **35**, 3599 (2002).

[110] P. Blakie, A. Bradley, M. Davis, R. Ballagh, and C. Gardiner, *Dynamics and statistical mechanics of ultra-cold Bose gases using c-field techniques*, Advances in Physics **57**, 363–455 (2008).

[111] A. Miller, D. Pines, and P. Nozières, *Elementary Excitations in Liquid Helium*, Phys. Rev. **127**, 1452–1464 (1962).

[112] Y. Kagan, G. V. Shlyapnikov, and J. T. M. Walraven, *Bose-Einstein Condensation in Trapped Atomic Gases*, Phys. Rev. Lett. **76**, 2670–2673 (1996).

[113] U. Schollwöck, *The density-matrix renormalization group in the age of matrix product states*, Annals of Physics **326**, January 2011 Special Issue, 96–192 (2011).

[114] P. Pippan, S. R. White, and H. G. Evertz, *Efficient matrix-product state method for periodic boundary conditions*, Phys. Rev. B **81**, 081103 (2010).

[115] S. Östlund and S. Rommer, *Thermodynamic Limit of Density Matrix Renormalization*, Phys. Rev. Lett. **75**, 3537–3540 (1995).

[116] S. Rommer and S. Östlund, *Class of ansatz wave functions for one-dimensional spin systems and their relation to the density matrix renormalization group*, Phys. Rev. B **55**, 2164–2181 (1997).

[117] D. Porras, F. Verstraete, and J. I. Cirac, *Renormalization algorithm for the calculation of spectra of interacting quantum systems*, Phys. Rev. B **73**, 014410 (2006).

[118] F. Bloch, *Über die Quantenmechanik der Elektronen in Kristallgittern*, Zeitschrift für Physik **52**, 555–600 (1929).

[119] A. M. Kosevich, V. V. Gann, A. I. Zhukov, and V. P. Voronov, *Magnetic soliton motion in a nonuniform magnetic field*, Journal of Experimental and Theoretical Physics **87**, 401–407 (1998).

[120] S. Bresolin, A. Roy, G. Ferrari, A. Recati, and N. Pavloff, *Oscillating Solitons and ac Josephson Effect in Ferromagnetic Bose-Bose Mixtures*, Phys. Rev. Lett. **130**, 220403 (2023).

[121] E. O. Brigham, *The Fast Fourier Transform: An Introduction to Its Theory and Application* (Prentice Hall: Upper Saddle River, NJ, USA, Nov. 1973).

[122] H. F. Trotter, *On the product of semi-groups of operators*, Proc. Amer. Math. Soc. **10**, 545–551 (1959).

[123] M. Suzuki, *Generalized Trotter's formula and systematic approximants of exponential operators and inner derivations with applications to many-body problems*, Communications in Mathematical Physics **51**, 183–190 (1976).

Curriculum vitae

Martin Will

Persönliche Daten

Adresse	Am Harzhübel 56 67663 Kaiserslautern
E-Mail	will_martin@web.de
Geburtsdatum/-ort	10.12.1993 in Grünstadt
Nationalität	Deutsch

Ausbildung

Seit 09.2019	**Promotion**
Thema	„Equilibrium-, non-equilibrium, and steady-state properties of quantum impurities in 1D Bose gases.“
Gruppe	Theoretische Quantenoptik, Prof. Dr. Michael Fleischhauer Technische Universität Kaiserslautern / RPTU Kaiserslautern
04.2014 – 09.2019	**Studium der Physik** Technische Universität Kaiserslautern Diplom mit Auszeichnung Note 1,0
08.2004 – 04.2013	**Gymnasium** Leininger Gymnasium Grünstadt Abitur Note 2,1

Berufserfahrung

04.2013-04.2014	**Freiwilliges Soziales Jahr** Protestantische Jugendzentrale Kirchheimbolanden Organisation und Durchführung von Kinder- und Jugendfreizeiten
Seit 09.2019	**Wissenschaftlicher Mitarbeiter** Technische Universität Kaiserslautern / RPTU Kaiserslautern Modellierung und Simulation komplexer physikalischer Systeme Präsentationen auf nationalen und internationalen Konferenzen Organisation und Betreuung von Vorlesungen und Übungsgruppen

Stipendien und Förderungen

2016-2019	**Deutschlandstipendium,** Technische Universität Kaiserslautern
Seit 01.2021	Promotionsstudent am **„Max Planck Graduate Center** **mit der Johannes Gutenberg-Universität Mainz“**

Ehrenamtliche Tätigkeiten

Seit 2016	**Mitglied der Deutsch Physikalischen Gesellschaft** (DPG) Organisation verschiedener Veranstaltungen der jungen DPG Regionalgruppe Kaiserslautern
Seit 2005	**Mitglied im „Landesverband evangelischer Posaunenchöre Pfalz**“ Tubist in verschiedenen Ensembles
2017-2023	Vorstandsmitglied des Landesverbands
Seit 2019	**Gründungsmitglied des Blechbläserensemble „Brassemble“** Tubist sowie Organisation von Auftritten und Proben

Publikationen

„Rotational cooling of molecules in a Bose-Einstein condensate”
Phys. Rev. A **99**, 062707 (2019)

„Polaron Interactions and Bipolarons in One-Dimensional Bose Gases in the Strong Coupling Regime”
Phys. Rev. Lett. **127**, 103401 (2021)

„Controlling superfluid flows using dissipative impurities”
SciPost Phys. **14**, 064 (2023)

„Dynamics of polaron formation in 1D Bose gases in the strong-coupling regime”
New J. Phys. **25** 083043 (2023)

Qualifikationen

Sprachen	Deutsch (Muttersprache) Englisch (verhandlungssicher)
Programmiersprachen	Python, Mathematica, Java, Haskell
Betriebssysteme	Windows, Linux
weitere Software	Latex, Microsoft Office, Inkscape, Fusion 360, Git

Acknowledgement

Die Fertigstellung einer Doktorarbeit erfordert viel Zeit und bringt zwischendurch immer wieder herausfordernde Phasen mit sich. Dies alles alleine zu bewältigen, wäre kaum möglich. Daher möchte ich an dieser Stelle meinen Dank an all diejenigen aussprechen, die mich während meiner Zeit als Doktorand auf vielfältige Weise unterstützt haben.
Zuerst bedanke ich mich bei meinem Doktorvater Michael Fleischhauer. Du hast mich in den letzten Jahren bestens unterstützt und mir vieles ermöglicht. Ich schätze es sehr, dass du zum einen wissenschaftlich und organisatorisch immer hoch professionell bist, aber zum anderen die Mitglieder deiner Arbeitsgruppe stets freundschaftlich behandelst. Auf diese Weise hast du ein Arbeitsumfeld geschaffen, in dem ich mich immer sehr wohl gefühlt habe!
Mein Dank gilt auch all den anderen Kooperationspartnern, mit denen ich während meiner Zeit als Doktorand zusammenarbeiten durfte. Ohne unsere produktive Zusammenarbeit wären die Erkenntnisse dieser Arbeit nicht möglich gewesen. Genannt seien hier Gregory Astrakharchik, Ryan Barnett, Jonas Jager, Jamir Marino, Benjamin Nagler, Herwig Ott, und Artur Widera.
Ich bedanke mich außerdem bei allen Mitgliedern der Arbeitsgruppe von Michael Fleischhauer und anderen Kollegen aus dem Fachbereich. Mit euch allen konnte man stets spannende wissenschaftliche Diskussionen führen, aber auch der eine oder andere Kaffee zusammen hat im Alltag geholfen mal den Kopf frei zu bekommen, um dann wieder ordentlich durchstarten zu können. Danke dafür an Benno, Carsten, Chris, Daniel, Dennis, Enrico, Eva, Julius, Lukas, Max, Razmik und Simon.
Ich danke allen, die diese Arbeit Korrektur gelesen haben. Eure konstruktive Kritik war äußerst wertvoll und hat maßgeblich zur Verbesserung dieser Arbeit beigetragen.
Ich bedanke mich beim Max Planck Graduate Center mit der Johannes Gutenberg-Universität Mainz für die Unterstützung und den interessanten Einblick in andere Fachbereiche.

Neben denjenigen, die mich während der Arbeitszeit unterstützt haben, gab es auch viele andere, die mir in den letzten Jahren geholfen haben, einen Ausgleich zum manchmal anstrengenden Arbeitsalltag zu finden.
Zunächst seien da alle Mitglieder des Brassemble genannt. Ihr seid eine großartige Truppe, und es ist für mich ein großes Privileg, mit euch allen gemeinsam bei Proben und Konzerten Musik zu machen. Dafür danke ich euch allen!
Mein Dank gilt auch allen Mitgliedern unserer Regionalgruppe der jDPG. Ich habe es sehr geschätzt, sowohl professionelle Veranstaltungen wie „Physiker im Beruf“ mit euch zu organisieren, als auch bei privaten Treffen wie gemütlichen Abenden mit Zwiwwelkuche und neiem Woi dabei zu sein.
Abschließend möchte ich meiner Familie, meinen Eltern Elfriede und Wolfgang und meinen Geschwister Anna und Thomas, danken. Ihr habt mich mein gesamtes Leben, von den ersten Schritten bis zur Promotion, begleitet und stets in allem unterstützt. Dafür gebührt euch mein größter Dank!

Fachbereich Physik

Rheinland-Pfälzische Technische
Universität Kaiserslautern Landau

Postfach 3049
67653 Kaiserslautern, Germany

https://physik.rptu.de/

Rheinland-Pfälzische
Technische Universität
Kaiserslautern
Landau